POLITECNICO DI MILANO

SCHOOL OF CIVIL, ENVIRONMENTAL AND LAND MANAGEMENT ENGINEERING

MASTER OF SCIENCE DEGREE IN CIVIL ENGINEERING
(OB2 - GEOTECHNICS)

THREE DIMENSIONAL PHYSICS BASED EARTHQUAKE SIMULATION SCENARIOS FOR THE SULMONA BASIN (ABRUZZO, ITALY)

Supervisor:
Prof. Roberto PAOLUCCI

Co-Supervisor:
Prof. Ilario MAZZIERI

Candidate:
Tolga YERLİKAYA (891887)

Academic Year of 2019/2020

Acknowledgements

First and foremost I wish to thank my advisor, Prof. Roberto Paolucci, he has been supportive since the days I started working on this project. I wish to express sincere thanks Ms.Manuela Vanini for her frequent help and technical support. I am really grateful to Prof.Ilario Mazzieri and Dr.Infantino for helping me to retain development of this work.

I also owe special thanks to Prof.Simonetta Cola, Prof. Fabio Gabrieli and Dr.Lorenzo Brezzi (Universita degli Studi di Padova) who welcomed me first in academic environment and impressed me to study my Master's degree in Italy. I am very thankful to Prof.Mustafa Kubilay Kelesoglu and Ing.Emine Ertekin who supported me during though times of my academic career. I am deeply indebted to Luca Norese who is a very supportive friend that I met at Politecnico di Milano. Last but no the least, I would like to thank my family, my mother, Pelin Yerlikaya; and my father, Nevzat Yerlikaya. Thanks to their encouragement and support during my stressful times.

Tolga Yerlikaya

I am willing to express my sincere appreciation to my supervisor Professor Roberto Paolucci who has given me the opportunity to work with him, been leading me in this tough yet enjoyable process. I am deeply grateful for all of the supports of Professor Ilario Mazzieri and Dr. Maria Infantino. I would have also been unable to complete this period without my colleague, Tolga Yerlikaya, to whom I show all my respect. Thank you for your vast reliance and credence.

I wish to acknowledge the great love of my family, my wife, Ekin; my mother, Meral; my father, Seyit Mehmet; my little brother, Ismail Cem; and my cat, Harun Duman. Their contribution and impact on me have been fabulous all this time, make me the person I am.

Onur Mercanligil

Abstract

The main scope this work is to carry out a set of 3-dimensional physics based numerical simulations for the Sulmona Basin (Abruzzo, Italy) in order to realize possible ground motion in case of possible earthquake take place, considering the 2009 L'Aquila earthquake occurred in the region of Abruzzo with 6.3 moment magnitude, dominant seismic event is considered the kinematic rupture model of Monte Morrone Fault (MMF) within the region and there is no strong ground motion recordings present in the literature. Additionally, seismic site response spectra and amplification functions in the near-source kinematic rupture model of earthquake simulation code are implemented for different seismic moment magnitude as 6.0 and 6.5, and different soil models are considered as linear visco-elastic and non-linear viscoelastic. All simulations are realized through Spectral Elements with Discontinuous Galerkin aproach (SPEED code) and low period of sets of site response spectra within the Sulmona Basin evaluted through Artifical Neural Networks training to make a correlation of Broad Band motion (ANN2BB). The synthetic ground motions are illustrated and compared with groups of simulations output motions are recorded on virtual situations. Concluding remarks are represented as spectral amplification ratio of the hypothetical scenarios depend on earthquake magnitude, mechanical soil models, and slip distributions, besides, 1-dimensional linear and non-linear analyses of ground motion response are calculated for comparison purposes with respect to 3-dimensional results.

Keywords: physics-based earthquake simulations; elastodynamics; artificial neural networks; non-linear soil model; spectral amplification

Sommario

Lo scopo principale di questo lavoro di tesi è quello di realizzare una serie di simulazioni numeriche tridimensionali basate sulla modellazione del Bacino di Sulmona (Abruzzo, Italia), al fine di prevedere la risposta del terreno in termini di moto sismico nel caso in cui avvenga un terremoto. Per le analisi sono stati considerati i dati relativi all'evento sismico che ha colpito la regione Abruzzo, ed in particolare il Comune dell'Aquila, nel 2009. Al terremoto in questione fu attribuito un valore di magnitudo momento pari 6.3. Particolare attenzione è stata prestata allo studio del modello di rottura cinematica relativo alla faglia di Monte Morrone (MMF) e ai conseguenti effetti di sorgente. Mediante un codice di simulazione numerica, sono stati implementati due valori di ampiezza del moto sismico pari a 6.0 e 6.5. Per entrambi gli scenari sismici, sono stati valutati gli spettri di risposta e le funzioni di amplificazione del terreno situato in prossimità della suddetta faglia.Tutte le simulazioni sono realizzate mediante l'utilizzo del codice di calcolo SPEED, basato sul metodo degli elementi spettrali.Per la valutazione dell'andamento degli spettri di risposta relativi al bacino di Sulmona, è stata eseguita mediante calibrazione di reti neurali artificiali (ANN). Il loro utilizzo ha permesso di ottenere l'andamento degli spettri di risposta per nel range di periodo compreso tra 0 e 0.75 secondi. Successivamente, tali risultati sono stati correlati con gli spettri di risposta relativi ad alti valori di periodo, ottenuti mediante simulazioni 3D. Gli scenari sintetici descriventi il moto sismico sono stati quindi illustrati e confrontati con i risultati ottenuti da diversi gruppi di simulazioni. Inoltre, analisi 1D lineari e non lineari relative al moto sismico sono state confrontate con simulazioni tridimensionali.Le osservazioni conclusive mostrano come i rapporti di amplificazione spettrale relativi agli ipotetici scenari considerati dipenda dall'entità del terremoto, dai modelli costitutivi del suolo e dalle distribuzioni di scorrimento relative alla sorgente sismica.

Parole chiave: simulazioni di terremoto "physics-based"; elastodinamicità; reti neurali artificiali; legami costitutivi non lineari; amplificazione spettrale

Contents

Acknowledgements . . . ii
Abstract . . . ii
Sommario . . . iii

1 Introduction, Preliminary Informations, and Scope of the work 1

2 Sulmona Basin : History, Geology, Tectonics 8
2.1 Introduction . . . 8
2.2 Geomorphology . . . 9
2.3 Mount Morrone Fault . . . 11
2.4 Geology . . . 12
2.5 Seismicity in Central Italy . . . 14

3 Ground Motion Prediction Equations and Numerical Modelling in Engineering Seismology 18
3.1 About Ground Motion Importance . . . 18
3.2 Main methods of predicting earthquake induced ground motion . . . 19
3.2.1 Ground Motion Prediction Equations (GMPEs) . . . 19
3.2.2 Emprical Green's Function (EGF) . . . 20
3.3 Physics-Based Modelling . . . 22

4 Spectral Elements in Elastodynamics with Discontinuous Galerkin (SPEED) Code 30
4.1 Inroduction and General Scheme of the Code . . . 30
4.2 The Pyshical Problem . . . 32
4.3 Spectral Elements' Spatial Discretization . . . 35
4.4 Numerical Integration and Functional Approximation . . . 39
4.5 Absorbing boundary conditions . . . 42

4.6 Time Conditions 43
4.7 Implementation of Seismic Excitation 44
4.7.1 Kinematic Rupture Model 44
4.8 Soil Models in SPEED 47
4.8.1 Linear Viscoelastic Behavior 47
4.8.2 Non-Linear Viscoelastic Behavior 49

5 Artificial Neural Network (ANN) Based Approach to Generate Broadband (BB) Ground Motions for 3D Physics Based Earthquake Numerical Simulations (ANN2BB procedure) 51
5.1 Introduction and Main Principles of ANN 51
5.2 ANN Performance 56
5.3 The ANN2BB Procedure to Produce Broad Band (BB) Strong Ground Motions from 3D PBS 58
5.4 A case Study, Application and Remarks 59

6 Earthquake Simulation Scenarios for the Sulmona Basin 67
6.1 Introduction 67
6.2 Fault Model 69
6.3 Summary of Properties of Simulations 70
6.4 Non-Linear Viscoelastic Behavior of Soil 71
6.5 Virtual Stations' Locations for Ground Motion Measurement 72

7 Time Series of Motion and Peak Ground Motion Maps for Selected Simulations 75
7.1 Time Histories of Acceleration and Peak Ground Acceleration Maps 76
7.2 Effect on Magnitude and Soil Model on the results 89

8 Response Spectra and Spectral Amplification calculations 90
8.1 Groups of Simulations 90
8.1.1 Response Spectra for Selected Virtual Stations . . . 90
8.1.2 GROUP 01: Mw 6.0 - Linear Visco-Elastic Simulations 91
8.1.3 GROUP 02: Mw 6.5 - Linear Visco-Elastic Simulations 93
8.1.4 GROUP 03: Mw 6.0 - Non-Linear Visco-Elastic Simulations 95
8.1.5 GROUP 04: Mw 6.5 - Non-Linear Visco-Elastic Simulations 97

8.2 Selected Spectral Amplification Functions 99
8.2.1 4755 by 1075 for cross-section AA' 100
8.2.2 4755 by 4650 for cross-section AA' 102
8.2.3 4995 by 1075 for cross-section AA' 104
8.2.4 4995 by 4650 for cross-section AA' 106
8.2.5 4412 by 6622 for cross-section BB' 108
8.2.6 4412 by 13429 for cross-section BB' 110
8.2.7 4787 by 6622 for cross-section BB' 112
8.2.8 4787 by 13429 for cross-section BB' 114
8.3 Comments on Affecting Factors for Response Spectra and for Spectral Amplification Ratios considering the Simulations 116
8.4 Comparison of Response Spectra and Spectral Amplifications in 1D vs in 3D analyses 116
8.4.1 Response Spectra in 1D vs in 3D 117
8.4.2 Spectral Amplification Ratio (SAR) in 1D vs 3D . . . 121
8.4.3 Chapter Summary 126

9 Summary and Conclusions **128**

Appendices **132**

A Appendix A - SPEED Scenario ID Cards **133**
A.1 VISCOELASTIC SOIL MODEL WITH Mw 6.0 133
A.2 VISCOELASTIC SOIL MODEL WITH Mw 6.5 138
A.3 NON-LINEAR VISCOELASTIC SOIL MODEL WITH Mw 6.0 141
A.4 NON-LINEAR VISCOELASTIC SOIL MODEL WITH Mw 6.5 143

B Appendix B - Time Histories, Fourier Amplitude Spectra and Response Spectra for selected scenarios and 1NN2BB traning results **146**
B.1 ITA SUL MMF MW6.0 S003 TOPO EL 147
B.1.1 Selected Stations on Soil 147
B.1.2 Selected Stations on Rock 151
B.2 ITA SUL MMF MW6.5 S003 TOPO EL 155
B.2.1 Selected Stations on Soil 155
B.2.2 Selected Stations on Rock 159
B.3 ITA SUL MMF MW6.0 S003 TOPO NEL 163
B.3.1 Selected Stations on Soil 163

B.3.2 Selected Stations on Rock 167
B.4 ITA SUL MMF MW6.5 S003 TOPO NEL 171
B.4.1 Selected Stations on Soil 171
B.4.2 Selected Stations on Rock 175

List of Figures

2.1 Map showing the Abruzzo Region and Sulmona 9
2.2 (above) Relief images showing the Sulmona Basin and the south-western part of Mount Morrone. (below) Active fault segments are represented with black lines (Gori,2014) . . . 9
2.3 Relief map of Abruzzo(Enrico and Tommaso,2011) 10
2.4 Geological structure map of the Abruzzo (Enrico and Tommaso,2011) 11
2.5 Illustration showing structural and geomorphic evolution of the Mt. Morrone. 1. Inactive thrust plane. 2. Active normal fault plane and related deformation zone. 3. Gravitational trough. 4. Gravitational sliding zone/plane. 5. Continental sedimentary sequences. 6. Mesozoic–Cenozoic limestone. 7. Miocene–Pliocene flysch and hemipelagic clays and marls.(adapted after Gori,2014) 12
2.6 Structural sketch map of the central Apennines. 1) Pleistocene marine and continental deposits; 2)Pleistocene volcanics; 3)Pliocene marine sediments; 4)Clastic deposits Early Pliocene 5) Messinian clastic deposits and evaporites; 6) foredeep siliciclastic deposits (Upper Miocene); 7) Meso-Cenozoic shallow-water limestones; 8) Meso-Cenozoic deep-water limestones; 9) thrust; 10) undifferentiated fault; 11) isobaths in meters of the base of the Pliocene deposits. Cosentino et al. (2010) 13

2.7 Geological-structural map of the SW slope of Montagna del Morrone(Miccadei et al., 2004). a) Bedrock units: 1) Superficial deposits; 2) bedded carbonate rocks; 3) massive carbonate rocks; 4) carbonate rocks in thick beds; 5) dolomite rocks; 6) attitude of strata and dip angle; 7) normal faults (a: visible slickenside; b: invisible slickenside); 8) faults. b)Quaternary continental deposits: 1) eluvial and colluvial deposits; 2) sands and gravels; 3) loose stratified carbonate breccias, slope; 4) loose carbonate gravel and breccias, alluvial fan ; 5) stratified carbonate breccias loose or poorly cemented, slope; 6) carbonate gravel and breccias loose or poorly cemented, alluvial fan; 7) heterometric carbonate gravel and breccias loose or poorly cemented, alluvial fan; 8) limestone and clayey-silt, lacustrine; 9) heterometric and chaotic breccias; 10) cemented carbonate gravel and breccias, alluvial fan; 11) bedrock formations ; 12) normal fault (a: visible slickenside; b: invisible slickenside); 13) fault 14
2.8 Simplified tectonic map of Italy and surrounding area s (main tectonic lineaments are redrawn from Polonia et al. 2011). 1) thrusts; 2) major undifferentiated faults. The AfricaEurasia plates configuration is shown in the inset Cadet, J.-P., - Funiciello R. Eds, 2004 Geodynamic map of the Mediterranean. seismic hazar 15
2.9 Map of the earthquakes in CPTI15. The solid blue line indicates the boundary of the area covered by the catalogue. Earthquakes of CPTI11 relocated outside the area are maintained in CPTI15 16
2.10 On the left, Epicenter map of seismicity of $M_L \geq 2.9$ in the Italy region during the period from 2005 to 2017 and on the right, map of the northern and central Italy where the six big magnitude of earthquake events are located. Red stars indicate the major earthquakes, Sulmona Basin is very close to the star number 1. (ML 5:5) listed in Table 1. 17

3.1 Schematic representation of the empirical Green's function method (after Irikura et al., 1997 21

3.2 Summary scheme of Finite Difference Method (adapted after Igel,2017) 24
3.3 Summary scheme of Pseudo-Spectral Method (adapted after Igel,2017) 25
3.4 Summary scheme of Finite Element Method (adapted after Igel,2017) 26
3.5 Summary scheme of Spectral Element Method (adapted after Igel,2017) 27
3.6 Summary scheme of Finite Volume Method (Igel,2017) . . 28
3.7 Summary scheme of Discontinuous Galerkin Method (adapted after Igel,2017) 29

4.1 A model of representing the propagation of seismic waves through a media Ω has to enclose a definite seismic source as kinematic or dynamic.Additinnaly, Ω should include the wave propagation path within a heterogeneous media and site or soil structure interaction (SSI) effects. Representing half-space domain is need to be trimmed by implementing an absorbing boundaries. Adapted after Smerzini (2010). . 34
4.2 Representation of a) conforming mesh algorithm and b) non-conforming mesh algorithm (Adapted from Smerzini(2010). 36
4.3 A representation of the model in the SPEED code which shows hexahedral non-conforming spectral element meshes with non-overlapping sub-domains. Main boundaries are exclusively highlighted. Discontinuous Galerkin approach lead to have (N-adaptivity, where, N1 = 2 in Ω_1 and N2 = in Ω_2) and also for variation of size of meshes locally (h-adaptivity between subdomains $\Omega_1, \Omega_2, \Omega_3$ and Ω_4) (from Mazzieri et al., 2013). 37
4.4 Plots show the 1D reference element with Legendre-Gauss-Lobatto integration points on it. Where reference element is defined by $\Omega_{ref} = [-1,+1]$ Right of the figure shows the conditions in 2D where N=3 and N=10. Adapted after Smerzini(2010) 40

4.5 Lagrange polynomials of degree $N = 4$, Ψq , associated to the q^{th} node on a reference interval $\Omega_{ref} = [-1,1]$. The corresponding $N+1$ Legendre-Gauss- Lobatto (LGL) nodes are plotted by dots on the horizontal axis. (Adopted from Smerzini et al. (2010), Hashemi,K (2017). 41
4.6 Representation of a numerically modelled an extended seismic source in SPEED. Where N_s^k is the spectral nodes of each subdivided major fault that each subfaults are defined as with its own parameters which are shear modulus (μ^k), source area (A^k), slip amplitude (Δu^k, rise time (τ_R^k),rupture velocity (V_R^k) and rake angle as (λ_f^k). (Figure is adapted after Smerzini,C., 2010) 46
4.7 Example of shear modulus degradation curves proposed by Seed and Idriss (1970) (top panels) and damping increment proposed by Idriss (1990) (bottom panels) for sand(right) and clay (left). 50

5.1 ANN Training work-flow scheme. Long period of spectral ordinates $T^* = 0.75s$ indicates the teaching input and the short period of spectral ordinates are predicted by ANN. Additionally, 30 neurons are placed in hidden layers. (i.e. $N_n^h = 30$] (Adapted after Paolucci et al.,(2018)). 54
5.2 Figure showing the main idea of Artificial Neural Network (ANN) approach to generate broadband ground motions. For a given ground motions which is short-period values of spectral ordinates ($T \leq T^*$), where T^* is the minimum period of validity of the physics-based numerical model, is obtained by the computation results of response spectral ordinates for long periods ($T > T^*$). (Adapted after Paolucci et al.,(2018)). 55
5.3 A case study performance of the ANN in prediction with respect to actual recordings based on logarithmic residuals of the response spectral ordinates and the ANN trained prediction for horizontal components.Legend for the bars is TRN for training, VLD for validation, for test set as TST(Adapted after Paolucci et al.,(2018)). 57

5.4 A case study performance of the ANN in prediction with respect to actual recordings based on logarithmic residuals of the response spectral ordinates and the ANN trained prediction for vertical components.Legend for the bars is TRN for training, VLD for validation, for test set as TST(Adapted after Paolucci et al.,(2018)). 58
5.5 Peak Ground Acceleration (PGA) map of geometric mean of horizontal directions, (a) is for ANN2BB approach, (b) is based on hybrid approach based on physics based simulations (PBS) and stochastic methods proposed by Sabetta and Pugliese (1996). (c) 1.5 Hz low pass filtering results of PBS results where dots represent the PGA values are taken from stations on each map. (d) The graph indicates ANN2BB trained values of PGA and recorded values of PGA as a function of Joyner-Boore distance (i.e. R_{JB}) compared to Ground Motion Prediction Equation (GMPE) of Bindi et al.(2014) (i.e. BI14) (Figure is adapted after Paolucci et al.,2018). 61
5.6 (Time Histories for Acceleration, velocity, and displacement (N–S) component at the Mirandola (MRN) station, for 29 May 2012 Po Plain earthquake. (Top to bottom) PBS (Physics Based Simulation) results which are filtered at f_c 1.5 Hz, stochastic waveform (STO) according to Sabetta and Pugliese (1996); (HYB) Hybrid synthetic results that are calculated by coupling PBS at low frequency ($\leq 1.5Hz$) and STO at high frequency ($> 1.5Hz$) with a crossover frequency of f_c = 1.5 Hz, BB synthetics (ANN2BB) are shown considering the HYB upon the ANN-based short-period spectral ordinates; and recorded waveforms (RECs). Adapted from the work of Paolucci et al.,2018) 63
5.7 Acceleration response (on the left) and Fourier spectra (on the right) for North-South (NS) component of motion for Mirandola station (MRN) (Figure is adapted after Paolucci et al.,2018). 63

5.8 Results from The 2012 Po Plain earthquake simulation (Paolucci et al.,2018): Comparison chart for between ANN2BB simulations and recordings at four accelerometric stations (MIR08, T0802, BON0, and MOG0) with respect to acceleration and velocity time histories, and acceleration response spectra. Station are plotted on Figure 5.5 (Figure is adapted after Paolucci et al.,2018). . . 65
5.9 Semivariograms are plotted as crosses for REC and as circles for the ANN2BB approach (circles) for PGA, SA at 0.2 s, SA at 1.0 s, and SA at 2.0 s. The corresponding best-fitting exponential models are denoted by solid line and dashed line for REC and ANN2BB, respectively. In case of short-period response spectral ordinates, the plots for semivariograms are represented as filled squares and best-fitting with solid lines from HYB.(Figure is adapted after Paolucci et al.,2018). 66

6.1 Clear 3D computational model for the Sulmona basin . . . 67
6.2 3D computational model for the Sulmona basin with detailed representation. 68
6.3 3D computational model for the Sulmona basin 69
6.4 3D computational model for the Sulmona basin 69
6.5 Flow chart for modelling kinematic finite-fault source with the UCSB method. (Crempien and Archuleta, 2015) 70
6.6 Fault model drawing and regarding source parameters and general table for the properties that are used in simulation implementations. 70
6.7 Groups and Properties of Scenarios, with respect to magnitude, soil model and slip distributions. 71
6.8 Shear Modulus Decay Curve and Damping Ratio Curve for adapted non-linear viscoelastic soil model. 71
6.9 Topograhphic Map of Sulmona Basin. Including Cross-Sections (AA’ and BB’), selected virtual stations and fault trace 72
6.10 Cross Setion AA’ : Illustrating layers, Virtual Stations and Fault Trace. 73
6.11 Sediment Thickness, $V_{S,30}$ value and Soil Class according to NTC (Italian Construction Code) for Cross Section AA’ . . . 73

6.12 Cross Setion BB' : Illustrating layers, Virtual Stations and Fault Trace. 74
6.13 Sediment Thickness, $V_{S,30}$ value and Soil Class according to NTC (Italian Construction Code) for Cross Section BB' . . . 74

7.1 (Top) Time Series of Acceleration recorded on selected virtual stations, (Bottom) PGA map of area, NS, EW and Vertical (from Left to right) for Simulation of Mw 6.0, Linear Visco-elastic, S003 77
7.2 (Top) Time Series of Acceleration recorded on selected virtual stations, (Bottom) PGA map of area, NS, EW and Vertical (from Left to right) for Simulation of Mw 6.5, Linear Visco-elastic, S003 78
7.3 (Top) Time Series of Acceleration recorded on selected virtual stations, (Bottom) PGA map of area, NS, EW and Vertical (from Left to right) for Simulation of Mw 6.0, Non-Linear Visco-elastic, S003 79
7.4 (Top) Time Series of Acceleration recorded on selected virtual stations, (Bottom) PGA map of area, NS, EW and Vertical (from Left to right) for Simulation of Mw 6.5, Non-Linear Visco-elastic, S003 80
7.5 (Top) Time Series of Velocity recorded on selected virtual stations, (Bottom) PGV map of area, NS, EW and Vertical (from Left to right) for Simulation of Mw 6.0, Linear Visco-elastic, S003 81
7.6 (Top) Time Series of Velocity recorded on selected virtual stations, (Bottom) PGV map of area, NS, EW and Vertical (from Left to right) for Simulation of Mw 6.5, Linear Visco-elastic, S003 82
7.7 (Top) Time Series of Velocity recorded on selected virtual stations, (Bottom) PGV map of area, NS, EW and Vertical (from Left to right) for Simulation of Mw 6.0, Non-Linear Visco-elastic, S003 83
7.8 (Top) Time Series of Velocity recorded on selected virtual stations, (Bottom) PGV map of area, NS, EW and Vertical (from Left to right) for Simulation of Mw 6.5, Non-Linear Visco-elastic, S003 84

7.9 (Top) Time Series of Displacement recorded on selected virtual stations, (Bottom) PGD map of area, NS, EW and Vertical (from Left to right) for Simulation of Mw 6.0, Linear Visco-elastic, S003 85
7.10 (Top) Time Series of Displacement recorded on selected virtual stations, (Bottom) PGD map of area, NS, EW and Vertical (from Left to right) for Simulation of Mw 6.5, Linear Visco-elastic, S003 86
7.11 (Top) Time Series of Displacement recorded on selected virtual stations, (Bottom) PGD map of area, NS, EW and Vertical (from Left to right) for Simulation of Mw 6.0, Non-Linear Visco-elastic, S003 87
7.12 (Top) Time Series of Displacement recorded on selected virtual stations, (Bottom) PGD map of area, NS, EW and Vertical (from Left to right) for Simulation of Mw 6.5, Non-Linear Visco-elastic, S003 88

8.1 Response Spectra for Group 01 for Station 4412 Geo-Mean of Horizontal Motion 91
8.2 Response Spectra for Group 01 for Station 4755 Geo-Mean of Horizontal Motion 92
8.3 Response Spectra for Group 01 for Station 4787 Geo-Mean of Horizontal Motion 92
8.4 Response Spectra for Group 01 for Station 4995 Geo-Mean of Horizontal Motion 93
8.5 Response Spectra for Group 02 for Station 4412 Geo-Mean of Horizontal Motion 93
8.6 Response Spectra for Group 02 for Station 4755 Geo-Mean of Horizontal Motion 94
8.7 Response Spectra for Group 02 for Station 4787 Geo-Mean of Horizontal Motion 94
8.8 Response Spectra for Group 02 for Station 4995 Geo-Mean of Horizontal Motion 95
8.9 Response Spectra for Group 03 for Station 4412 Geo-Mean of Horizontal Motion 95
8.10 Response Spectra for Group 03 for Station 4755 Geo-Mean of Horizontal Motion 96

8.11 Response Spectra for Group 03 for Station 4787 Geo-Mean of Horizontal Motion 96
8.12 Response Spectra for Group 03 for Station 4995 Geo-Mean of Horizontal Motion 97
8.13 Response Spectra for Group 04 for Station 4412 Geo-Mean of Horizontal Motion 97
8.14 Response Spectra for Group 04 for Station 4755 Geo-Mean of Horizontal Motion 98
8.15 Response Spectra for Group 04 for Station 4787 Geo-Mean of Horizontal Motion 98
8.16 Response Spectra for Group 04 for Station 4995 Geo-Mean of Horizontal Motion 99
8.17 Spectral Amplification Ratio (SAR) for Station 4755 by Station 1075 for Group 01 - (geometric mean of horizontal direction 100
8.18 Spectral Amplification Ratio (SAR) for Station 4755 by Station 1075 for Group 02 - (geometric mean of horizontal direction 100
8.19 Spectral Amplification Ratio (SAR) for Station 4755 by Station 1075 for Group 03 - (geometric mean of horizontal direction 101
8.20 Spectral Amplification Ratio (SAR) for Station 4755 by Station 1075 for Group 04 - (geometric mean of horizontal direction 101
8.21 Spectral Amplification Ratio (SAR) for Station 4755 by Station 4650 for Group 01 - (geometric mean of horizontal direction 102
8.22 Spectral Amplification Ratio (SAR) for Station 4755 by Station 4650 for Group 02 - (geometric mean of horizontal direction 102
8.23 Spectral Amplification Ratio (SAR) for Station 4755 by Station 4650 for Group 03 - (geometric mean of horizontal direction 103
8.24 Spectral Amplification Ratio (SAR) for Station 4755 by Station 4650 for Group 04 - (geometric mean of horizontal direction 103

8.25 Spectral Amplification Ratio (SAR) for Station 4995 by Station 1075 for Group 01 - (geometric mean of horizontal direction 104
8.26 Spectral Amplification Ratio (SAR) for Station 4995 by Station 1075 for Group 02 - (geometric mean of horizontal direction 104
8.27 Spectral Amplification Ratio (SAR) for Station 4995 by Station 1075 for Group 03 - (geometric mean of horizontal direction 105
8.28 Spectral Amplification Ratio (SAR) for Station 4995 by Station 1075 for Group 04 - (geometric mean of horizontal direction 105
8.29 Spectral Amplification Ratio (SAR) for Station 4995 by Station 4650 for Group 01 - (geometric mean of horizontal direction 106
8.30 Spectral Amplification Ratio (SAR) for Station 4995 by Station 4650 for Group 02 - (geometric mean of horizontal direction 106
8.31 Spectral Amplification Ratio (SAR) for Station 4995 by Station 4650 for Group 03 - (geometric mean of horizontal direction 107
8.32 Spectral Amplification Ratio (SAR) for Station 4995 by Station 4650 for Group 04 - (geometric mean of horizontal direction 107
8.33 Spectral Amplification Ratio (SAR) for Station 4412 by Station 6622 for Group 01 - (geometric mean of horizontal direction 108
8.34 Spectral Amplification Ratio (SAR) for Station 4412 by Station 6622 for Group 02 - (geometric mean of horizontal direction 108
8.35 Spectral Amplification Ratio (SAR) for Station 4412 by Station 6622 for Group 03 - (geometric mean of horizontal direction 109
8.36 Spectral Amplification Ratio (SAR) for Station 4412 by Station 6622 for Group 04 - (geometric mean of horizontal direction 109

8.37 Spectral Amplification Ratio (SAR) for Station 4412 by Station 13429 for Group 01 - (geometric mean of horizontal direction 110
8.38 Spectral Amplification Ratio (SAR) for Station 4412 by Station 13429 for Group 02 - (geometric mean of horizontal direction 110
8.39 Spectral Amplification Ratio (SAR) for Station 4412 by Station 13429 for Group 03 - (geometric mean of horizontal direction 111
8.40 Spectral Amplification Ratio (SAR) for Station 4412 by Station 13429 for Group 04 - (geometric mean of horizontal direction 111
8.41 Spectral Amplification Ratio (SAR) for Station 4787 by Station 6622 for Group 01 - (geometric mean of horizontal direction 112
8.42 Spectral Amplification Ratio (SAR) for Station 4787 by Station 6622 for Group 02 - (geometric mean of horizontal direction 112
8.43 Spectral Amplification Ratio (SAR) for Station 4787 by Station 6622 for Group 03 - (geometric mean of horizontal direction 113
8.44 Spectral Amplification Ratio (SAR) for Station 4787 by Station 6622 for Group 04 - (geometric mean of horizontal direction 113
8.45 Spectral Amplification Ratio (SAR) for Station 4787 by Station 13429 for Group 01 - (geometric mean of horizontal direction 114
8.46 Spectral Amplification Ratio (SAR) for Station 4787 by Station 13429 for Group 02 - (geometric mean of horizontal direction 114
8.47 Spectral Amplification Ratio (SAR) for Station 4787 by Station 13429 for Group 03 - (geometric mean of horizontal direction 115
8.48 Spectral Amplification Ratio (SAR) for Station 4787 by Station 13429 for Group 04 - (geometric mean of horizontal direction 115

8.49 Response Spectra evaluation of Station 4412 for Simulation Group 01 with respect to 1D (top) and 3D (below) results. (Geometric mean of horizontal direction 118
8.50 Response Spectra evaluation of Station 4412 for Simulation Group 02 with respect to 1D (top) and 3D (below) results. (Geometric mean of horizontal direction 119
8.51 Response Spectra evaluation of Station 4412 for Simulation Group 03 with respect to 1D (top) and 3D (below) results. (Geometric mean of horizontal direction 120
8.52 Response Spectra evaluation of Station 4412 for Simulation Group 04 with respect to 1D (top) and 3D (below) results. (Geometric mean of horizontal direction 121
8.53 Spectral Amplification Ratio (SAR) for Station 4412 by Station 13429 for Group 01 - Magnitude Mw 6.0 - Linear Visco-elastic. Comparison of 1D (above) and 3D (below) results. (Geometric mean of horizontal direction 123
8.54 Spectral Amplification Ratio (SAR) for Station 4412 by Station 13429 for Group 01 - Magnitude Mw 6.5 - Linear Visco-elastic. Comparison of 1D (above) and 3D (below) results. (Geometric mean of horizontal direction 124
8.55 Spectral Amplification Ratio (SAR) for Station 4412 by Station 13429 for Group 03 - Magnitude Mw 6.0 - Non-linear Visco-elastic. Comparison of 1D (above) and 3D (below) results. (Geometric mean of horizontal direction 125
8.56 Spectral Amplification Ratio (SAR) for Station 4412 by Station 13429 for Group 04 - Magnitude Mw 6.5 - Non-linear Visco-elastic. Comparison of 1D (above) and 3D (below) results. (Geometric mean of horizontal direction 126

A.1 ITA SUL MMF MW60 S001 TOPO EL Page 1 of 2 133
A.2 ITA SUL MMF MW60 S001 TOPO EL Page 2 of 2 134
A.3 ITA SUL MMF MW60 S002 TOPO EL Page 1 of 2 134
A.4 ITA SUL MMF MW60 S002 TOPO EL Page 2 of 2 135
A.5 ITA SUL MMF MW60 S003 TOPO EL Page 1 of 2 135
A.6 ITA SUL MMF MW60 S003 TOPO EL Page 2 of 2 136
A.7 ITA SUL MMF MW60 S004 TOPO EL Page 1 of 2 136
A.8 ITA SUL MMF MW60 S004 TOPO EL Page 2 of 2 137
A.9 ITA SUL MMF MW60 S005 TOPO EL Page 1 of 2 137

A.10 ITA SUL MMF MW60 S005 TOPO EL Page 2 of 2 138
A.11 ITA SUL MMF MW65 S002 TOPO EL Page 1 of 2 138
A.12 ITA SUL MMF MW65 S002 TOPO EL Page 2 of 2 139
A.13 ITA SUL MMF MW65 S003 TOPO EL Page 1 of 2 139
A.14 ITA SUL MMF MW65 S003 TOPO EL Page 2 of 2 140
A.15 ITA SUL MMF MW65 S005 TOPO EL Page 1 of 2 140
A.16 ITA SUL MMF MW65 S005 TOPO EL Page 2 of 2 141
A.17 ITA SUL MMF MW65 S003 TOPO NEL Page 1 of 2 141
A.18 ITA SUL MMF MW60 S003 TOPO NEL Page 1 of 2 142
A.19 ITA SUL MMF MW60 S003 TOPO NEL Page 2 of 2 142
A.20 ITA SUL MMF MW60 S004 TOPO NEL Page 1 of 2 143
A.21 ITA SUL MMF MW60 S004 TOPO NEL Page 2 of 2 143
A.22 ITA SUL MMF MW65 S003 TOPO NEL Page 1 of 2 144
A.23 ITA SUL MMF MW65 S003 TOPO NEL Page 2 of 2 144
A.24 ITA SUL MMF MW65 S005 TOPO NEL Page 1 of 2 145
A.25 ITA SUL MMF MW65 S005 TOPO NEL Page 2 of 2 145

B.1 STATION 4412 : ITA SUL MMF MW6.0 S003 TOPO EL . . 147
B.2 STATION 4755 : ITA SUL MMF MW6.0 S003 TOPO EL . . 148
B.3 STATION 4787 : ITA SUL MMF MW6.0 S003 TOPO EL . . 149
B.4 STATION 4995 : ITA SUL MMF MW6.0 S003 TOPO EL . . 150
B.5 STATION 1075 : ITA SUL MMF MW6.0 S003 TOPO EL . . 151
B.6 STATION 4650 : ITA SUL MMF MW6.0 S003 TOPO EL . . 152
B.7 STATION 6622 : ITA SUL MMF MW6.0 S003 TOPO EL . . 153
B.8 STATION 13429 : ITA SUL MMF MW6.0 S003 TOPO EL . . 154
B.9 STATION 4412 : ITA SUL MMF MW6.5 S003 TOPO EL . . 155
B.10 STATION 4755 : ITA SUL MMF MW6.5 S003 TOPO EL . . 156
B.11 STATION 4787 : ITA SUL MMF MW6.5 S003 TOPO EL . . 157
B.12 STATION 4995 : ITA SUL MMF MW6.5 S003 TOPO EL . . 158
B.13 STATION 1075 : ITA SUL MMF MW6.5 S003 TOPO EL . . 159
B.14 STATION 4650 : ITA SUL MMF MW6.5 S003 TOPO EL . . 160
B.15 STATION 6622 : ITA SUL MMF MW6.5 S003 TOPO EL . . 161
B.16 STATION 13429 : ITA SUL MMF MW6.5 S003 TOPO EL . . 162
B.17 STATION 4412 : ITA SUL MMF MW6.0 S003 TOPO NEL . 163
B.18 STATION 4755 : ITA SUL MMF MW6.0 S003 TOPO NEL . 164
B.19 STATION 4787 : ITA SUL MMF MW6.0 S003 TOPO NEL . 165
B.20 STATION 4995 : ITA SUL MMF MW6.0 S003 TOPO NEL . 166
B.21 STATION 1075 : ITA SUL MMF MW6.0 S003 TOPO NEL . 167

B.22 STATION 4650 : ITA SUL MMF MW6.0 S003 TOPO NEL . 168
B.23 STATION 6622 : ITA SUL MMF MW6.0 S003 TOPO NEL . 169
B.24 STATION 13429 : ITA SUL MMF MW6.0 S003 TOPO NEL . 170
B.25 STATION 4412 : ITA SUL MMF MW6.0 S003 TOPO NEL . 171
B.26 STATION 4755 : ITA SUL MMF MW6.0 S003 TOPO NEL . 172
B.27 STATION 4787 : ITA SUL MMF MW6.0 S003 TOPO NEL . 173
B.28 STATION 4995 : ITA SUL MMF MW6.0 S003 TOPO NEL . 174
B.29 STATION 1075 : ITA SUL MMF MW6.0 S003 TOPO NEL . 175
B.30 STATION 4650 : ITA SUL MMF MW6.0 S003 TOPO NEL . 176
B.31 STATION 6622 : ITA SUL MMF MW6.0 S003 TOPO NEL . 177
B.32 STATION 13429 : ITA SUL MMF MW6.0 S003 TOPO NEL . 178

List of Tables

5.1 Selection of Broadband (BB) Earthquake Ground-Motion Simulation Case Studies Relying on Hybrid (HYB) Approaches (Adapted from Paolucci et al.,2018) 53

Chapter 1

Introduction, Preliminary Informations, and Scope of the work

In this work, a set of 3-dimensional physics based numerical simulations for the Sulmona Basin (Abruzzo, Italy) are analysed in order to define possible ground motions with respect to high magnitudes of earthquakes take place, considering the 2009 L'Aquila earthquake occurred in the region of Abruzzo with 6.3 moment magnitude, Sulmona region is within a tectonically active location therefore it is necessary to determine future possible earthquake induced ground motion parameters to be used in engineering practice due to lack of seismic records for the Sulmona Basin.

Special attention to the site effects must be discussed for the preliminary details of this work.Site effects have an important role on results of seismic wave propagation. In short, site effects can be described as effects on complete path from the source to receiver. They may be characterized by how much seismic waves are suspected to modification. Local sedimentary cover, effect of sedimentary basins, effect of alluvial valleys, local topography profile and water table can be considered most important factors to affect propagation of seismic waves. Site effects can amplify or de-amplify the seismic motions before the wave reaching the surface. We cannot neglect them in engineering practice. One may use to classify the soil in-site to estimate site effect. First version of them can be seen in works of Aki (1988) but yet nowadays it is not enough to use soil

classification to estimate the site effects precisely. Site amplification factors are strongly frequency and site dependent, which cannot be generalized for any site. (Kawase, 2003). One may use a technique to obtain site amplification ratio in the frequency domain from the observed records on site, considering recorded ground motion as final product of source, path, and site effects, all combined. Then, the only process to do is extracting the site effects from the obtained data. For example, taking response spectral ratios of two adjacent records with different soil classes. Additionally, horizontal to vertical spectral ratios also can be considered. What is more, physical modelling of seismic wave equation in-site can be used through numerical approaches. Propagation of seismic waves from the source to the virtual receiver can be considered a very advanced and a detailed technique. One may implement configuration and equilibrium equations within simulations, to detect ground motions induced by an arbitrary source of vibration. In case of, having an intense incident wave, soft-soil sediments' behaviour should be characterized within the nonlinear regime, implementing nonlinear mechanical constitutive relationship is necessary for this case for the physical model.
Furthermore, Paolucci et al.(2018) indicated that although ground motion prediction equations (GMPEs) can be considered as most important ingredients of seismic hazard assessment, yet, in engineering practice, they have a lot of main shortcomings such as; proving only peak values of motion; calibration need of a GMPE cover the variety of situations with respect to different combinations of magnitude, distance, fault-slip distribution, directivity, and shallow geological condition with having great amount of variability of ground motions in terms of amplitude, duration, and frequency content; varying empirical coefficients even if calibration is carried out; neglecting the site-specific features, such as surface or buried topographies, basin edges, and irregular soil layering; and not being capable of producing the peak values of motion at multiple sites, strongly limiting their use for seismic hazard and risk assessment study at regional scale, such as within large urban areas. Then, it is necessary to validate earthquake simulation methods and propose their application by engineering applications.

For most of the cases in site-effect studies a 1-D medium means a vertically varying structure. If we have variations in both horizontal directions then it will be a three dimensional (3-D) medium. As the number of varying dimensions increases, the degree of complexity in wave propagation increases and so does the difficulty of modeling and calculation.If the spatial variation is only on the surface of a homogeneous medium, the effects of such a surface irregularity, often called a topographic irregularity, should be much simpler than the variation inside the medium. In the last section we briefly describe topographic effects.

When considering 1D seismic wave propagation model, very simple but effective model for evaluation site effects for ground, layers over a half-space which extended infinitely in horizontal direction. In case of obtaining seismic amplification factor for this model, solving a simple wave equation with sinusoidal input e^{iwt}. Such an evaluation for 2 layered model can be illustrated as, β_0 and β_1 as propagation speeds in halfspace and in soil layer respectively. (either S or P waves can be selected.) Most commonly used amplification factor can be shown as below.

$$|U_1(\omega)| = 2[cos^2(k_1 h) + \gamma^2 (sin)^2 (k_1 h)]^{-0.5} \tag{1.1}$$

where $k_1 = \omega/\beta_1$ is the wavenumber in the surface layer and $\gamma = \rho_1\beta_1/\rho_0\beta_0$ is the impedance contract of two mediums where ρ_0 and ρ_1 are the densities of half-space and surface layer, respectively. If angular frequency $\omega = 2\pi f$ goes to zero, amplification also goes to 2. Also amplification factor for the surface with respect to ground motion at the bottom of the surface layer if it is depth of h below the surface. Then,

$$|U_1(\omega)/U_0(\omega)| = [cos(k_1 h)]^{-1} \tag{1.2}$$

Remarking that, if impedance contrast goes to zero, equation 1.1 directly becomes as equation 1.2 except for factor of 2 which means amplification factor within borehole motion analysis directly corresponds to the same amplification factor with a rigid basement surface. Even though 1-D models provides us to have satisfactory results, however, it is very difficult to analyse all peak frequencies in results. Damping factors, or Q factors as an inverse of damping parameters for surface layers can be implemented through laboratory results to improve the results considering non-linear effect of material behaviour. Because, if the input motion to soft-surface layers, shear strains are built up inside the layer then reaches a certain peak limit, then soil behaves nonlinearly which this behaviour is characterized by reduction of shear modulus and, hence, reduction of shear wave velocity, and increase of damping factor. Considering site effects, this results in prolongation of the predominant periods and reduction of amplification factors.

Furthermore, for modelling of soil layers in 1-D, the soil layers are assumed as flat and they extend infinitely in the horizontal directions. However, in realistic case, in sedimentary basin, as we have in this Sulmona Basin case, there is a confinement for soil and sedimentary rock layers due to intact rock. Additionally, at the edges of the basin, strong seismic wave diffraction takes place because of large velocity contrast. When the existence of vertically or near vertical incident body waves is definite, diffractions at the edge cause to have basin-induced diffracted waves, which are transformed into surface waves rapidly.

The surface waves which induced by presence of the basin, propagate in the horizontal direction inside the basin and these waves generally will arrive later than the direct body waves on the surface of the basin simply because of high aspect ratios (in horizontal extent/in vertical extent) as surface waves have a longer path to travel. The site i.e. Sulmona Region with inhabitants are close to the edge of the basin. Thus, this effect should be taken into account critically. Kawase (1996) named the effect mentioned above as "The Edge Effect" and attributed the damage concentration formed during the Hyogo-ken Nanbu (Kobe) earthquake. Similar amplitude deficiency for basin-induced surface waves can be seen in 2D and 3D models which reported in the literature (Yamanaka et al., 1989; Graves, 1998).

Smerzini (2011) also stated the 3D basin model with a 3D kinematic seismic source has huge advantage over 1D model with vertical plane-wave propagation. Because 1D synthetics can be obtained by convolution of the 1D transfer function with respect to input motion thus leading to have 1D simulations underestimates the spectral amplification factor calculated through ground motion inside the alluvial basin. Then, 3D seismic vibration modes tend to spread the ground motion amplification over a much broader frequency range than in 1D.

Propagation of basin induced diffracted and surface waves and incidence of body waves from the bottom of the basin are formed at the same time. If they meet at some point, then very constructive effect can be expected and thus, amplitude of ground motion will definitely become much larger than a simple 1-D response which can we evaluate in 3D simulations. Kawase et al. (1998) showed that the edge effect is present whatever the source of incident wave, and a 1-D response of the basin without the constructive interference with the edge-induced waves is not sufficient to cause the damage concentration seen in Kobe.

When the source of seismic motion is distant and shallow, regarding incident wave to a basin will consist mainly of surface waves. When the waves reach the basin, some incident wave energy is reflected back yet the rest has effect inside the basin. At the edge of the basin, complex transformation from one mode of surface waves for the surrounding rock to different modes for the basin sediments. Kawase (1993) defined these types of surface waves inside the basin as "Basin-Transduced Surface Waves". Another site effect considering the basin if there irregular bottom shape of the basin exists and it is subjected to a body wave incidence below, one can expect focusing effects where seismic rays propagating in different paths located at the same point, and together at certain points on the surface. At these points, there would be strong amplification or de-amplification can be observed which is can be seen only in 3D model.

Regarding the explanations above, surficial soil layers, seismic waves may be strongly amplified due to contrast between these layers and, possibly, to topographic effects around crests and hills. As the study concerns the Sulmona Basin with sedimentary layers and close to the one of the major faults within the Central Italy, one expects the influence of the geometry of alluvial basins on the amplification factor could be large. What is more, many heterogeneities and complex geometries are not easy to implement into all numerical methods. Three dimensional (3D) models are essential in this case study, and of course, the accuracy of the numerical method is extremely important. Considering seismic radiation conditions for absorbing boundaries are also used in this work to attenuate imaginary wave reflections. Additionally, as a certain point to be indicated, strong earthquakes have nonlinear effects in surficial soil layers. To model strong ground motion, it is thus necessary to consider the nonlinear dynamic behavior of soils and simultaneously investigate seismic wave propagation in complex 3D geological model. As it is used in this work, the spectral element method has been increasingly considered to analyze 2D/3D wave propagation in linear media with a good accuracy because of its spectral convergence properties (Paolucci et al., 2015, Chaljub et al. 2007; Faccioli et al. 1996; Komatitsch and Vilotte 1998).

When dealing with wave propagation in unbounded domains each method has specific advantages and disadvantages. In this work, there is combination of two methods to take advantage of their peculiarities are presented which named as Spectral Elements in Elasto-dynamics with Discontinuous Galerkin (SPEED Code) . SPEED is developed by the Laboratory for Modelling and Scientific Computing (MOX) of the Department of Mathematics and by the Department of Civil and Environmental Engineering (DICA) of Politecnico di Milano. Additionally (Mazzieri, 2013) stated that non-conforming approaches (used in the SPEED code) is very useful and applicable (Chapter 4) in case of evaluating seismic wave propagation more precisely, when complex geometries with different mechanical properties of the medium is present.
In this thesis, chapter organizations are as follows. Chapter 2 covers main tectonic system around Central Appennines with emphasis of geological and geomorphological features of Abruzzo region with a detailed explanation of the system of Monte Morrone Fault (MMF) and general comment of seismicity in Italy.

Chapter 3 includes the main properties of ground motion prediction equations in the literature and general informations such as stochastic and physics-based modelling, additional organization charts for implementing simulations through finite differences, finite volumes, finite elements, pseudo spectral method, spectral elements and discontinuous galerkin elements.

Chapter 4 explains the main philosophy and implementation way of simulations within the SPEED code with specific emphasis on formulations of wave equation problem within a media using spectral elements with discontinuous galerkin scheme providing with kinematic model of rupture and soil material model.

Chapter 5 is devoted to training scheme of ANN2BB approach which is based on artificial neural networks (ANNs) trained on earthquake induced motion records to have correlation of response spectra plots of short periods taking into account of long period response spectra.

Chapter 6 shows the numerical model which is adapted for Sulmona basin with including number of elements, degree of freedom of the system with different groups of scenarios based on different magnitude and different soil models with other relevant parameters and properties within the basin model.

Chapter 7 summarizes time series of motion, peak ground acceleration, peak ground velocity and peak ground displacement values for 4 selected simulations which are described by having same slip distribution but for different moment magnitude of earthquakes and different soil models in order to make emphasis on the observed comments for differences between results.

Chapter 8 illustrates group of simulations' average values of site response spectra and spectral amplifications are for virtual stations and, moment magnitude and soil models are discussed based on their influence of results, and finally comparison of 1d vs 3d spectral amplifications for soil models..

In Appendix A, scenario id cards for all the simulations are placed that showing fault source parameters, site location map, slip distribution, rupture time, rise time and corresponding peak ground motion maps and spectral acceleration value maps for specific time periods.

In Appendix B, comparison of stochastic, physics based simulations and ANN2BB trained ground motion time plots, Fourier amplitude spectra and response spectra charts can be seen for the 4 selected simulations with different magnitude and different soil models.

Chapter 2

Sulmona Basin : History, Geology, Tectonics

2.1 Introduction

Galadini and Galli (1999) indicated two parallel sets of seismogenic normal-fault systems are dominant along the central Appennines. Accordingly, Abruzzo region is located on the eastern central Apennines. Very complex setting of geological and structural framework and their evolution are totally related to the main geomorphological evolution of the region because of the formation of the Mediterranean mountain system within the Central Appennine thrust belt in late Miocene. Main triggering geomorphological activities can be summarized as due to extensional tectonics, uplift processes and substantial morphostructural affected the region (Enrico and Tommasso, 2011). Main interest on this work is one of the eastern-most intermountain depression of the Central Apennines as the Sulmona Basin which is also known as Peligna Valley which elongated through NW-SE direction. (Figure 2.1 and 2.2)

Figure 2.1: Map showing the Abruzzo Region and Sulmona

Figure 2.2: (above) Relief images showing the Sulmona Basin and the south-western part of Mount Morrone. (below) Active fault segments are represented with black lines (Gori,2014)

2.2 Geomorphology

Subduction of the Adriatic microplate caused to formation of the east-direction very deep chained orogenic activities during

Neogene-Quaternary, these processes reshaped the Abruzzo region's main geomorphological setting. Thus, the Abruzzo region is considered as tectonically very active region and additionally after Pliocene by extensional tectonics had started to give the shape of the initial formation of the Sulmona basin, uplift processes and substantial morpho-structural processes that have activated tectonics of the basin (Miccadei et al., 2017 and D'Alessandro et al., 2003). The relief features within the Abruzzo region are shaped by a series of ridges which have directions from NW-SE to N-S, divided one another with narrow valleys, parallel to the ridges, or by wide intermontane depressions (Coltorti and Pieruccini, 2000). Furthermore, NW-SE fault systems are considered to be related with regional uplift and caused to have a topographic bulge and the formation of inter-montane basins related to local tectonic subsidence, where one of them is the Sulmona basin. (Doglioni et al., 1998; Miccadei et al., 2002). Finally, and D'Alessandro et al. (2003) have stated that within these chains, exhumed thrust ridges are separated by valleys which are formed due to tectonics, fault lines, and basins which are formed by regional tectonics, partially filled up crustal deposits. (Figure 2.3 and Figure 2.4) The most important morphological elements in the Piedmont Periadriatic region are the homoclinic relief (softly NE dipping), mesa relief, dip-stream valleys (SW-NE), and alluvial plains. The latter grade goes eastwards to the coastal plain and the tectonic Sulmona basin. The integrated morpho-tectonic approach to the study of the central Apennine chain's mountain landscape allows us to delineate the main steps of the escarpment between Montagna del Morrone and the Sulmona basin(Miccadei et al., 2002).

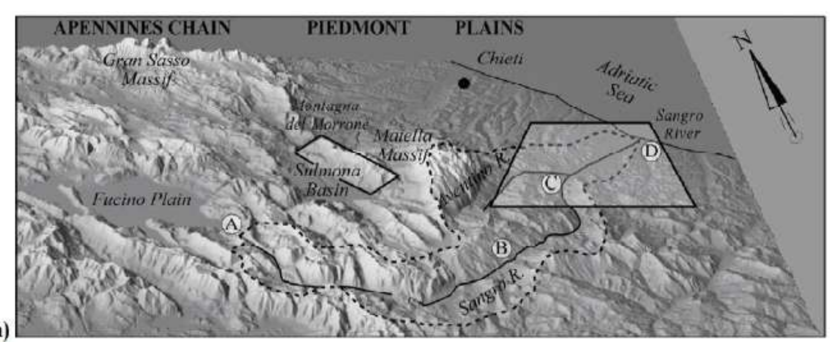

a)

Figure 2.3: Relief map of Abruzzo(Enrico and Tommaso,2011)

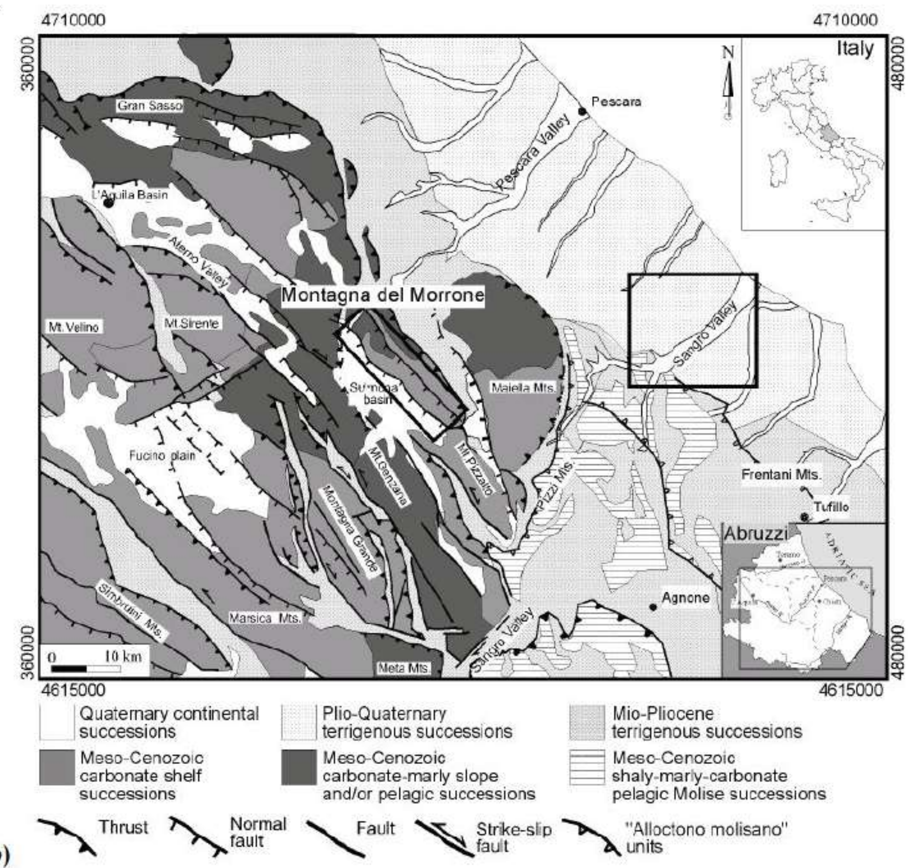

b)

Figure 2.4: Geological structure map of the Abruzzo (Enrico and Tommaso,2011)

2.3 Mount Morrone Fault

(Galadini and Galli 2000)stated that faults in the western region of the Central Italy is main actor for strong historical earthquakes of which are up to M_w 7.0. According to Galadini and Galli (2001) and Ceccaroni et al. (2009), Regarding fault system was tectonically caused to that great magnitude of earthquakes around 1800 years ago. Thereby, since last its activation, re-occurrence or reactivation of faults in central Apennines are expected near future where the Mt. Morrone fault is taken into account as one of the most troublesome Italian tectonic situations.(Figure 2.5) Additionally, (Barchi et al., 2000 and Galadini and Galli 2000) indicated that Central Italy's recent active tectonics is mostly affected by the active natural faults within the central Apennines.

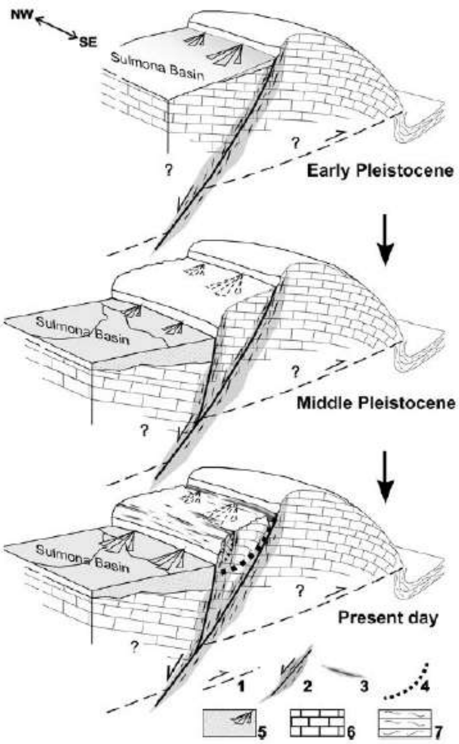

Figure 2.5: Illustration showing structural and geomorphic evolution of the Mt. Morrone. 1. Inactive thrust plane. 2. Active normal fault plane and related deformation zone. 3. Gravitational trough. 4. Gravitational sliding zone/plane. 5. Continental sedimentary sequences. 6. Mesozoic–Cenozoic limestone. 7. Miocene–Pliocene flysch and hemipelagic clays and marls.(adapted after Gori,2014)

2.4 Geology

Cosentino et al. (2010) briefly explains the local geology as the Central Appennines are characterized by orogenic peri-Mediterranean belt which is formed in Neogene due to the collision and convergence of European and African plates, additionally, stratigraphic analyzes pointed out to existences of outcropping formations of Meso-Cenozoic carbonates and Miocene terrigenous.

Main basin is formed in Late Triassic with shallow-water carbonate sediments due to rifting stage affected the Neotethyan region during the Middle Liassic (Ciarapica and Passeri., 2002). Enrico and Tommaso (2011) showed that main bedrock units are examined as carbonate rocks from Lias to Paleogene age, and quaternary continental deposits within the Sulmona Basin are breccias and conglomerates that can be referred to talus slope and debris cones, alluvial fans and colluvial coverings which are placed between the Early Pleistocene and the Holocene, based on comparisons with the Sulmona basin sector South west scarp of Mount Morrone Fault (MMF) is formed by the limb of the anticline structure are dislocated due movement of normal faults, known as the Monte Morrone fault zone.(Miccadei et al., 2002, 2004). Regarding geomorphology and bedrock formations and superficial deposits are illustrated below (Figure 2.5 and 2.6)

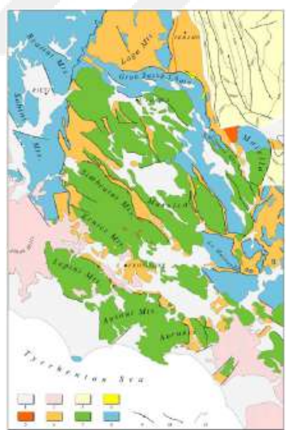

Figure 2.6: Structural sketch map of the central Apennines. 1) Pleistocene marine and continental deposits; 2)Pleistocene volcanics; 3)Pliocene marine sediments; 4)Clastic deposits Early Pliocene 5) Messinian clastic deposits and evaporites; 6) foredeep siliciclastic deposits (Upper Miocene); 7) Meso-Cenozoic shallow-water limestones; 8) Meso-Cenozoic deep-water limestones; 9) thrust; 10) undifferentiated fault; 11) isobaths in meters of the base of the Pliocene deposits. Cosentino et al. (2010)

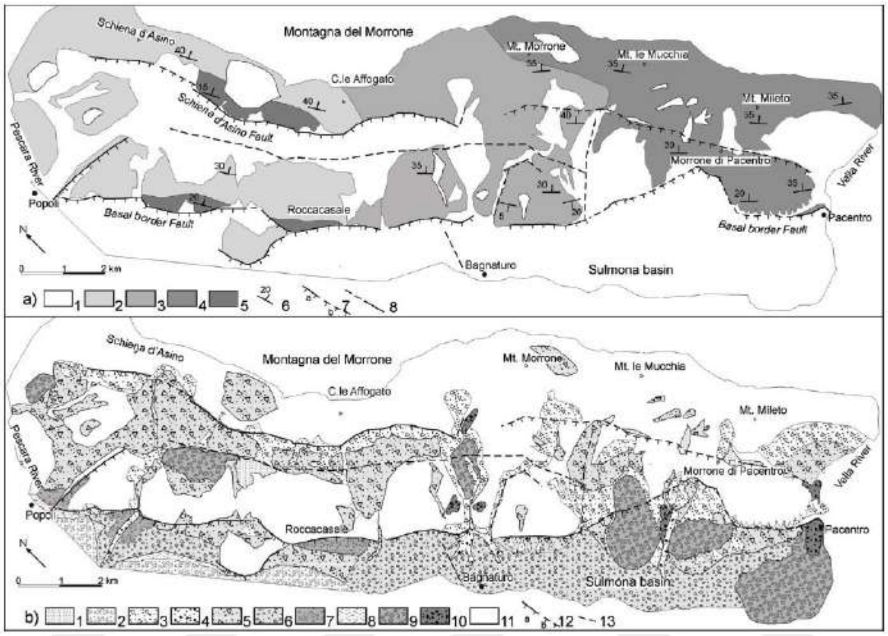

Figure 2.7: Geological-structural map of the SW slope of Montagna del Morrone(Miccadei et al., 2004). a) Bedrock units: 1) Superficial deposits; 2) bedded carbonate rocks; 3) massive carbonate rocks; 4) carbonate rocks in thick beds; 5) dolomite rocks; 6) attitude of strata and dip angle; 7) normal faults (a: visible slickenside; b: invisible slickenside); 8) faults. b)Quaternary continental deposits: 1) eluvial and colluvial deposits; 2) sands and gravels; 3) loose stratified carbonate breccias, slope; 4) loose carbonate gravel and breccias, alluvial fan ; 5) stratified carbonate breccias loose or poorly cemented, slope; 6) carbonate gravel and breccias loose or poorly cemented, alluvial fan; 7) heterometric carbonate gravel and breccias loose or poorly cemented, alluvial fan; 8) limestone and clayey-silt, lacustrine; 9) heterometric and chaotic breccias; 10) cemented carbonate gravel and breccias, alluvial fan; 11) bedrock formations ; 12) normal fault (a: visible slickenside; b: invisible slickenside); 13) fault

2.5 Seismicity in Central Italy

Between Miocene and Pliocene, tectonics of the central Mediterranean region are mostly dominated by a phase of opening of the Tyrrhenian basin and the formation of the Apennines chain which now cause to formation of a thrust belt around Central Italy. (Patacca and Scandone, 1989) (See Figure 2.8). The Italian region holds a prominent role in the Mediterranean region, one of the most geodynamically diverse of the Earth's regions. Due to the collision of African and Eurasian plates, this region is active (e.g., Doglioni et al . 1998).

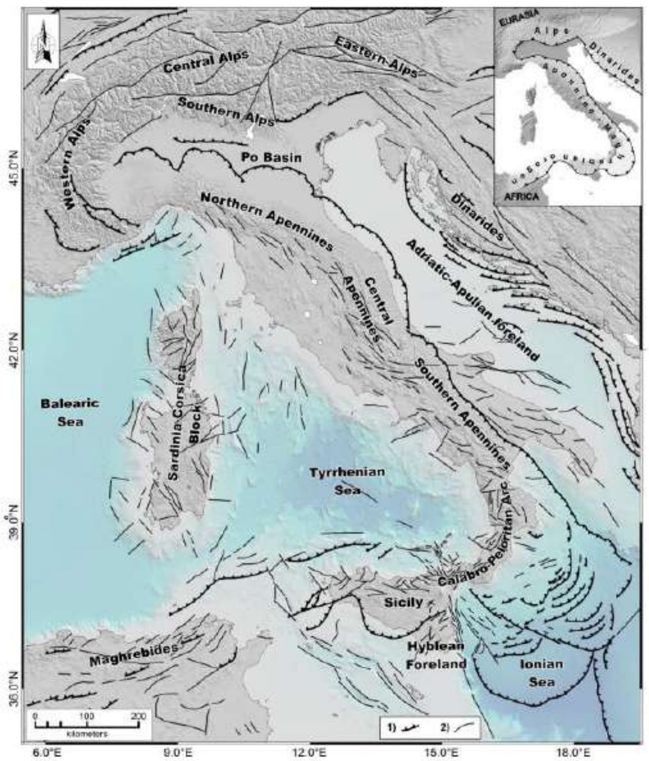

Figure 2.8: Simplified tectonic map of Italy and surrounding area s (main tectonic lineaments are redrawn from Polonia et al. 2011). 1) thrusts; 2) major undifferentiated faults. The AfricaEurasia plates configuration is shown in the inset Cadet, J.-P., - Funiciello R. Eds, 2004 Geodynamic map of the Mediterranean. seismic hazar

In Quaternary, active thrust system in the Central Italy cause to have extension movement due the formations of a zone of normal fault running along the mountain range crest which is approximately 30 km long and is defined by an region of observable extension pressure (D'Agostino et al., 2012). Observation and records of the earthquakes which are $M_L \geq$

5.5, these regions have been the most seismically active areas of Italy in the last twelve years (Zhuang, 2018) and additionally Italian Earthquake Catalogue Map (CPTI15)(Catalogo Parametrico dei Terremoti Italiani) is illustrated. (Figure 2.9).

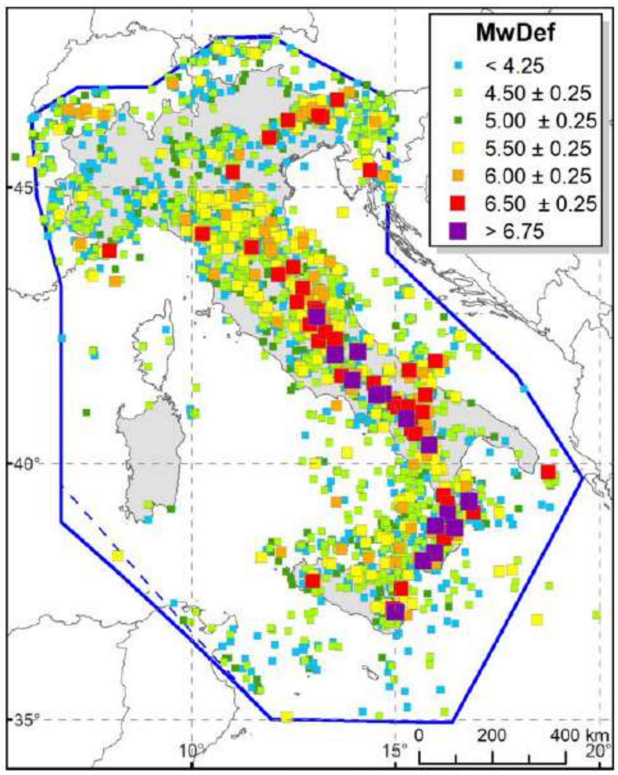

Figure 2.9: Map of the earthquakes in CPTI15. The solid blue line indicates the boundary of the area covered by the catalogue. Earthquakes of CPTI11 relocated outside the area are maintained in CPTI15

The findings obtained suggest that the triggering of Monte-Morrone may result in a catastrophic earthquake in the heavily populated sector of the Sulmona plain and surrounding areas, where numerous villages (such as Sulmona, with approximately 25,000 inhabitants, Pratola Peligna, Popoli and Pacentro) are located, significant motorways, monuments and archaeological remains. This picture indicates that future applied work activities will be approached at generating seismic microzonations and hazard scenarios in order to provide effective preparation for the action required to minimize this seismic risk.(See Figure 2.10)

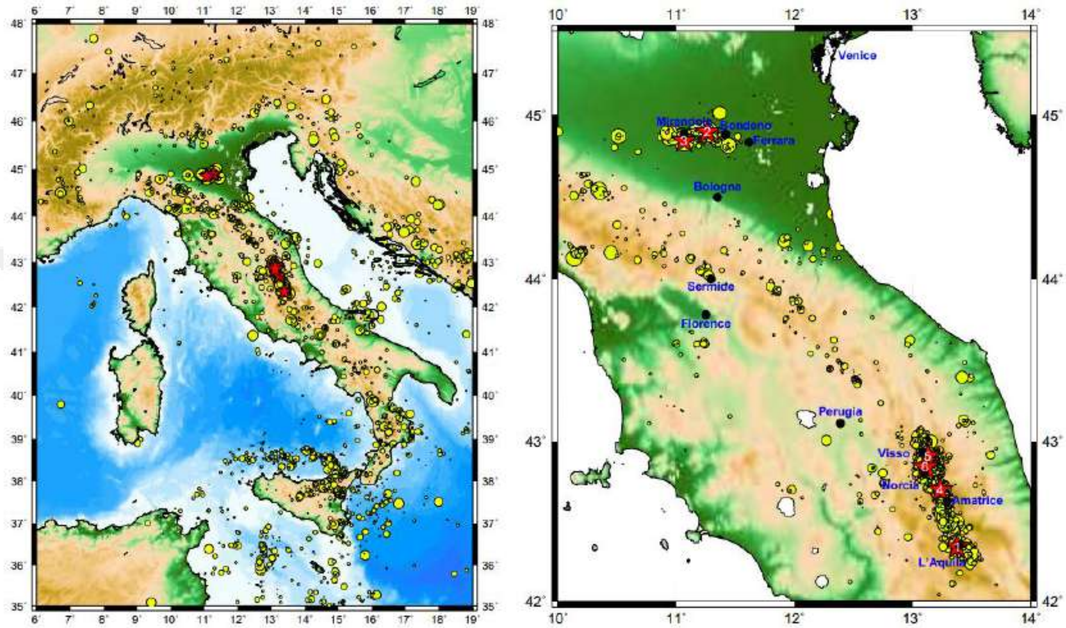

Figure 2.10: On the left, Epicenter map of seismicity of $M_L \geq 2.9$ in the Italy region during the period from 2005 to 2017 and on the right, map of the northern and central Italy where the six big magnitude of earthquake events are located. Red stars indicate the major earthquakes, Sulmona Basin is very close to the star number 1. (ML 5:5) listed in Table 1.

Chapter 3

Ground Motion Prediction Equations and Numerical Modelling in Engineering Seismology

3.1 About Ground Motion Importance

In order to predict parameters of a large magnitude earthquake induced ground motions in terms of amplitude, duration etc. are very essential in engineering seismology. Furthermore, to determine an interval with reasonable error range for possible earthquake induced damage, economic loss and injuries, ground motion predictions has a very important part to estimate seismic hazard for a site to be sure about seismic design for structures and for the lands in use. These parameters in detail can be considered as peak ground acceleration (PGA), peak velocity (PGV), peak ground displacement (PGD), spectral response acceleration (SA), spectral response velocity (SV), spectral response displacement (SD). Within a specific accuracy for the design, estimation of ground motion parameters may be evaluated through, regarding presence of accurate ground motion time history for a seismic event

3.2 Main methods of predicting earthquake induced ground motion

3.2.1 Ground Motion Prediction Equations (GMPEs)

In brief, a ground motion prediction equation shows a possible prediction of ground motions parameters based on as a function of $Y = f(M, R, S, X_i)$ and are expressed as a set of empirical coefficients that obtained through regression analyses that are applied to ground motion recordings. GMPEs has the main key role in order to make assessments of seismic hazards because they are used in detail to predict the value of the probabilistic distribution of ground movement at a specific site, in general as form of a log-normal distribution).

i.Magnitude of Earthquake M
ii.Distance R,
iii .Near surface site characteristics S, and
iv. in some case, other variables X_i

Note that, where Y is the ground motion parameter of interest. Then Y could be a value of
i. PGA - Peak Ground Acceleration
ii. PGV - Peak Ground Velocity
iii. PGD - Peak Ground Displacement
iv. S_a - Spectral Acceleration
v. S_v - Spectral Velocity
vi. S_d - Spectral Displacement.

Functional form as it minimizes the number of empirical coefficients and allows for better confidence interval for statistical analysis when using empirical relationships to situations (in terms of magnitude and distances from source to site) that are poorly described in the large motion database. Douglas (2003) presented a detailed analysis of the equations for numerical calculation of peak ground motion parameters and spectral response ordinates, for further details please refer to that author. The most common types of laws on empirical attenuation can be summarized as below.

Firstly, Ground motion parameters (Y) are distributed log-normally, then linear or non-linear regression is carried out for logY. Then, LogY can be considered as proportional to M which depends on the concept of magnitude M (Hanks and Kanamori, 1979; Kanamori, 1977). Followed by, for body waves, geometric spreading produces amplitude that decreases with distance according to 1 = R with computation of source-to-site distances: hypocentral R_{hy}, epicentral R_e, rupture R_f (distance to surface rupture) and Joyner-Boore distance R_{JB} (distance to the surface projection of the rupture plane of the fault) are commonly used. Additionally, Source features like focal mechanism, source depth, directivity and local site conditions such as rock location, soft rock location, and alluvium site. Relative ground motion plots within the near source region of a large magnitude of earthquake is the main feature of the dataset used to construct ground motion prediction equations.

One should ask how to have accurate predictions for near-fault earthquake ground movements. If one uses the GMPEs based on very rich dataset of high-quality strong motion records, the records regarding to small and large magnitude of earthquake occurred win the near-source area do not show major deviations from the predictions obtained from recent observational attenuation rules. For large magnitude of earthquakes, however, it is possible that the relationship between the chosen GMPEs and close fault data will deteriorate. Moreover, these models cannot replicate the observed variability of heavy ground movement in the vicinity of the seismic source, since they have an isotropic distribution of the expected parameters of ground motion. Some

3.2.2 Emprical Green's Function (EGF)

The Empirical Green's Function (EGF) can be explained as a major earthquake is simulated by combining several small earthquake records based on spatial scaling relationships with source parameters measured in the studied field from earthquake events. In this approach, one can use utilize provided effects of propagation path, local site and rupture propagation on the fault plane and the geometric relationship between

the source and the motion recording station. Irikura (1983) used this technique for to calculate the number of small events needed in the superposition from the seismic moment ratio between large and small events.
The basic principle of the Empirical Green's Function (EGF) process, based on the works of Hartzell (1978) and Irikura (1983) that utilization of reports of minor earthquakes are used to predict the ground motions caused by a major earthquake which is in general indicated as the target event. Idea was simple, gathering a collection of records of minor earthquakes from the same seismogenic source of the target. In addition, observations of minor earthquakes are correlated with a very specific source process such that the observed uncertainty can be related to the propagation direction from source to location, rather than to the source itself, through the crust. In detail, from the foreshocks or aftershocks of a mainshock of small magnitude of earthquake considered as point dislocation functions to model the possible major earthquake, considering the same fault and the same direction of propagation for the target earthquake and the minor earthquakes are similar to each other. A schematic simulation of the EGF method is given in Figure 3.1 Additionally, Irikura (1986) and Irikura et al. (1997) enhanced this technique by implementation of exponential slip function to enrich low frequency energy in predictions. (Figure 3.1)

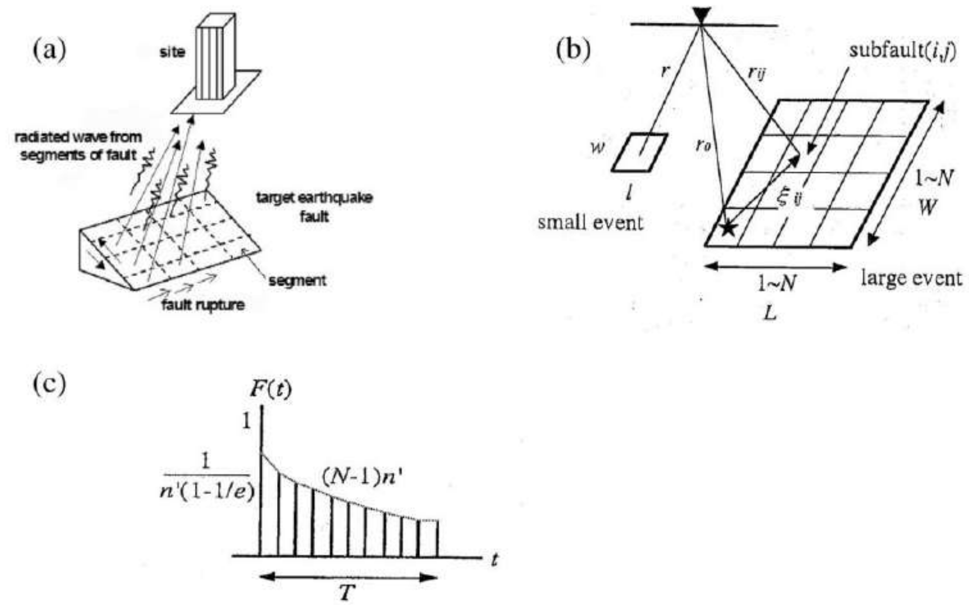

Figure 3.1: Schematic representation of the empirical Green's function method (after Irikura et al., 1997

3.3 Physics-Based Modelling

Thanks to advancements of increase of number computational resources and computational power, three dimensional physics-based numerical simulations (PBS) approach to evaluate seismic wave propagation within media, are started to use in academics frequently and especially in cases where complex geometry of faults, different geological settings and various topographical structures and also for soil-structure interaction processes can be evaluated due to having a great impact on ground movement and ground motion records. Recent developments can be seen in various published academic papers.(Paolucci et al., 2018, Raza ndrakoto et al., 2018; Bradley et al., 2017; Evangelista et al., 2017; Taborda et al., 2016; Goulet et al., 2015; Paolucci et al., 2015; Taborda and Bielak, 2013; Smerzini and Villani, 2012; Guidotti et al., 2011; Pilz et al., 2011).

In short, Physics-based numerical simulations are carried out of two stages which are modelling fault rupture and simulating the seismic wave

propagation. Kinematic source models are used to simulate the rupture process within time dependent scheme and indicating the displacement field on the fault plane except for the forces along the fault plane.
By solving the elasto-dynamic equations of motion under a specified constitutive rule (friction model), the slip distribution and the temporal evolution of the break are accomplished. Within the models of dynamic rupture are works from: Guatteri et al. (2003, 2004); Aochi and Douglas (2006); Ripperger et al . (2008). To simulate the wave propagation in the called physical domain, the computational techniques involve a discretization into a grid of geometrical elements where the equation of wave propagation is solved by a correct discrete spatio-temporal approximation of the solution in terms of the displacement values at n grid points (nodal displacements). One of the major distinctions between the different methods is based on the space-dependent elds being discretized. For further details and for the physics based modelling that is used to in this work, please refer to chapter 4.
As an addition, different number of modelling techniques in computational seismology for earthquake simulations can be summarized as follows (Igel, 2017). The Finite Difference Method (FDM) (Fig 3.2), where series-extension methods to make approximations for the arbitrary function f(x) by a sum of other base functions over the whole domain itself. To get vector-series coupling (such as normal spaced grid points and Fourier series), the arbitrary equation at the grid points can be interpolated precisely (together with its derivatives). If the derivatives are calculated using Fourier transforms, the Fourier Pseudo-spectral Approach method can be taken into account(Fig 3.3)is renamed. For, Finite Element Methods (FEM) where the physical domain is divided into finite elements and main technique of approximation to solution fields are obtained through linear functions which are defined for each elements which are totally continuous across the boundaries of the elements.(Fig 3.4) Taken into account of possibility to use of higher-order polynomial approximations may lead to have more precise results. In case of Spectral Element Methods (SEM),where polynomial approximations of the higher order are Lagrange polynomials. (Fig 3.5). Then, as an another method consists of defining finite volumes where a mean of function values are implemented. Since here the approximate fields inside the cells are discontinuous across the boundaries of the cells, it is necessary to exchange the definition of fluxes between the cells. This

property of implementation can be seen both in the Finite Volume Method and the Discontinuous Galerkin Method. (Fig 3.6) Due to the fact that, lack of a definite and an accurate model for high frequencies is one of the main negative aspects for the physics based simulation, which for correction regarding ANN2BB training will be taken into account in chapter 5 for that reason. While referring the reader to Igel (2017) for a detailed review, Figures (3.2) to (3.7) summarize the main features, advantages , limitations and key references of the most relevant numerical procedures based on physics, with particular attention being paid to the Spectral Element with Discontinuous Galerkin approach adopted in this thesis, in detail please refer to chapter 4 and chapter 5.

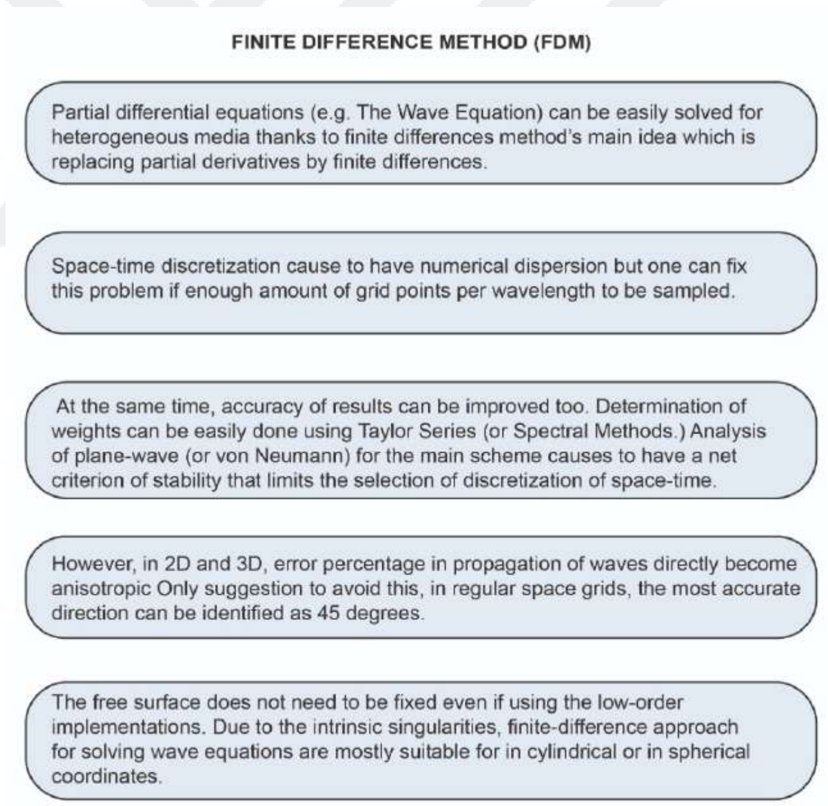

Figure 3.2: Summary scheme of Finite Difference Method (adapted after Igel,2017)

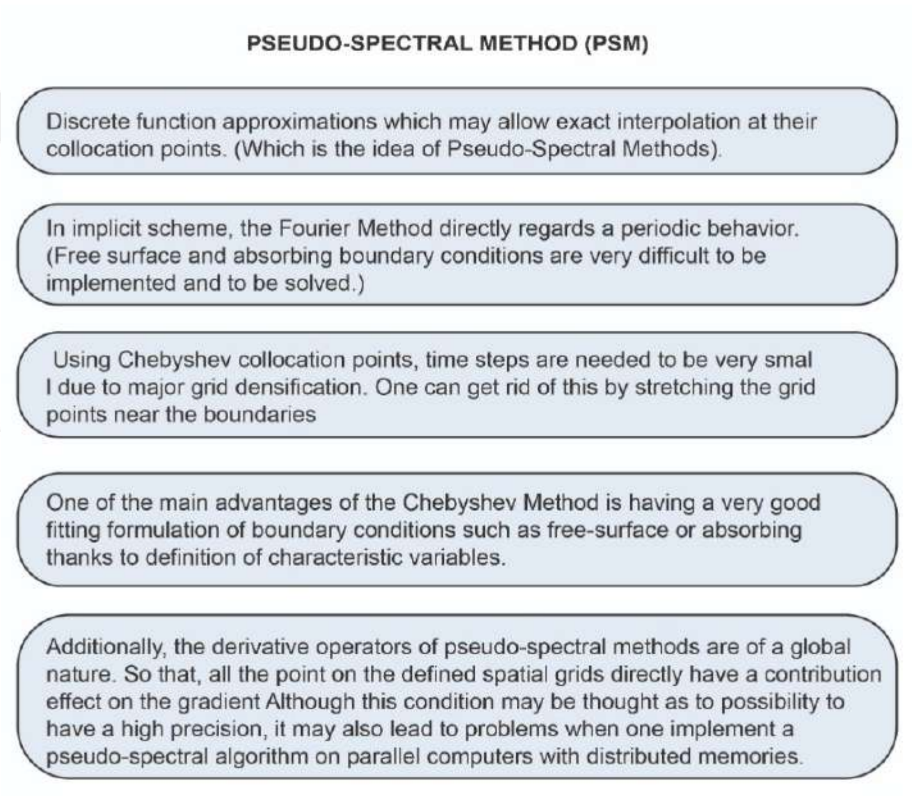

Figure 3.3: Summary scheme of Pseudo-Spectral Method (adapted after Igel,2017)

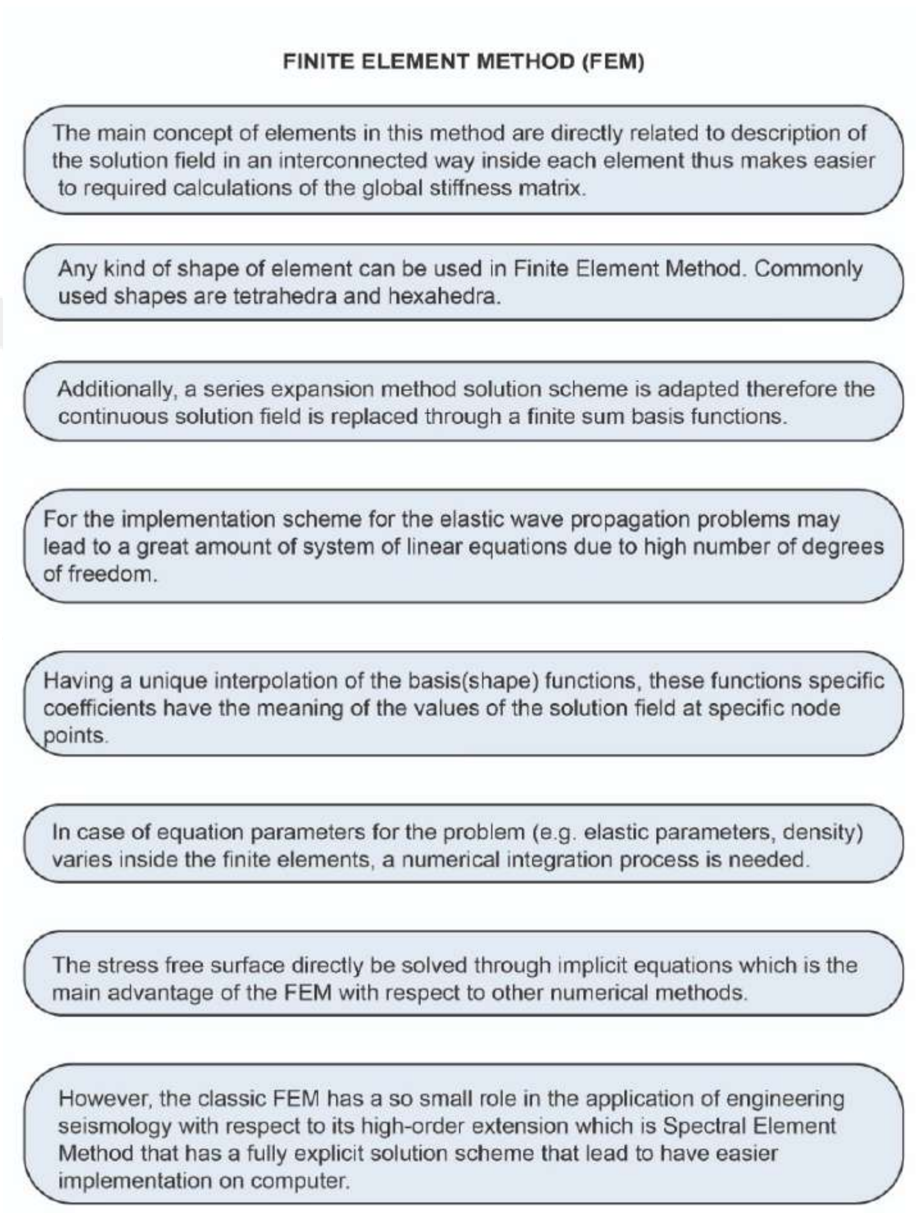

Figure 3.4: Summary scheme of Finite Element Method (adapted after Igel,2017)

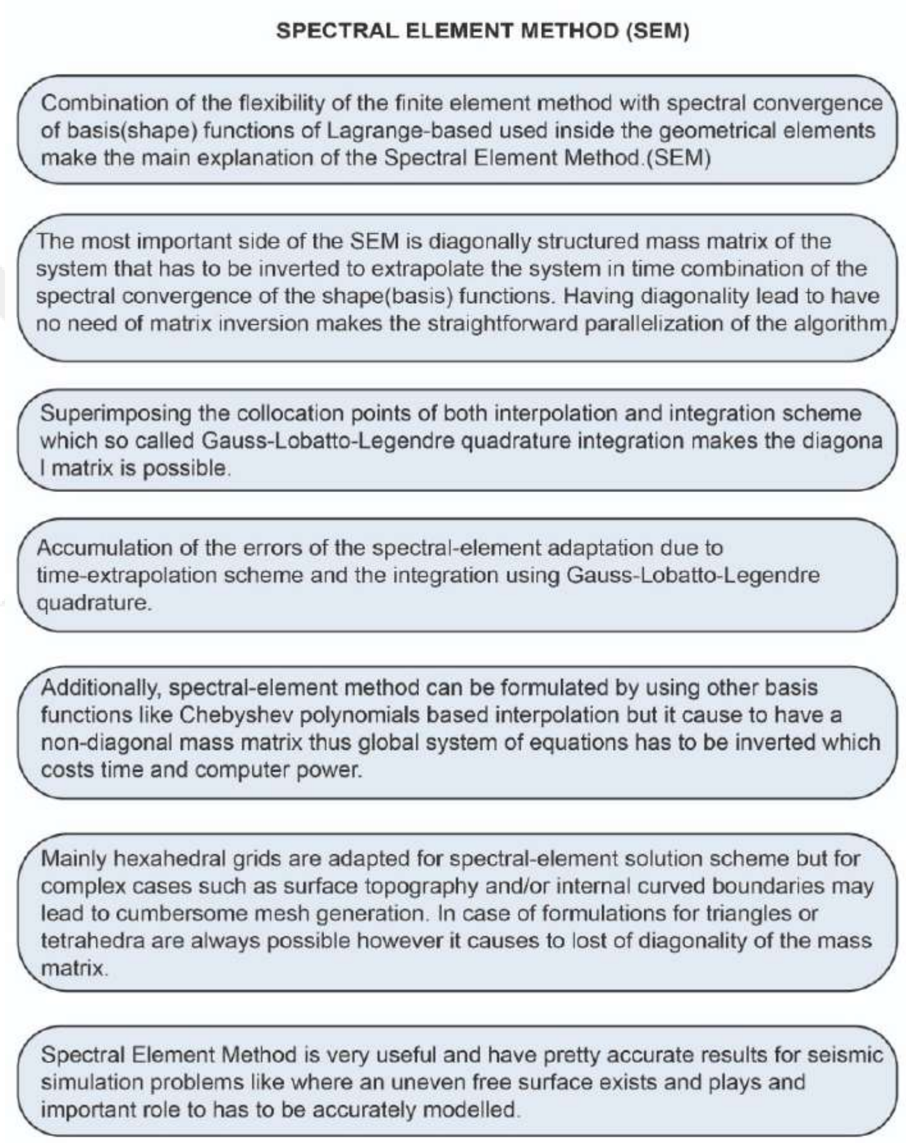

Figure 3.5: Summary scheme of Spectral Element Method (adapted after Igel,2017)

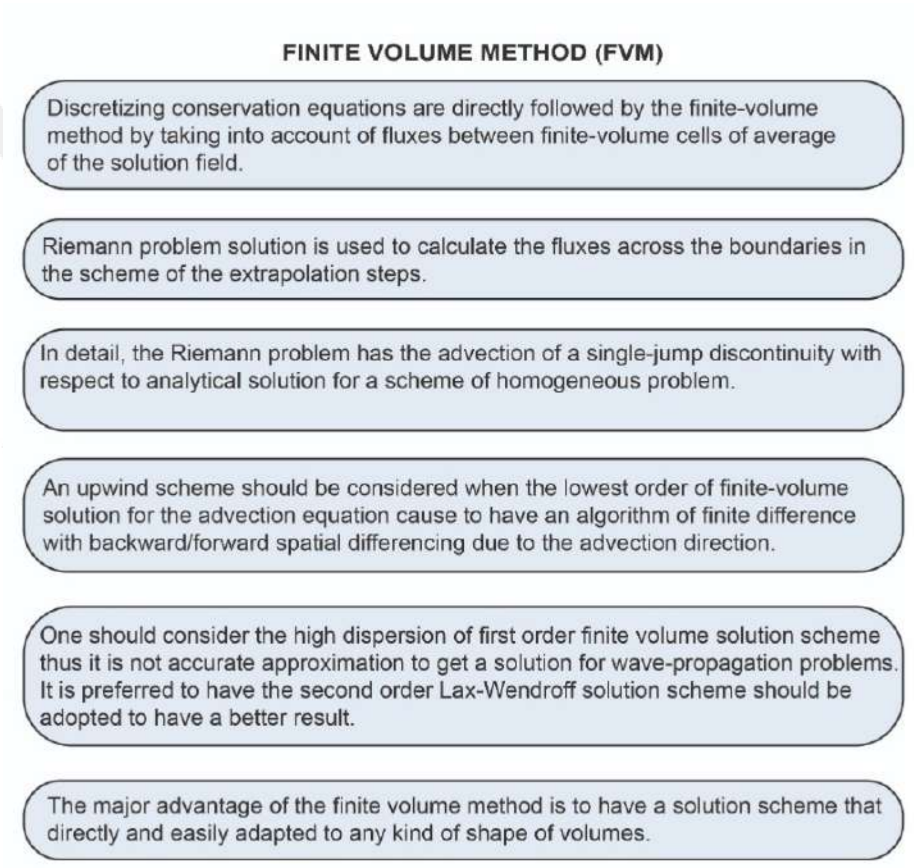

Figure 3.6: Summary scheme of Finite Volume Method (Igel,2017)

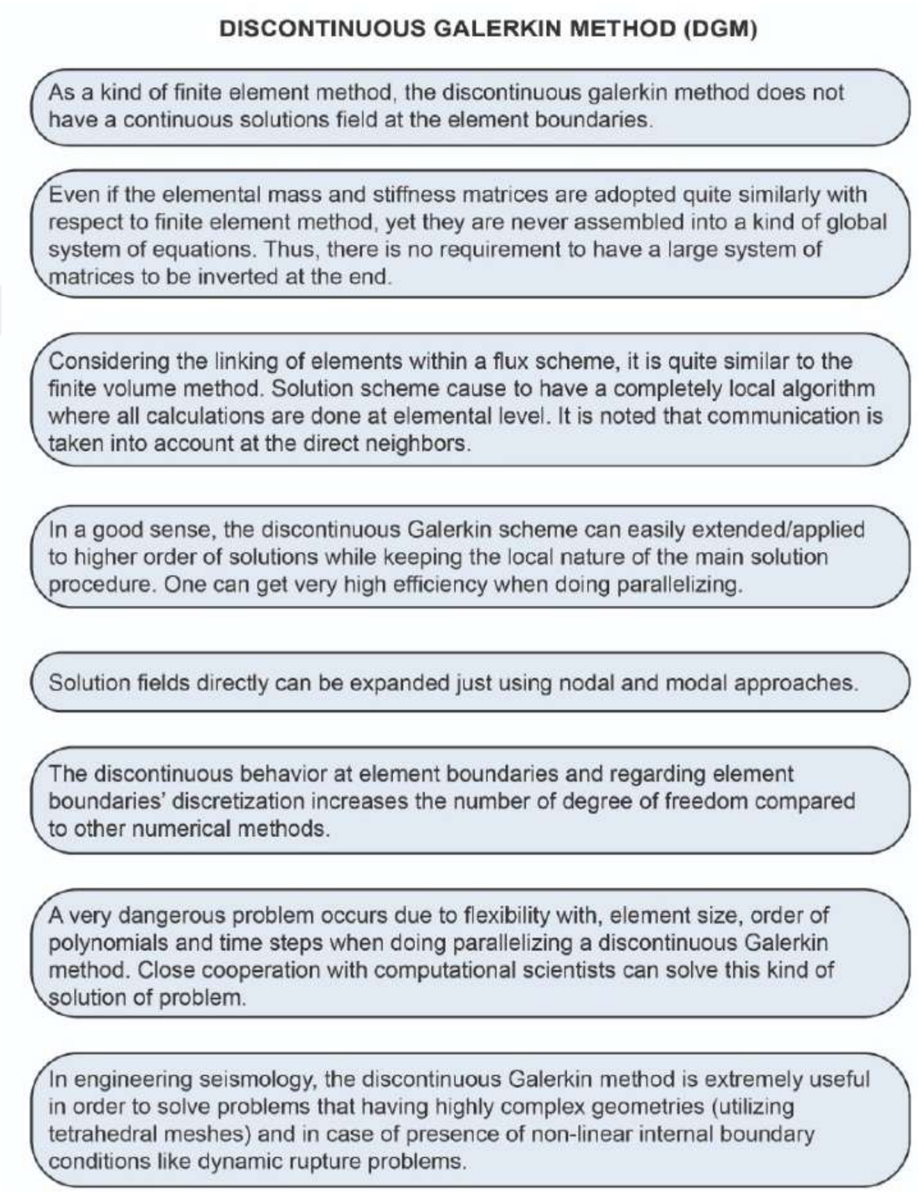

Figure 3.7: Summary scheme of Discontinuous Galerkin Method (adapted after Igel,2017)

Chapter 4

Spectral Elements in Elastodynamics with Discontinuous Galerkin (SPEED) Code

4.1 Inroduction and General Scheme of the Code

A recently developed numerical code of non-conforming approach for seismic wave propagation analysis in visco-elastic heterogeneous three-dimensional media on both local and regional scale is an one of the main works developed by the Laboratory for Modeling and Scientific Computing (MOX) of the Department of Mathematics and by the Department of Civil and Environmental Engineering (DICA) of Politecnico di Milano. The code is named as Spectral Elements in Elastodynamics with Discontinuous Galerkin (SPEED). Mazzieri et al.,(2013). One definitely can consider the one of the most effective and accurate method in order to solve three dimensional seismic wave propagation in heterogeneous media is the spectral element method(SEM) because of providing results with great level of performance of parallel computing. As indicated in previous chapter, high-order piecewise interpolants made the main construction of the SEM in detail the Lagrangian polynomials are sampled at the

Legendre-Gauss-Lobatto (LGL) quadrature points. Indeed, retaining of the geometrical flexibility of the finite elements (low-order ones) although having an accuracy of ordinary SEM. Additionally, having an ability to provide an arbitrarily accurate numerical solution just by increasing the polynomial approximation technique. Due to being based on the elastodynamics equations' weak formulation this method easily overcomes the interface continuity and the free boundary condition with a very precise computation of surface and interface waves.(Mazzieri et al.(2013),Canuto et al.,(2006)).

Due to multi-scale nature of seismic wave propagation with very extended range of wavelengths, complex geometries and constraints, high computational requirements for three dimensionally scaled heterogeneous media, flexible numerical strategies are definitely be required to make a accurate simulations. To overcome those problems a non-conforming approachs like discontinuous Galerkin (DG) technique is coupled with the spectral element method (SEM) algorithm. (Mazzieri et al.,2013)Hereafter the main algoritm will be defined as discontinuous galerkin with spectral elements as DGSE. DGSE methods can deal with a non-uniform polynomial degree distribution (N-adaptivity), as well as a locally varying mesh. size (h-adaptivity) (Mazzieri et al.2013).

Use of the SPEED code can be found in literature as, April 6th 2009 L'Aquila Earthquake (Smerzini and Villani, 2012), February 22nd 2011 Christchurch seismic sequence (Guidotti et al., 2011) and the May 29th 2012 Po Plain earthquake (Paolucci et al., 2015), Even re-construction of January 13th 1915 Marsica Eartquake (Paolucci et al, 2015). And 1978 Volvi earthquake reconstruction in Thessaloniki(Smerzini et al., 2016)To predict an earthquake in Marmara Sea Region as an Istanbul case study (Paolucci et al., 2018).

Regarding in the detailed explanation of the work of Infantino (2020),implementation and computation of the SPEED code is based on MATLAB environment where one can create different earthquake induced motion scenarios and for post-processing MATLAB outputs of these scenarios can be computed to correct broadband (BB) peak ground values (PGA,PGV,PGV), time histories which can be filtered, site response spectra can be formed, scenario id cards that describing fault

kinematics, site mechanical properties, and related rupture parameter by time can be illustrated in post-processing. SPEED code is developed on Fortran90 environment also suitable for Fortran95 standards. As a being designed for multi-core processor computers, yet it is compatible on single processor computers. It is worth to indicate that SPEED is capable of using the hybrid parallel programming The regarding meshes are used in simulations can be generated through a CUBIT software (http://cubit.sandia.gov/)
The current version of the code includes the following features:

A. Selection of conforming/non-conforming mesh.
B. Kinematic and dynamic source model for earthquake motion.
C. Linear and/or nonlinear visco-elastic soil materials.
D. Various models for soil attenuation with frequency proportional quality factor (Stupazzini et al., 2009) or frequency constant quality factor (Moczo et al., 2014)
E. Paraxial absorbing boundary conditions (Stacey, 1988); (v) time integration by either the second order accurate explicit leap-frog scheme or the fourth order accurate explicit Runge–Kutta scheme.

4.2 The Pyshical Problem

Statement of the balance of linear momentum equation as

$$\rho \dot{v} - \nabla \cdot \sigma - \rho b = 0 \tag{4.1}$$

where

t and x indicates the time and spatial coordinates respectively
$\rho(x,t)$ is the mass density
v (x,t) is the velocity
σ (x,t) is the Cauchy Stress, and
ρb is the body force density

One can adopt the equation (1) for the seismic wave propagation as

$$\begin{bmatrix}\sigma_{11}\\ \sigma_{22}\\ \sigma_{33}\\ \sigma_{23}\\ \sigma_{13}\\ \sigma_{12}\end{bmatrix} = \begin{bmatrix}2\mu+\lambda & \lambda & \lambda & 0 & 0 & 0\\ \lambda & 2\mu+\lambda & \lambda & 0 & 0 & 0\\ \lambda & \lambda & 2\mu+\lambda & 0 & 0 & 0\\ 0 & 0 & 0 & \mu & 0 & 0\\ 0 & 0 & 0 & 0 & \mu & 0\\ 0 & 0 & 0 & 0 & 0 & \mu\end{bmatrix} * \begin{bmatrix}\epsilon_{11}\\ \epsilon_{22}\\ \epsilon_{33}\\ 2\epsilon_{23}\\ 2\epsilon_{13}\\ 2\epsilon_{12}\end{bmatrix} \tag{4.2}$$

$$\rho\frac{\partial^2 u}{\partial t^2} = \nabla\sigma(u) + f \tag{4.3}$$

where
$f = f(x,t)$ is a known body force
$u = u(x,t)$ is displacement vector

Small strain tensor is below.

$$\epsilon_{ij}(u) = \frac{1}{2}(\frac{\partial u_i}{\partial x_j} + \frac{\partial u_j}{\partial x_i}) \tag{4.4}$$

Additionally, P-wave and S-wave velocities can be calculated as

$$V_P = \sqrt{\frac{\lambda + 2\mu}{\rho}} \tag{4.5}$$

$$V_S = \sqrt{\frac{\mu}{\rho}} \tag{4.6}$$

where λ and μ is the Lame coefficients.

• Considering the elastic media which is placed in a finite region as Ω where $\Omega \subset Re^d$ with a boundary is indicated as $\Gamma = \Gamma_N \cap \Gamma_D \cap \Gamma_{NR}$ Specifically, Γ_D is allocated where displacement vector $\vec{u}$ has prescribed values. Γ_N is defined where its partition under traction, and Γ_{NR} is imaginary non-reflecting boundary where the seismic waves are penetrated without any disturbance as an absorbing part of the model.

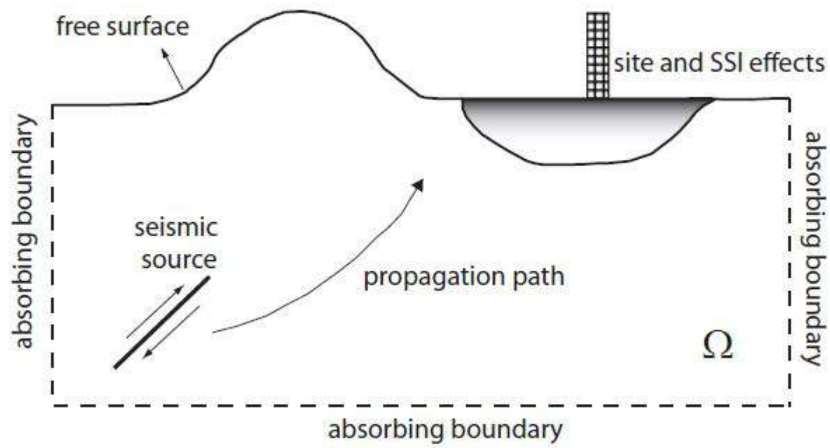

Figure 4.1: A model of representing the propagation of seismic waves through a media Ω has to enclose a definite seismic source as kinematic or dynamic.Additinnaly, Ω should include the wave propagation path within a heterogeneous media and site or soil structure interaction (SSI) effects. Representing half-space domain is need to be trimmed by implementing an absorbing boundaries. Adapted after Smerzini (2010).

(Figure 4.1)

One can consider the weak form of balance of momentum equation of the seismic waves in an elastic media. In order to get that form, multiplication of the equation (1) with $v = v(x)$ can be considered and it is resulted as

$$\frac{\partial^2}{\partial t^2}\int_\Omega \rho \underline{u}\cdot\underline{v}\,d\Omega + \int_\Omega \sigma_{ij}(\underline{u})\epsilon_{ij}(\underline{v})\,d\Omega = \int_\Omega \underline{f}\cdot\underline{v}\,d\Omega + \int_{\Gamma_N}\underline{t}\cdot\underline{v}\,d\Gamma + \int_{\Gamma_{NR}}\underline{t^*}\cdot\underline{v}\,d\Gamma \tag{4.7}$$

where

$f = f(x,t)$ is fixed body force
$t = t(x,t)$ is external traction fixed on Γ_N
$t^* = t^*(x,t)$ is traction vector on Γ_{NR} (absorbing)
$u = u(x,t)$ is the unknown value in order to be found.
at t = 0

In order to get results from equation (1.7), Initial conditions can be implemented as below. (Equation 1.8)

$$u(x,t) = \frac{\partial^1 u(x,t=0)}{\partial t^1} = 0 \tag{4.8}$$

It should be noted that there should be an idea of boundary conditions like stress-free condition which is analoguous to vanishing surface traction as on the earth surface but it is perpendicular to free surface.

4.3 Spectral Elements' Spatial Discretization

Spectral Element Method (SEM) like Finite Element Method (FEM) has its calculating method based on the classic Galerkin Approach which is based on the principle of virtual work. Yet, SEM, may define the main functions for the elements as they have spectral accuracy like Chebyshev or Legendre polynomials. And the SEM is based on a generalized Galerkin approximation of the weak form of (4.7)

Numerical parts of all variable of the main wave equation are listed by subindex N. Approximated solution of $\underline{u}_N$

$$\underline{u}_N = \underline{r}_j \underline{\widetilde{u}_j} \tag{4.9}$$

where $\underline{r}_j$ indicates a family of non-dependent polynomials $\in \underline{V}_N^0$ and $\underline{\widetilde{u}}_j$ are the unknowns of the problem. To make the equation 1.1 is more compact, $\underline{v_N}$ is considered as equal to $\underline{r_j}$ $\forall$ nodes $_j$. And the problem is defined for weak equation of motion to be calculated as, Find $\underline{u}_N \in \underline{V}_N^0$ that $\forall$t$\in (0,T)$

$$\frac{\partial^2}{\partial t^2}\int_\Omega \rho \underline{u_N}\cdot\underline{v_N} d\Omega + \int_\Omega \sigma_{ij}(\underline{u_N})\epsilon_{ij}(\underline{v_N})d\Omega = \int_\Omega \underline{f}\cdot\underline{v_N}d\Omega + \int_{\Gamma_N}\underline{t}\cdot\underline{v_N}d\Gamma + \int_{\Gamma_{NR}}\underline{t^*}\cdot\underline{v_N}d\Gamma \tag{4.10}$$

$\underline{v}_N$ $\forall$ $\underline{v}_N^0$ - Reminding that $\underline{v}_N^0$ is defined as a subset of polynomial having a degree of N which disappear on the Γ_D where allocated displacement vector $\vec{u}$ has prescribed values.

One can indicate the number of nodes (grid points) in order to get approximated values of exact solution for a displacement field $u(x,t)$ by superposition of shape (basis) functions. ($\phi_i(x)$) where $i = 1,....N$ - (N is total number of nodes) multiplied by time-dependent coefficients as $u_i(t)$ to indicate the displacement value of i^th node of the system.

$$\overline{u}(x,t) = \sum_{1}^{N} u_i(t)\phi_i(x) \tag{4.11}$$

according to the Galerkin principle the test function v (Equation 4.7) is assumed the same basis function adopted to approximate the unknown displacement in Equation (4.10)

In order to make a splitted computational domain Ω in to a kind of set as (E) that having non-overlapping elements. (Ω_e) (e.g quadrilaterals in 2D, hexahedrals in 3D,) a mesh design should be done.

$$\Omega_E = \sum_{e=1}^{E} \tag{4.12}$$

For hexahedral elements, one can utilize tensor product of one dimensional shape functions which lead to have diagonal mass matrix in the system. In case of using tetrahedral elements, loss of tensorization can be expected. A sole constraint for the meshing process is related to geometrical conformity that positions the two adjacent element that having same vertex/edge/face. In order to overcome this problem, non conforming computational domains should be adapted. (Mazzieri et al.,(2013),Smerzini,C.(2010))(See Figure 4.2).

In detail for the speed code, the classical algorithm of SEM is modified to have discontinuous galerkin spectral elements (DGSE) (Mazzieri et al., 2013; Antonietti et al., 2012). The motivation reason of DGSE is to accomplish a good fit with a non-uniform polynomial degrees distribution which called as N-adaptivity and also for the varying the size of meshes which called as h-adaptivity. (Figure 4.3).

In case of distorted meshes due to physical constraints like topography a master element (un-deformed reference element) Ω_{ref} can be defined as $[-,+1]^2 or [-1,+1]^3$ for square or cubic elements respectively. In short,

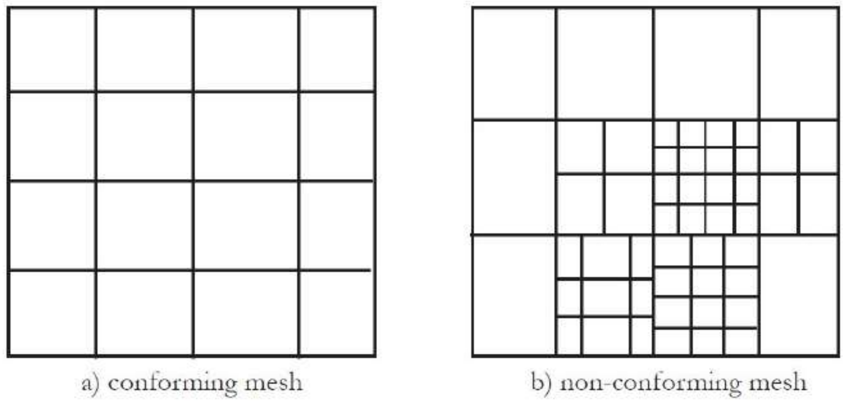

Figure 4.2: Representation of a) conforming mesh algorithm and b) non-conforming mesh algorithm (Adapted from Smerzini(2010).

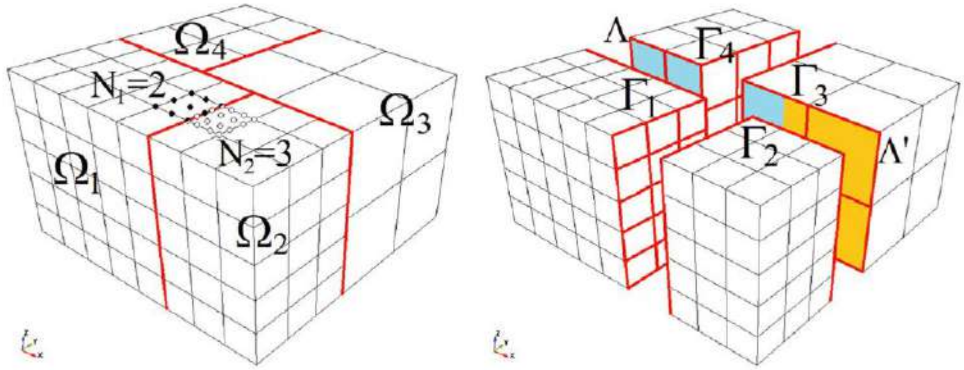

Figure 4.3: A representation of the model in the SPEED code which shows hexahedral non-conforming spectral element meshes with non-overlapping sub-domains. Main boundaries are exclusively highlighted. Discontinuous Galerkin approach lead to have (N-adaptivity, where, N1 = 2 in Ω_1 and N2 = in Ω_2) and also for variation of size of meshes locally (h-adaptivity between subdomains $\Omega_1, \Omega_2, \Omega_3$ and Ω_4) (from Mazzieri et al., 2013).

the sub-domain Ω_e can be defined after using projection of the master element(Ω_{ref}) with a logical transformation that obeys the equation below.

$$\underline{x} = \underline{F^e}(\underline{\xi}) \tag{4.13}$$

where

$\underline{x}$ and $\underline{\xi}$ are the cartesian coordinates in Ω_{ref} and Ω_e. and

$\underline{F^e}$ is defined by Jacobian of $J^e(\underline{\xi})$ where it makes the element transformation by mapping technique.

A simple 2D linear mapping can be applied by the equation as

$$(x, y) = F^e(\xi, \eta) = \sum_{k=1}^{4} N_k(\xi, \eta) a_k \tag{4.14}$$

where

$N_k(\xi, \eta)$ is the main shape functions for the control points (ξ, η) and a_k is the corners of the deformed element.

To deal with curve boundaries and interfaces, higher degree mapping, at least quadratic, can be envisaged. In a quadratic mapping the number of control points is 9 in 2D (see Figure 3.4) and 27 in 3D.

In case of dynamic equations, one should check the spatial discretization techniques. According to the Nyquist theorem, in order to have maximum number of sampling points show the minimum wavelength equal to 2. $G_{\lambda,min} = 2$

$$\Delta x = \frac{\lambda_{min}}{G_\lambda} = \frac{\lambda_{min}}{2} \tag{4.15}$$

and

$$\lambda_{min} = \frac{V_{min}}{f_{max}} \tag{4.16}$$

where

Δx is the maximum step of spatial sampling,V_{min} and f_{max} denote the minimum wave propagation velocity and the maximum frequency to propagate respectively.

If one consider the research of Faccioli et al. (1997), in order to have more accurate results for a homogeneous medium, the mesh should be designed such a way that there should be more than 2.5 points for each minimum wavelength. i.e. $G_\lambda \geq 2.5$ additionally, if a strong material discontinuities exists, $G_\lambda \geq 3.5-4$ is much more reliable. Just to remind that low order FEM or FDM mostly require $G_\lambda \geq 10-12$.

Δx is absolutely equal to the spatial step for the mesh in finite differences. Yet, in spectral elements this value is not constant and also it can be indicated as an average inter-nodal distance between adjacent Legende-Gauss-Lobatto (LGL) nodes. For very low spectral degrees i.e. ($S_D \leq 5$), the characteristic dimension of the spectral element Δl could be expressed very roughly as below.

$$\Delta l \leq \frac{\lambda_{min}}{G_\lambda} S_D \tag{4.17}$$

as SD defined as the degree of the interpolant polynomial, the main mesh design is always depend on that polynomial. Thus, this expression can be considered as the main advantage of the spectral element method that accuracy of the problem can always be increased either by refining the mesh structure by reducing (Δl) or by implementing higher SD values.
——————-

4.4 Numerical Integration and Functional Approximation

When discretization part is completed, the weak form of the integrals should be implemented to be solved with respect to Legende-Gauss-Lobatto (LGL) integration scheme that having a degree of accuracy as 2N-1, indicating N is the number of integration points for element edges. One can let the q be a function on Ω_{ref}, so that integral of q can be represented as below.

$$\int_{Q_{ref}} q d\Omega \asymp \sum_{t=0}^{N} q_t \xi_t \omega_t \tag{4.18}$$

where

ξ_t the integration points for Legende-Gauss-Lobatto (LGL) nodes in $\Omega_r ef$ and ω_t is the integration weights.

If one consider 1D, the LGL nodes ξ_i are directly expresses as the roots of the first order space derivatives of the Legendre polynomial with degree N, L_N (Abramovitz and Stegun, 1966)

$$i = 0; \xi_0 = -1 \tag{4.19}$$

$$i = 1, ...N-1 : \xi_i = L_N^{'}(\xi_i) = 0 \tag{4.20}$$

$$i = N : \xi_i = 1 \tag{4.21}$$

$$\omega_i = \frac{2}{N(N+1)} \frac{1}{L_N^2(\xi)} \tag{4.22}$$

Thus, for N degree having legendre polynomials mean existence of N+1 LGL nodes for each space, N-1 zeros of $L_N^{'}$ the two extreme points. Regarding as an example of LGL nodes for 1D reference element as N^{th} order polynomial interpolant with N = 1,.....N is represented.(Figure 4.4 and 4.5).For further details please refer to Smerzini,C.(2010).

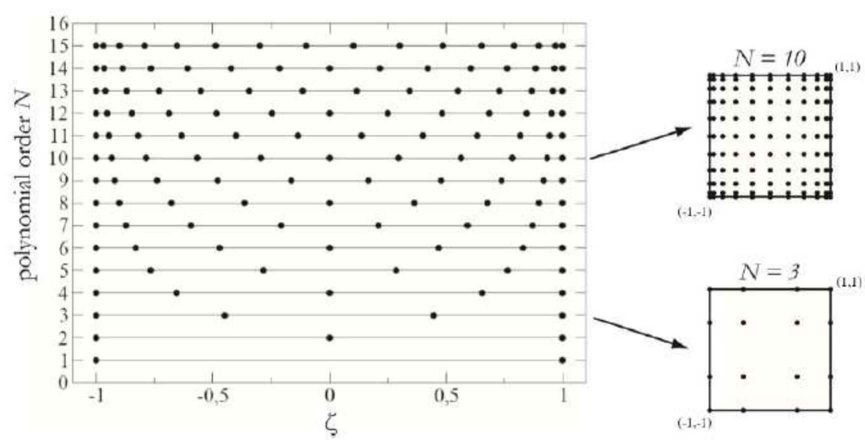

Figure 4.4: Plots show the 1D reference element with Legendre-Gauss-Lobatto integration points on it. Where reference element is defined by $\Omega_{ref} = [-1, +1]$ Right of the figure shows the conditions in 2D where N=3 and N=10. Adapted after Smerzini(2010)

After having LGL nodes, the unknown parameters of the wave equation can be implemented. Additionally, the true implementation for the polynomial basis $\underline{r_j}$ is the Lagrange polynomial with a degree of N which is directly equal to j^{th} node of LGL and completely disappears at all the other nodes of the system.One of the reasons is that it preserves the exponential accuracy of the spectral method and in addition, it efficiently reduces the computational effort that is required to solved since it yields diagonal matrices.

If one considers $((\zeta_i)_{i=0,1....N}$ be the N+1 degree of LGL integration points, the regarding Lagrange interpolants are the N+1 polynomial of φ_q with degree of N which directly makes the relation below.

$$\varphi_q(\zeta_i) = \delta_{qi} = \begin{cases} 1 & if \quad q = i \\ 0 & if \quad q \neq i \end{cases} \tag{4.23}$$

As a representation of the q^{th} Lagrange polynomial with a degree of N can defined as below.

$$\varphi_q(\zeta) = \frac{\zeta - \zeta_0}{\zeta_q - \zeta_0} \frac{\zeta - \zeta_{q-1}}{\zeta_q - \zeta_{q-1}} .... \frac{\zeta - \zeta_N}{\zeta_q - \zeta_N} \tag{4.24}$$

For example, for N = 4 there can be defined 5 LGL nodes and therefore, 5 Lagrange polynomials as illustrated in Figure below.

In order to have a basis of continuity of the wave equation solution, the global model of grid of LGL node, as expressed as $\underline{x}_q$ thus assembly process of the integration points for each sub reference domain Ω_e in equation (1.19) for a one-dimensional case. So that i^{th} component for the displacement can have the relation below.

$$u_{iN}(x) = u_{iq}\varphi_q(\underline{x}) \tag{4.25}$$

where $u_{iq} = u_{iN}(\underline{x}_q), \varphi_q$ is directly represents the q^{th} node of the Lagrange polynomial with degree of N. For further details, please refer to Smerzini,C.(2010).

$$\Psi_{ijk}(\underline{\zeta}) = \Psi_i\Psi_j\Psi_k \tag{4.26}$$

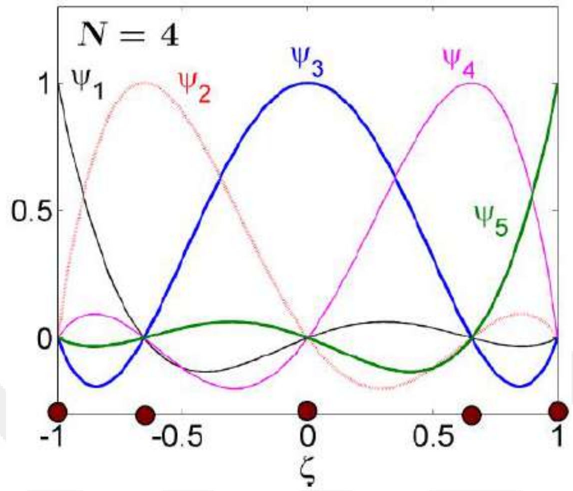

Figure 4.5: Lagrange polynomials of degree $N = 4$, Ψq , associated to the q^{th} node on a reference interval $\Omega_{ref} = [-1, 1]$. The corresponding $N + 1$ Legendre-Gauss- Lobatto (LGL) nodes are plotted by dots on the horizontal axis. (Adopted from Smerzini et al. (2010), Hashemi,K (2017).

After integration of the equation (1.10) with LGL quadratures, each domain and each component assembly into equation (1.25) can expressed as finally. Plese refer to Smerzini(2010) for details. As an ordinary system of differential equations with respect to time represented as below.

$$\underline{K}U + \underline{M}\ddot{U} = \underline{F^{ext}}(t) + \underline{T}(t) + \underline{T^{*}}(t) \tag{4.27}$$

where $\underline{U}$ is the nodal displacement vector, M is the mass matrix and $\underline{F}^{ext}$,$\underline{F}^{int}$,$\underline{T}$ and $\underline{T}^{*}$ refer to external forces, internal forces, tractions, and non-reflecting boundary conditions. Mass Matrix can be defined as

$$\underline{F^{int}}(t) = \underline{K}U(t) = \int_{\Omega} = B^{T}\sigma d\Omega \tag{4.28}$$

$$\underline{M}_{ij} = \int_{\Omega_e} \Psi_i \rho \Psi_j d\Omega \tag{4.29}$$

$$\underline{F}_i(t) = \int_{\Omega_e} \Psi_r{}^{(i)} t_i d\Omega \tag{4.30}$$

$$\underline{T}_i(t) = \int_{\Gamma_N} \Psi_r^{(i)} t_i d\Omega \tag{4.31}$$

$$\underline{T}_i^*(t) = \int_{\Gamma_{NR}} \Psi_r^{(i)} t_i^* d\Omega \tag{4.32}$$

4.5 Absorbing boundary conditions

For an unbounded media, one can implement an artificial boundary after dividing the model into pieces. Additionally, implementation of a fictitious boundary causes to existence of false reflections that are initiated by the domain's outer edges. For this reasons, it is essential to make an implementation of a boundary that absorbs the waves on the outward direction this kind of boundary conditions is names as absorbing boundary conditions (i.e. ABC). In previous studies, a significant amount of non-reflecting boundary conditions are presented that depend on Paraxial Approximation (PA) for elastic wave propagation equations. (Clayton and Engquist, 1977) Idea is can be simply explained as splitting the outward wave-field and the inward wave-field and implementing non-reflecting boundary conditions. In SPEED code, there is P3 paraxial boundary conditions are implemented because of having stability for an extended range. For further details, please refer to Stacey (1988) and additionally Faccioli et al.(1997). For extended studies related to background of P3 PA and main applications can be found in Casadei and Gabellini (1997), Stupazzini (2004) and Mazzieri (2012).Regarding ABC are shown in Equation (4.7) as fictitious/imaginary value of tractions as t^*

4.6 Time Conditions

There are three options to compute time integration scheme present in the speed code as

i. 2^{nd} order Leap-Frog (LP2),
ii. 2^{nd} prder Backward (B2) and
iii. 4^{th} order Runge-Kutta scheme (Quarteroni et al.,2007)

Differ from implicit time scheme algorithms (unconditionally stable), explicit algorithm have to satisfy the Courant-Friedrichs-Levy (CFL) condition which expressed below.

$$\Delta t \leq \gamma \frac{\Delta x_{min}}{V_{max}} \tag{4.33}$$

where γ is a constant depending on the modelled medium's dynamic properties e.g. poisson ratio. γ has to be positive and less than 1. (i.e. $0 \leq \gamma \leq 1$). Δx_{min} is the shortest distance between LGL nodes, and V_{max} is the maximum propagation velocity.

As an example 2^{nd} order of Leap-Frog and 2^{nd} order of Backward (LP2-B2), time iteration algorithm can be expressed as in the equations below.

$$(\frac{\partial^2 u}{\partial t^2})^n = \frac{1}{\Delta t^2}(u^{n+1} - 2u^n + u^{n-1}) + O(\Delta t^2) \tag{4.34}$$

$$(\frac{\partial u}{\partial t})^n = \frac{2}{\Delta t}(3u^n - 4u^{n-1} + u^{n-2}) + O(\Delta t^2) \tag{4.35}$$

where u^n is the vector of nodal displacements at $t_n = n\Delta t$

4.7 Implementation of Seismic Excitation

In SPEED code, there are 5 different options to model implementation of seismic excitation as
i. Kinematic seismic rupture model
ii. Dynamic seismic rupture model (in verification)
iii Plane wave propagation
iv.. Neumann surface load, and
v. Volume force load

4.7.1 Kinematic Rupture Model

Spatial changes of time dependent displacement field of earthquake induced fault are defined as kinematic fault models where the term and theories are firstly introduced to the literature by Maruyama,(1963),Burridge and Knopoff(1964) and Haskell(1964 and 1966).In SPEED code, kinematic seismic fault models are implemented as a source of distributions regarding double-couple point sources that having following expression as moment tensor density as below and regarding drawing (Figure 4.6).

$$m_{i,j}(x,t) = \frac{M_0(x,t)}{V}(\nu_i n_j + \nu_j n_i) \tag{4.36}$$

where $M_0(\underline{x},t)$ is the time history of seismic moment release for the source point in the elementary source volume V $\underline{x}$, $\underline{n}$ and $\underline{v}$ represents the unit vector to fault normal and unit vector for slip respectively. Finally, one can understand that m_{ij} is equivalent to a body distribution (Madariaga, 2007) as represented below with a force vector of seismic body force that allows us to define external force from inclusion of seismic moment tensor for a elastic continuous media. (Equation 1.37) At a specific generic spectral node (x^n) where a double couple point source acted on, the m_{ij} can be expressed as in (Equation 1.38).(where δ is the Dirac delta function.)

$$f_i = -\frac{\partial m_{ij}}{\partial x_j} \tag{4.37}$$

$$m_{ij}(x,t) = M_{ij}(t)\delta(x - x^n) \tag{4.38}$$

To express an extended heterogeneous source model, the physical finite model of the fault is sectioned into a finite number of subfaults (triangular shaped to be practical) where it will be defined as a family of spectral nodes at $\underline{x}_s^n$ where $n = 1,2....,N_s$ as in the figure below. (Figure 4.6). These triangular subfaults have a size very closely equal to hexahedral elements of the soil model placed around the fault. Each fault (k), $k = 1,2,.....L_{sism}$ are defined exclusively by rake angle λ_f^k, rise time τ_R^k, rupture time t_R^k, rupture velocity V_R^k and regarding seismic moment tensor M_{ij}^k. Where M_{ij}^k can be expressed as below.

$$M_{ij}^k = \mu^k A^k \Delta u^k (\nu_i^k n_j + \nu_j^k n_i) M_0^k(t) \tag{4.39}$$

where for each subfault
$\mu^k$is the elastic shear modulus, A^k is the subfault area Δu^k is the slip amplitude, $\underline{\nu^k}$ is the unit slip vector, $\underline{n}$ is the unit vector normal to the fault, V_R^k is the rupture velocity,τ_R^k is the rise time corresponding to the defined source time function $s^k(t)$ and $\underline{x}_h y$is the location of the hypocenter. The unit vectors$\underline{\nu}$ and $\underline{n}$ can be defines as a function of the strike ϕ_f dip $\delta_f$and rake $\lambda_f$as follows where the first two parameters are constant across the fault plane while the slip vector λ_f^k may variate as below.

$$\begin{bmatrix} \nu_x \\ \nu_y \\ \nu_z \end{bmatrix}^T = \begin{bmatrix} cos(\lambda_f^k)sin(\phi_f) - sin(\lambda_f^k)cos(\delta_f)cos(\phi_f) \\ cos(\lambda_f^k)cos(\phi_f) + sin(\lambda_f^k)cos(\delta_f)cos(\phi_f) \\ sin(\phi_f)sin(\delta_f) \end{bmatrix} \tag{4.40}$$

$$\begin{bmatrix} n_x \\ n_y \\ n_z \end{bmatrix}^T = \begin{bmatrix} sin(\delta_f)cos(\phi_f) \\ -sin(\delta_f)sin(\phi_f) \\ cos(\delta_f) \end{bmatrix} \tag{4.41}$$

Additionally, each subfault should has at least one LGL point so that where the source nodes having $N_s^k \geq 1$, there is a seismic load. Regarding seismic moment release tensor at each source node with coordinates of $\underline{x}_s^n$ is depend on the slip function $s(t)$ and it is directly shifted in time depend on the distance from the hypocenter ($\underline{x}_{hy}$) as below.

$$M_0^{n,k} = s(t - t_R^{n,k}, \tau_R^k) \tag{4.42}$$

with

$$t_R^{n,k} = \frac{|x_{hypo} - x_s^{n,k}|}{V_R^k} \tag{4.43}$$

where τ_R^n and V_R^n are the time rise and rupture velocity (respectively) for the n^{th} point source in the k^{th} subfault which are totally same for the all nodes in the same subfault element. If there is a value of rupture time (t_R^k for the barycenter of each subfault ($x^{b,k}$), regarding time of rupture for the n^{th} source inside the k^{th} subfault can be calculated through weighting

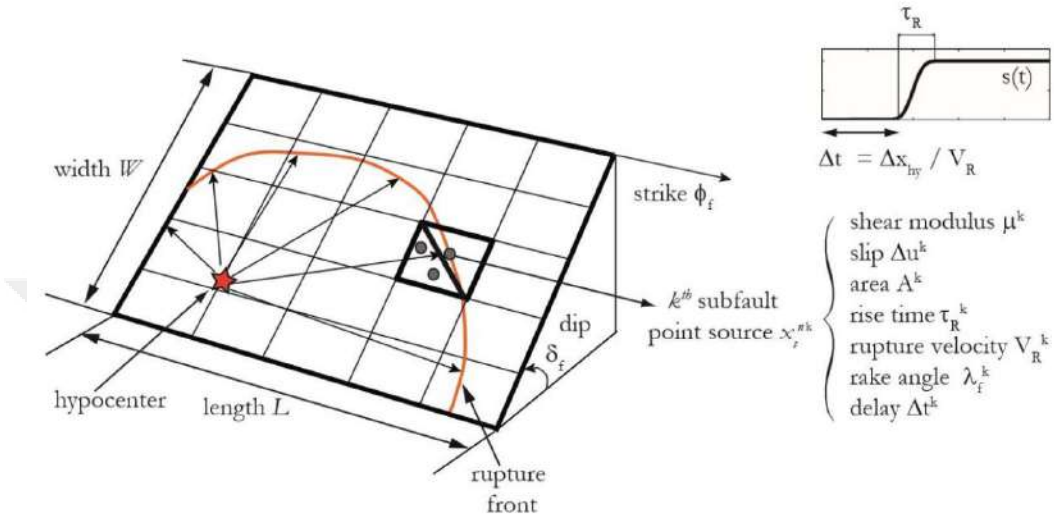

Figure 4.6: Representation of a numerically modelled an extended seismic source in SPEED. Where N_s^k is the spectral nodes of each subdivided major fault that each subfaults are defined as with its own parameters which are shear modulus (μ^k), source area (A^k), slip amplitude (Δu^k, rise time (τ_R^k),rupture velocity (V_R^k) and rake angle as (λ_f^k). (Figure is adapted after Smerzini,C., 2010)

t_R^k for the distance between hypocenter and source relative to the distance between hypocenter and barycenter for the regarind fault as below.

$$t_R^{n,k} = t_R^k \frac{|x_{hypo} - x_s^{n,k}|}{|x_{hypo} - x^{b,k}|} \tag{4.44}$$

Elementary volume in equation 4.36 is for the n^{th} point source inside the k^{th} subfault i.e. $V^{n,k}$ is calculated through nodal volume of the point source is divided by the total volume of the subfault as below.

$$V^{n,k} = \frac{V^n}{V^k} \tag{4.45}$$

Numerical adaptation of seismic source in the spectral element method's domain, regarding seismic moment sources are taken into account as external forces and added as a vector of forces into equation of motion as a term of $\underline{F}^{seismmic}$ into equation 4.27 as below.

$$\underline{M}\ddot{U} = \underline{F}^{external}(t) + \underline{F}^{seismic}(t) - \underline{F}^{internal}(t) + \underline{T}(t) + \underline{T^*}(t) \tag{4.46}$$

where

$$\underline{F}^{seismic} = \int_{\Omega} B^T m d\Omega \tag{4.47}$$

where

$\underline{U}$ is the vector containing displacements of the nodes, M is the mass matrix, and the left $\underline{F}^{external}(t)$, $\underline{F}^{internal}(t)$, $\underline{T}(t)$, $\underline{F}^{seismic}(t)$ and $\underline{T^*}(t)$ are the external,internal,traction,absorbing and seismic forces.

4.8 Soil Models in SPEED

4.8.1 Linear Viscoelastic Behavior

As of 2020, SPEED is able to carry out analyses of series of linear visco-elastic and non-linear visco-elastic analyses of the soil and rock.(Infantino,2020) For non-linear visco-elastic media two options are present, frequency proportional quality factor (Stuppazzini et.al,2009) or constant frequency quality factor(Moczo et al.,2014) respectively. As a suitable technique of discrete grid time domain procedure is applied for the equation of motion with a courtesy of Graves (1996) and Kosloff and Kosloff (1986). That can be applied as spatially varying visco-elastic materials that parametrized by a defined decay factor $\xi(s^{-1})$

If one consider Equation (4.17), Viscous volume force can be expressed in the partial differentiated equation of motion as,

$$\underline{K}U + \underline{M}\ddot{U} = \underline{F} + \underline{F}^{external}_{viscoelastic} \tag{4.48}$$

Acceleration term is replaced by Kosloff and Kosloff 1986 with equivalent term as

$$\rho \frac{\partial^2 u}{\partial t^2} = (\underline{\ddot{u}} + \xi \underline{\dot{u}} + \xi^2 \underline{u}) \tag{4.49}$$

where

ξ is the decay parameter, ρ is the mass density and u is the displacement field.

$$(\underline{\ddot{u}} + \xi \underline{\dot{u}} + \xi^2 \underline{u}) \tag{4.50}$$

where

$$\underline{F}^{external}_{viscoelastic} = -M(2\xi \underline{\dot{u}} + \xi^2 \underline{u}) = -C^c \underline{\dot{u}} - C^k \underline{u} \tag{4.51}$$

For further details please refer to (Smerzini,C.,2010, Infantino,M.,2020).

Accordingly, it can be shown that, by this substitution, the solution of the modified equation of motion is the same as the one of un-damped system, just all frequency components are equally attenuated by a factor of $e^{-\xi t}$ The decay factor ξ represents the attenuation of the propagating wave in the soil medium and is related to the quality factor Q through:

$$\xi = \frac{\pi f}{Q} \tag{4.52}$$

where f denotes the frequency. Hence, it comes out that the soil damping coefficient ξ, as well as the quality factor Q, depends linearly on frequency. Therefore, the frequency proportional quality factor is defined as:

$$Q = Q_0 \frac{f}{f_0} \tag{4.53}$$

where $Q_0 = \frac{\pi f_0}{\xi}$ and f_0 is a reference frequency within the frequency range to be propagated.

4.8.2 Non-Linear Viscoelastic Behavior

For non-linear visco-elastic (NLE) materials, generalization of three-dimensional load factors are taken into account. Thus a modulus reduction and damping ratio increment curves are implemented as the same implementation scheme adapted for one-dimensional linear equivalent approaches like Kramer(1996). In the speed code, there are two experimental curves are adapted to facilitate to adapt this behavior. (Figure 4.7)

1) $(G/G_0 - \gamma)$ curve is used to implement shear modulus (G) decay relative to initial shear modulus G_0) $(\gamma]$

2) $(\xi - \gamma)$ curve is used to implement when damping ratio ξ increment makes the same energy loss in a cyclic stress-strain hysteresis behavir in a loop as an irreversible soil deformation in case of presence of increment of γ

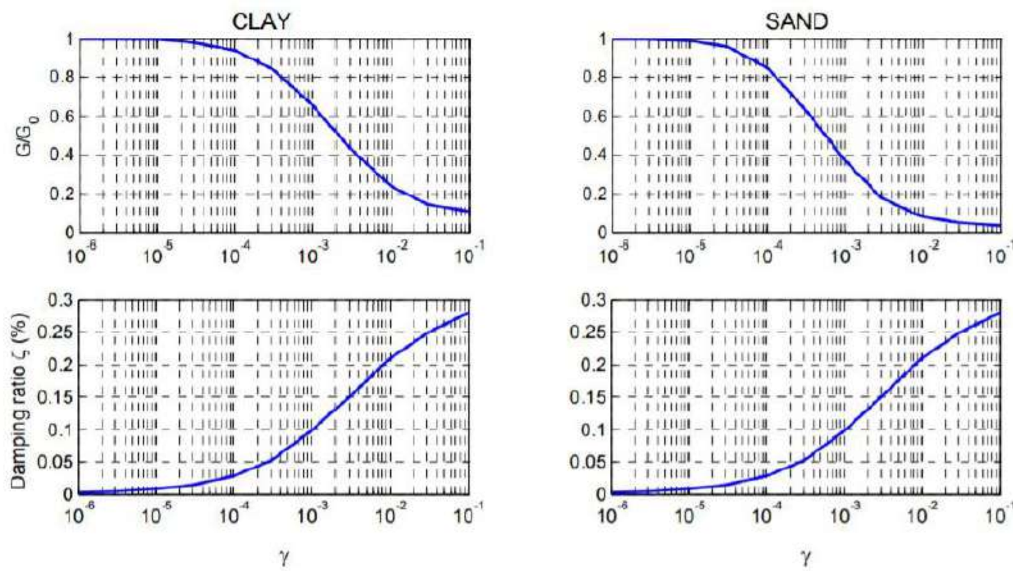

Figure 4.7: Example of shear modulus degradation curves proposed by Seed and Idriss (1970) (top panels) and damping increment proposed by Idriss (1990) (bottom panels) for sand(right) and clay (left).

Essentially, all of the regarding computations are done in the frequency domain with an iterative procedure thus at the i^{th} iteration is completed with the at that corresponding degraded value of shear modulus without indicating its evolution with respect to time. Thereby, an advanced time scheme algorithm should be define for maximum value of strain at the each element. Utilizing three-dimensional stress-strain states can be defined by $(G/G_0 - \gamma)$ and $(\xi - \gamma)$ curves. Measure of shear strain can be represented as averaged as for each spectral element can be expressed as below.

$$\gamma_{max}(x,t) = max(|\epsilon_I(x,t) - \epsilon_{II}(x,t)|, |\epsilon_I(x,t) - \epsilon_{III}(x,t)|, |\epsilon_{II}(x,t) - \epsilon_{III}(x,t)|) \tag{4.54}$$

where

$epsilon_I, epsilon_{II} and epsilon_{III}$ are the principal strains. If $\gamma_m ax$ is determined for a given position and time (x, t_n) regarding decayed shear modulus (G_n) and damping coefficient (ξ_n) can be determined too from the related decay curves. And finally one can calculate the regarding shear wave velocity (V_s) and quality factor (Q) at $t = t_n$ using the equations below.

$$V_{S,n} = \sqrt{\frac{G_n}{\rho}} \tag{4.55}$$

$$Q_n = \frac{1}{2\xi_n} aaa \tag{4.56}$$

where ρ is the density which is assumed constant all the time.

Chapter 5

Artificial Neural Network (ANN) Based Approach to Generate Broadband (BB) Ground Motions for 3D Physics Based Earthquake Numerical Simulations (ANN2BB procedure)

5.1 Introduction and Main Principles of ANN

Due to limited accuracy of PBS in the high frequency ranges, a main goal to fix this issue is frequency band of synthetics in order to make the output of PBS is much more reliable in practice of earthquake engineering area. (refer to Smerzini and Villani (2012) and Goulet at al.,(2015). Broad-band (BB) waveforms can be obtained by a hybrid approach technique with combination of deterministic physics based simulation's low-frequency results and stochastic approaches' high-frequency signals. (Boore, 2003). In general hybrid approaches has main negative impacts for the regarding results such as low and high frequency contents are correlated very poorly due to different approaches and using cross-over frequency i.e. f_c which is the fourier spectra of the motion that multiplied by weighting functions then summation is carried out. This process cause to regarding fourier spectrum to has artificial holes around the f_c then a difficult site-specific calibration of f_c is required (Ameri et al.,2012). Table 5.1 shows the list of broad-band earthquake ground motions are calculated with respect to low-frequency 3D PBS and high-frequency stochastic contributions' coupling.

ANN2BB is a new and original technique for generating broad-band (BB) ground motions that couples the physics based earthquake simulation outputs with a prediction scheme of an Artificial Neural Network (ANN)
Main routines of this technique are presented below.

1-) ANN-Training for a strong-motion dataset, correlating short period ($T \leq T^*$) spectral ordinates with the long period spectral ordinates ($T > T^*$) where T^* is the specific period that beyond it, PBS results are accurate.

2-) ANN is always used for training on short periods.

3-) In the long periods of time histories of PBS are enhanced at high frequencies thanks to application of an iterative spectral matching technique up to response spectra being equal to the short-period results that are processed on ANN.

Artificial Neural Networks (ANNs) is used for an estimation for a non-linear relation between highly populated vector set of input variables and a vector set of output unknowns because for these cases, fast and closed form of rules cannot be implemented in an easy way. Additionally, in case of mild mathematical conditions, a problem related to continuous mapping between vector spaces are only be approximated within an error tolerance due to having arbitrary precision by ANNs. In order to indicate a correlation between ordinates of long-period response spectra N_{SA}^{LP} are defined for $T \geq T^*$ where T^* is the threshold period that refers to the variability region of the physics based simulations where N_{SA}^{LP} is the ordinates of the short-period response spectra for $T < T^*$

Table 5.1: Selection of Broadband (BB) Earthquake Ground-Motion Simulation Case Studies Relying on Hybrid (HYB) Approaches (Adapted from Paolucci et al.,2018)

Publications	f_c(Hz)	Methods (LF + HF)	Study Area	Validation
Caussse et al.(2009)	1.0	SE + EGF	Grenoble, France	Against GMPE
Graves and Pitarka(2010)	1.0	FD + SFF	California	1979 M_w 6.4 Imperial Valley,1989 M_w 6.9 Loma Prieta,1992 M_w 7.3 Landers ,1994 M_w 6.7 Northridge
Mena et al. (2010)	0.5	FD + Sc-GF	San Andreas Fault,California	Against GMPE
Roten et al. (2010)	0.5	FD + Sc-GF	Salt Lake City, Utah	Against GMPE
Smerzini and Villani (2012)	2.5	SE+SFF	L'Aquila, Italy	2009 m_W 6.3 L'Aquila
Seyhan et al. (2013)	1.0	FD+SFF	California, USA	Against GMPE
Ramirez-Guzman et al.(20159	1.0	FD, FE + SFF, St-GF	New Madrid Seismic Zone	Against GMPE
Iwaki et al. (2016)	1.0	FD + St-GF	Japan	2000 M_w 6.7 Tottori, 2004 M_w 6.6 Chietsu
Razafindrakoto et al. (2016)	1.0	FD + SFF	Christchurch area, New Zealon	2010-11 earthquake sequence
Akinci et al. (2017)	1.0	FD +SFF	Marmara Sea, Turkey	Against GMPE

Low-frequency (LF) methods: FD, finite difference; FE, finite element; SE, spectral element. High-frequency (HF) methods: SFF, stochastic finite fault (Boore, 2003; Motazedian and Atkinson, 2005; Graves and Pitarka, 2010); EGF, empirical Green's functions (Hartzell, 1978); Sc-GF, scattering Green's functions (Mai et al., 2010); St-GF, stochastic Green's functions (Kamae et al., 1998). f_c is the crossover frequency where low - frequency (from physics-based numerical simulation) and high-frequency (stochastic) synthetics are combined. (Table is adapted after Paolucci et al. (2018).)

Referring to Smerzini et al.(2014),a high-quaility dataset for strong ground motiton (SIMBAD). is used in training.SIMBAD has $N_{db} \sim 500$ three-component records from around 130 shallow crustal earthquakes worldwide. (Distributed from M_w 5 to 7.3 in range with epicentral distance $R_{epi} < 35$ km below ground surface. For the site characterizations, $V_{S,30}$ are provided for all the station in that case. Two different ANNs are took into account and processed independently. (One is for geometric mean of the horizontal components of the ground motion and the other one is for vertical component of the ground motion. A feed-forward multilayer perception neural networks is used. In detail, a hidden layer having N_n^h sigmoid hidden neurons and a linear output neuron. Where the size of input and output vector are denoted as N_n^i and N_n^o respectively and they equal to number of input variables and target output values as N_{SA}^{LP} and N_{SA}^{SP} respectively.

A built-in neural network fitting tool which is available on MATLAB database, on (https://mathworks.com/solutions/deep-learning.html), also know as nftool, is used.

The nftool package is very useful to solve the problems regarding data fitting by utilizing a feed-forward network with Levenberg – Marquardt algorithm. A simple process scheme related to main operations that is done by ANNs are illustrated on the figure below.

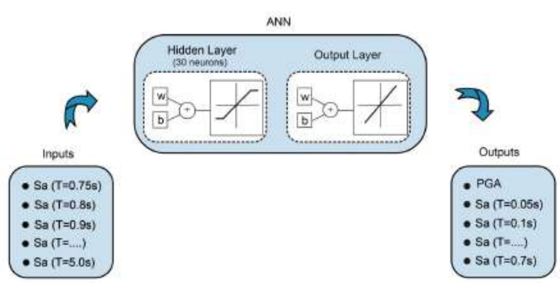

Figure 5.1: ANN Training work-flow scheme. Long period of spectral ordinates $T^* = 0.75s$ indicates the teaching input and the short period of spectral ordinates are predicted by ANN. Additionally, 30 neurons are placed in hidden layers. (i.e. $N_n^h = 30$] (Adapted after Paolucci et al.,(2018)).

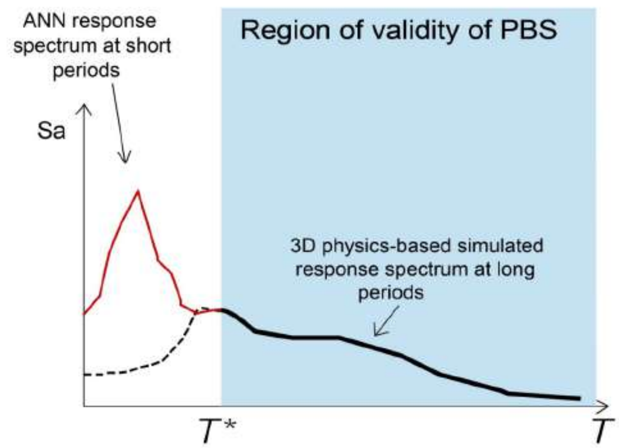

Figure 5.2: Figure showing the main idea of Artificial Neural Network (ANN) approach to generate broadband ground motions. For a given ground motions which is short-period values of spectral ordinates ($T \leq T^{*}$), where T^{*} is the minimum period of validity of the physics-based numerical model, is obtained by the computation results of response spectral ordinates for long periods ($T > T^{*}$). (Adapted after Paolucci et al.,(2018)).

In the previous representations (Figure 5.1 and Figure 5.2), the N_{LP}^{SA} input parameters are $log_{10}[SA(T_j)]_{j=1}^{N_{SA}^{LP}}$ where SA is the acceleration value from response spectral ordinates at the period T_j, ranges from T^{*} up to 5 seconds. Regarding outputs are N_{SA}^{SP} ground motion parameters. In detail $log_{10}[SA(T_k)]_{k=1}^{N_{SA}^{SP}}$ at the period from $T_k = 0$ which is peak ground acceleration up to T^{*}. ANN response is denoted as multiple outputs from multiple inputs. Main processing scheme of ANN is random subdivision of the whole dataset which corresponding to N_{db} input-output data into three different subsets. Which are

1-) A training set, in order to do calibration of weight of ANN.

2-) A validation set, using parameters, except from the ones in the tranining set, are used to monitoring the ANN's model accuracy in whole training procedure.

3-) A test set, which is not used during ANN training and validation, yet is it necessary to do an evaluation for the network capability of generalization while having a new set of data.

Number of hidden neurons are determined as N_n^h) = 30. After having a reasonable accuracy. For further details please refer to Paolucci et al.,(2018) and Gatti (2017).

5.2 ANN Performance

Based on the case study of Paolucci et al.,(2018), the performance of ANN's about the prediction of the real recording that has been evaluated by calculating the logarithmic residual of response spectral ordinate that is from $ANN(SA_{ANN})$ with respect to SIMBAD data set which is regarded as observed ones. (i.e. $log_{10}(SA_{ANN}/SA_{observed})$) In the figure below (Figure 5.3) shows the residual bars which refer to $(+/-\sigma)$ fo the geometric of horizontal components, with indicating different (T/T^*) ratios and for different T^*s which correspond to different intervals for the PBS results. As recalling that number of input parameters and number of output paramaters are denoted as $(N_{SA}^{LP}$ and $(N_{SA}^{SP}$ respectively and which are in the filure below (Fig 1.3) their values are (22,6),(20,9) and (17,11) respectively. The results include training (TRN), validation (VLD) and test (TST) phases of computation. Interestingly, in terms of normalized period, performance is so close in case of different values of T^* having a net appeal of big uncertainties when the period is decreased, as more distant then the corner period $T^(*)$. Additionally and generally, the accuracy of estimation of peak ground acceleration (PGA) is much higher. If it is applied in non-normalized terms one can indicate that the lower T^* values means a much more accuracy in the estimation. The error range for validation and test phases is limited to $+/-0.3$ in log scale. (i.e. factor of 2) that is equivalent to total standard deviation (σlog_{10}) of a standard GMPE. (e.g. Cauzzi et al.,2015). Finally, besides the emprical approaches, reduction in uncertainty is improved if the period of time getting closer to $Tm*$.

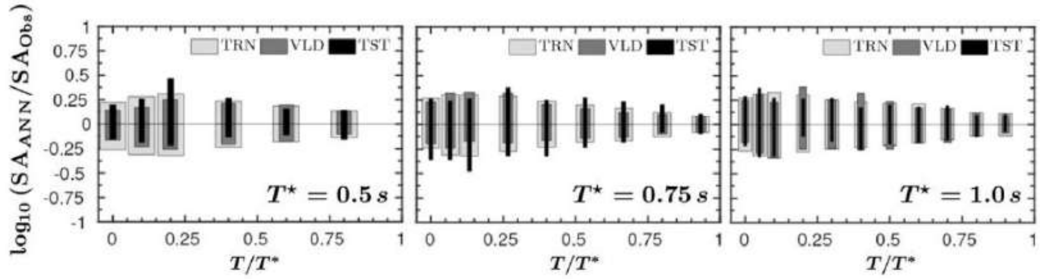

Figure 5.3: A case study performance of the ANN in prediction with respect to actual recordings based on logarithmic residuals of the response spectral ordinates and the ANN trained prediction for horizontal components.Legend for the bars is TRN for training, VLD for validation, for test set as TST(Adapted after Paolucci et al.,(2018)).

Additionally, ANN is used to for training, validating, and testing to estimate a short-period vertical spectral ordinates which are illustrated in the figure below(Figure 5.4). As one can expect that the performance of the results are a bit worse relative to horizontal one because of poor correlation of short and long period of of spectral ordinates of vertical ground motions that can be seen very clearly for $T^* = 1$ seconds. Also for the charts (in Figure 1.4) has error bar range for validation and testing phases are 3 which is 0.5 in log_{10} scale and having a very obvious bias on negative which indicates for both validation and test datasets with ANN predictions have a great underestimation of the observations. Yet, the results become much more better in case of decreased values of T^* as clearly showing that $T^* = 0.75$s, the error bars are not pass higher a factor of 0.4 in log_{10} scale and the regarding bias is getting reduced as expected.

The previously trained horizontal and vertical ANNs are applied through a dataset containing more or less 500 three-component waveforms that containing records of strong ground motions having limited epicentral distance and magnitude ranges. Due to the fact that, there is no much improvement of the results when distance and magnitude are taken into account as an extra input parameters for the phase of training. Besides, much more specifically designed ANNs could be trained on different subsets of records if a goal of application on larger datasets, different site conditions such as stiff or soft soil conditions to have much more accuracy about site-specific evaluations.

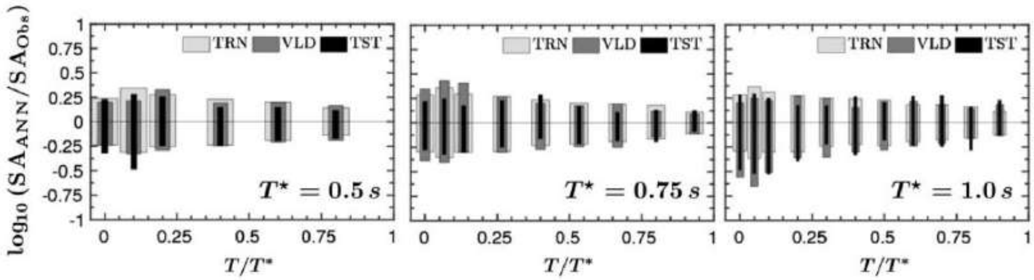

Figure 5.4: A case study performance of the ANN in prediction with respect to actual recordings based on logarithmic residuals of the response spectral ordinates and the ANN trained prediction for vertical components.Legend for the bars is TRN for training, VLD for validation, for test set as TST(Adapted after Paolucci et al.,(2018)).

5.3 The ANN2BB Procedure to Produce Broad Band (BB) Strong Ground Motions from 3D PBS

Different ANNs can be adapted for different values of T^* with respect to the frequency resolution of the numerical model. Here it is used as $T^* = 0.75$ is taken into account. Thus the initial step allows one to compute for all PBSs that having a range of validity as $T > T^*$ to a site-specific ANN-based broad band response spectrum (i.e. ANN2BB) also for creating maps of peak values of short-period ground motion. At this point, such broad-band (BB) spectrum is not refer to a definite specific waveform.

In order to get BB time histories from ANN2BB spectra, there is a spectral matching technique is adopted, similar to the previously adapted a real accelerogram for a prescribed target spectrum. (National Institute of Standards and Technology [NIST],2011) where records are scaled in an iterative mode (e.g. Shahbazian and Pezesk, 2010) or by wavelet transforms (e.g. Atik and Abrahamson, 2010), without phase changing up to response spectrum approaches the target with a pre-determined tolerance of error. In the case described here, instead of a recorded accelerogram, Paolucci et al.,(2018) consider the time history of motion that is obtained from PBSs and, as a target, the ANN2BB spectrum. Here, Paolucci et al. (2018) determined scaling in the frequency domains, yet other procedure of spectral matching also be adapted and used too. The main difficulty regarding the standard spectral matching techniques due to simulated time history's low frequency band limited nature that means waveforms with high frequency content has numerical noises which are not logical to use to scale. To fix that issue, before spectral matching for previously determined target ANN2BB spectrum, the high-frequency portion of the simulated wave form is directly suspected to enrichment by a defined stochastic component by jointing the parts of high frequency and low frequency with respect to the procedure that explained in Smerzini and Villani, (2012). In detail that scheme can be summarized as BB synthetics are created by combination of waveforms with low frequency (LF) thanks to deterministic simulation amd high frequency (HF) waveform components from stochastic approaches. And for the high frequency signals such as Sabetta and Pugliese (1996) and the Boore (2003) approaches.

In short, the main steps of ANN2BB procedure can be explained below.
i. 3D Physics Based Simulation (PBS) for a specific ground-motion scenario is carried out. Its accuracy of response spectral ordinates is limited for $T \geq T^{*}$.
ii. An ANN training is carried on depend on strong-motion dataset to estimate short-period of spectral ordinates ($T < T^{*}$) depend on the long period of spectral ordinates ($T \geq T^{*}$).
iii. ANN2BB response spectra is calculated for each simulated regarding waveforms. Additionally, regarding spectral ordinates for ($T \geq T^{*}$), matched with the simulated ones, yet for ($T < T^{*}$) are gathered from ANN. Horizontal ordinates' accuracies are much higher with respect to vertical ones.

5.4 A case Study, Application and Remarks

One of the main case studies is inspected by Paolucci et al.,(2013) that two major earthquakes on May 20^{th} and May 29^{th} in the Po Plain area with having magnitude of M_w 6.1 and 6.0 respectively. The latter earthquake's motion is recorded in detail with use of accelerometric networks that is capable of showing high-quality strong motions in the near source of major thrust within a basin with soft sediments. More than 30 recordings were ready to process with epicentral distances lower than 30 kilometers below the surface with regard to being critical to validate the results of 3D PBSs.

Taken into account of work of Paolucci et al., (2015) where the spectral elements model's basic properties are of 75 km × 51 km × 20 km that having wave propagation up to frequency of 1.5 Hz with Mirandola fault's kinematic source model, 3D velocity model of the Po Plain and a linear visco-elastic soil model is characterized by frequency proportional quality factor Q. As one can see below in the maps (Figure 5.5) regarding simulated PGA for geometric mean of horizontal components.

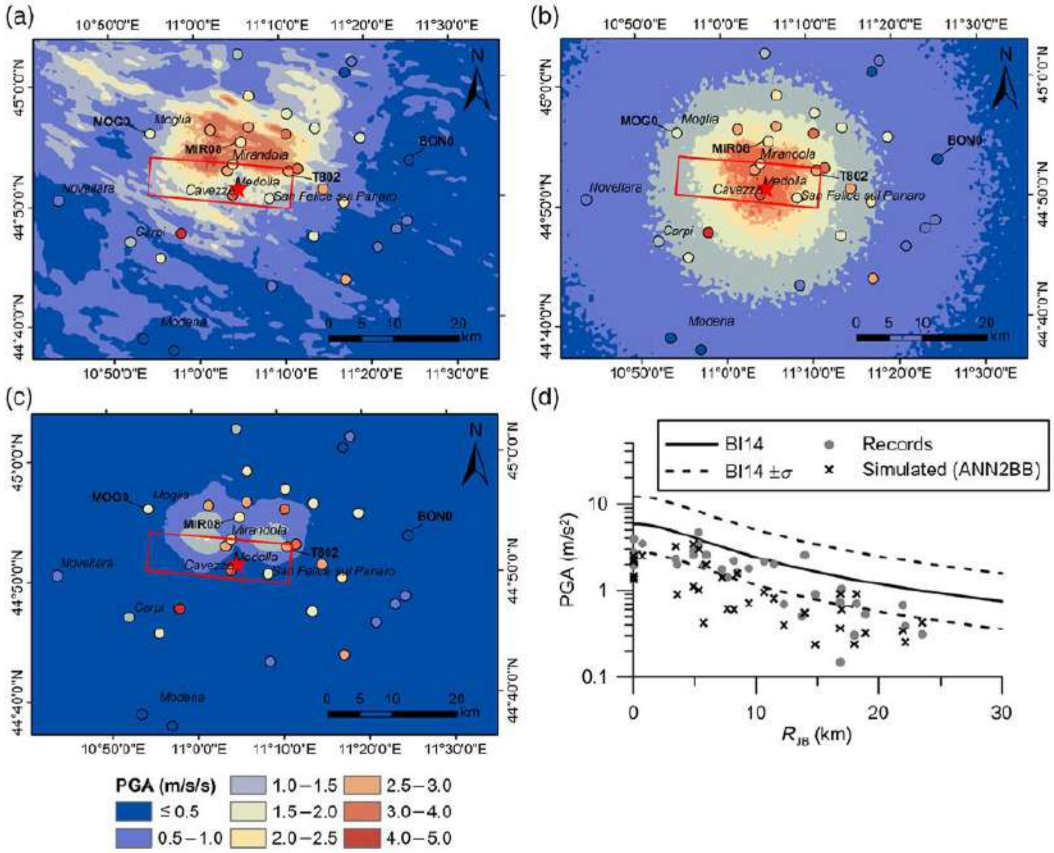

Figure 5.5: Peak Ground Acceleration (PGA) map of geometric mean of horizontal directions, (a) is for ANN2BB approach, (b) is based on hybrid approach based on physics based simulations (PBS) and stochastic methods proposed by Sabetta and Pugliese (1996). (c) 1.5 Hz low pass filtering results of PBS results where dots represent the PGA values are taken from stations on each map. (d) The graph indicates ANN2BB trained values of PGA and recorded values of PGA as a function of Joyner-Boore distance (i.e. R_{JB}) compared to Ground Motion Prediction Equation (GMPE) of Bindi et al.(2014) (i.e. BI14) (Figure is adapted after Paolucci et al.,2018).

As it can be seen in the results that, ANN2BB technique is applied in order to provide high-frequency ground motion predictions to be correlated to low-frequency motions that are computed by PBSs. In the figures 5.5a (ANN2BB) and 5.5c (PBS) ,it is clearly seen as the similarity of spatial pattern related to source effects. And in the figures 5.5a and 5.5b, it is shown clearly that the PGA values are obtained by the present approach shows a set of physical features such as relate to wave propagation directivity and directionality and site conditions which are not present in the stochastic approach that can be seen in detail in Paolucci et al.,(2015).

Additional performance of the ANN2BB technique can be indicated by comparing the BB simulated ground motions, in the figure (Figure 1.6) the acceleration, velocity and displacement time histories of north-south (N-S) direction of motion for the Mirandola (MRN) stations are plotted for the results of PBS from Paolucci et al.(2015), stochastic (STO) using Sabetta and Pugliese (1996) technique, hybrid (HYB) technique waveform with a combination of low frequency (LF) results of PBS and high frequency (HF) of high frequency with a cross-over frequency (f_c) as 1.5Hz. Additionally, ANN2BB waveforms are acquired by scaling HYB to the target response spectrum based on PBS spectral ordinates are processed in ANN technique, finally last row of motion records shows the actual recorded waveform. And in the figure (figure 5.7), detailed comparison of in terms of response spectra and fourier spectra is illustrated.

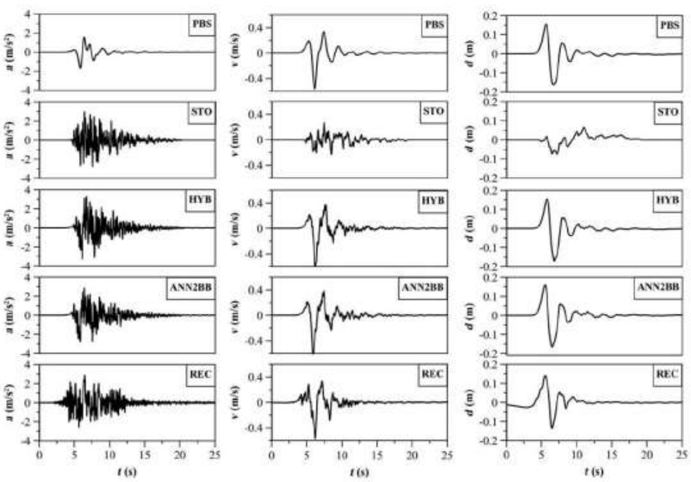

Figure 5.6: (Time Histories for Acceleration, velocity, and displacement (N–S) component at the Mirandola (MRN) station, for 29 May 2012 Po Plain earthquake. (Top to bottom) PBS (Physics Based Simulation) results which are filtered at f_c 1.5 Hz, stochastic waveform (STO) according to Sabetta and Pugliese (1996); (HYB) Hybrid synthetic results that are calculated by coupling PBS at low frequency ($\leq 1.5Hz$) and STO at high frequency ($> 1.5Hz$) with a crossover frequency of $f_c = 1.5$ Hz, BB synthetics (ANN2BB) are shown considering the HYB upon the ANN-based short-period spectral ordinates; and recorded waveforms (RECs). Adapted from the work of Paolucci et al.,2018)

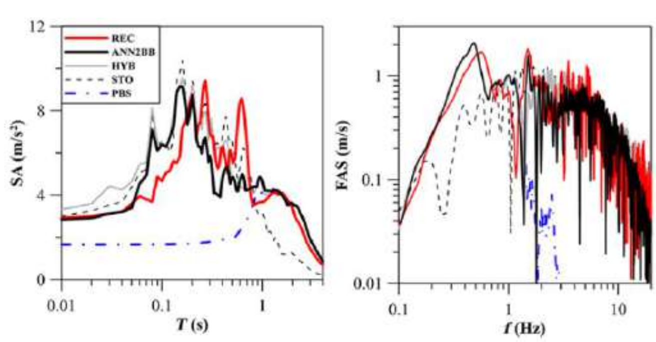

Figure 5.7: Acceleration response (on the left) and Fourier spectra (on the right) for North-South (NS) component of motion for Mirandola station (MRN) (Figure is adapted after Paolucci et al.,2018).

Considering excellent results are obtained by ANN2BB and HYB approximation techniques with respect to both in time and frequency domain, for comparison for the large set of stations,the results are shown in the time histories of motion for the station. (see Figure 5.8) Yet, ANN2BB results are shown as less satisfactory for the MOG0 stations. If one consider the spatial correlation of peak values of ground motion, ANN2BB performance with respect to HYB technique, high frequency part is directly related to low frequency part of values thanks to ANN. To be sure about low-frequency and high-frequency parts of peaks of ground-motion should have a spatial correlation which is close to realistic situation. However, high-frequency part is not done by numerical simulations.

Additionally, exponential fitting for spatial correlations (Figure 5.9) on the ANN2BB results are in good agreement. For further details see Paolucci et al., 2018.In the cases on the semivariograms range of values is from 19 km to 25 km with with a relative error between the two range estimates (REC and ANN2BB)are bounded between 1 percent(for SA 0.2 s) and 20 percent (for PGA). Then, once can say that ANN2BB technique succeeded in reproduction of response spectral ordinates' spatial correlations. Additionally, HYB technique shows a nearly flat semivariogram. (for PGA and SA = 0.2 s). Finally, trend of ranges are gathered by ANN2BB technique increases with respect to vibration period.(from 20 km for PGA to 24 km for SA = 0.2 s).For further details and spatial an-isotropy , please refer to Paolucci et al.,(2015).

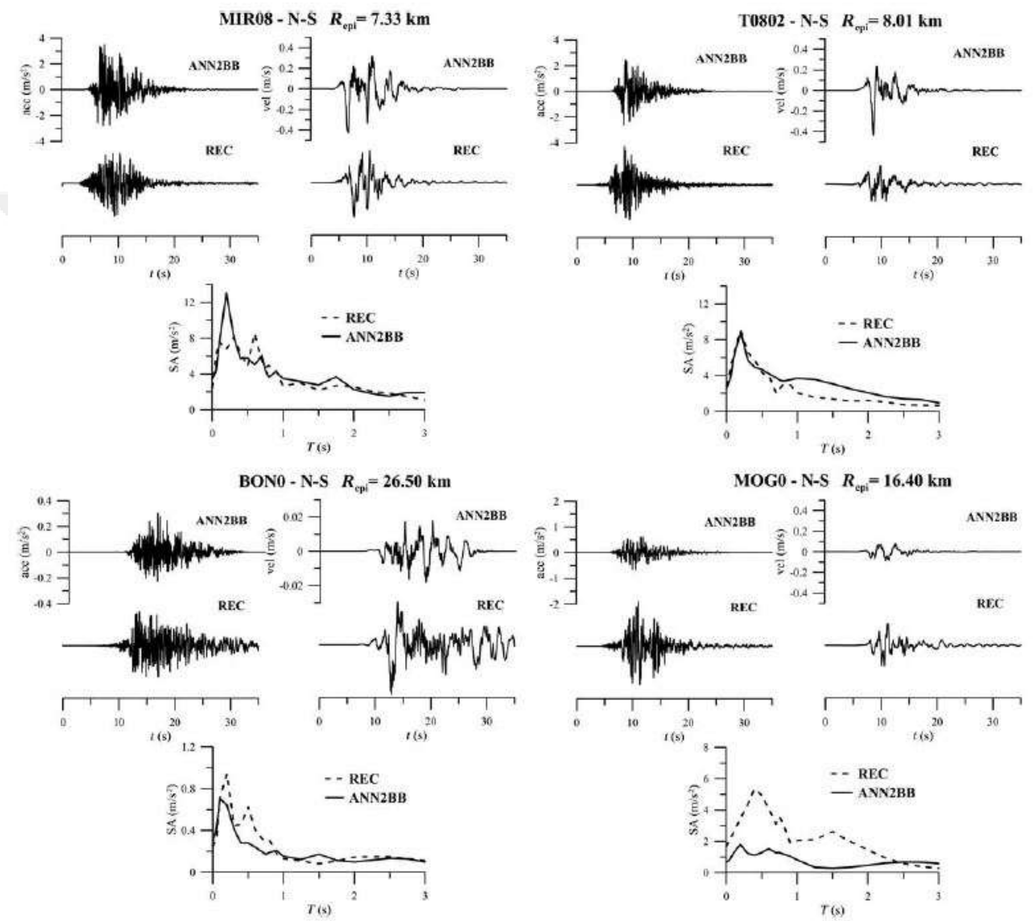

Figure 5.8: Results from The 2012 Po Plain earthquake simulation (Paolucci et al.,2018): Comparison chart for between ANN2BB simulations and recordings at four accelerometric stations (MIR08, T0802, BON0, and MOG0) with respect to acceleration and velocity time histories, and acceleration response spectra. Station are plotted on Figure 5.5 (Figure is adapted after Paolucci et al.,2018).

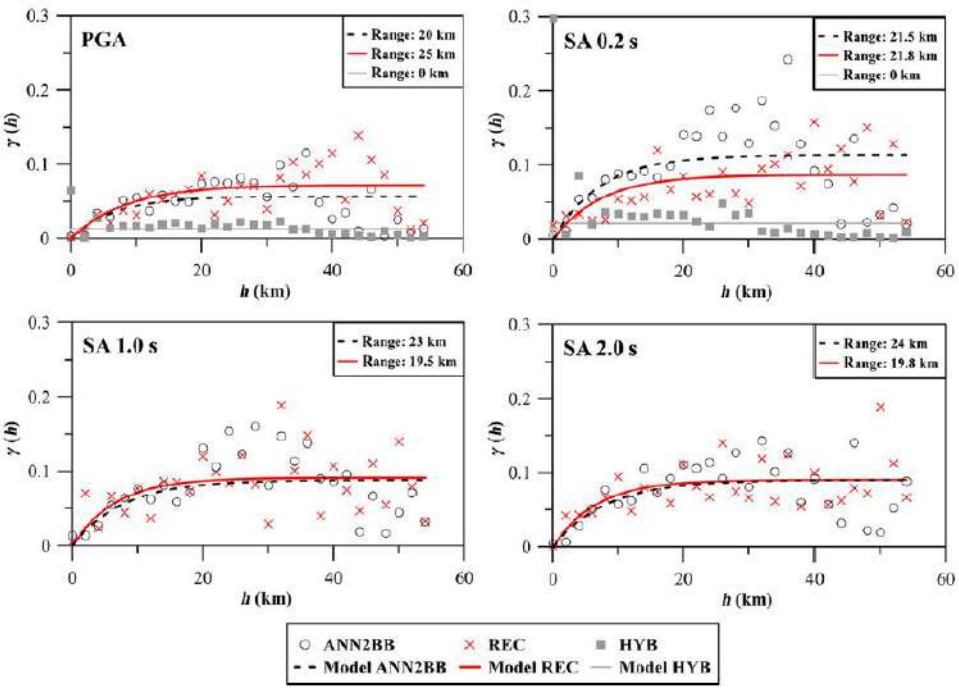

Figure 5.9: Semivariograms are plotted as crosses for REC and as circles for the ANN2BB approach (circles) for PGA, SA at 0.2 s, SA at 1.0 s, and SA at 2.0 s. The corresponding best-fitting exponential models are denoted by solid line and dashed line for REC and ANN2BB, respectively. In case of short-period response spectral ordinates, the plots for semivariograms are represented as filled squares and best-fitting with solid lines from HYB.(Figure is adapted after Paolucci et al.,2018).

Chapter 6

Earthquake Simulation Scenarios for the Sulmona Basin

6.1 Introduction

To implement SPEED code, one needs to have main ingredients for constructing the 3D model of simulations which are, the topography model, the kinematic model for fault movement, the 3 dimensional basin model with mechanical parameters of seismic motion. Details and characteristic parameters of simulations are briefly explained in the following sections.

Figure 6.1: Clear 3D computational model for the Sulmona basin

Computational properties of the basin includes maximum frequency as f_{max} = 1.5Hz and 3^{rd} degree of polynomial approximation with approximately degree of freedom of the system is around 35 million. Minimum and maximum element sizes are 83m (for the basin) and 1000m (for the deep rock) respectively. (Figure 6.1, 6.2, 6.3, 6.4)

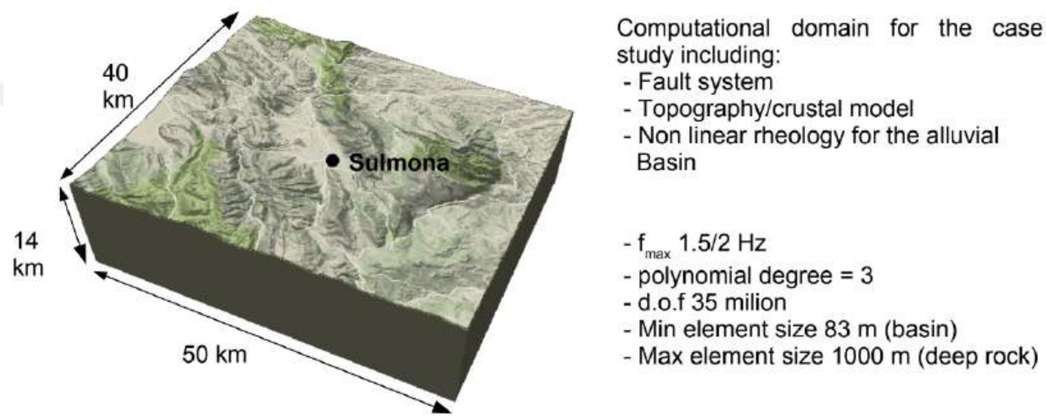

Sediments thickness [km]	Density [kg/m³]	Vs [m/s]	Vp [m/s]	Qs [-]
alluvial basin	1900 + 0.125 z	500 + 19.0 $\sqrt{z}$	1000 + 1.2 z	Vs/10
1.2	2000	1200	2400	100
1.5	2400	2200	4000	100
1	2600	2666	4800	150
3	2800	3055	5500	250
6.3	2900	3500	6300	300

Figure 6.2: 3D computational model for the Sulmona basin with detailed representation.

Regarding the parameters of motion such as V_s,V_p,Q_s are illustrated on the figure above. (Fig 6.2)
Model has a size of 40km x 50km x 14km with 384711 elements with motion is computed for 30 seconds of duration with 0.0005 seconds of time interval. Details and parameters of the simulation below can be seen in the figures below. (Fig 6.3 and Fig 6.4)

COUNTRY	LOCATION	FAULT
ITA	SUL	MMF

VELOCITY MODEL

(1) BASIN / SUPERFICIAL MODEL

Geological Unit	Depth z (m)(i)	ρ(kg/m^3) (ii)	V_S (m/s) (iii)	V_P (m/s) (ii)	Q_S (-)(iii)	Damping Type (iv)	Soil (v)
-	[0, z_B)	$c_1 = 1900$ $c_2 = 0.125$	$c_1 = 500$ $c_2 = 0.19$ $c_3 = 0.5$	$c_1 = 1000$ $c_2 = 1.2$	*100*	FP	LVE Or NLVE

(i) z_B: depth of the Quaternary deposits

(ii) $\rho = c_1 + c_2 \cdot z$

(ii) $V_S = c_1 + c_2 \cdot z^{c_3}$

(iv) $V_P = c_1 + c_2 \cdot z$

(iii) $Q_S = 100$

(iv) FP: frequency proportional

(v) LVE: linear visco-elastic, NLVE: non-linear visco-elastic

Figure 6.3: 3D computational model for the Sulmona basin

(2) CRUSTAL MODEL

Geological Unit	Depth z (m)	ρ(kg/m^3)	V_S (m/s)	V_P (m/s)	Q_S (-)	Damping Type
	[z_B -1200]	2000	1200	2400	200	FP

MESH

Model Volume (kmxkmxkm)	# Elements	Spectral Degree	Δt (s)	Duration (s)	fmax (Hz)
40x50x14	384711	3	0.0005	30	1.5

Figure 6.4: 3D computational model for the Sulmona basin

6.2 Fault Model

In SPEED code, Crempien and Archuleta (2015) i.e. CA15 model of UCSB Method for Simulation of Broadband Ground Motion from Kinematic Earthquake Sources method is used for further details please refer to Author. (Figure 6.5)

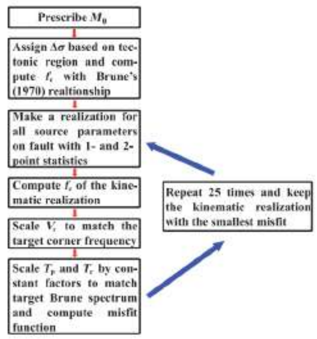

Figure 6.5: Flow chart for modelling kinematic finite-fault source with the UCSB method. (Crempien and Archuleta, 2015)

Source parameters and their values of present study is illustrated on figure below. (Fig. 6.6)

Source Parameters	Present Study
Focal Mechanism	Normal
Fault Origin FO (Latitude, Longitude)	42.17, 13.8
Top Z above sea level of the Fault (km)	-1.2
Strike	135
Dip	60
Rake	-90
Maximum Length along the the strike L (km	22
Maximum Width along Dip W (km)	11
Effective Length along the strike L (km)	12
Effective Width along the strike L (km)	9.12
Moment Magnitude Mw	*6 or 6.5 depends on the scenario*
Source model	CA15
Epicenter (Latitude, Longitude)	*Differs for each Simulation*
Hypocenter Z above sea level (km)	*Differs for each Simulation*

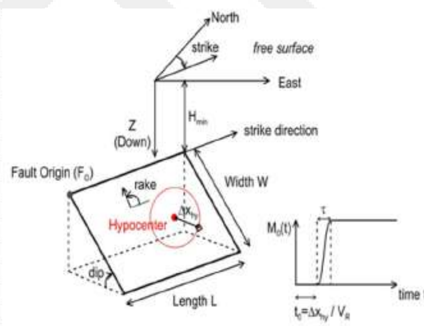

Figure 6.6: Fault model drawing and regarding source parameters and general table for the properties that are used in simulation implementations.

6.3 Summary of Properties of Simulations

In order to analyse different magnitude (Mw), soil model and different slip distribution realizations are implemented to the simulation and their properties are represented in the figure below(Fig 6.7). For further detailed charts for simulations and scenario ID cards, the reader is referred to Appendix A.

Group No	Simulation No	Mw	Linear Elastic / Non-Linear Visco Elastic	Slip Distribution No
01	1	6.0	Linear Elastic	S001
	2	6.0	Linear Elastic	S002
	3	6.0	Linear Elastic	S003
	4	6.0	Linear Elastic	S004
	5	6.0	Linear Elastic	S005
02	6	6.5	Linear Elastic	S002
	7	6.5	Linear Elastic	S003
	8	6.5	Linear Elastic	S005
03	9	6.0	Non-Linear Visco Elastic	S003
	10	6.0	Non-Linear Visco Elastic	S004
04	11	6.5	Non-Linear Visco Elastic	S003
	12	6.5	Non-Linear Visco Elastic	S005

Figure 6.7: Groups and Properties of Scenarios, with respect to magnitude, soil model and slip distributions.

6.4 Non-Linear Viscoelastic Behavior of Soil

In order to enhance the accuracy of the soil behaviour under seismic environment, the linear viscoelastic modelling and the non-linear elastic modelling are implemented into analyses. In the literature, non-linear visco-elastic model results has been shown minimum error of simulation results for soil behaviour under earthquake induced movement simulations. For further details, please refer to Jankowski (2005). The non-linear soil model implemented in this work are represented in the Figure 6.9.

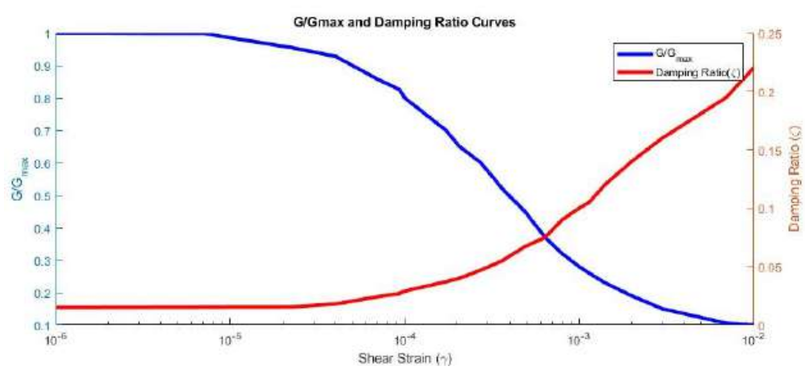

Figure 6.8: Shear Modulus Decay Curve and Damping Ratio Curve for adapted non-linear viscoelastic soil model.

6.5 Virtual Stations' Locations for Ground Motion Measurement

To have precise values of analysis of motion for simulation results, 2 different cross-sections are defined and along these 10 different virtual stations (Fig 6.9) are selected(Fig 6.10, Fig 6.12). Additional details of soil layers and their mechanical properties beneath these virtual stations are shown in Fig 6.11 and Fig 6.13

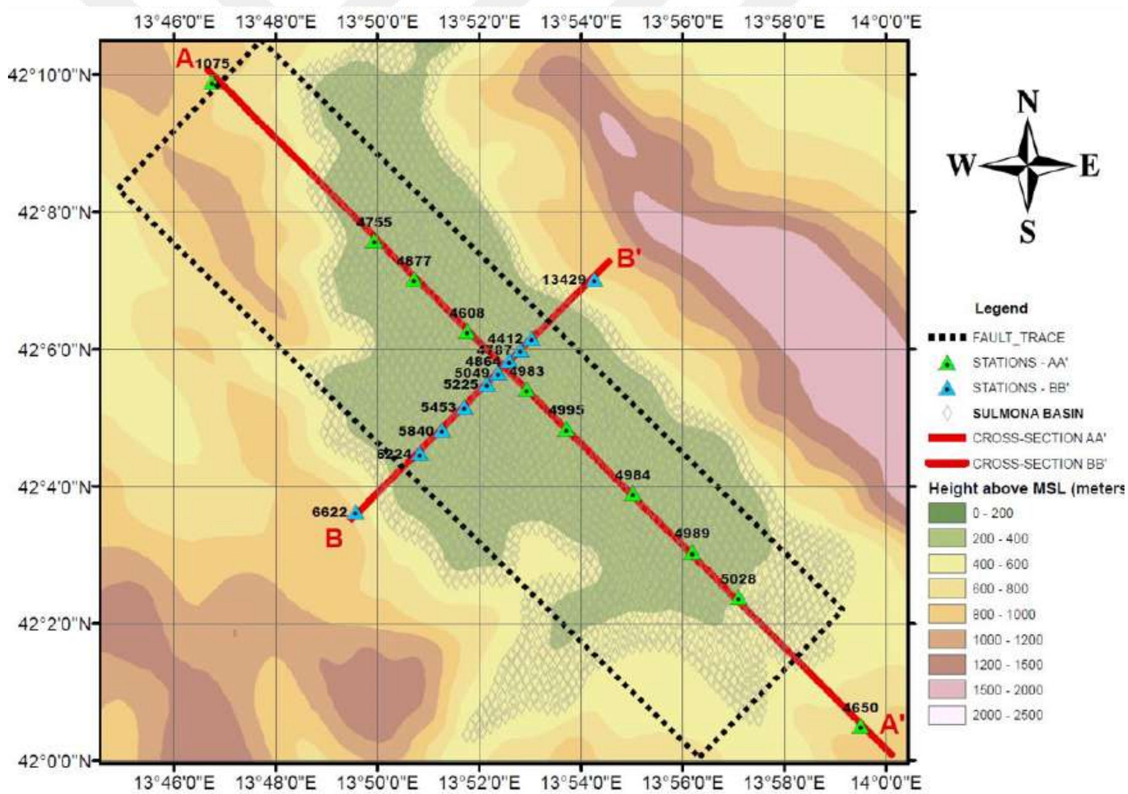

Figure 6.9: Topograhphic Map of Sulmona Basin. Including Cross-Sections (AA' and BB'), selected virtual stations and fault trace

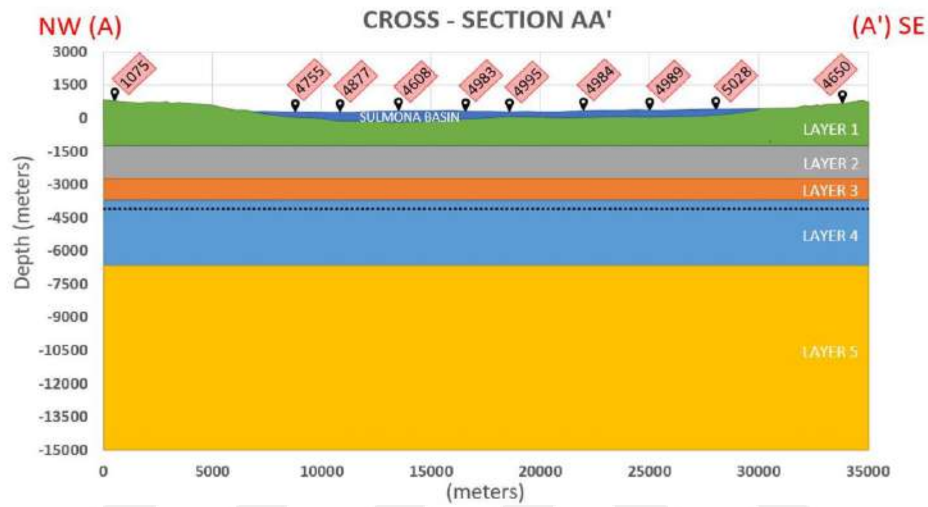

Figure 6.10: Cross Setion AA' : Illustrating layers, Virtual Stations and Fault Trace.

Station No	TOPOGRAPHY	BASIN SURFACE	SEDIMENT THICKNESS	Vs,30	Soil Class
CROSS SECTION A-A'	(above sea level m)	(wrt sea level m)	(m)	(m/s)	-
1075	841.92	OUTCROP	NO	2200	A
4755	310.59	147.9	162.69	567.86	B
4877	268.78	-21.03	289.81	567.86	B
4608	351.54	-128.16	479.7	567.86	B
4983	330.69	7.25	323.44	567.86	B
4995	310.57	88.02	222.55	567.86	B
4984	339.27	67.19	272.08	567.86	B
4989	371.56	91.3	280.26	567.86	B
5028	402.704	127.23	275.474	567.86	B
4650	728.54	OUTCROP	NO	2200	A

Figure 6.11: Sediment Thickness, $V_{S,30}$ value and Soil Class according to NTC (Italian Construction Code) for Cross Section AA'

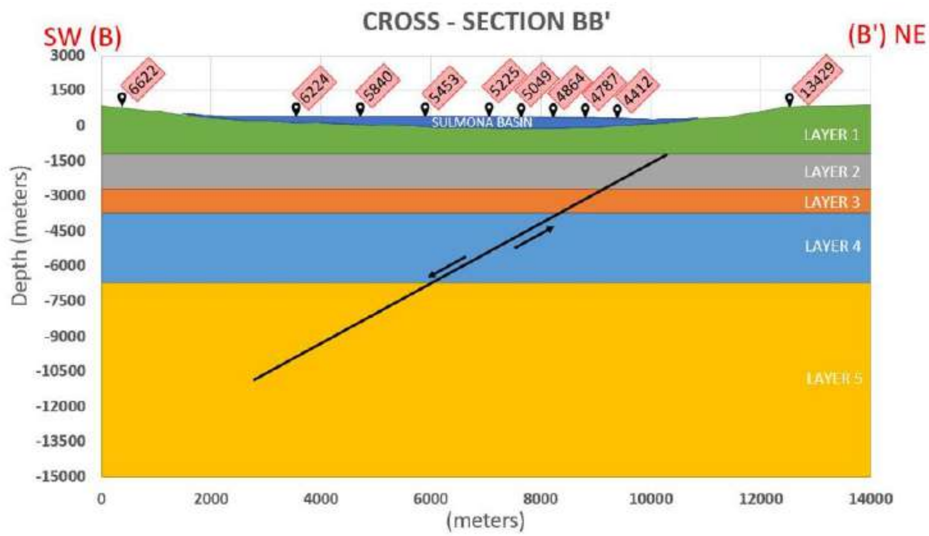

Figure 6.12: Cross Setion BB′ : Illustrating layers, Virtual Stations and Fault Trace.

Station No	TOPOGRAPHY	BASIN SURFACE	SEDIMENT THICKNESS	Vs,30	Soil Class
CROSS SECTION B-B'	(above sea level m)	(wrt sea level m)	(m)	(m/s)	-
6622	765.206	*OUTCROP*	NO	2200	A
6224	364.41	160.12	204.29	567.86	B
5840	357.28	69.24	288.04	567.86	B
5453	356.06	0.42	355.64	567.86	B
5225	352.27	-54.72	406.99	567.86	B
5049	344.41	-67.48	411.89	567.86	B
4864	338.71	-61.23	399.94	567.86	B
4787	323.12	-37.81	360.93	567.86	B
4412	291.26	11.55	279.71	567.86	B
13429	750.07	*OUTCROP*	NO	2200	A

Figure 6.13: Sediment Thickness, $V_{S,30}$ value and Soil Class according to NTC (Italian Construction Code) for Cross Section BB′

Chapter 7

Time Series of Motion and Peak Ground Motion Maps for Selected Simulations

In order to indicate the effect of earthquake magnitude and/or soil model for simulations, 4 different scenarios are selected to represent their time series of ground motion and their peak ground acceleration (PGA), peak ground velocity (PGV) and peak ground displacement (PGD) maps are created after ANN2BB training is carried out for the SPEED computations. Selected scenarios are, 1) M_w = 6.0 with Linear Visco-elastic (LVE) model - slip distribution no as S003, 2) M_w = 6.5 with Linear Visco-elastic (LVE) model - slip distribution no as S003, 3) M_w = 6.0 with Non-linear Visco-elastic (NLVE) model - slip distribution no as S003 and lastly, 4) M_w = 6.5 with Non-linear Visco-elastic (NLVE) model - slip distribution no as S003. Main effect on non-linearity is observed for all the three directions (E-W,N-S and vertical) with lower value of acceleration, velocity and displacement with respect to same magnitude but elastic soil models. Additionally, magnitude effect on the simulations are represented but regarding ground motion parameters for seismic design such as response spectrum and site amplification factor with detailed comments can be found in the next chapter. (Chapter 8) In order to construct a seismic hazard map and ground motion prediction equations such cases, it is necessary to obtain site response parameters such as peak ground acceleration (PGA), peak ground velocity (PGV) and peak ground displacement (PGD). In this section, results of peak ground response values are obtained after ANN2BB training on the SPEED simulation results for the same 4 selected different characteristics having simulation scenarios. All values for 14442 virtual station are interpolated through ordinary kriging analysis then PGA, PGV and PGD maps are prepared on ArcMap software.

7.1 Time Histories of Acceleration and Peak Ground Acceleration Maps

The synthetic 3D simulation of earthquake scenarios of SPEED code results shown Earthquake Moment magnitude increase cause to logarithmic increase of PGA, PGV, PGD as increase from $M_w = 6.0$ to $M_w = 6.5$ cause to more or less doubling the value of peak ground motion values are observed within Fig 7.1 to 7.12 for time series and Fig 6.37 to 6.72 for peak ground motion values at a glance, further observation regarding response spectra and spectral amplification ratios will be evaluated in detail in the following chapter.Additionally, in strong motion cases i.e. $M_w \geq 6.0$ in present case, non-linearity of soil model show very slight reduction of records in ground motion and also for the peak ground motion values as observed. (Fig 7.1 to 7.12)

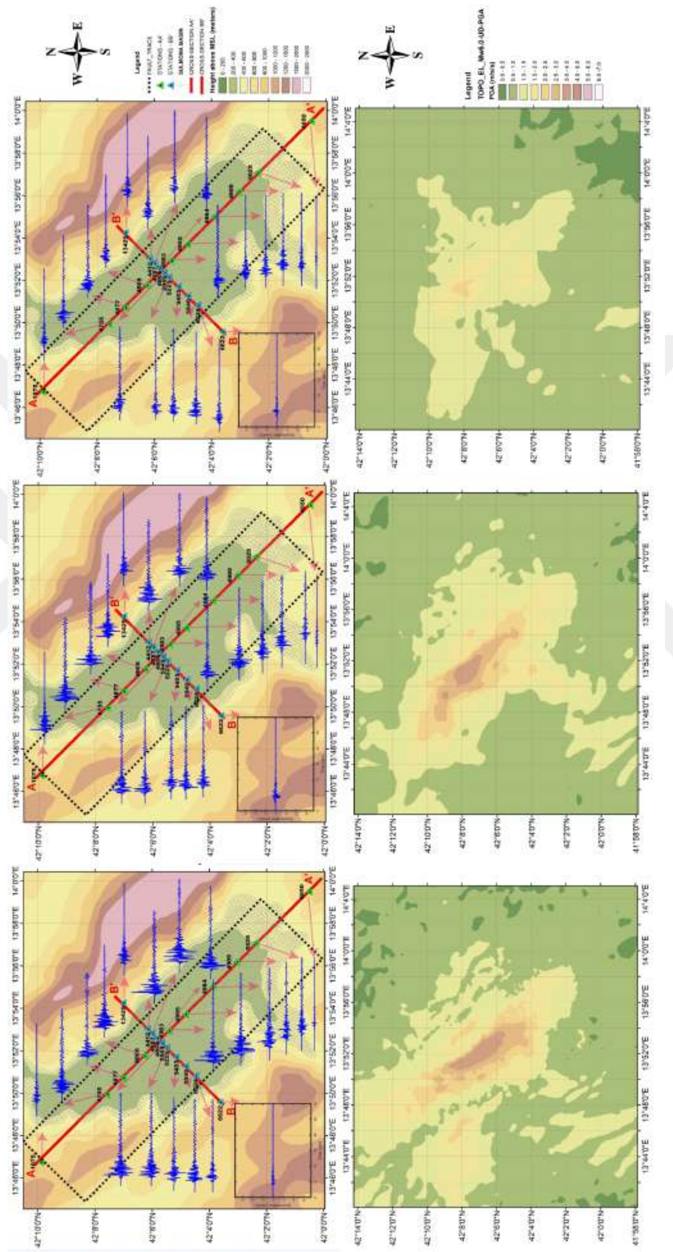

Figure 7.1: (Top) Time Series of Acceleration recorded on selected virtual stations, (Bottom) PGA map of area, NS, EW and Vertical (from Left to right) for Simulation of Mw 6.0, Linear Visco-elastic, S003

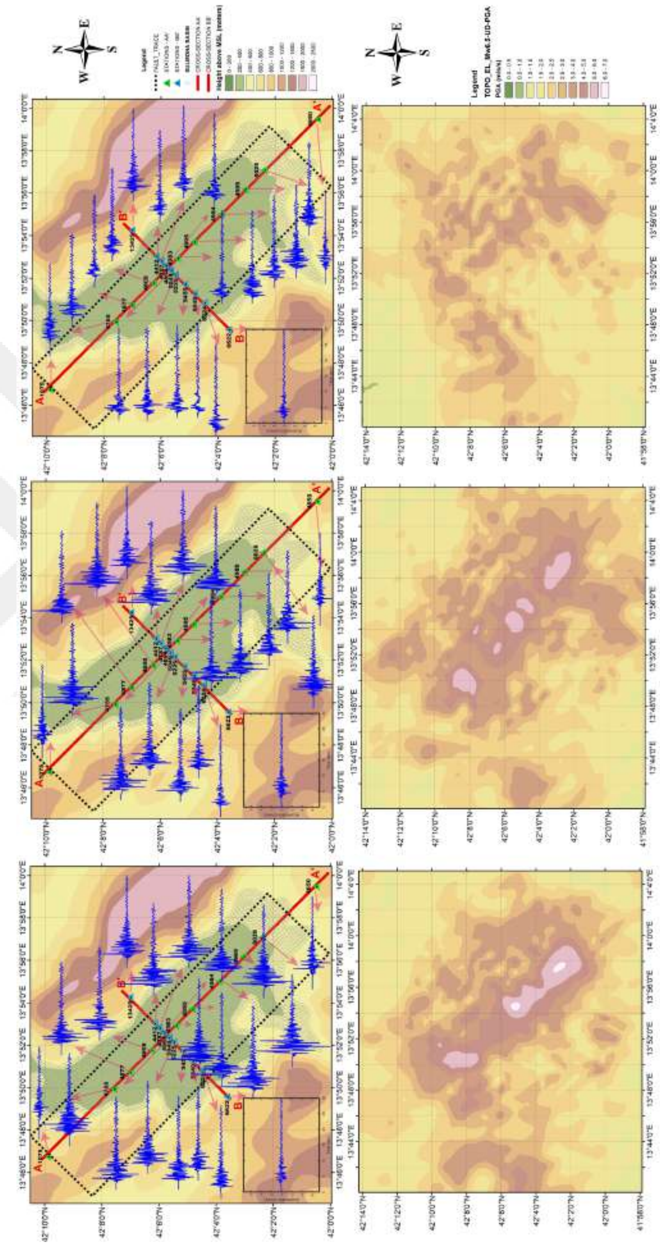

Figure 7.2: (Top) Time Series of Acceleration recorded on selected virtual stations, (Bottom) PGA map of area, NS, EW and Vertical (from Left to right) for Simulation of Mw 6.5, Linear Visco-elastic, S003

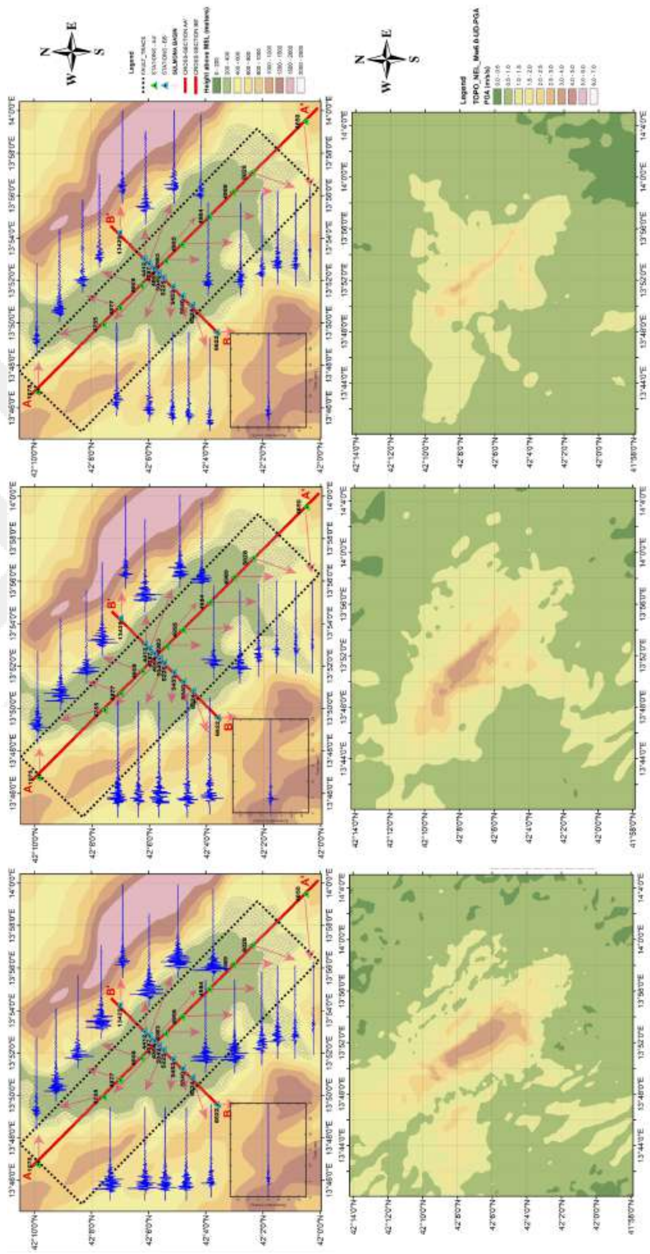

Figure 7.3: (Top) Time Series of Acceleration recorded on selected virtual stations, (Bottom) PGA map of area, NS, EW and Vertical (from Left to right) for Simulation of Mw 6.0, Non-Linear Visco-elastic, S003

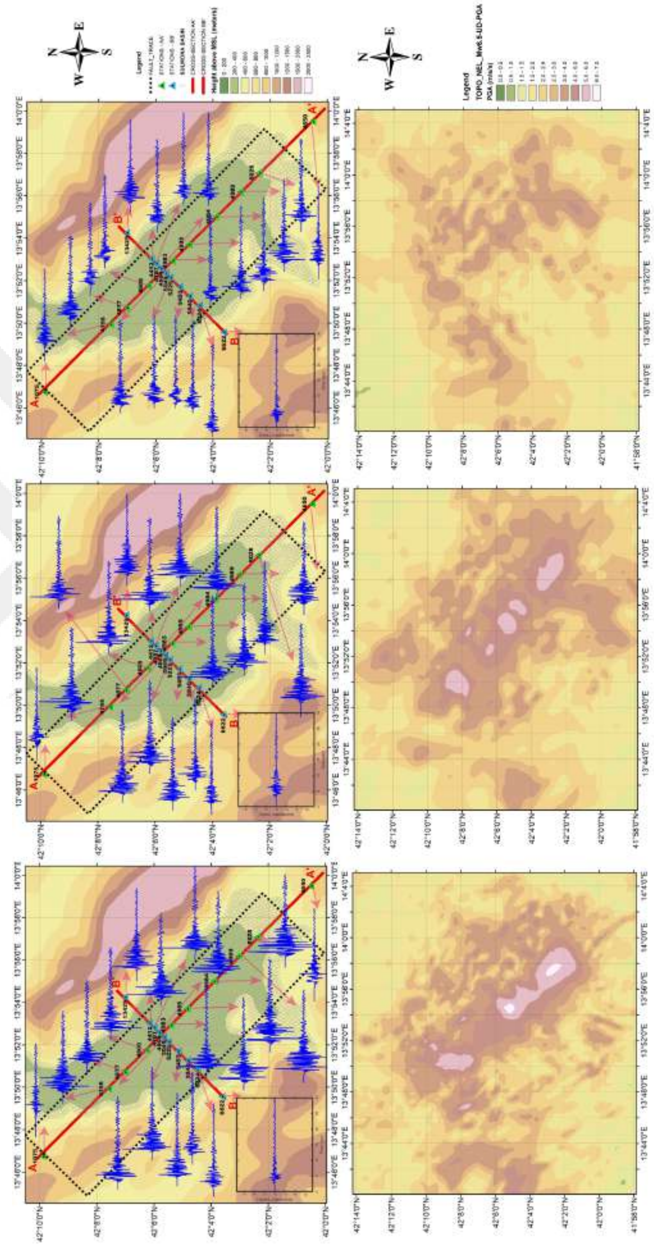

Figure 7.4: (Top) Time Series of Acceleration recorded on selected virtual stations, (Bottom) PGA map of area, NS, EW and Vertical (from Left to right) for Simulation of Mw 6.5, Non-Linear Visco-elastic, S003

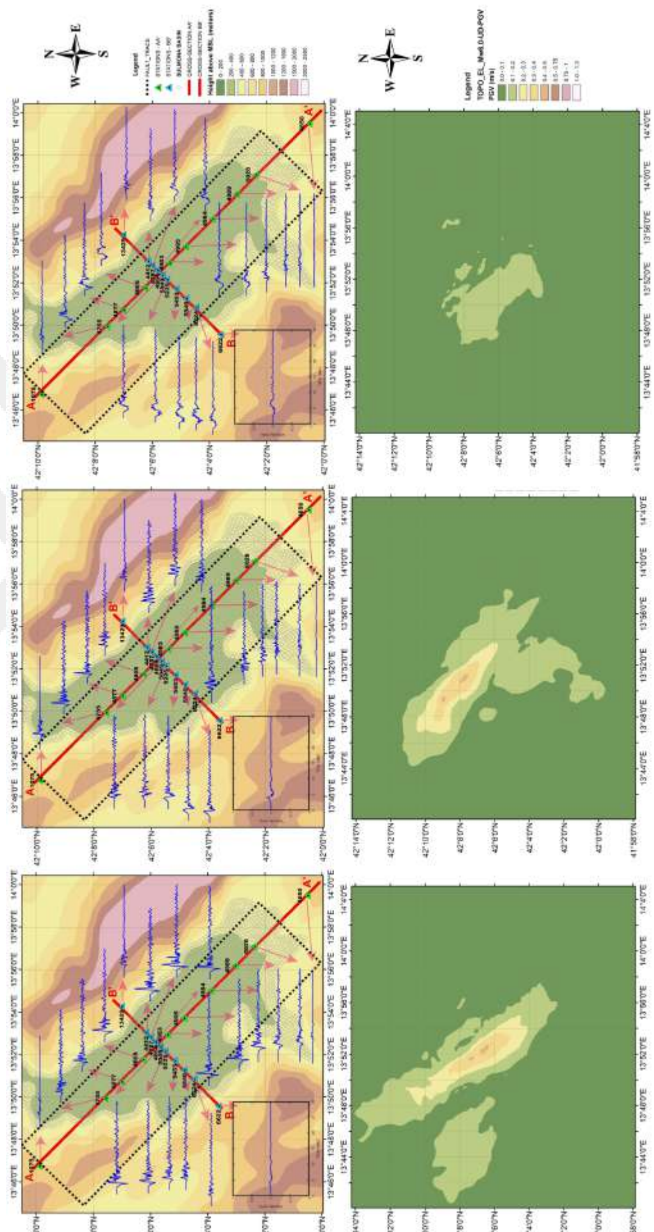

Figure 7.5: (Top) Time Series of Velocity recorded on selected virtual stations, (Bottom) PGV map of area, NS, EW and Vertical (from Left to right) for Simulation of Mw 6.0, Linear Visco-elastic, S003

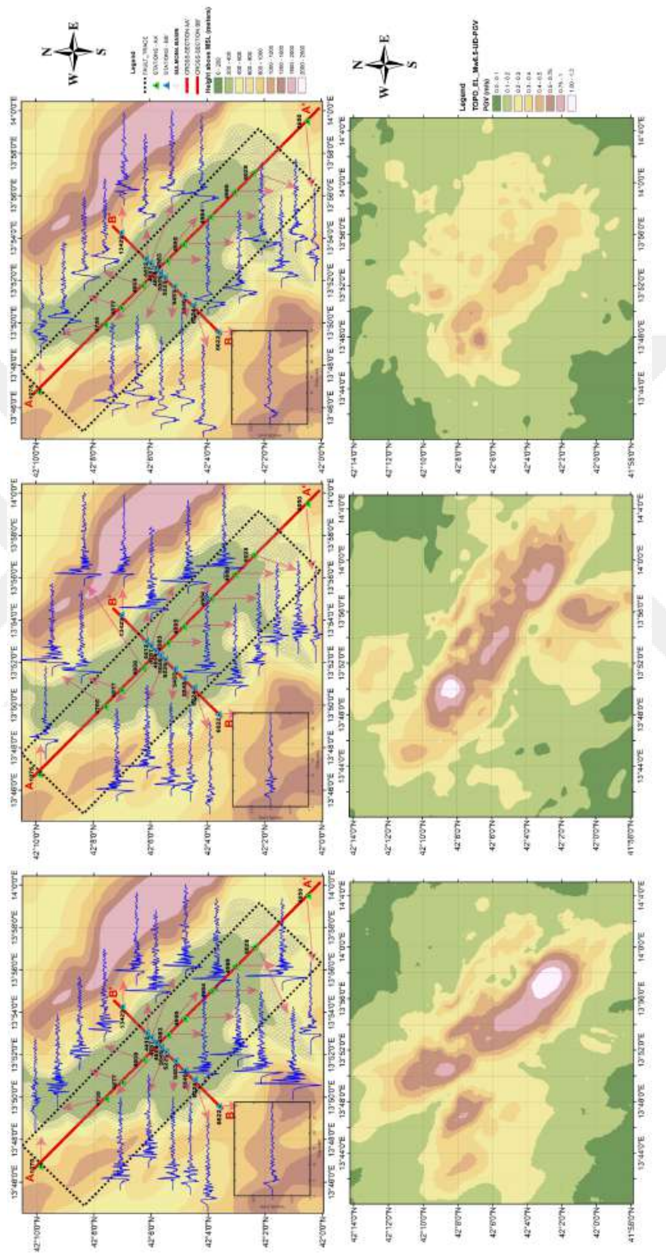

Figure 7.6: (Top) Time Series of Velocity recorded on selected virtual stations, (Bottom) PGV map of area, NS, EW and Vertical (from Left to right) for Simulation of Mw 6.5, Linear Visco-elastic, S003

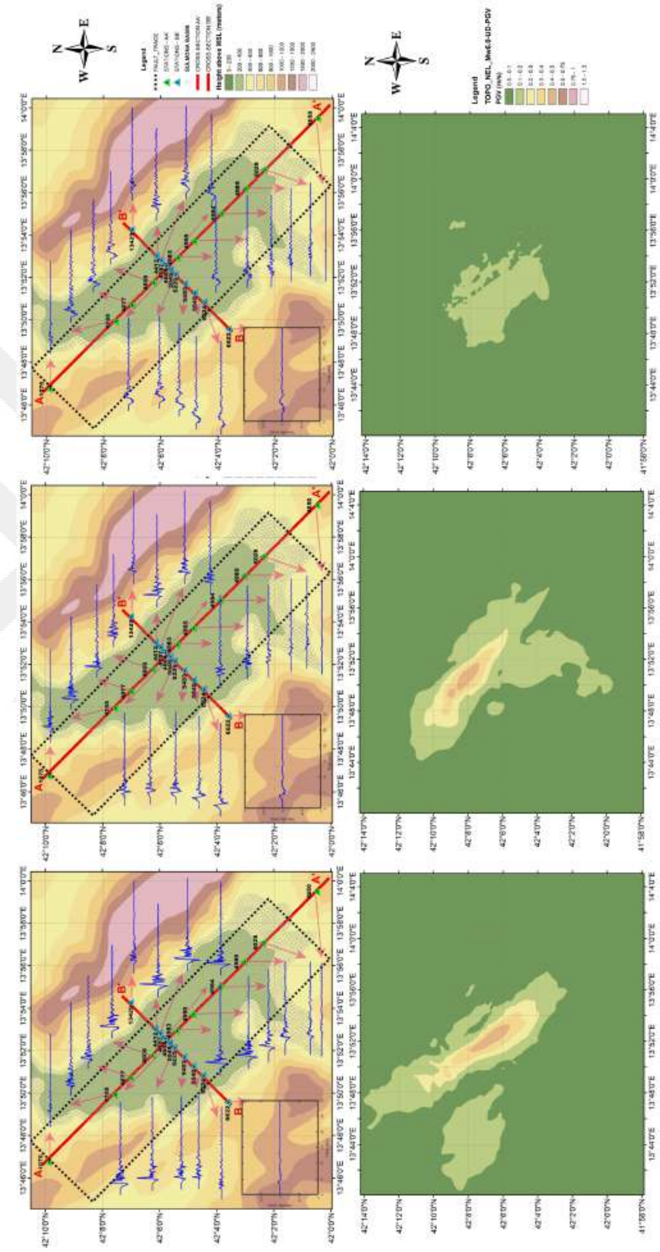

Figure 7.7: (Top) Time Series of Velocity recorded on selected virtual stations, (Bottom) PGV map of area, NS, EW and Vertical (from Left to right) for Simulation of Mw 6.0, Non-Linear Visco-elastic, S003

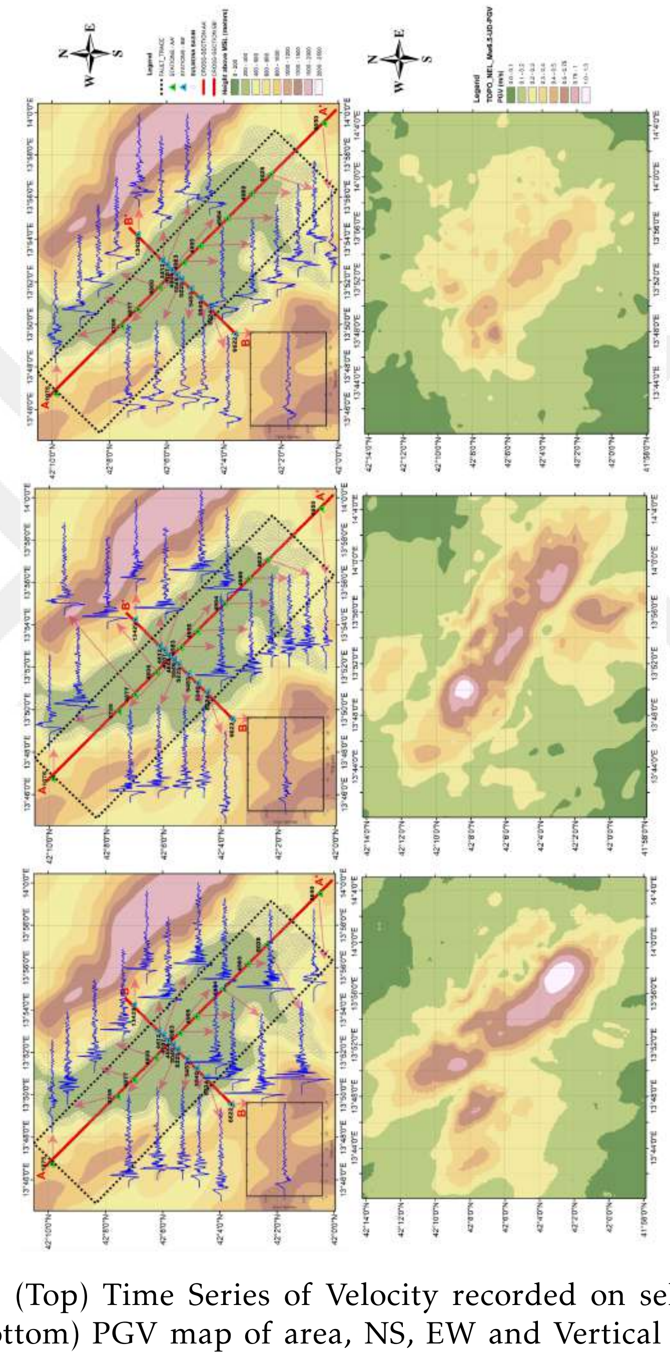

Figure 7.8: (Top) Time Series of Velocity recorded on selected virtual stations, (Bottom) PGV map of area, NS, EW and Vertical (from Left to right) for Simulation of Mw 6.5, Non-Linear Visco-elastic, S003

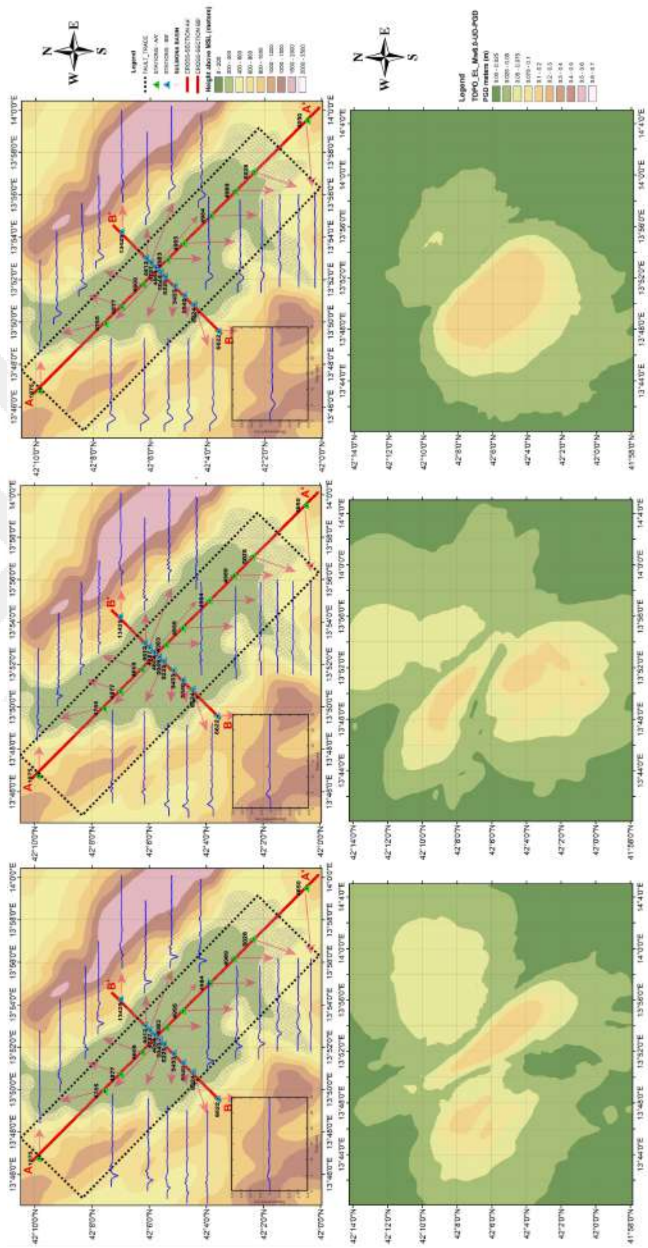

Figure 7.9: (Top) Time Series of Displacement recorded on selected virtual stations, (Bottom) PGD map of area, NS, EW and Vertical (from Left to right) for Simulation of Mw 6.0, Linear Visco-elastic, S003

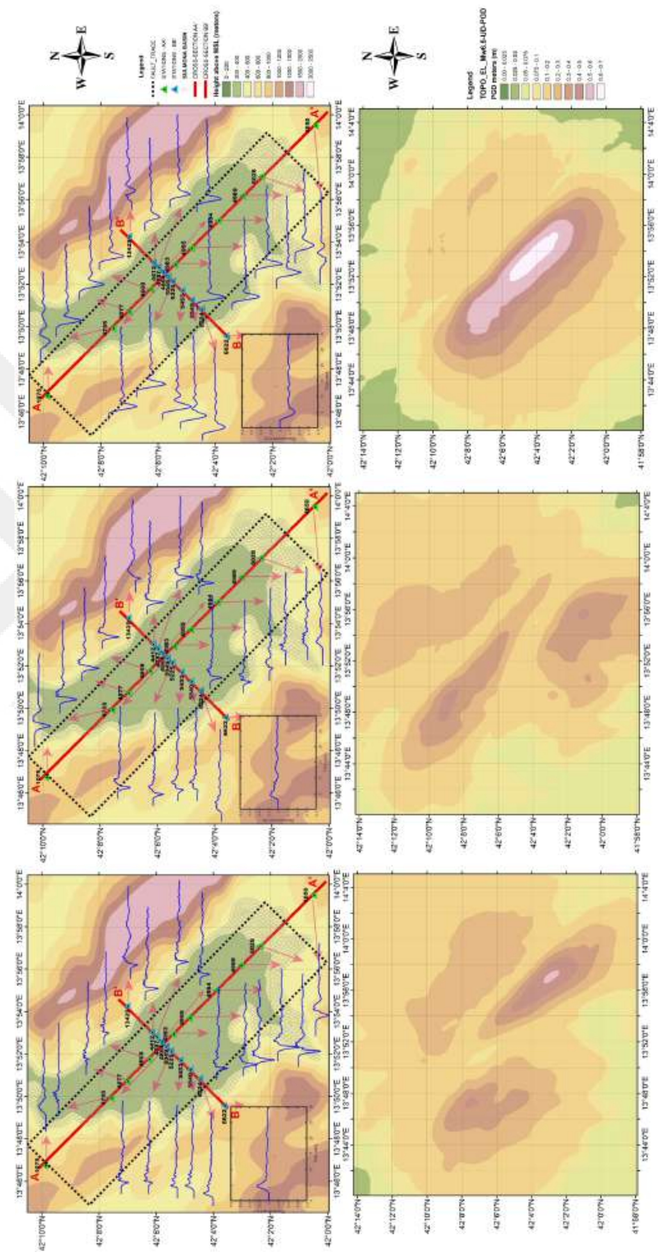

Figure 7.10: (Top) Time Series of Displacement recorded on selected virtual stations, (Bottom) PGD map of area, NS, EW and Vertical (from Left to right) for Simulation of Mw 6.5, Linear Visco-elastic, S003

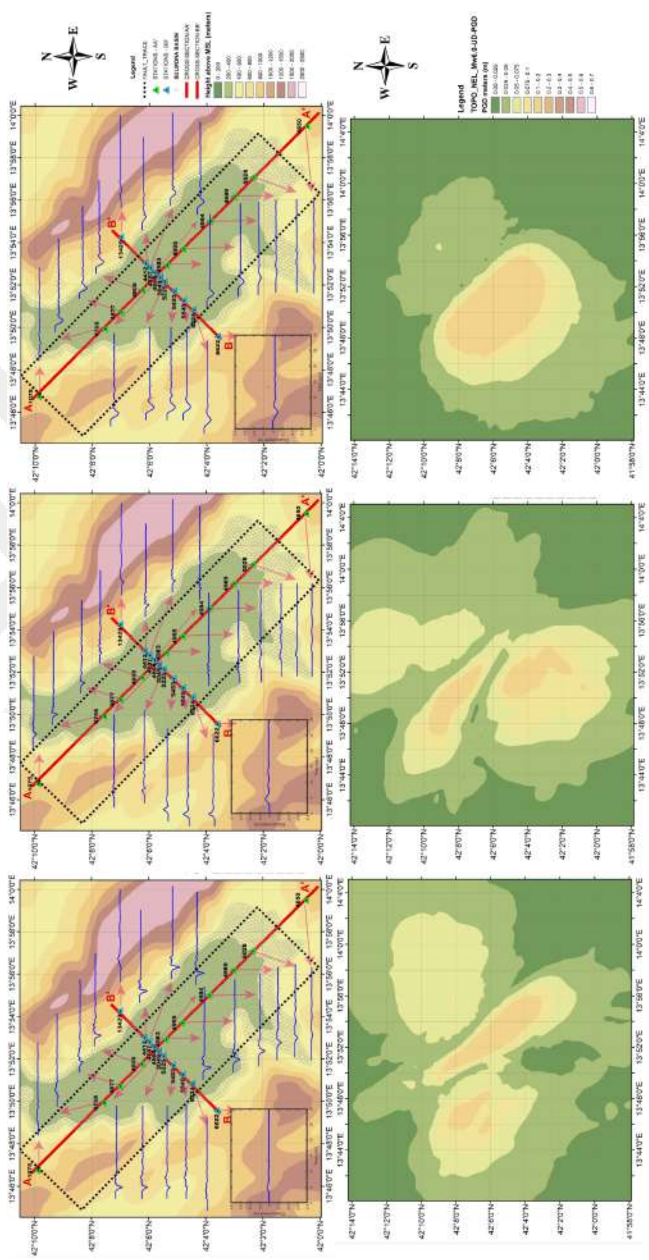

Figure 7.11: (Top) Time Series of Displacement recorded on selected virtual stations, (Bottom) PGD map of area, NS, EW and Vertical (from Left to right) for Simulation of Mw 6.0, Non-Linear Visco-elastic, S003

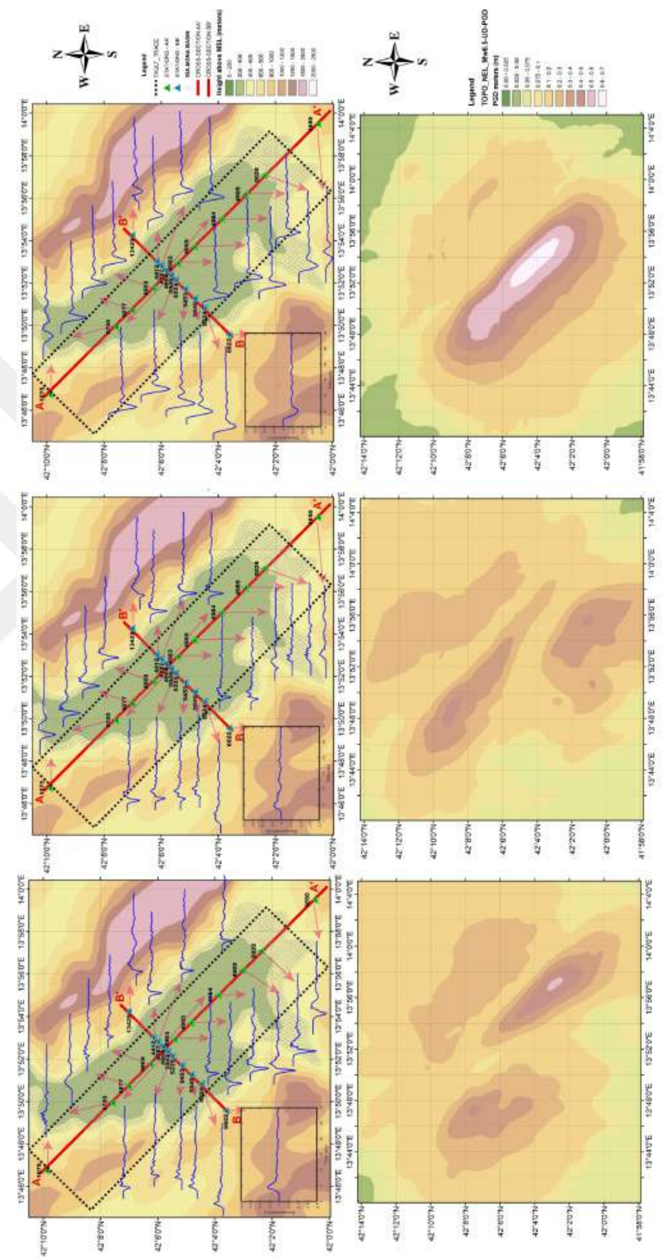

Figure 7.12: (Top) Time Series of Displacement recorded on selected virtual stations, (Bottom) PGD map of area, NS, EW and Vertical (from Left to right) for Simulation of Mw 6.5, Non-Linear Visco-elastic, S003

7.2 Effect on Magnitude and Soil Model on the results

Seismic moment magnitude relations can be considered as accounted for the energy release. Thereby, Earthquake magnitude and seismic moment are positively related to the amplitude of the ground displacement. Results are appropriate to make seismic hazard analysis including ground motion prediction equations. Considering non-linear visco-elastic soil model that viscous damper is active during the earthquake induced collision case then regarding energy dissipation can expected but high moment magnitude of earthquake case there is only a slight reduction of ground motion with respect to linear-visco elastic case. However, important point is can be indicated as both models have the mechanical implementation of response of rapid increase in case of seismic loading and decrease in the force with lower unloading rate during the recovery time interval. Yet, non-linear viscoelastic model affects the additional reduction of force before separation. One may consider non-linear viscoelastic model as more accurate than the linear viscoelastic model because loss of energy during earthquake induced force not much significant but theoretically more correct implementation with respect to linear-viscoelastic model of nature. However, practical implementation for non-linear viscoelastic model need more the knowledge of soil behavior as having additional parameters in calculations. It is correct to approximate the hysteresis behavior of alluvial deposits that is present in Sulmona Basin undergoing dynamic excitations. This non-linear behaviour again to be observed in nature as the reduction of shear modulus and the increase of damping ratio are related to the second invariant of the strain tensor during multi directional loading cases such as here considered as earthquake simulation case.

Chapter 8

Response Spectra and Spectral Amplification calculations

8.1 Groups of Simulations

8.1.1 Response Spectra for Selected Virtual Stations

Response spectra is commonly used in engineering seismology and structural engineering in order to define possible earthquake induced ground motion on the resisting load capacity of the buildings. The amplitudes of the ground motion could be indicated as of acceleration, velocity and displacement. Most commonly as peak ground acceleration (PGA) which refers to the maximum spike of the ground motion acceleration. Yet, PGA does not provide any solid information or an answer in order to have a quantitative value that affects the seismic amplification of building motion caused by earthquake induced cyclic ground motion in time or frequency domain. Additionally, tall buildings with long fundamental periods of vibration always respond totally different than short buildings with short periods of vibration induced motion. Response spectra is used to obtain these characteristics for the buildings. If one determine the peak acceleration value (Spectral Acceleration - S_a of the single degree of freedom system, in correspondence to the a range of time or frequency domain of vibration, surely, one can also determine the locus of points may be used to create a response spectrum of a system with respect to a definite ground motion.Thereby, if one knows period of vibration, this lead to have maximum acceleration from the response spectra. Nominal percentage of critical damping is taken into account to provide and to concern viscous damping of a linear-elastic single degree of freedom system, which is generally five-percent. Here four different groups of simulations, each simulation's response spectra for the each groups are statistically calculated for each virtual station that two of them are on the cross section AA' and the rest of two are on the cross section BB'. Acceleration response spectra obtained through SPEED simulations and ANN2BB traning, are indicated by the geometric mean of the horizontal components (NS and EW component of the motion). Additionally, for those response spectra, there is a good relation with the ground motion prediction equations such as CAEA15. (see appendix for the plots.)

8.1.2 GROUP 01: Mw 6.0 - Linear Visco-Elastic Simulations

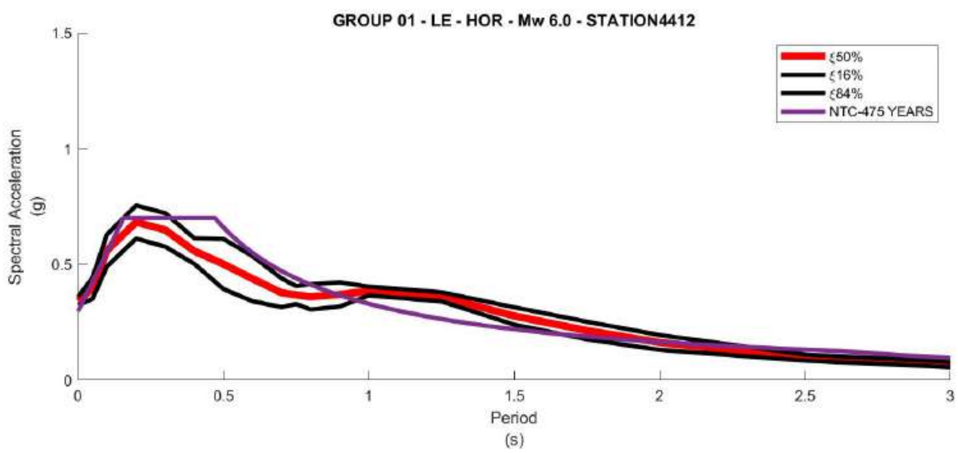

Figure 8.1: Response Spectra for Group 01 for Station 4412 Geo-Mean of Horizontal Motion

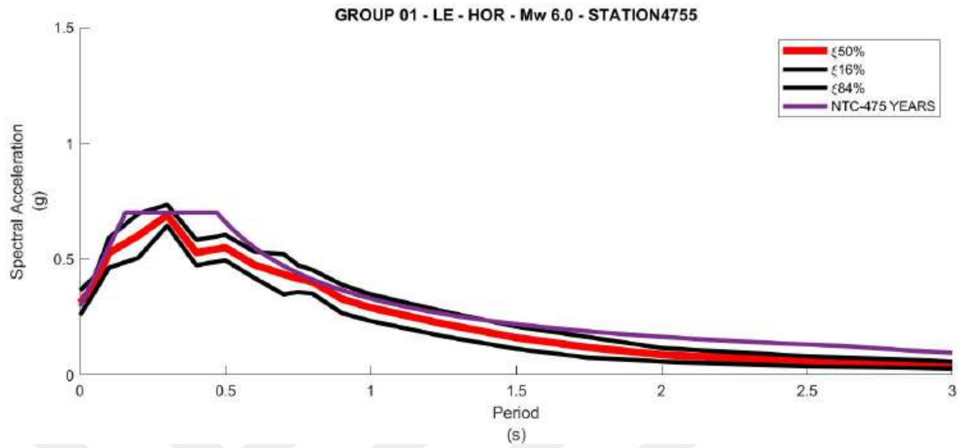

Figure 8.2: Response Spectra for Group 01 for Station 4755 Geo-Mean of Horizontal Motion

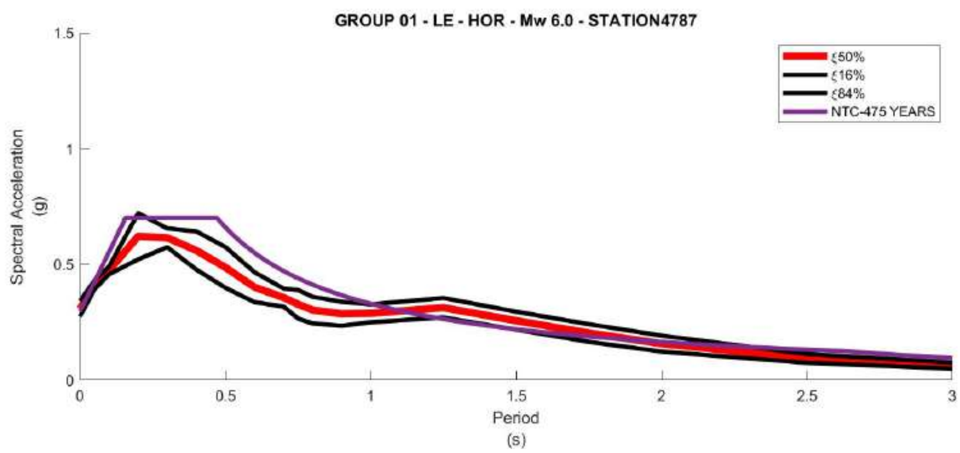

Figure 8.3: Response Spectra for Group 01 for Station 4787 Geo-Mean of Horizontal Motion

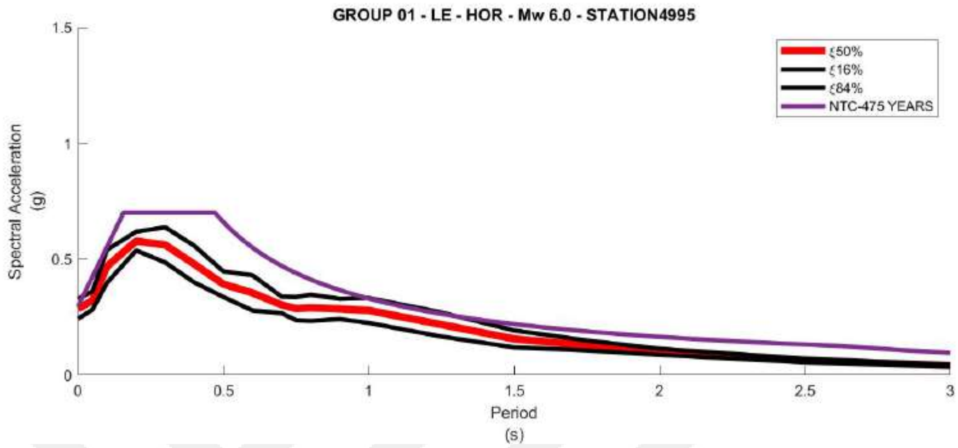

Figure 8.4: Response Spectra for Group 01 for Station 4995 Geo-Mean of Horizontal Motion

8.1.3 GROUP 02: Mw 6.5 - Linear Visco-Elastic Simulations

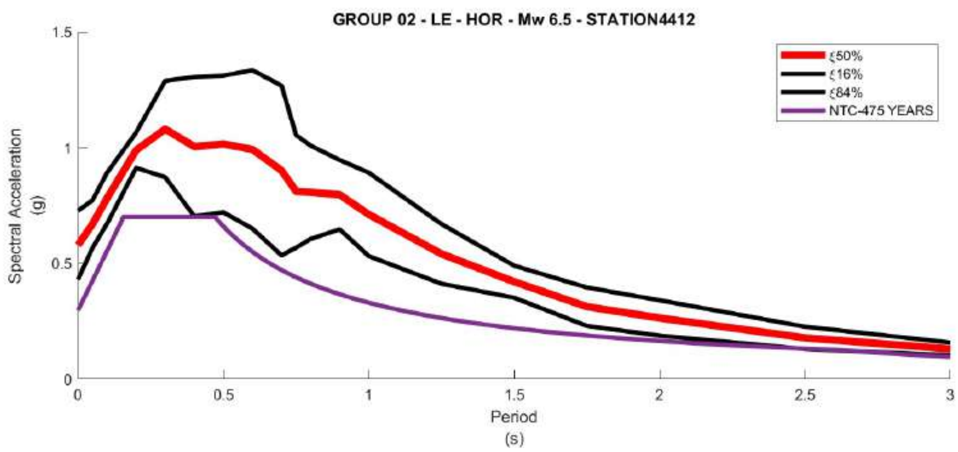

Figure 8.5: Response Spectra for Group 02 for Station 4412 Geo-Mean of Horizontal Motion

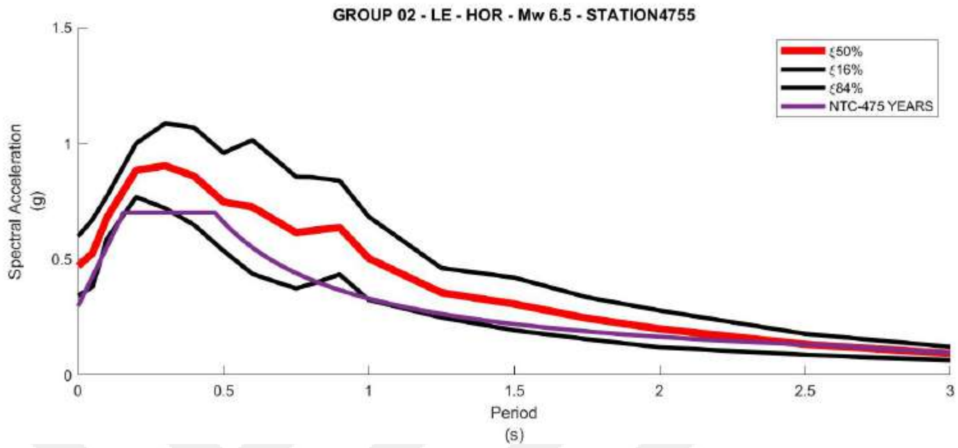

Figure 8.6: Response Spectra for Group 02 for Station 4755 Geo-Mean of Horizontal Motion

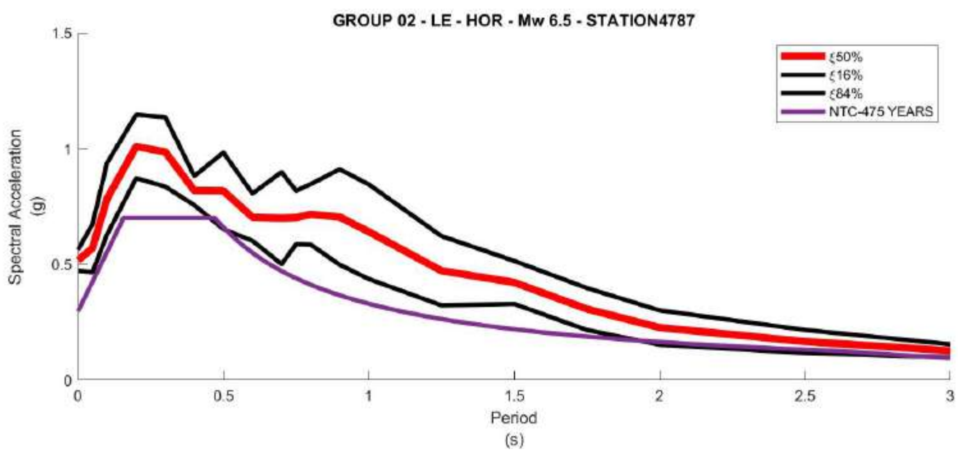

Figure 8.7: Response Spectra for Group 02 for Station 4787 Geo-Mean of Horizontal Motion

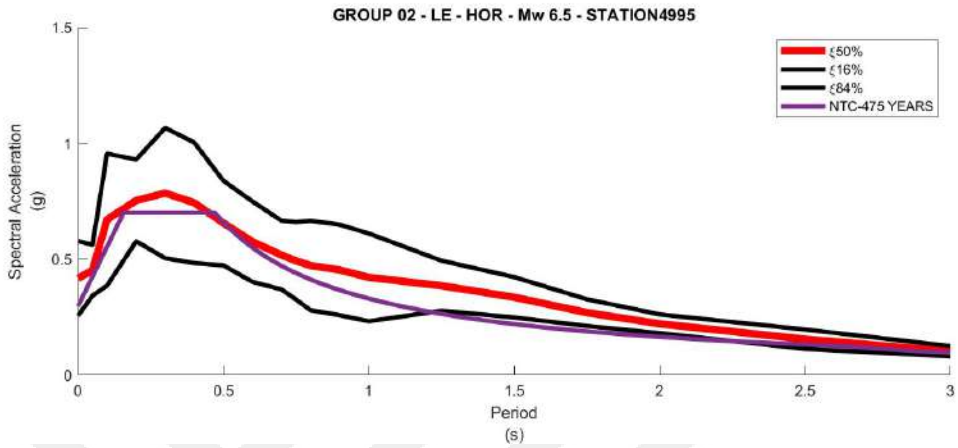

Figure 8.8: Response Spectra for Group 02 for Station 4995 Geo-Mean of Horizontal Motion

8.1.4 GROUP 03: Mw 6.0 - Non-Linear Visco-Elastic Simulations

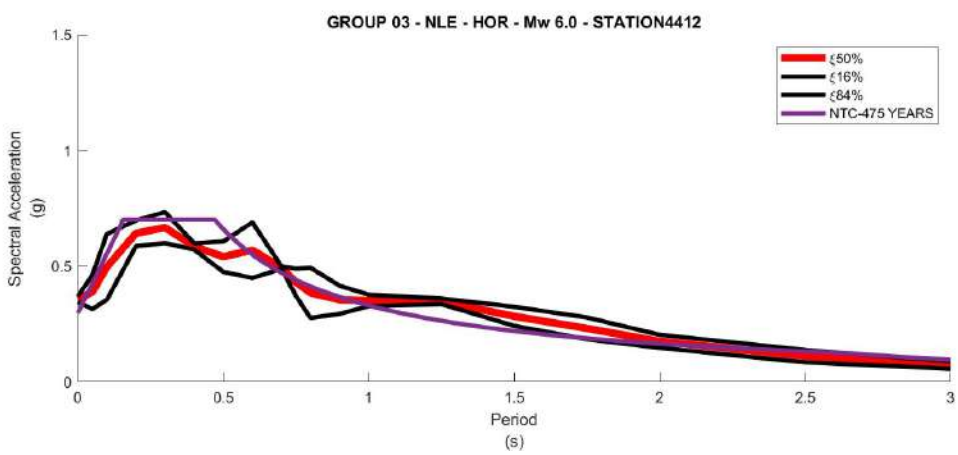

Figure 8.9: Response Spectra for Group 03 for Station 4412 Geo-Mean of Horizontal Motion

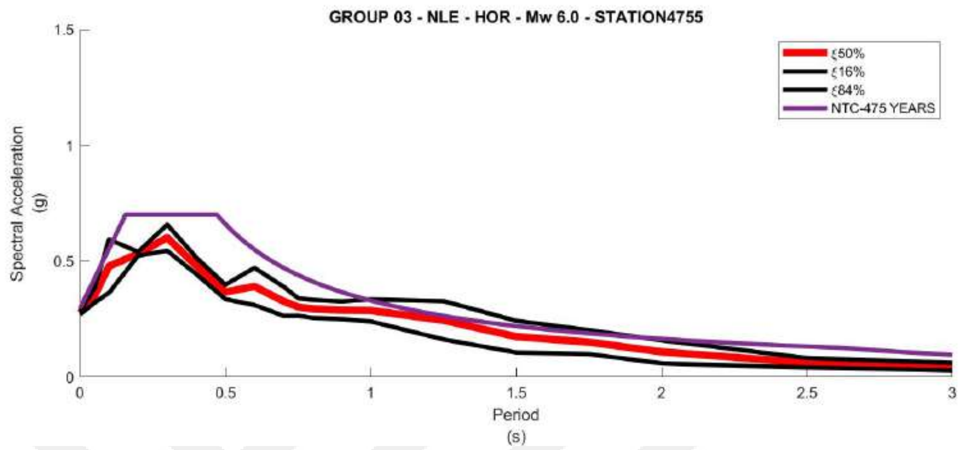

Figure 8.10: Response Spectra for Group 03 for Station 4755 Geo-Mean of Horizontal Motion

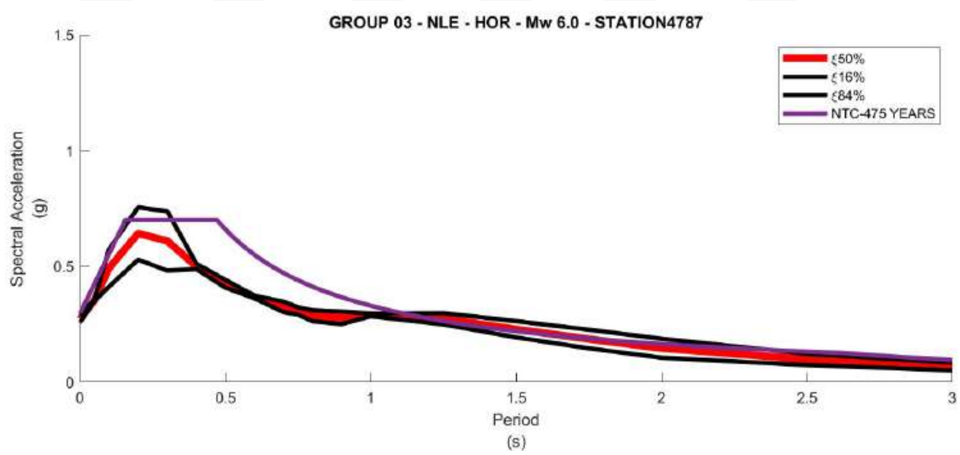

Figure 8.11: Response Spectra for Group 03 for Station 4787 Geo-Mean of Horizontal Motion

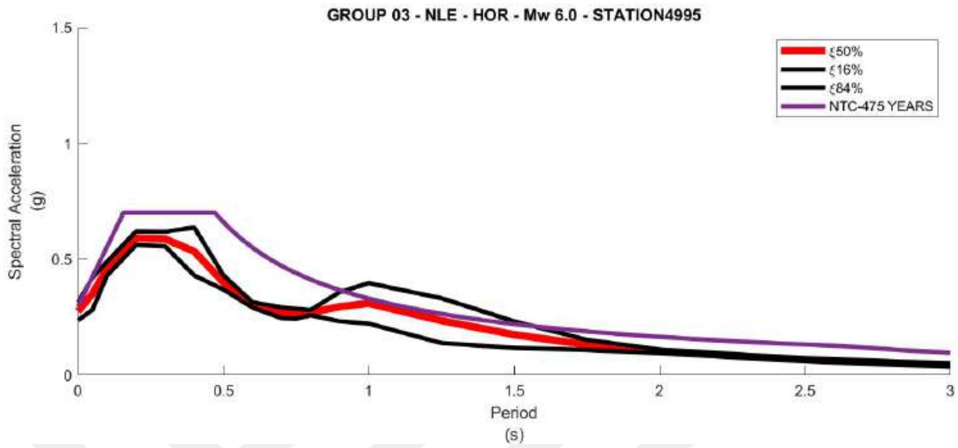

Figure 8.12: Response Spectra for Group 03 for Station 4995 Geo-Mean of Horizontal Motion

8.1.5 GROUP 04: Mw 6.5 - Non-Linear Visco-Elastic Simulations

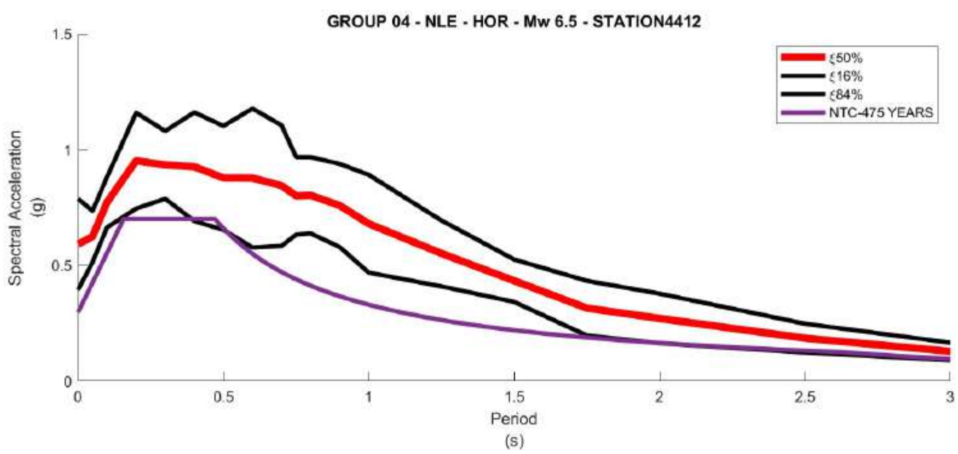

Figure 8.13: Response Spectra for Group 04 for Station 4412 Geo-Mean of Horizontal Motion

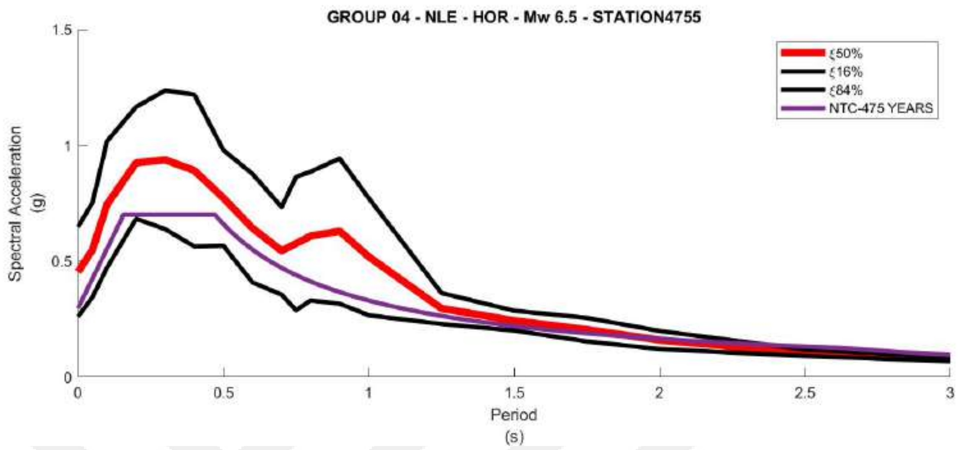

Figure 8.14: Response Spectra for Group 04 for Station 4755 Geo-Mean of Horizontal Motion

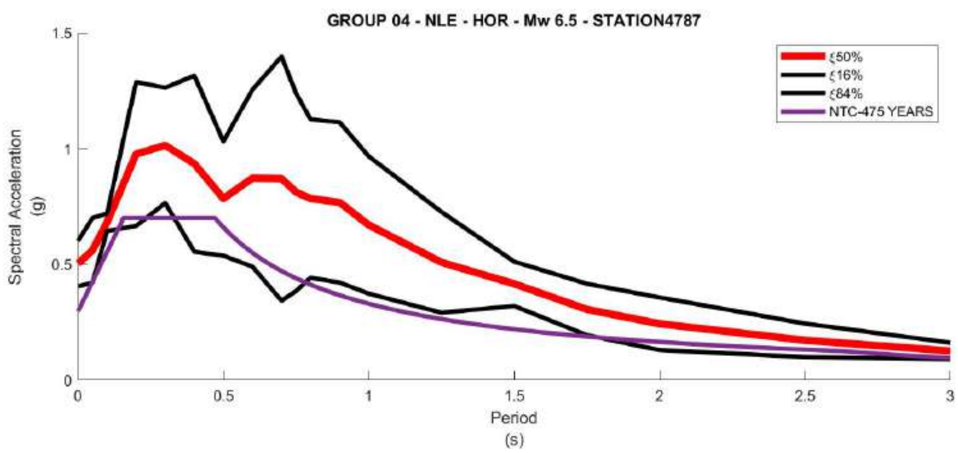

Figure 8.15: Response Spectra for Group 04 for Station 4787 Geo-Mean of Horizontal Motion

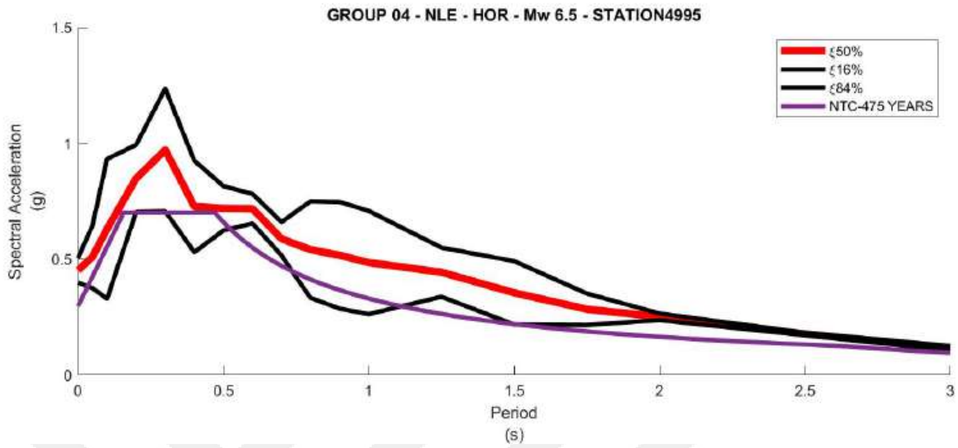

Figure 8.16: Response Spectra for Group 04 for Station 4995 Geo-Mean of Horizontal Motion

8.2 Selected Spectral Amplification Functions

Another method to predict seismic intensity, one may consider to take into account of the local site effects, that is can be achieved through site amplification factors of response spectra which are obtained from dividing response spectra for the soil profile by response spectra for outcropping rock in site. In short, local site amplification ratio can be defined as the ground motion amplification with respect to a rock reference at the same location. Most recent, seismic design codes for construction considers the site effects utilizing through spectral amplification factor/function or ratio (SAF/SAR), briefly as a parameter related to the velocity profile at the site under consideration. Then, one may use this factor/ratio for practical purposes in seismic design, additionally, identifying the site parameters based on frequency-dependent reference amplification is very reliable to use it. Here are, site spectral amplification ratios for each group of simulation (4 in total), 2 reference station on soil mass on each cross section (4 in total) with respect to 2 reference station on outcropping rock in site are plotted. (32 spectral amplification ratios in total). These plots will be discussed at the end of this chapter considering, stations' properties, their closeness to the hypo-center, effects of earthquake magnitude, effects of soil model that is selected and other considerations.

8.2.1 4755 by 1075 for cross-section AA'

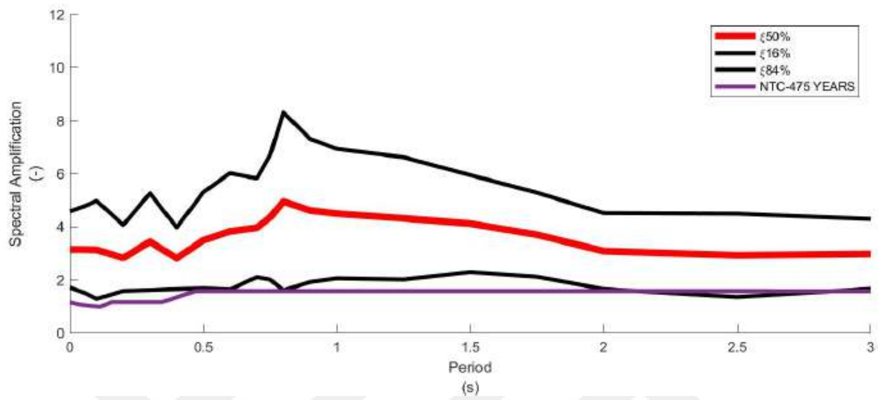

Figure 8.17: Spectral Amplification Ratio (SAR) for Station 4755 by Station 1075 for Group 01 - (geometric mean of horizontal direction

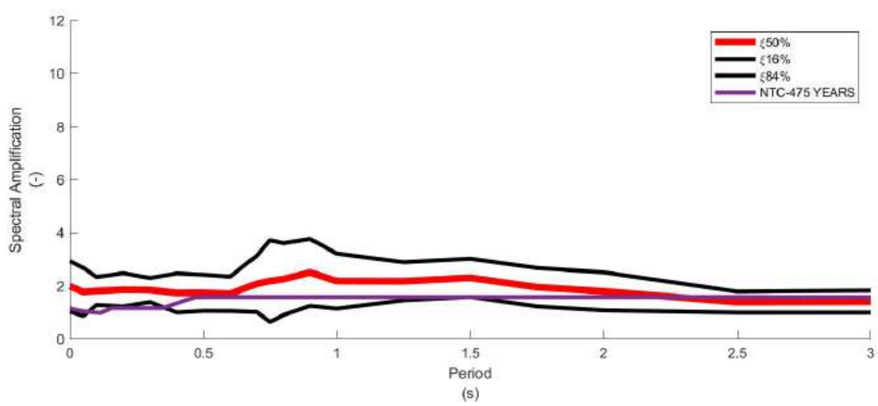

Figure 8.18: Spectral Amplification Ratio (SAR) for Station 4755 by Station 1075 for Group 02 - (geometric mean of horizontal direction

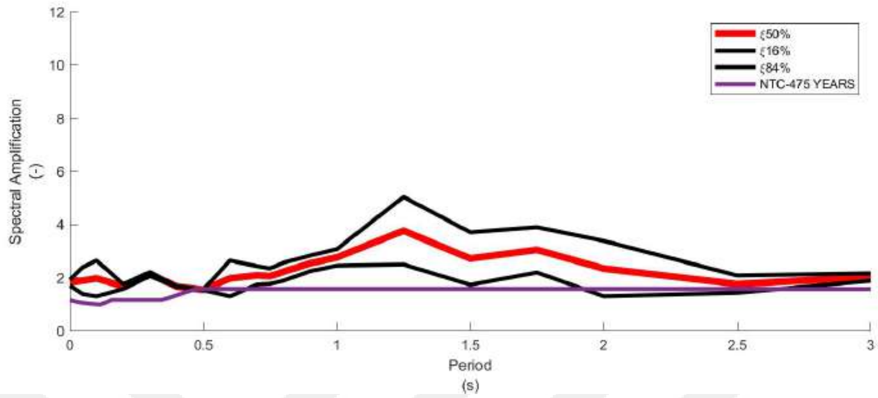

Figure 8.19: Spectral Amplification Ratio (SAR) for Station 4755 by Station 1075 for Group 03 - (geometric mean of horizontal direction

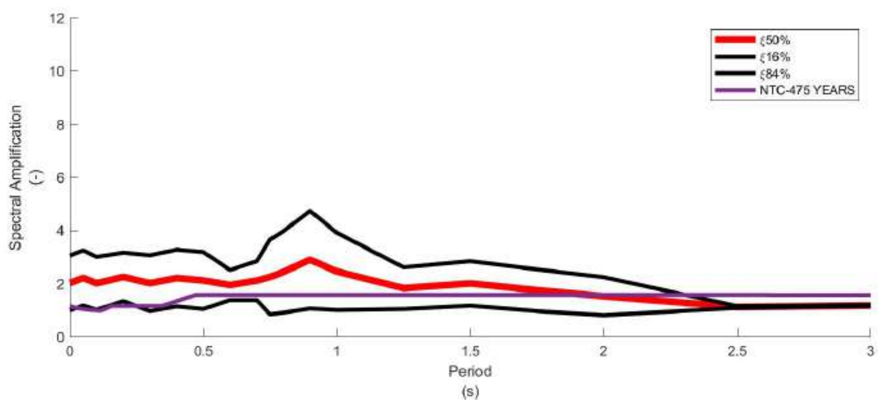

Figure 8.20: Spectral Amplification Ratio (SAR) for Station 4755 by Station 1075 for Group 04 - (geometric mean of horizontal direction

8.2.2 4755 by 4650 for cross-section AA’

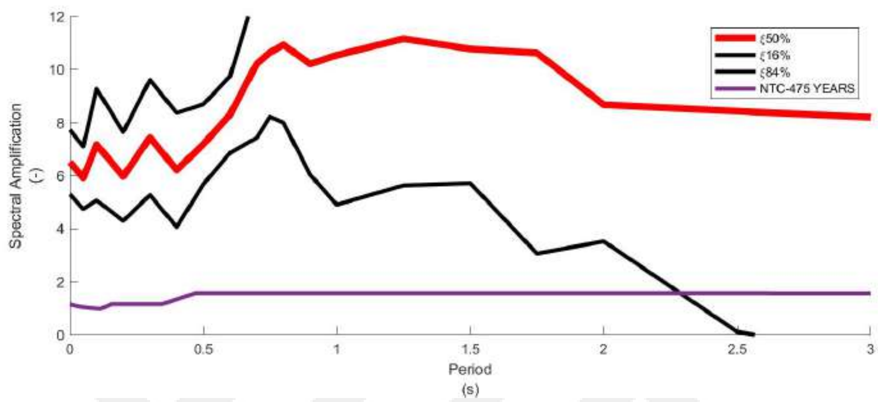

Figure 8.21: Spectral Amplification Ratio (SAR) for Station 4755 by Station 4650 for Group 01 - (geometric mean of horizontal direction

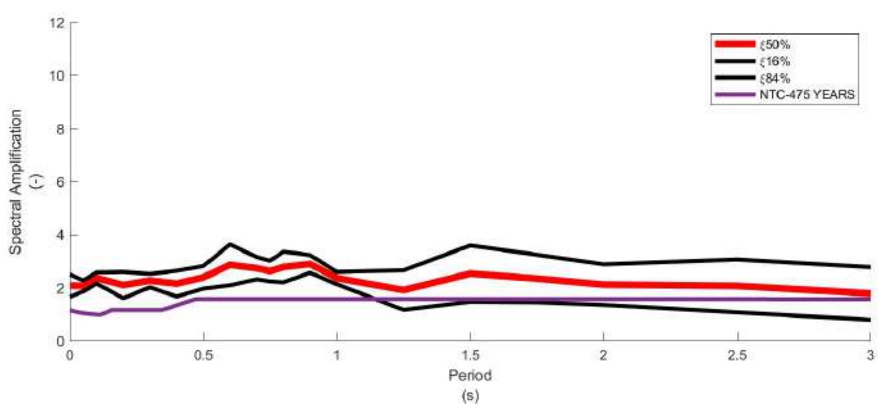

Figure 8.22: Spectral Amplification Ratio (SAR) for Station 4755 by Station 4650 for Group 02 - (geometric mean of horizontal direction

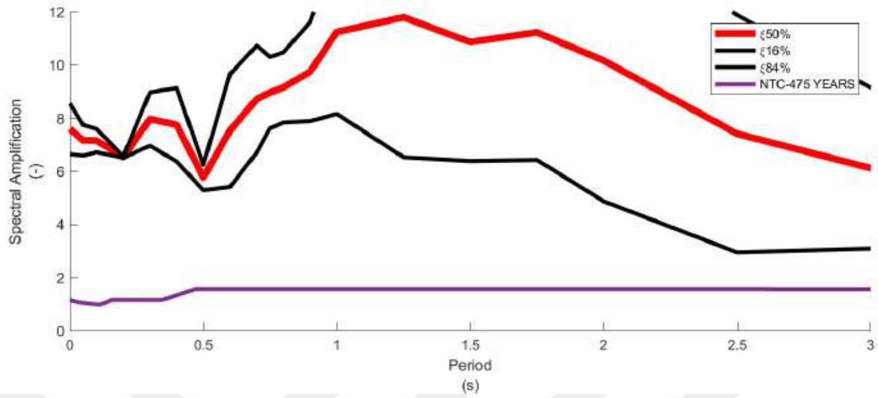

Figure 8.23: Spectral Amplification Ratio (SAR) for Station 4755 by Station 4650 for Group 03 - (geometric mean of horizontal direction

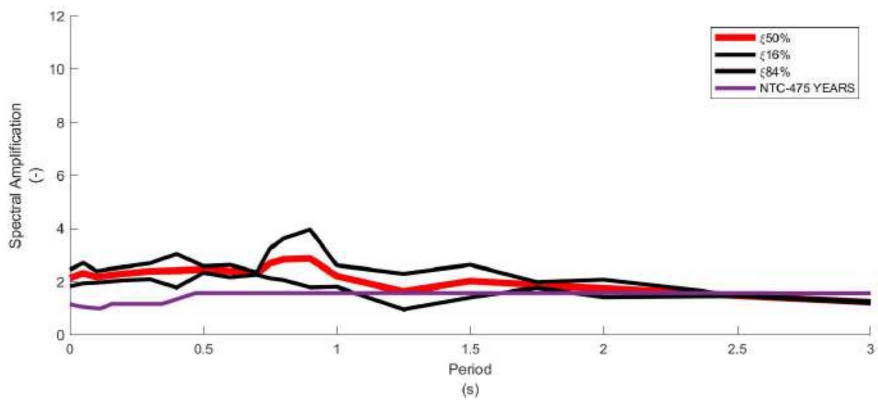

Figure 8.24: Spectral Amplification Ratio (SAR) for Station 4755 by Station 4650 for Group 04 - (geometric mean of horizontal direction

8.2.3 4995 by 1075 for cross-section AA’

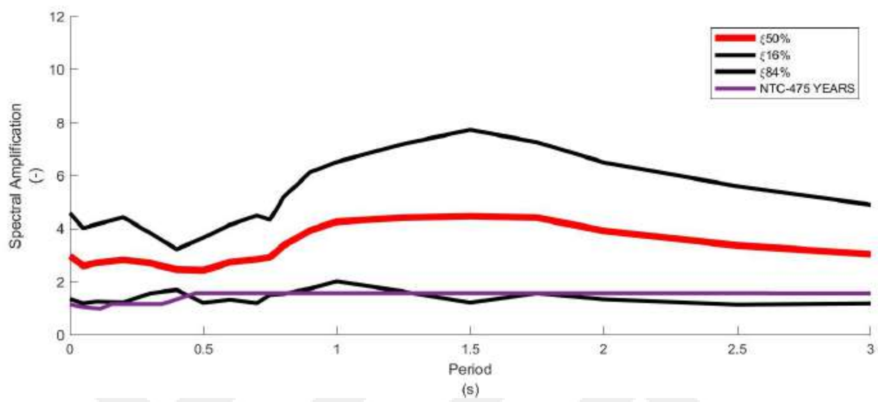

Figure 8.25: Spectral Amplification Ratio (SAR) for Station 4995 by Station 1075 for Group 01 - (geometric mean of horizontal direction

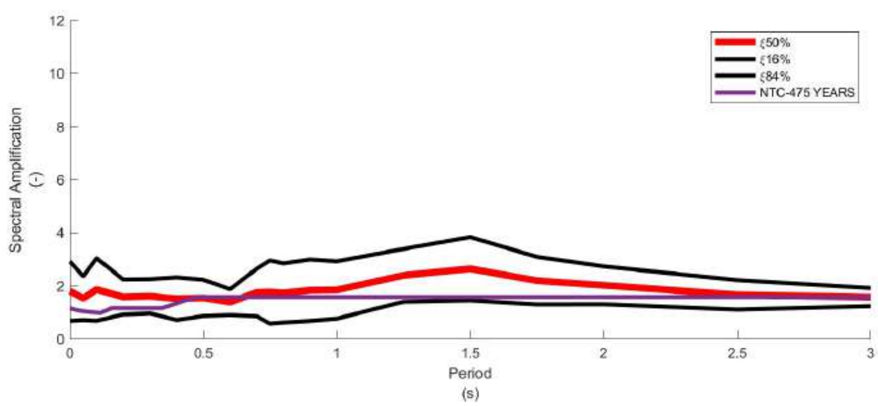

Figure 8.26: Spectral Amplification Ratio (SAR) for Station 4995 by Station 1075 for Group 02 - (geometric mean of horizontal direction

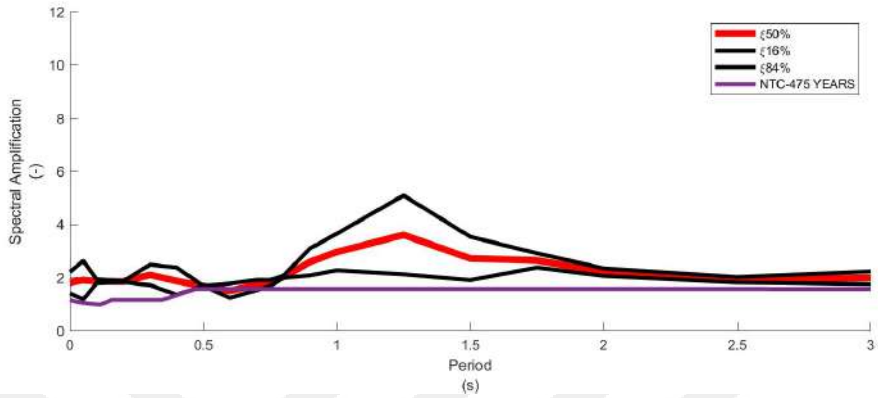

Figure 8.27: Spectral Amplification Ratio (SAR) for Station 4995 by Station 1075 for Group 03 - (geometric mean of horizontal direction

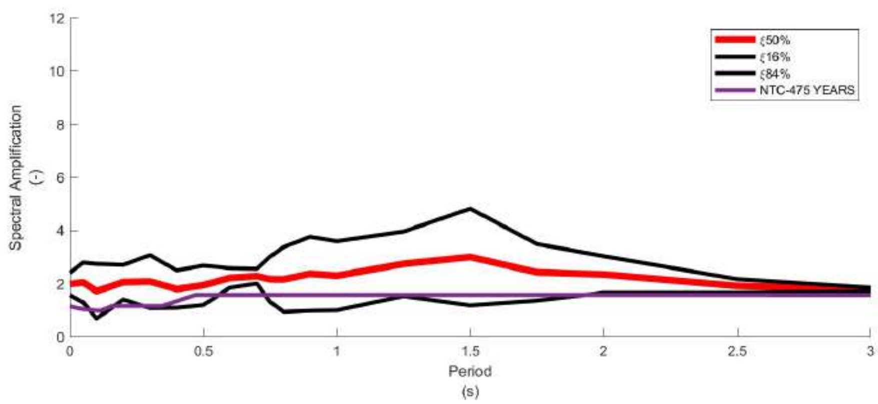

Figure 8.28: Spectral Amplification Ratio (SAR) for Station 4995 by Station 1075 for Group 04 - (geometric mean of horizontal direction

8.2.4 4995 by 4650 for cross-section AA'

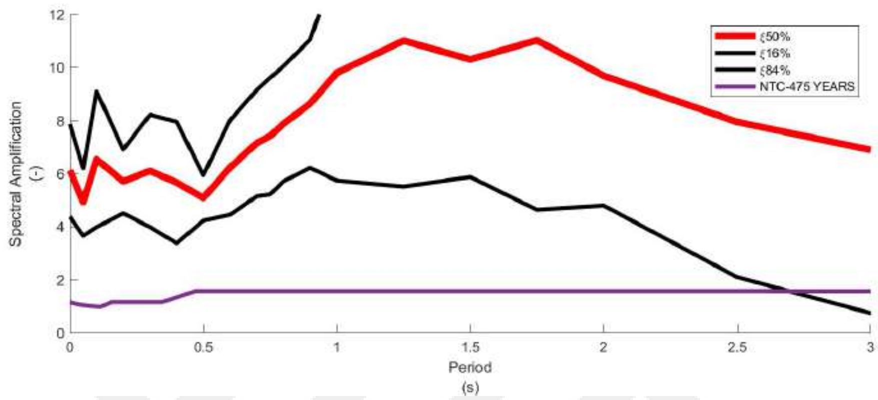

Figure 8.29: Spectral Amplification Ratio (SAR) for Station 4995 by Station 4650 for Group 01 - (geometric mean of horizontal direction

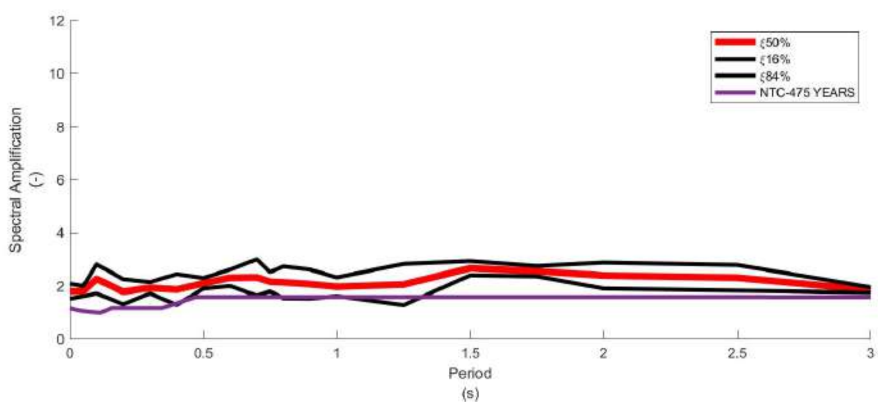

Figure 8.30: Spectral Amplification Ratio (SAR) for Station 4995 by Station 4650 for Group 02 - (geometric mean of horizontal direction

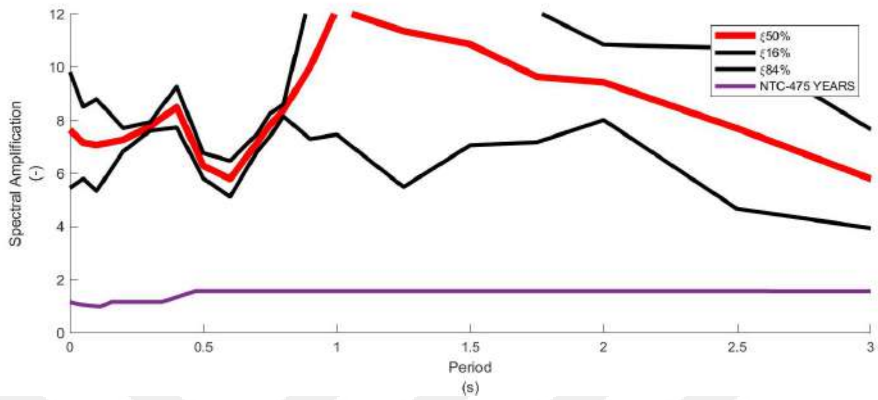

Figure 8.31: Spectral Amplification Ratio (SAR) for Station 4995 by Station 4650 for Group 03 - (geometric mean of horizontal direction

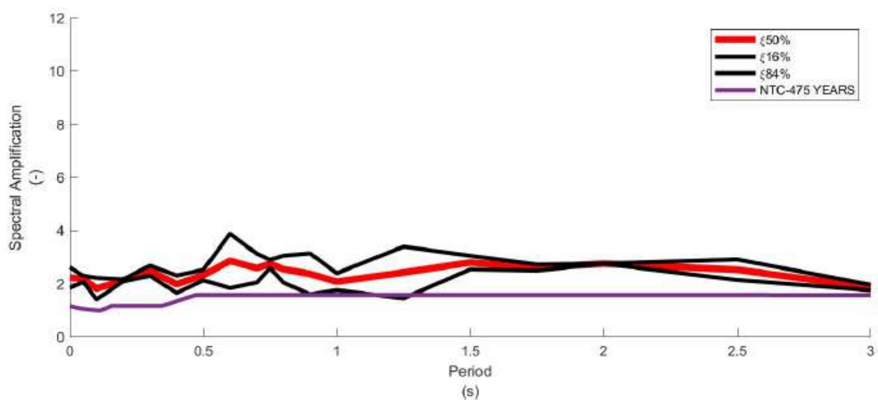

Figure 8.32: Spectral Amplification Ratio (SAR) for Station 4995 by Station 4650 for Group 04 - (geometric mean of horizontal direction

8.2.5 4412 by 6622 for cross-section BB'

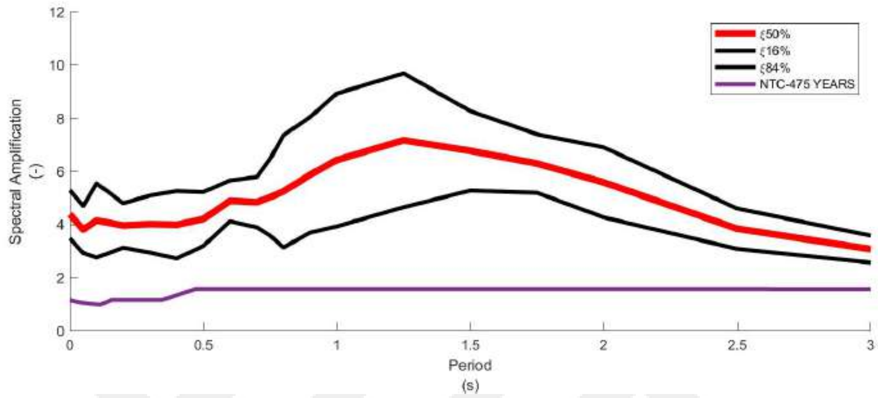

Figure 8.33: Spectral Amplification Ratio (SAR) for Station 4412 by Station 6622 for Group 01 - (geometric mean of horizontal direction

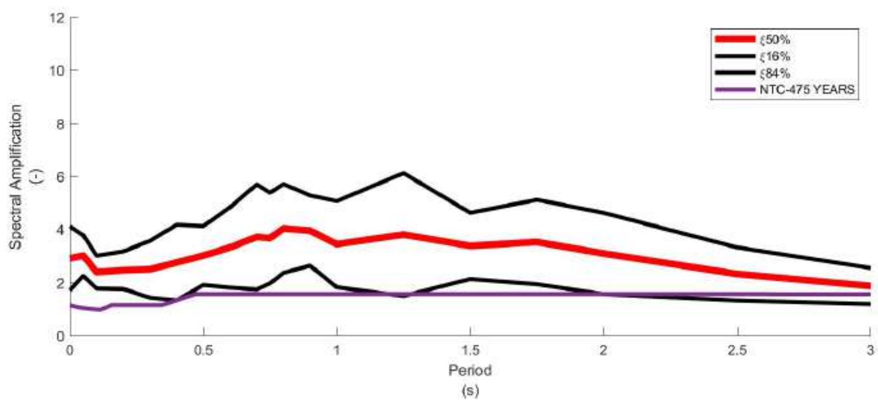

Figure 8.34: Spectral Amplification Ratio (SAR) for Station 4412 by Station 6622 for Group 02 - (geometric mean of horizontal direction

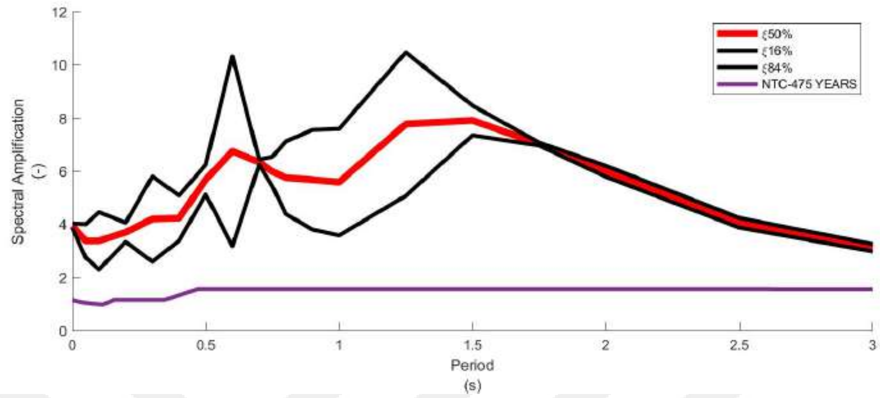

Figure 8.35: Spectral Amplification Ratio (SAR) for Station 4412 by Station 6622 for Group 03 - (geometric mean of horizontal direction

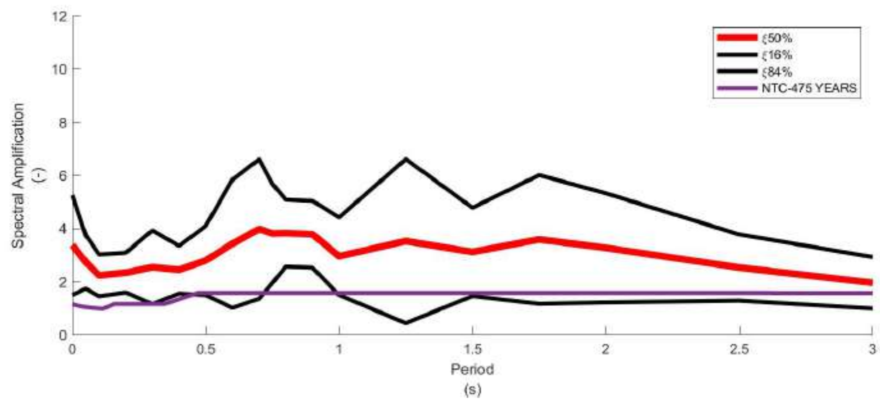

Figure 8.36: Spectral Amplification Ratio (SAR) for Station 4412 by Station 6622 for Group 04 - (geometric mean of horizontal direction

8.2.6 4412 by 13429 for cross-section BB′

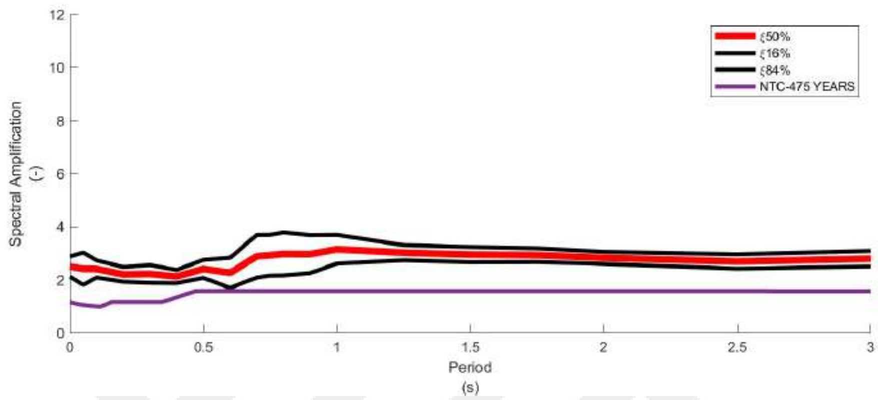

Figure 8.37: Spectral Amplification Ratio (SAR) for Station 4412 by Station 13429 for Group 01 - (geometric mean of horizontal direction

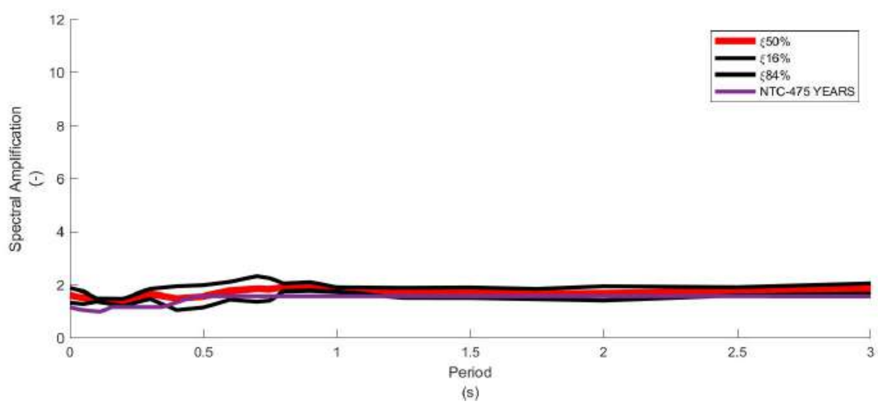

Figure 8.38: Spectral Amplification Ratio (SAR) for Station 4412 by Station 13429 for Group 02 - (geometric mean of horizontal direction

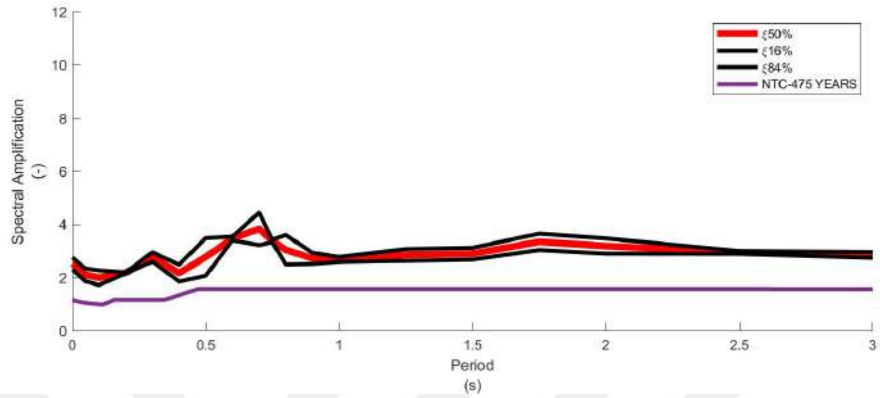

Figure 8.39: Spectral Amplification Ratio (SAR) for Station 4412 by Station 13429 for Group 03 - (geometric mean of horizontal direction

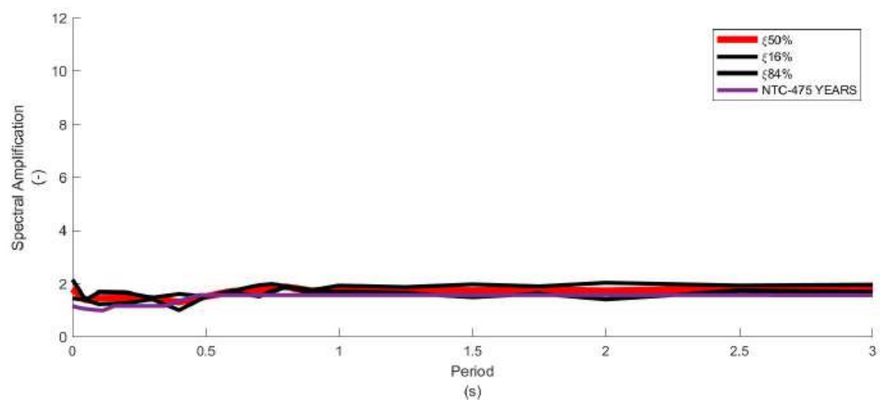

Figure 8.40: Spectral Amplification Ratio (SAR) for Station 4412 by Station 13429 for Group 04 - (geometric mean of horizontal direction

8.2.7 4787 by 6622 for cross-section BB’

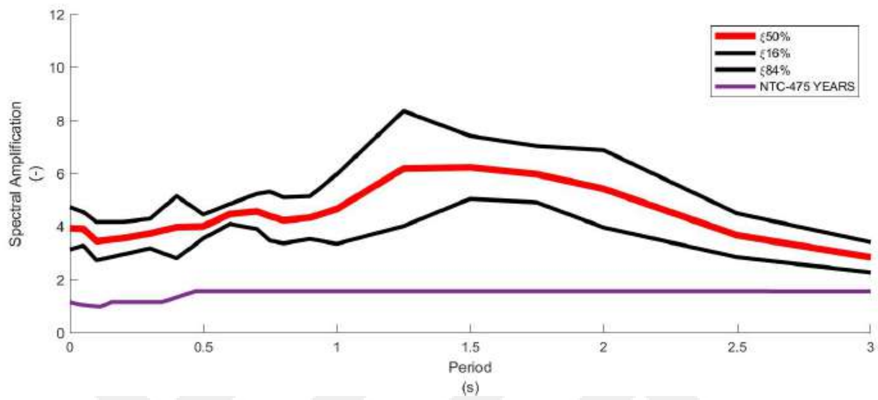

Figure 8.41: Spectral Amplification Ratio (SAR) for Station 4787 by Station 6622 for Group 01 - (geometric mean of horizontal direction

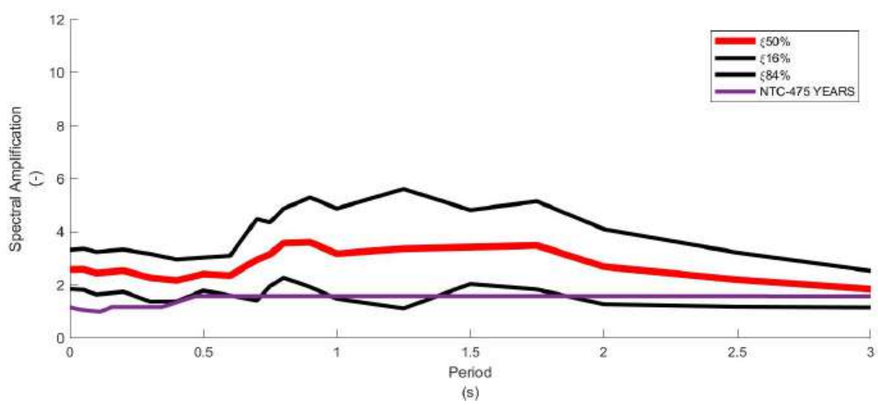

Figure 8.42: Spectral Amplification Ratio (SAR) for Station 4787 by Station 6622 for Group 02 - (geometric mean of horizontal direction

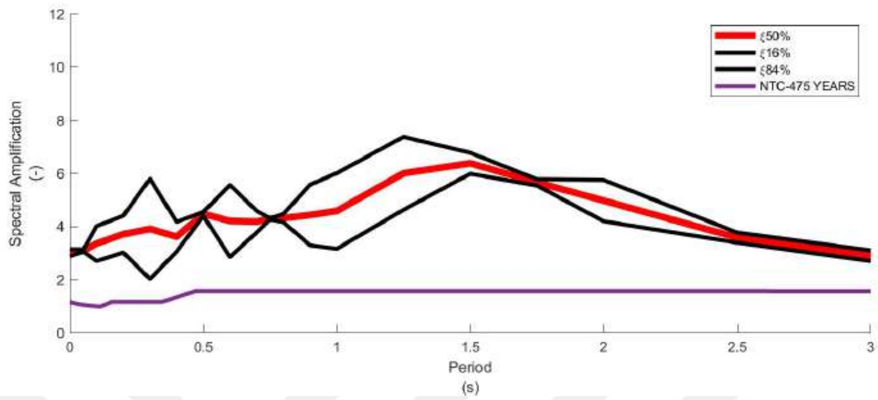

Figure 8.43: Spectral Amplification Ratio (SAR) for Station 4787 by Station 6622 for Group 03 - (geometric mean of horizontal direction

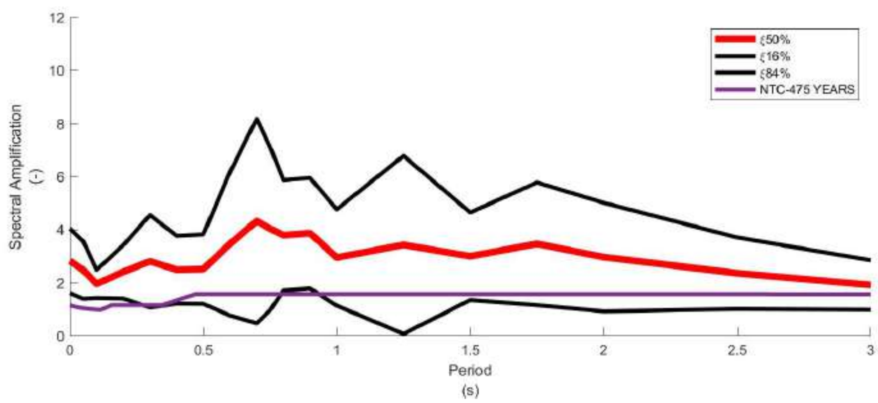

Figure 8.44: Spectral Amplification Ratio (SAR) for Station 4787 by Station 6622 for Group 04 - (geometric mean of horizontal direction

8.2.8 4787 by 13429 for cross-section BB′

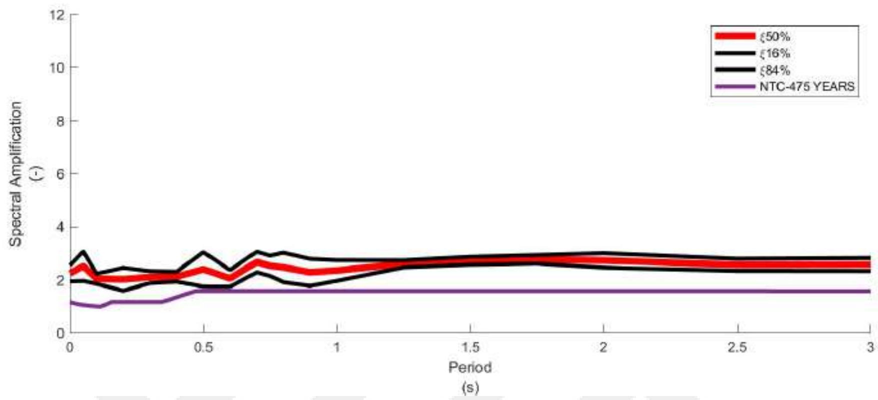

Figure 8.45: Spectral Amplification Ratio (SAR) for Station 4787 by Station 13429 for Group 01 - (geometric mean of horizontal direction

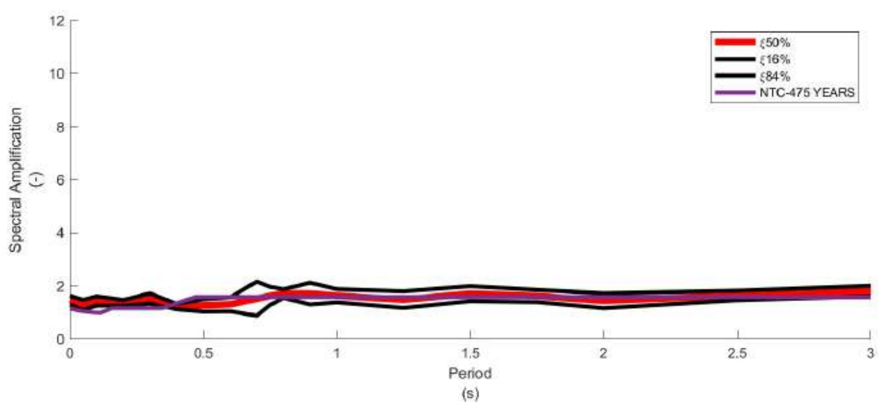

Figure 8.46: Spectral Amplification Ratio (SAR) for Station 4787 by Station 13429 for Group 02 - (geometric mean of horizontal direction

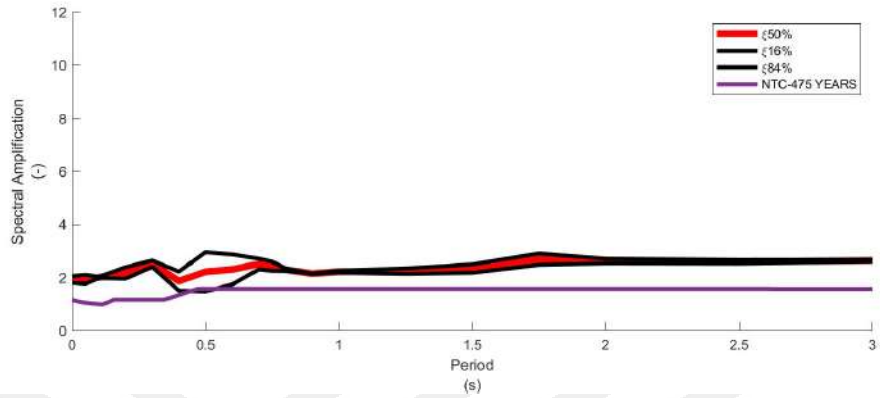

Figure 8.47: Spectral Amplification Ratio (SAR) for Station 4787 by Station 13429 for Group 03 - (geometric mean of horizontal direction

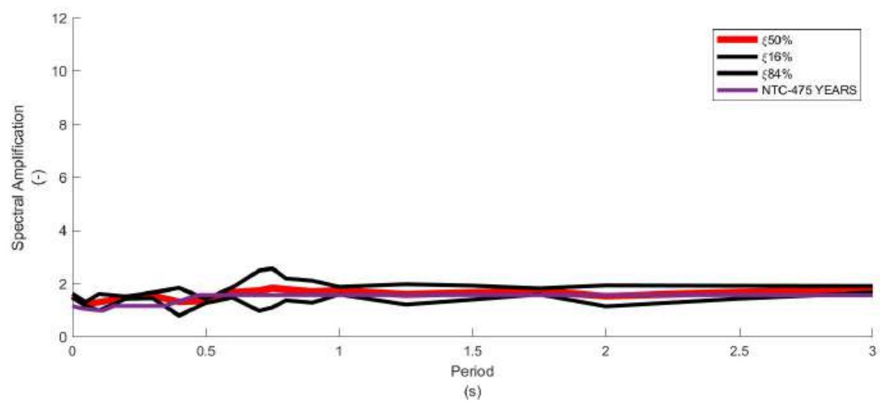

Figure 8.48: Spectral Amplification Ratio (SAR) for Station 4787 by Station 13429 for Group 04 - (geometric mean of horizontal direction

8.3 Comments on Affecting Factors for Response Spectra and for Spectral Amplification Ratios considering the Simulations

As a begin with, response spectra for selected stations have higher acceleration of motion close to the basin center.(from closest to the basin centre to the farthest in order, 4412, 4787, 4995 4755) even tough average location of epicentre and hypo-centre of the earthquake is closely same for the groups of simulations. The analysis of seismic wave propagation in alluvial basins as we have in this Sulmona case study, it is a very difficult process because various affecting phenomena are took place at different scale such as resonance at whole basin and soil non linear behaviour at the site. However, for the simulations having non-linear soil model has slightly lower acceleration, spectral acceleration and spectral amplification ratio, the main impact of change of these values mainly affected by different moment magnitude of the earthquakes. Although, 3D nonlinear viscoelastic model is considered to implement the hysteric behaviour of alluvial material inside the basin due to dynamic excitations, reduction of shear modulus and the increase of damping in case of high magnitude of earthquakes, there is slight reduction of dynamic response.

8.4 Comparison of Response Spectra and Spectral Amplifications in 1D vs in 3D analyses

As previously mentioned, simulation groups are classified as group 01 stands for $M_w = 6.0$ with linear visco-elastic soil model, group 02 stands for $M_w = 6.5$ with linear visco-elastic soil model, group 03 stands for $M_w = 6.0$ with non-linear visco-elastic soil model, group 04 stands for $M_w = 6.5$ with non-linear visco-elastic soil model. In the response spectra plots for the results obtained from 1d analyses which computed from DEEPSOIL software and from 3d analyses which the ones obtained from

SPEED simulations.

8.4.1 Response Spectra in 1D vs in 3D

1D analyses always provided higher value of response spectrum with respect to 3D ones, because in theoretical assumptions, 1D model is suspected to only vertical plane-wave propagation, however 3D model has the effect of 3D kinematic characterization and wave propagation including the adsorbing boundary conditions which is more reliable. In this case, 1D analyses overestimate the response spectra with respect to 3D cases. (Figures 8.49 to 8.52)

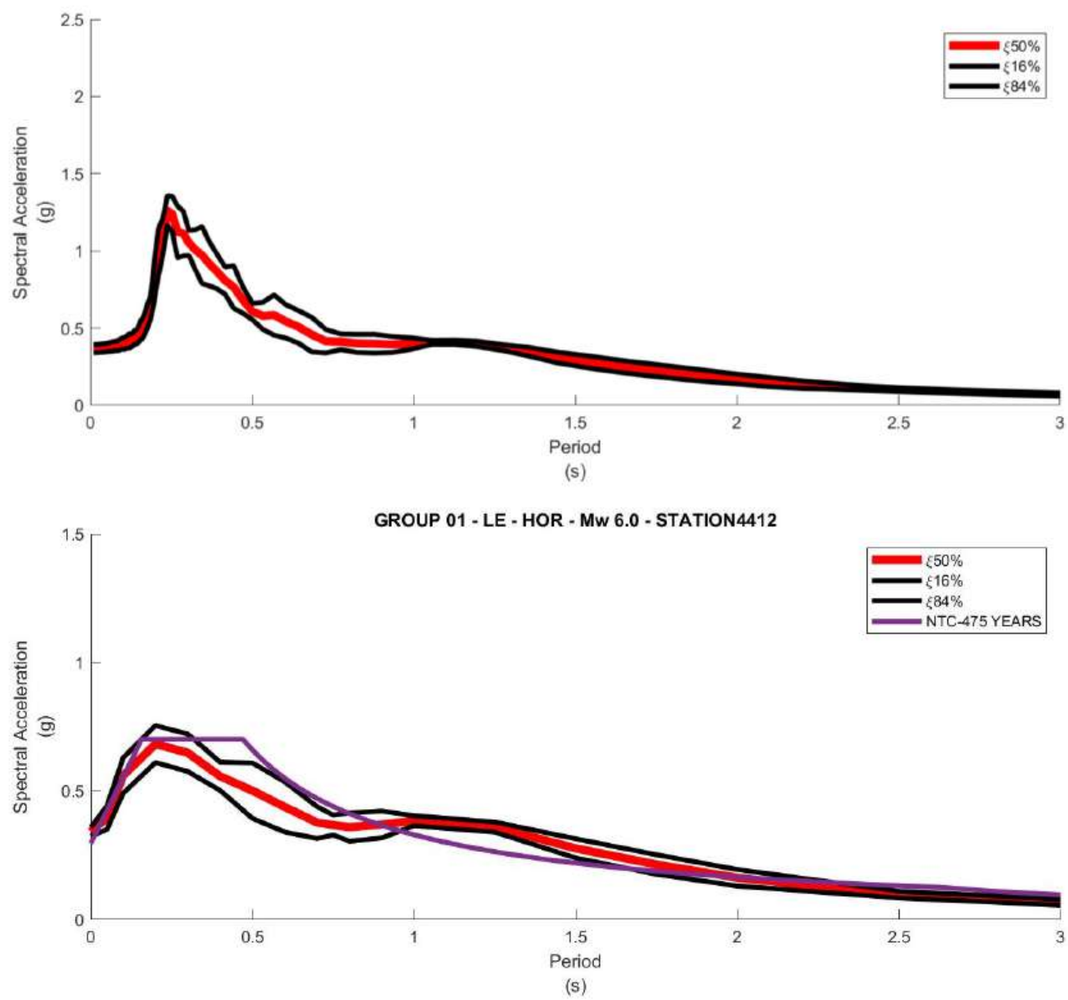

Figure 8.49: Response Spectra evaluation of Station 4412 for Simulation Group 01 with respect to 1D (top) and 3D (below) results. (Geometric mean of horizontal direction

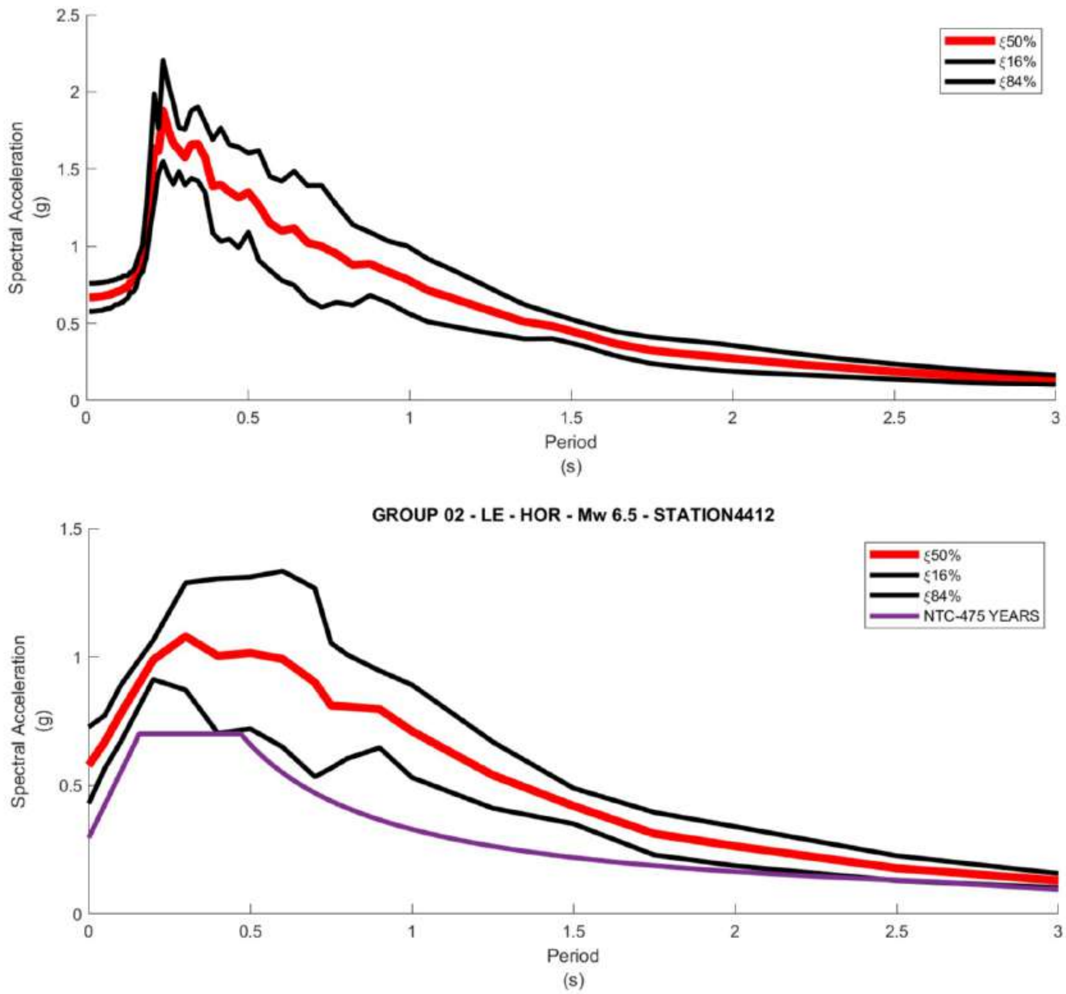

Figure 8.50: Response Spectra evaluation of Station 4412 for Simulation Group 02 with respect to 1D (top) and 3D (below) results. (Geometric mean of horizontal direction

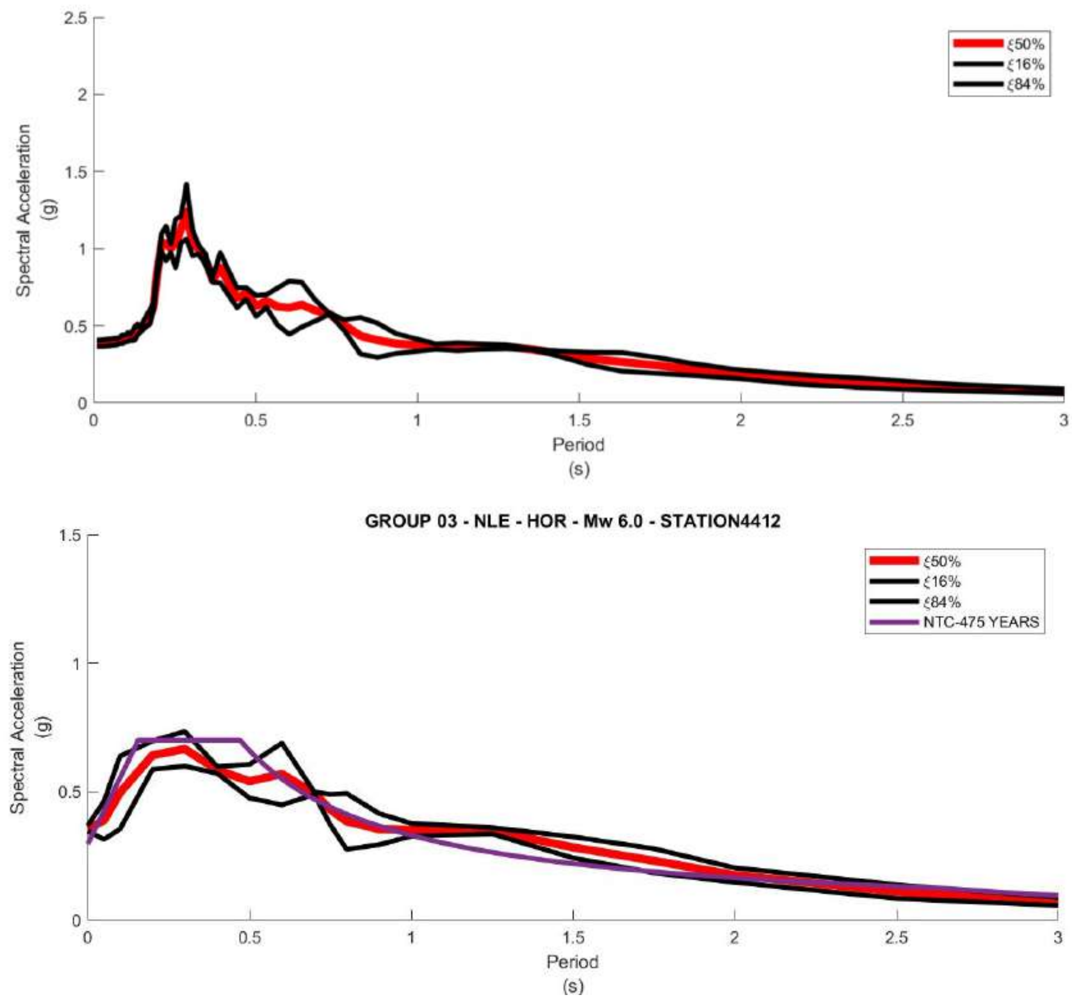

Figure 8.51: Response Spectra evaluation of Station 4412 for Simulation Group 03 with respect to 1D (top) and 3D (below) results. (Geometric mean of horizontal direction

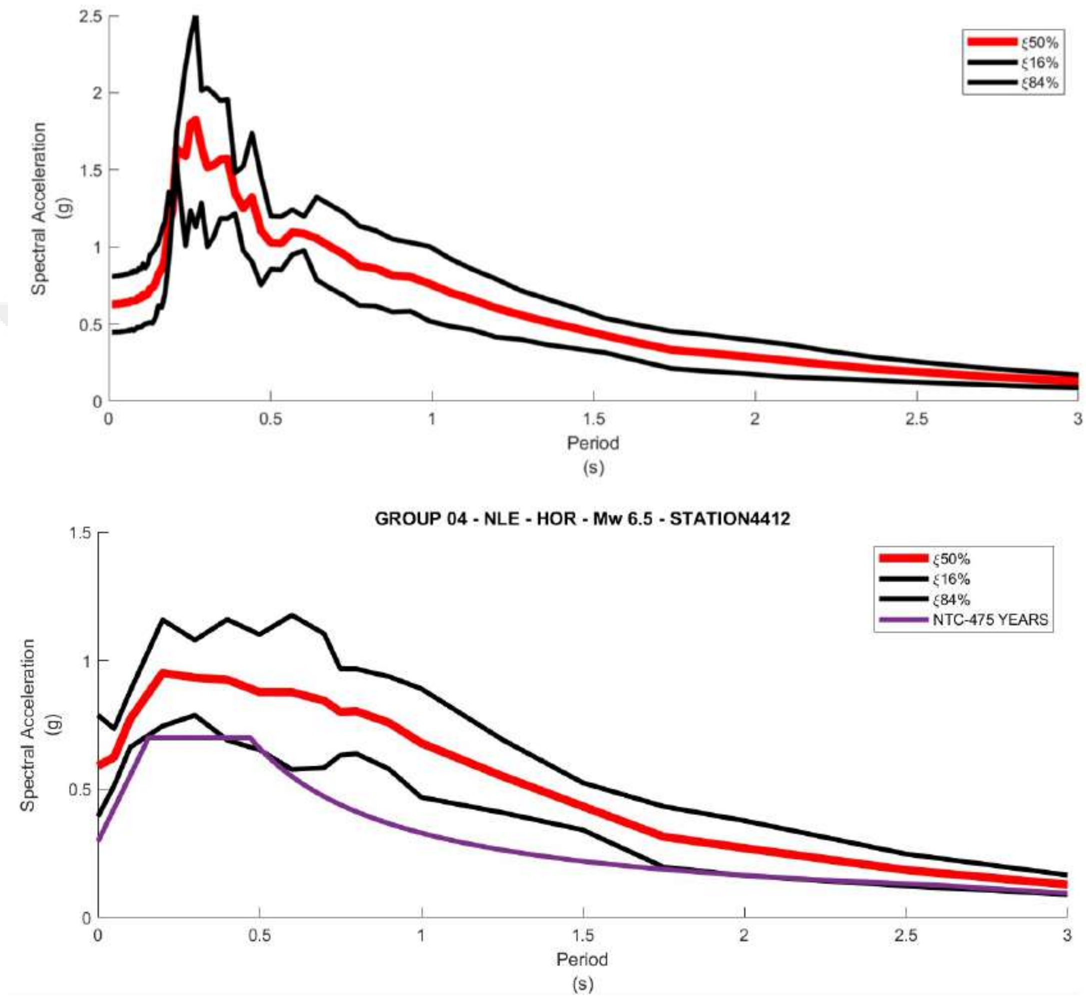

Figure 8.52: Response Spectra evaluation of Station 4412 for Simulation Group 04 with respect to 1D (top) and 3D (below) results. (Geometric mean of horizontal direction

8.4.2 Spectral Amplification Ratio (SAR) in 1D vs 3D

As a beginning, it is worth to indicate that 1D spectral amplification ratios (SAR) are calculated through convolution using 1D transfer functions. Additionally, taking into account vertical plane waves only , obtained SARs underestimate the 3D SARs. On the other hand, 3D numerical simulations include complexity of seismic response, adsorbing boundary conditions and kinematic source model of the fault shows more reliable results. (Figures 8.53 to 8.56). Due to the fact that 3D wave propagation spreads along a much broader frequency range than in 1D, and 3D results provide much higher value of spectral amplification due to underestimate the high-frequency amplitude decay with respect to implemented value of frequency-proportional Q factor(Smerzini et al.2011). Moreover, spectral amplification ratio factors are decreased with strain is depicted in results obtained, and one can say that displacements values maximum in both linear and non-linear cases are controlled by frequencies de-amplified by non-linearity, which results to have lower spectral amplification ratio for $M_w = 6.5$ earthquakes in group 02 and 04 with respect to $M_w = 6.0$ in group 01 and group 3. (Figure 8.53 to 8.56)

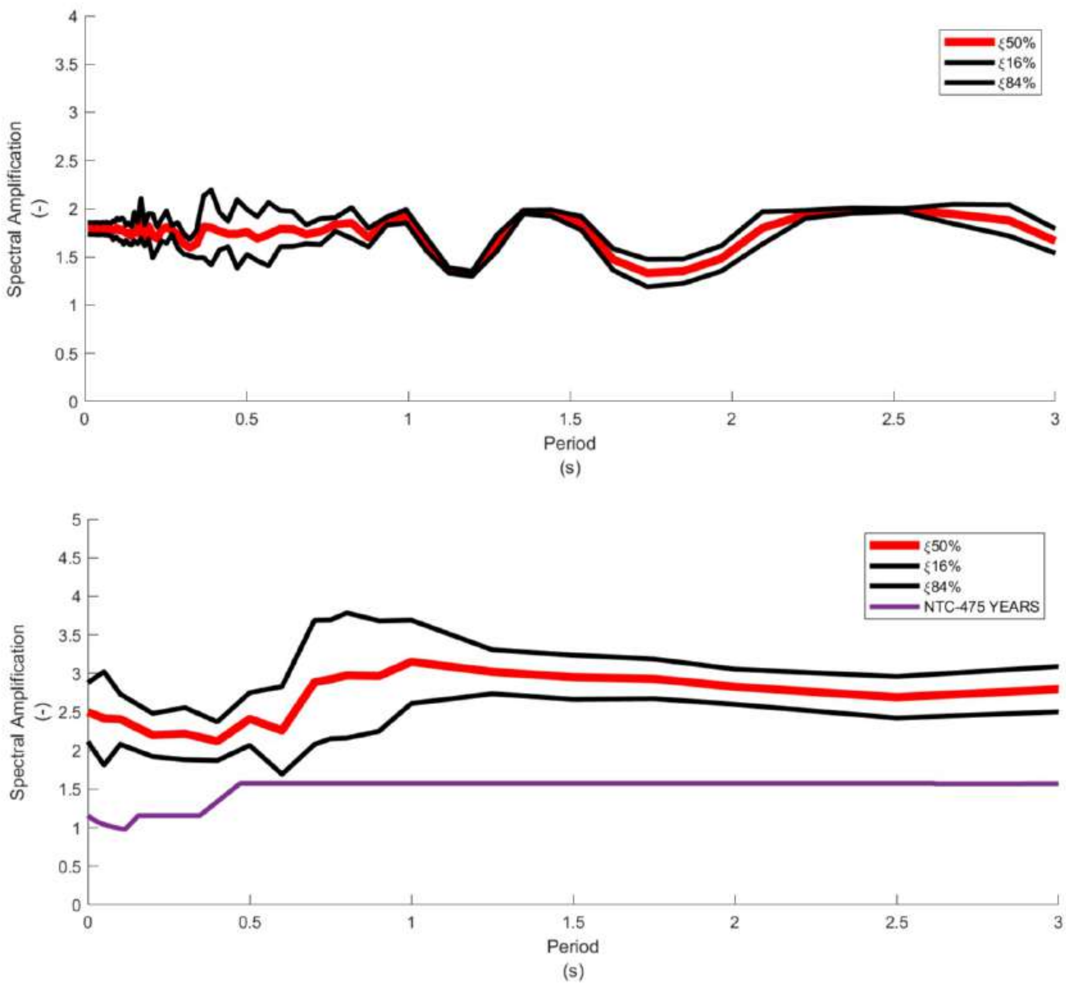

Figure 8.53: Spectral Amplification Ratio (SAR) for Station 4412 by Station 13429 for Group 01 - Magnitude Mw 6.0 - Linear Visco-elastic. Comparison of 1D (above) and 3D (below) results. (Geometric mean of horizontal direction

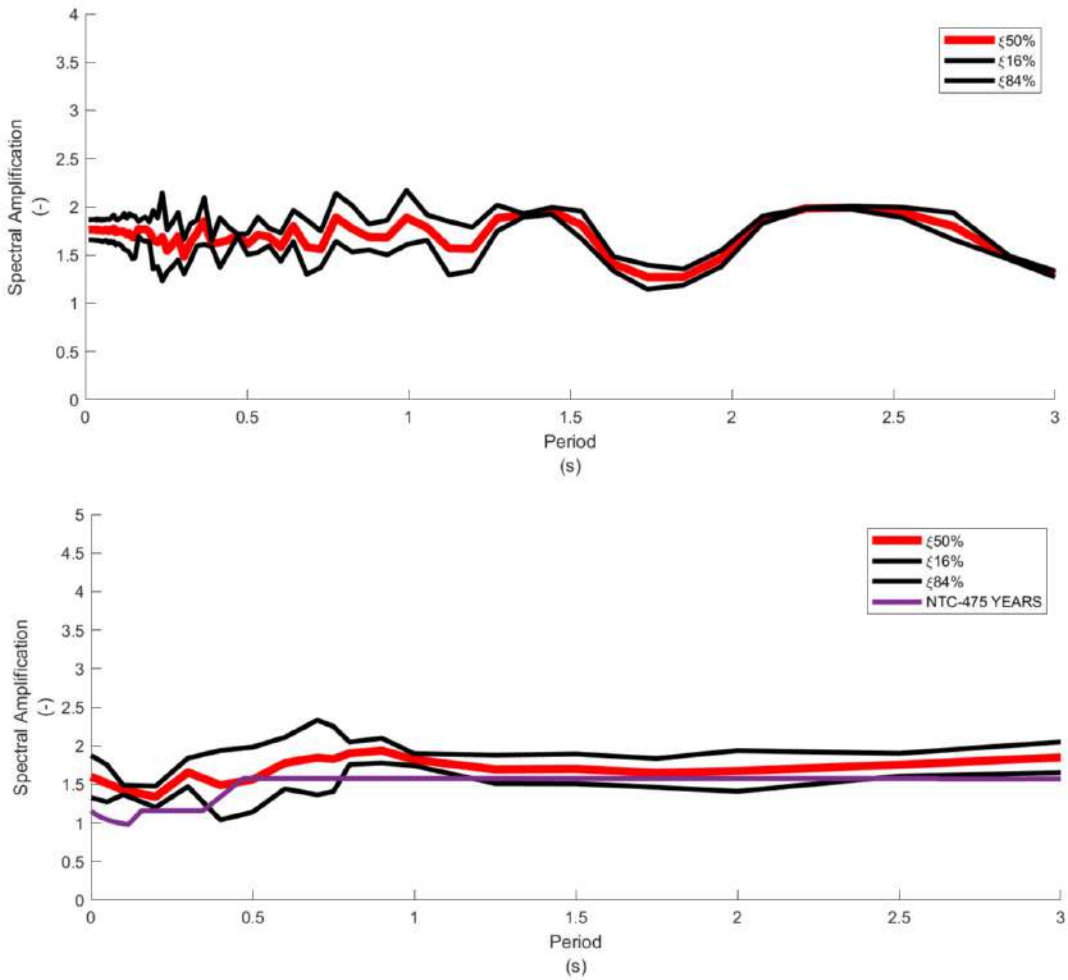

Figure 8.54: Spectral Amplification Ratio (SAR) for Station 4412 by Station 13429 for Group 01 - Magnitude Mw 6.5 - Linear Visco-elastic. Comparison of 1D (above) and 3D (below) results. (Geometric mean of horizontal direction

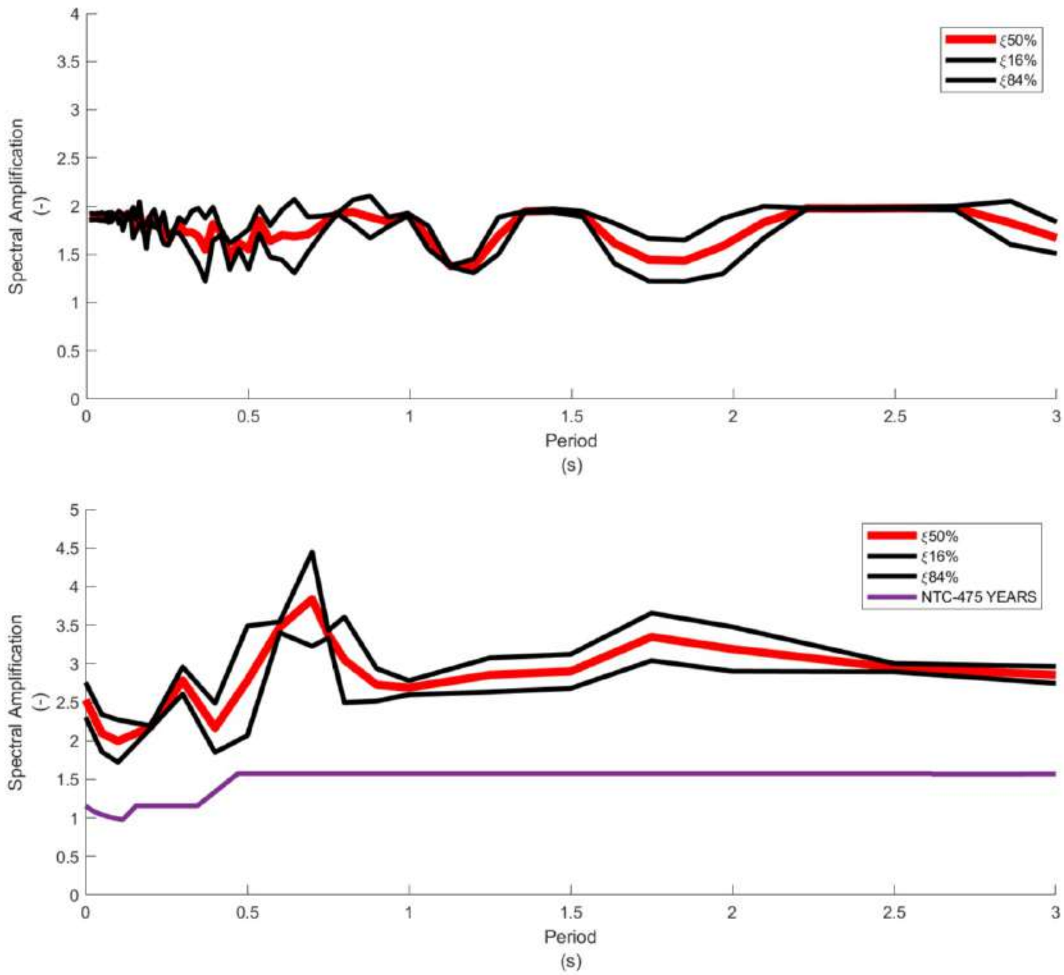

Figure 8.55: Spectral Amplification Ratio (SAR) for Station 4412 by Station 13429 for Group 03 - Magnitude Mw 6.0 - Non-linear Visco-elastic. Comparison of 1D (above) and 3D (below) results. (Geometric mean of horizontal direction

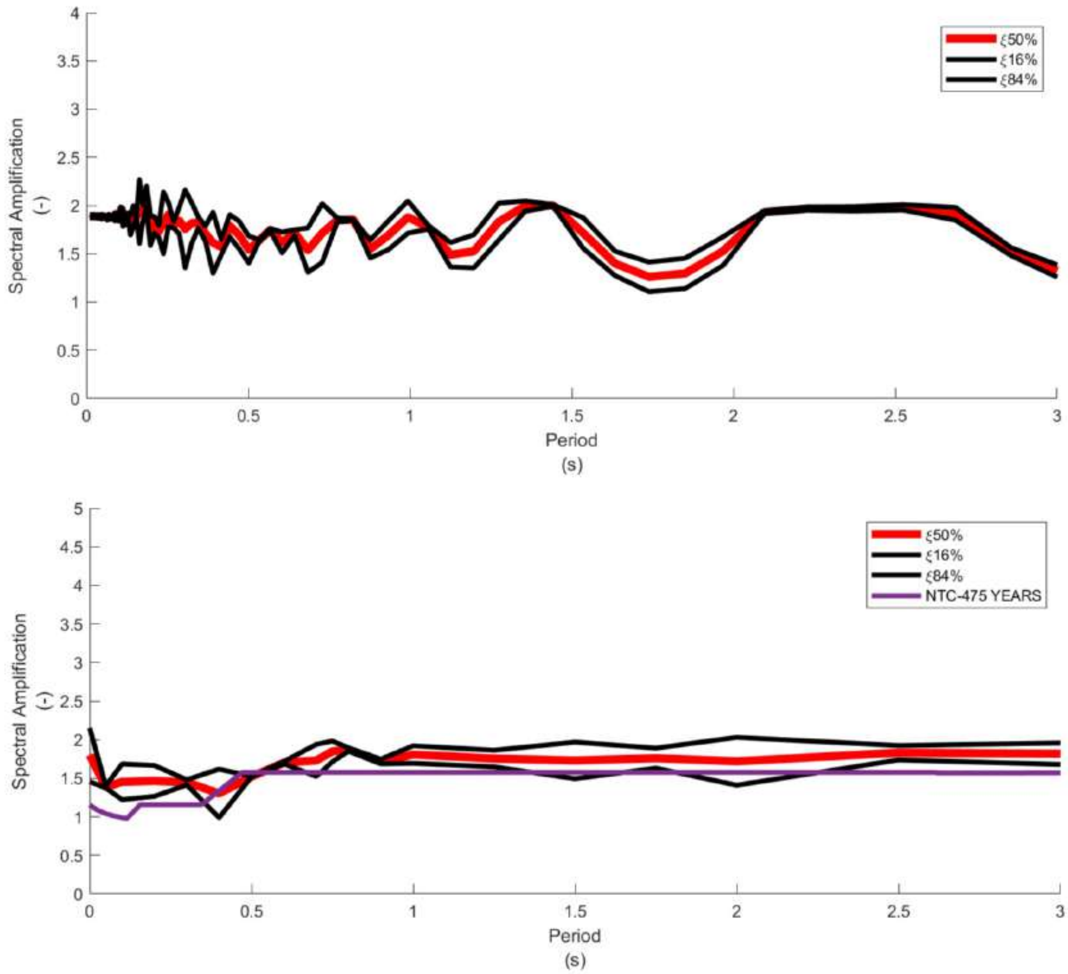

Figure 8.56: Spectral Amplification Ratio (SAR) for Station 4412 by Station 13429 for Group 04 - Magnitude Mw 6.5 - Non-linear Visco-elastic. Comparison of 1D (above) and 3D (below) results. (Geometric mean of horizontal direction

8.4.3 Chapter Summary

Response spectrum for selected stations from closest to the basin center to the farthest in order, 4412, 4787, 4995 4755. For the simulations having non-linear soil model have provided slightly lower acceleration, spectral acceleration and spectral amplification ratio, the main impact of change of these values mainly affected by different moment magnitude of the earthquakes. Taking into account of 3D nonlinear viscoelastic model as is considered to implement the hysteric behaviour of alluvial material inside the basin due to dynamic excitations, reduction of shear modulus and the increase of damping in case of high magnitude of earthquakes, there is slight reduction of dynamic response. Investigated simulation groups are classified as group 01; M_w = 6.0 with linear visco-elastic soil model, group 02 ; M_w = 6.5 with linear visco-elastic soil model, group 03; M_w = 6.0 with non-linear visco-elastic soil model, group 04; M_w = 6.5 with non-linear visco-elastic soil model. Response spectra plots for the results obtained from 1D analyses which computed from DEEPSOIL software and from 3d analyses which the ones obtained from SPEED simulations.From 1D analyses, obtained value of response spectrum with respect to 3D ones, due to the fact that 1D model is suspected to only vertical plane-wave propagation, besides 3D model has the effect of 3D kinematic characterization and wave propagation including the adsorbing boundary conditions. In this case, 1D analyses overestimate the response spectra with respect to 3D cases. Additionally, it is worth to indicate that 1D spectral amplification ratios (SAR) are calculated through convolution using 1D transfer functions. Additionally, taking into account vertical plane waves only obtained SARs underestimate the 3D SARs. On the other hand, 3D numerical simulations include complexity of seismic response, adsorbing boundary conditions and kinematic source model of the fault shows more reliable results. (Figures 8.53 to 8.56). Due to the fact that 3D wave propagation spreads along a much broader frequency range than in 1D, and 3D results provide much higher value of amplification. SAR factors are decreased with strain is depicted in results obtained, and one can say that displacements values maximum in both linear and non-linear cases are controlled by frequencies de-amplified by non-linearity, which results to have lower spectral amplification ratio for M_w = 6.5 earthquakes in group 02 and 04 with respect to M_w = 6.0 in group 01 and group 3.

Chapter 9

Summary and Conclusions

As indicated in the previous chapters, the main aspects of the site effects are reviewed by focusing on how to implement appropriate model for seismic wave propagation within an area with basin effect. The seismic wave amplification initially considered as to be characterized by 1-D modelling of the alluvial basin above the rock layer, then considering non-linear effects are taken into account. However, due to the mentioned basin effect and regarding cause of seismic wave amplifications, edge effects, basin-transduces surface waves and focusing effects, the main decision for the model is based on physics-based numerical simulations to have a precise results. Considering numerous site effects may cause to increase of possible damage concentration, combination of two methods to take advantage of their peculiarities are presented which named as Spectral Elements in Elasto-dynamics with Discontinuous Galerkin (SPEED Code). SPEED is developed by the Laboratory for Modelling and Scientific Computing (MOX) of the Department of Mathematics and by the Department of Civil and Environmental Engineering (DICA) of Politecnico di Milano. Additionally, non-conforming approaches is very useful and applicable in engineering purposes in case of evaluating seismic wave propagation more precisely, when complex geometries with different mechanical properties of the medium is present. Due to the high earthquake re-occurrence risk within the Sulmona Basin (Abruzzo,Italy), 3D physics-based numerical simulation methods are carried out for the Sulmona Basin (Abruzzo, Italy). Then, ANN2BB training is carried out to predict strong ground motion record on virtual stations to correlate short-period spectral ordinates based on long-period ones through Artificial Neural Networks. This process lead to have full spatial correlation of ground motion in the whole frequency range of interest for engineering applications. Effect of earthquake magnitude and soil model for simulations regarding the analyses of 4 different scenarios are computed anc correlated within time series of ground motion and their peak ground acceleration (PGA), peak ground velocity (PGV) and peak ground displacement (PGD) maps scheme. ANN2BB training is carried out for the SPEED computations for PGA calculations. Selected scenarios are (and also for the groups with different slip distribution), in order, M_w = 6.0 with Linear Visco-elastic (LVE) model, M_w = 6.5 with Linear Visco-elastic (LVE) model, M_w = 6.0 with Non-linear Visco-elastic (NLVE) model and M_w = 6.5 with Non-linear Visco-elastic (NLVE) model - slip distribution no as S003. In case of strong ground motion i.e. $M_w \geq 6.0$ in present simulation results, non-linearity of soil model show very less reduction of value within the records also for the peak ground motion values as observed with respect to linear-elastic cases. Seismic moment magnitude relations can be considered as accounted for the energy release concept. Thereby, Earthquake magnitude and seismic moment are positively related to the amplitude of the ground displacement. Results are appropriate to make seismic hazard analysis including ground motion prediction equations. Comments indicated that non-linear visco-elastic model is considered to be more accurate than the linear visco-elastic model because loss of energy during earthquake induced loading force not much significant but theoretically more correct implementation with respect to linear-visco-elastic model of nature. Four different groups of simulations, each simulation's response spectra for the each groups are statistically calculated for each virtual station that two of them are on the cross section AA' and the rest of two are on the cross section BB'. Acceleration response spectra obtained through SPEED simulations and ANN2BB training. response spectra for selected stations have higher acceleration of motion close to the basin center.(from closest to the basin centre to the farthest in order, 4412, 4787, 4995 4755) even tough average location of epicentre and hypocentre of the earthquake is closely same for the groups of simulations. The analysis of seismic wave propagation in alluvial basins as we have in this Sulmona case study, it is a very difficult process because various affecting phenomena are took place at different scale such as resonance at whole basin and soil non linear behaviour at the site. However, for the simulations having non-linear soil model has slightly lower acceleration, spectral acceleration and spectral amplification ratio, the main impact of change of these values mainly affected by different moment magnitude of the earthquakes. 3D non-linear visco-elastic model is considered to implement the hysteric behavior of alluvial material inside the basin due to dynamic excitations, reduction of shear modulus and the increase of damping in case of high magnitude of earthquakes, there is slight reduction of dynamic response. While comparison of 1D vs 3D site amplification ratios, the reduction of shear modulus is controlled by a hyperbolic law with only one parameter estimated from the experimental knowledge of the shear modulus decay curve for 1D analysis that leads to have dissipation properties are directly derived from the hyperbolic law and from two other characteristic parameters responsible for the minimum and maximum loss of energy at lower and larger strain values as ϵ_0 and ϵ_{max}. Although its sufficient to give an overall description of the unloading and reloading phases during the seismic sequence. Yet site amplification is found to be much larger than predicted through 1D analyses. Response spectrum for selected stations from closest to the basin center to the farthest in order, 4412, 4787, 4995 4755 were indicated before, then for the simulations having non-linear soil model have provided slightly lower acceleration, spectral acceleration and spectral amplification ratio, the main impact of change of these values mainly affected by different moment magnitude of the earthquakes. Taking into account of 3D nonlinear viscoelastic model as is considered to implement the hysteric behavior of alluvial material inside the basin due to dynamic excitations, reduction of shear modulus and the increase of damping in case of high magnitude of earthquakes, there is slight reduction of dynamic response. Investigated simulation groups are classified as group 01 stands for M_w = 6.0 with linear visco-elastic soil model, group 02 stands for M_w = 6.5 with linear visco-elastic soil model, group 03 stands for M_w = 6.0 with non-linear visco-elastic soil model, group 04 stands for M_w = 6.5 with non-linear visco-elastic soil model. Response spectra plots for the results obtained from 1D analyses which computed from DEEPSOIL software and from 3d analyses which the ones obtained from SPEED simulations.From 1D analyses, obtained value of response spectrum with respect to 3D ones, due to the fact that 1D model is suspected to only vertical plane-wave propagation, besides 3D model has the effect of 3D kinematic characterization and wave propagation including the adsorbing boundary conditions. In this case, 1D analyses overestimate the response spectra with respect to 3D cases. Additionally, it is worth to indicate that 1D spectral amplification ratios (SAR) are calculated through convolution using 1D transfer functions. Additionally, taking into account vertical plane waves only obtained SARs underestimate the 3D SARs. On the other hand, 3D numerical simulations include complexity of seismic response, adsorbing boundary conditions and kinematic source model of the fault shows more reliable results. (Figures 8.53 to 8.56). Due to the fact that 3D wave propagation spreads along a much broader frequency range than in 1D, and 3D results provide much higher value of spectral amplification. Spectral amplification ratio factors are decreased with strain is depicted in results obtained, and one can say that displacements values maximum in both linear and nonlinear cases are controlled by frequencies de-amplified by nonlinearity, which results to have lower spectral amplification ratio for M_w = 6.5 earthquakes in group 02 and 04 with respect to M_w = 6.0 in group 01 and group 3. These analyses are completed and illustrated properly to used in case of occurrence of large magnitude of earthquake within Sulmona Basin and regarding engineering design may consider the seismological values and parameters to be used.

Appendices

Appendix A

Appendix A - SPEED Scenario ID Cards

A.1 VISCOELASTIC SOIL MODEL WITH Mw 6.0

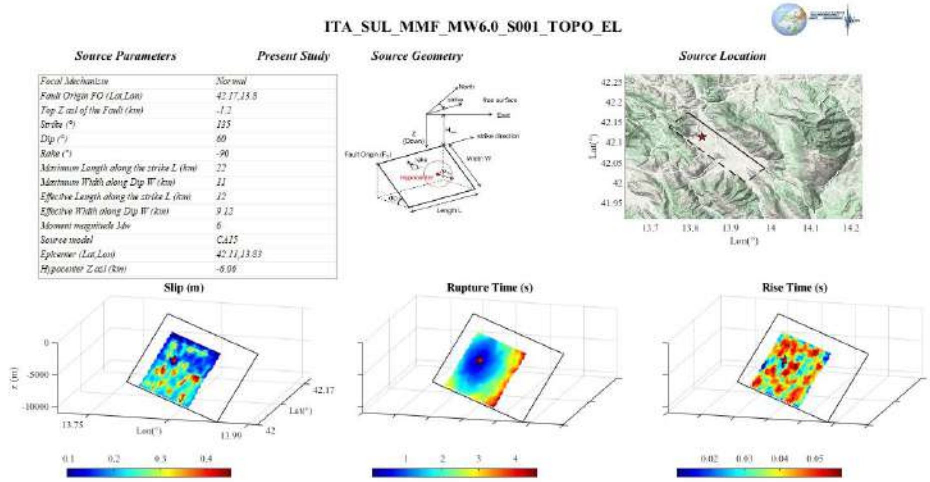

Figure A.1: ITA SUL MMF MW60 S001 TOPO EL Page 1 of 2

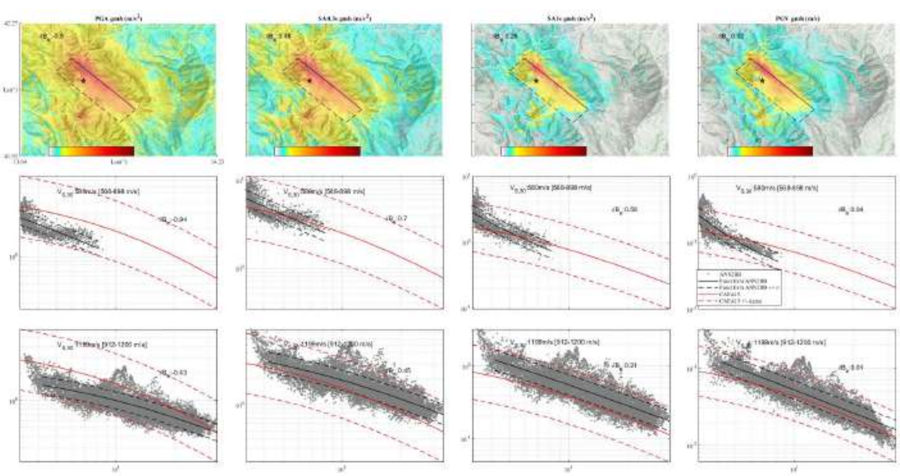

Figure A.2: ITA SUL MMF MW60 S001 TOPO EL Page 2 of 2

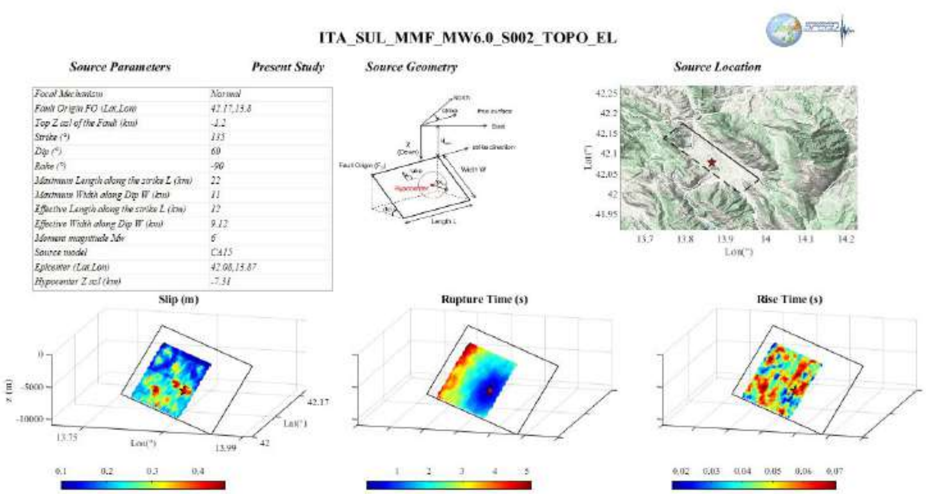

Figure A.3: ITA SUL MMF MW60 S002 TOPO EL Page 1 of 2

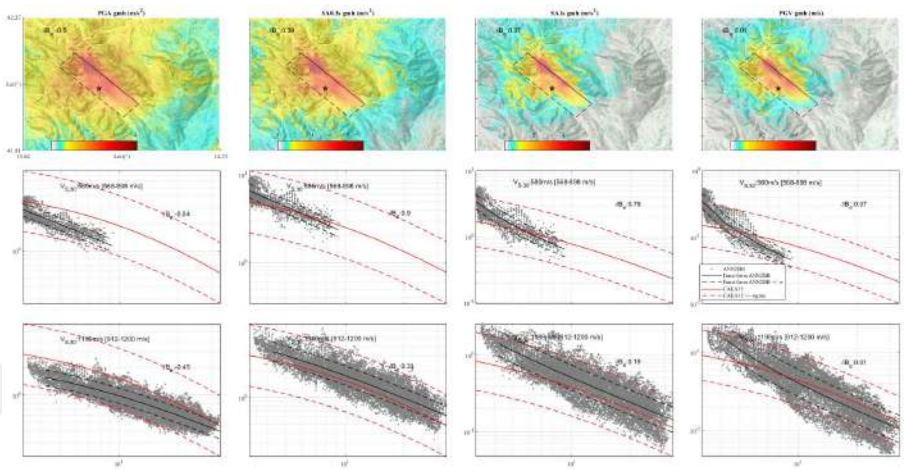

Figure A.4: ITA SUL MMF MW60 S002 TOPO EL Page 2 of 2

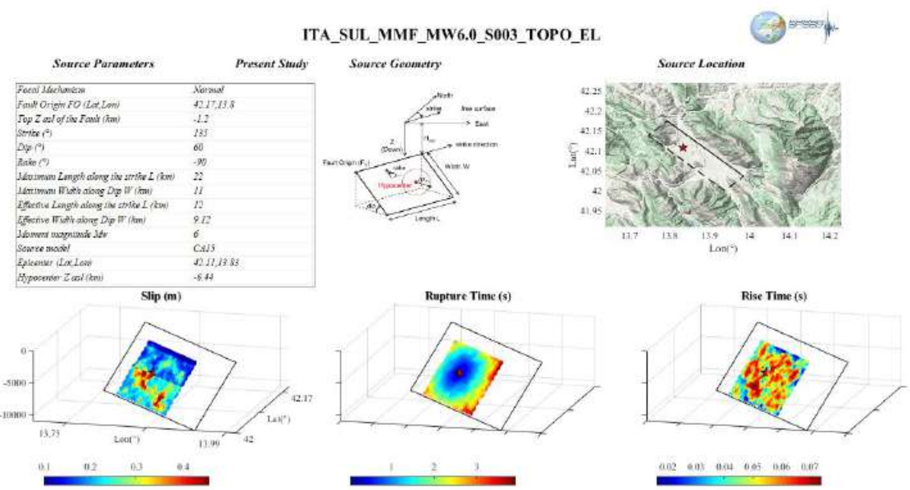

Figure A.5: ITA SUL MMF MW60 S003 TOPO EL Page 1 of 2

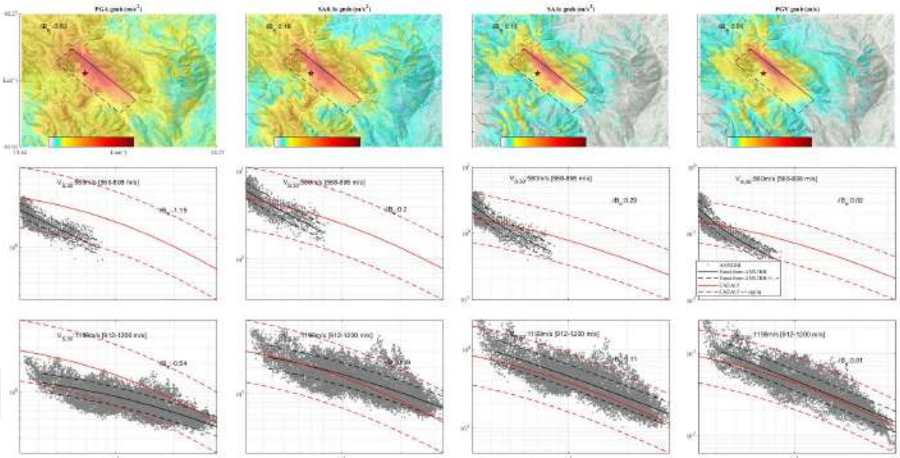

Figure A.6: ITA SUL MMF MW60 S003 TOPO EL Page 2 of 2

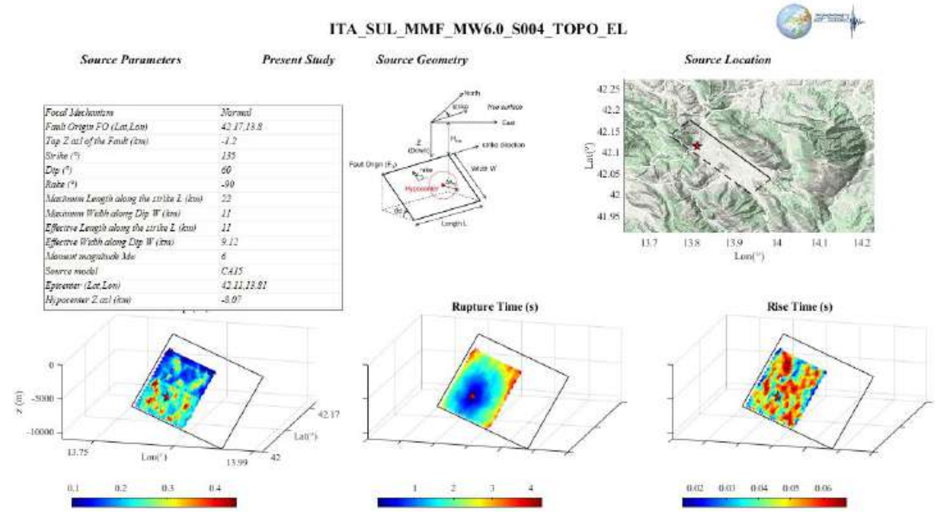

Figure A.7: ITA SUL MMF MW60 S004 TOPO EL Page 1 of 2

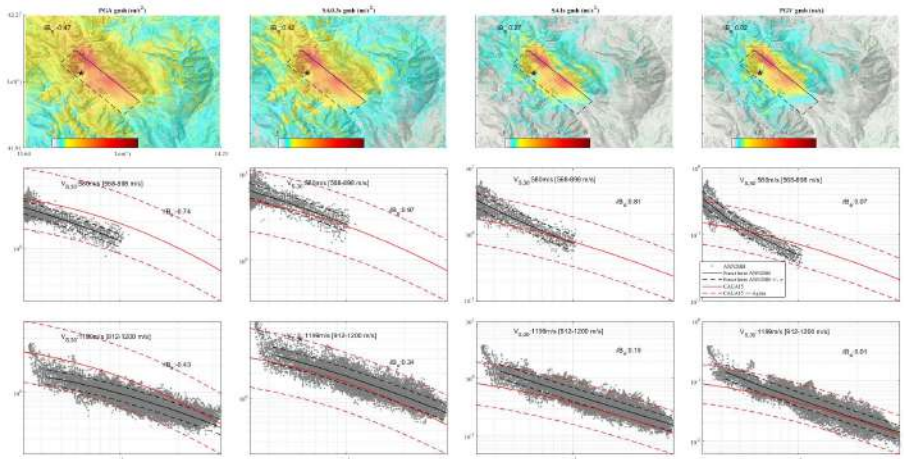

Figure A.8: ITA SUL MMF MW60 S004 TOPO EL Page 2 of 2

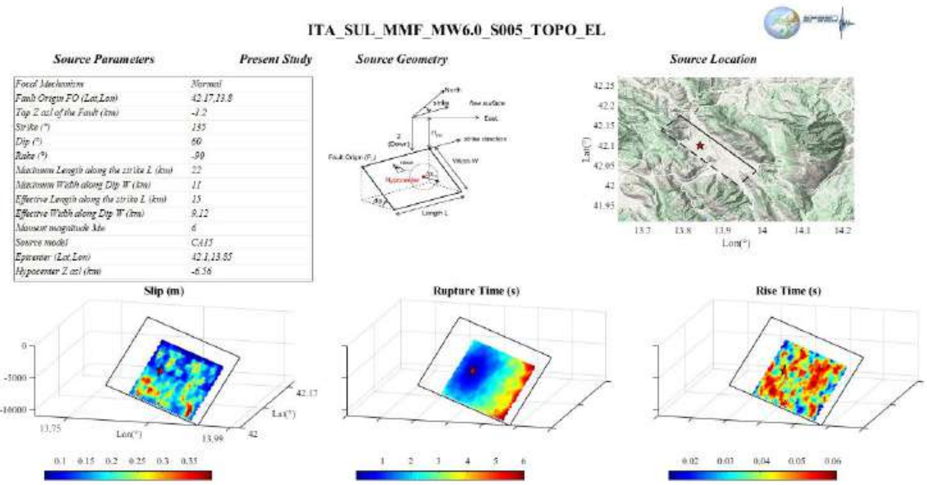

Figure A.9: ITA SUL MMF MW60 S005 TOPO EL Page 1 of 2

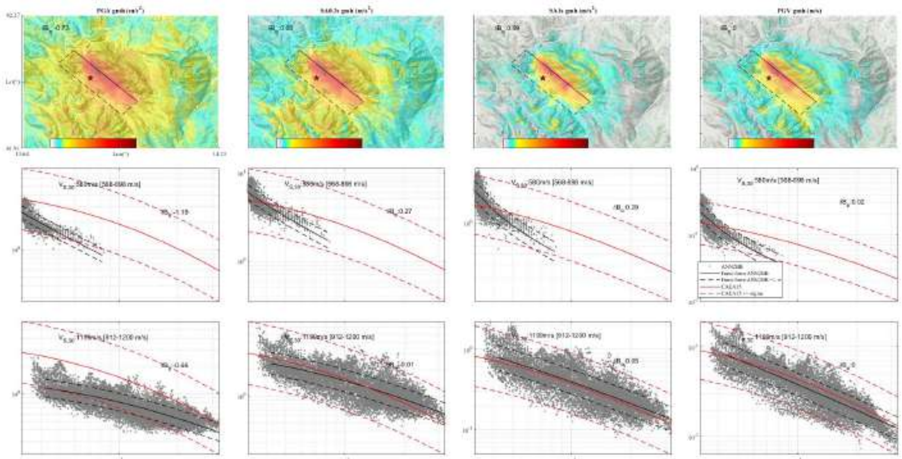

Figure A.10: ITA SUL MMF MW60 S005 TOPO EL Page 2 of 2

A.2 VISCOELASTIC SOIL MODEL WITH Mw 6.5

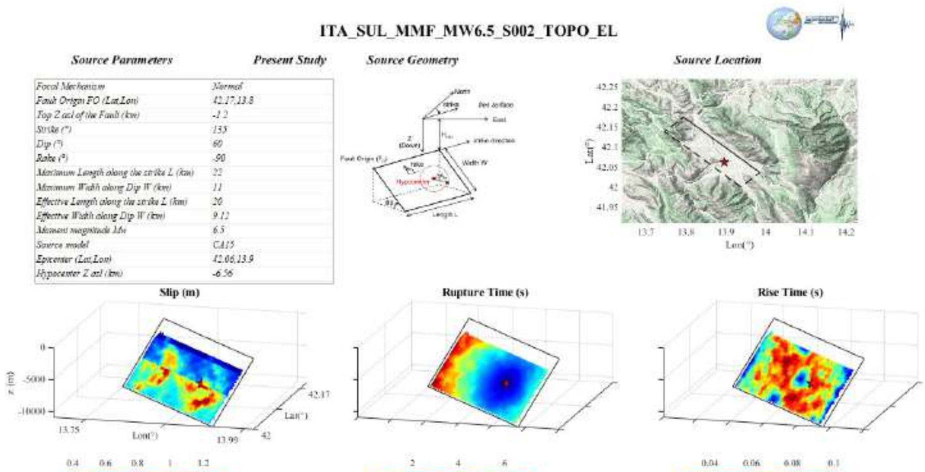

Figure A.11: ITA SUL MMF MW65 S002 TOPO EL Page 1 of 2

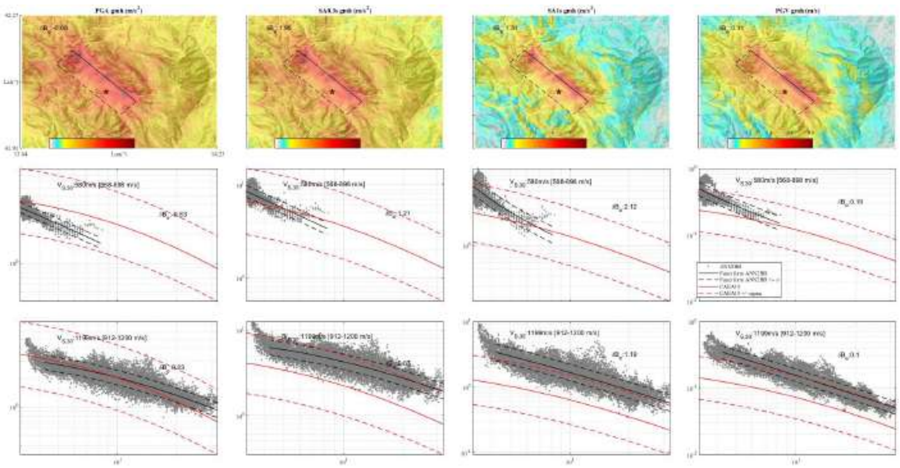

Figure A.12: ITA SUL MMF MW65 S002 TOPO EL Page 2 of 2

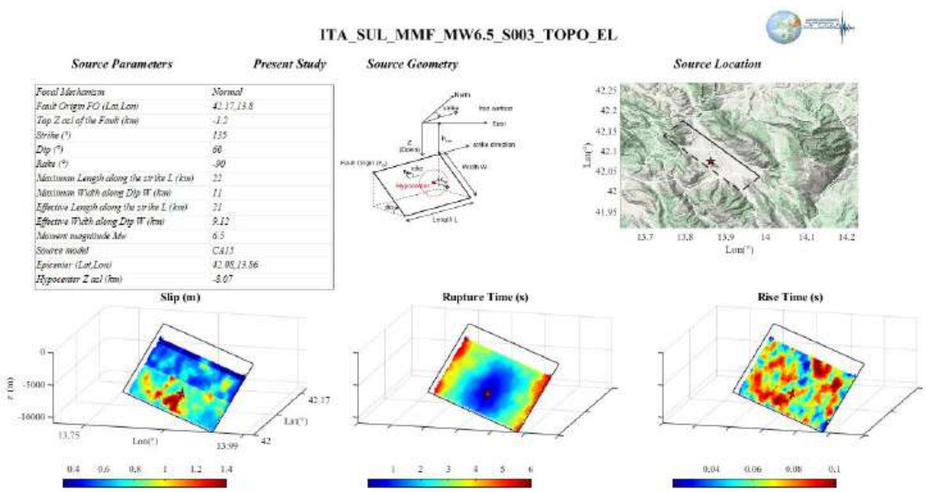

Figure A.13: ITA SUL MMF MW65 S003 TOPO EL Page 1 of 2

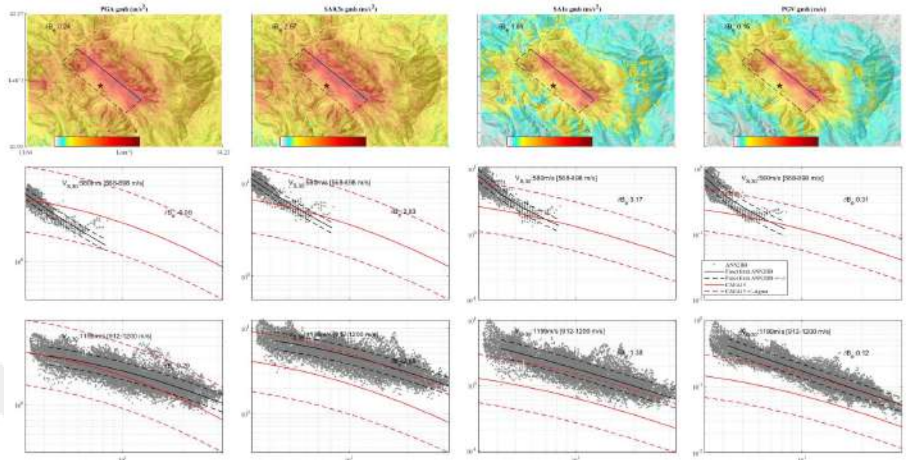

Figure A.14: ITA SUL MMF MW65 S003 TOPO EL Page 2 of 2

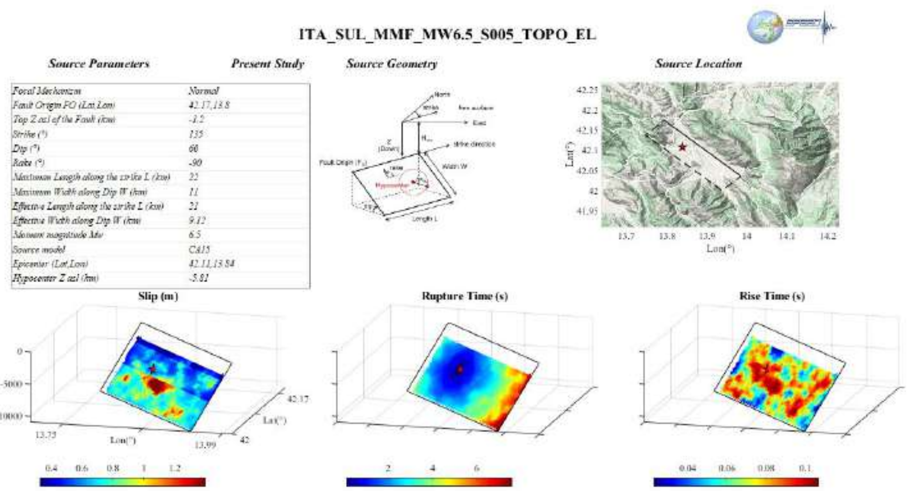

Figure A.15: ITA SUL MMF MW65 S005 TOPO EL Page 1 of 2

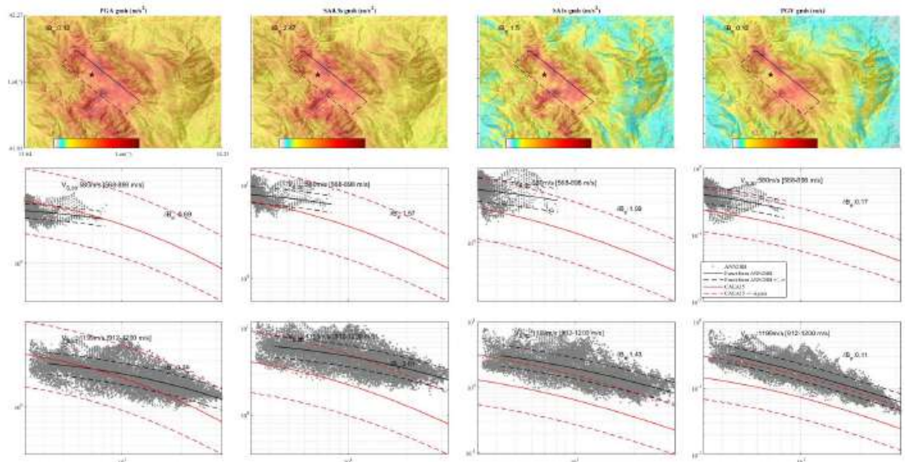

Figure A.16: ITA SUL MMF MW65 S005 TOPO EL Page 2 of 2

A.3 NON-LINEAR VISCOELASTIC SOIL MODEL WITH Mw 6.0

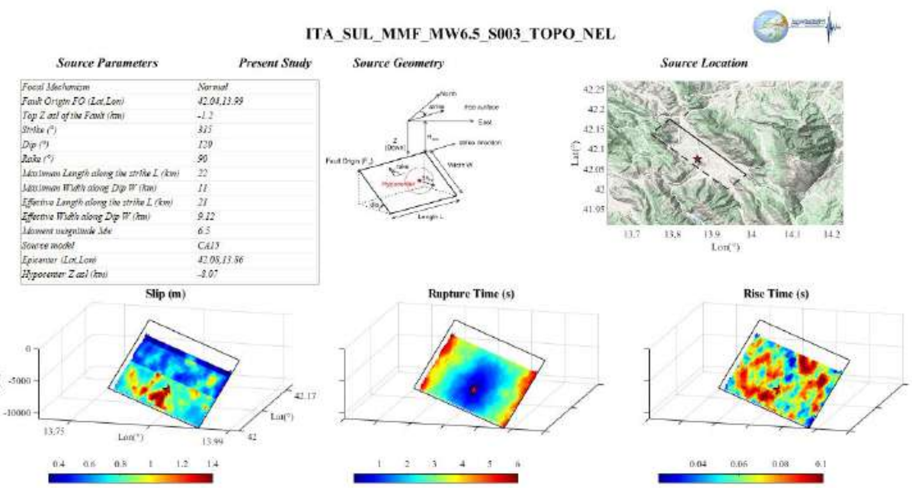

Figure A.17: ITA SUL MMF MW65 S003 TOPO NEL Page 1 of 2

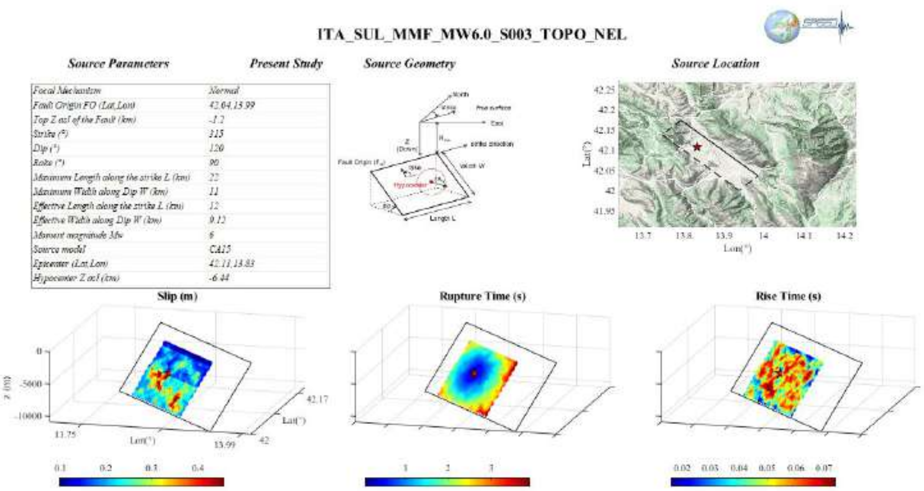

Figure A.18: ITA SUL MMF MW60 S003 TOPO NEL Page 1 of 2

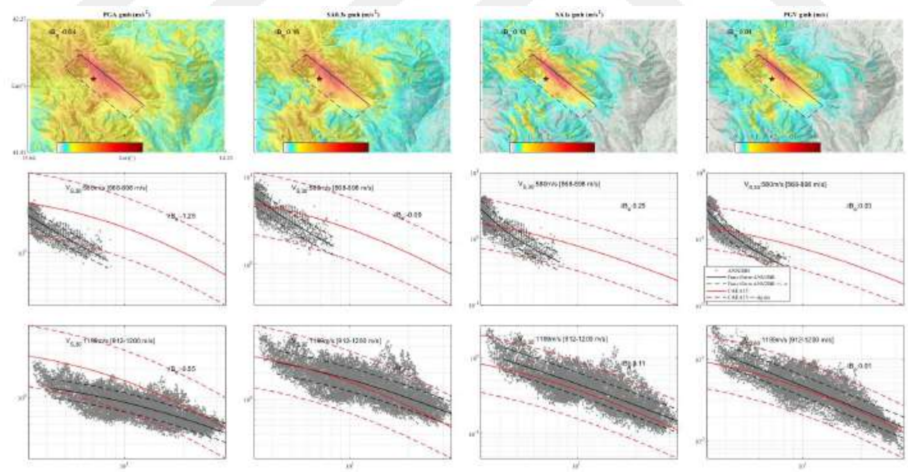

Figure A.19: ITA SUL MMF MW60 S003 TOPO NEL Page 2 of 2

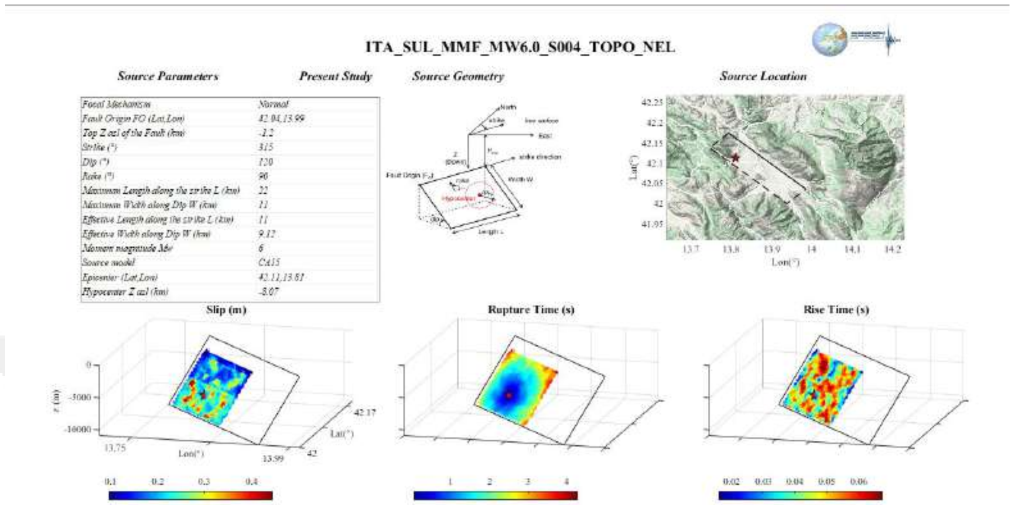

Figure A.20: ITA SUL MMF MW60 S004 TOPO NEL Page 1 of 2

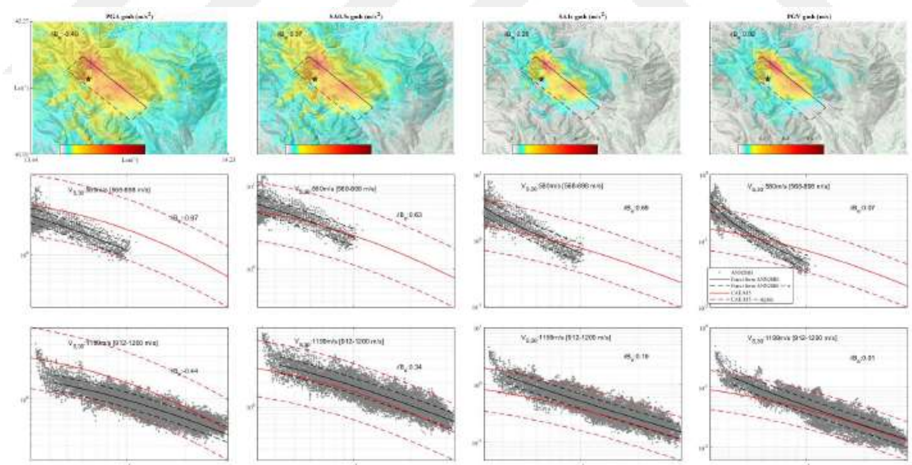

Figure A.21: ITA SUL MMF MW60 S004 TOPO NEL Page 2 of 2

A.4 NON-LINEAR VISCOELASTIC SOIL MODEL WITH Mw 6.5

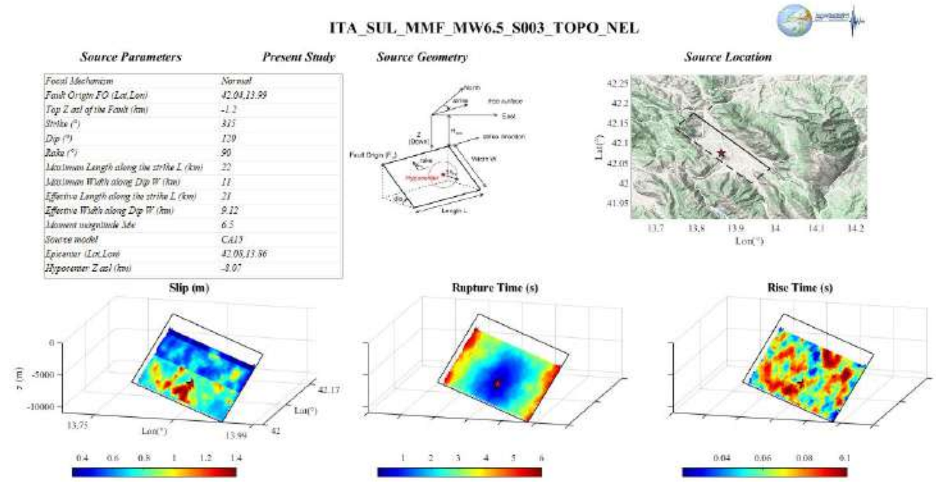

Figure A.22: ITA SUL MMF MW65 S003 TOPO NEL Page 1 of 2

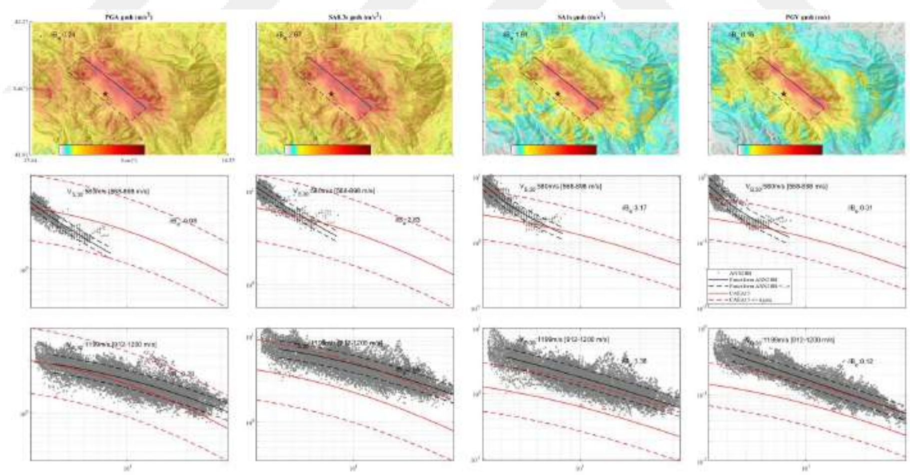

Figure A.23: ITA SUL MMF MW65 S003 TOPO NEL Page 2 of 2

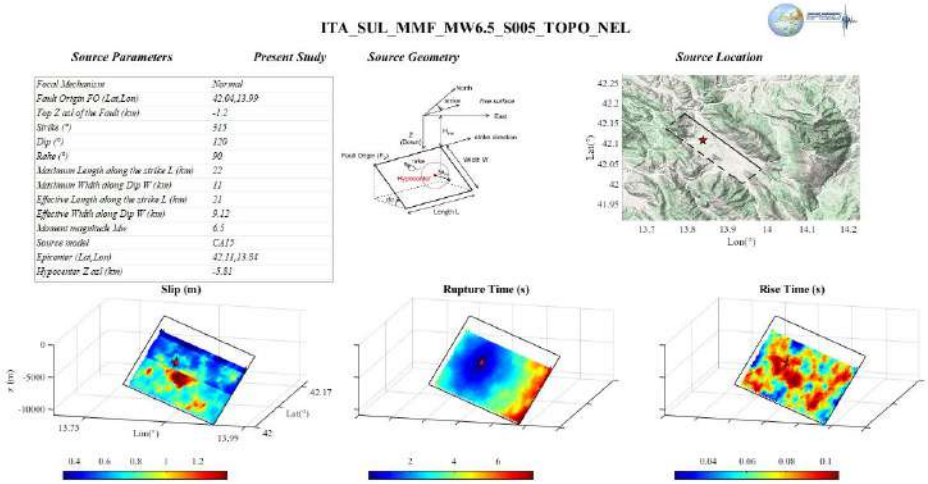

Figure A.24: ITA SUL MMF MW65 S005 TOPO NEL Page 1 of 2

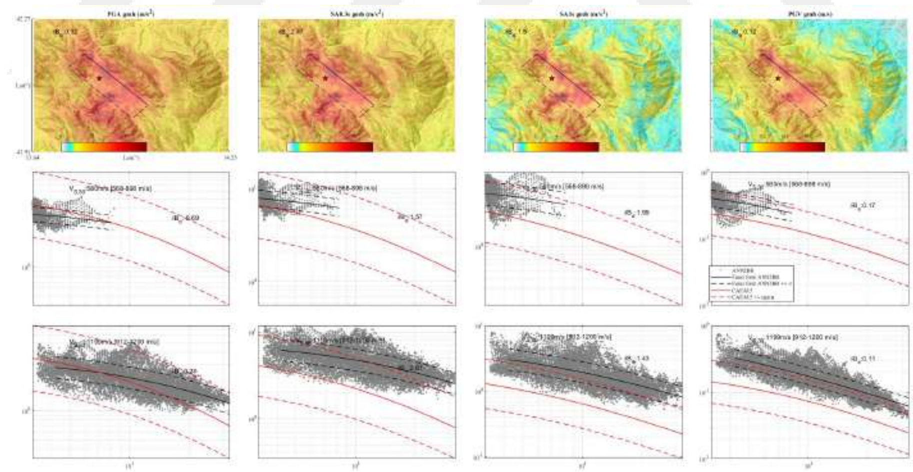

Figure A.25: ITA SUL MMF MW65 S005 TOPO NEL Page 2 of 2

Appendix B

Appendix B - Time Histories, Fourier Amplitude Spectra and Response Spectra for selected scenarios and 1NN2BB traning results

B.1 ITA SUL MMF MW6.0 S003 TOPO EL

B.1.1 Selected Stations on Soil

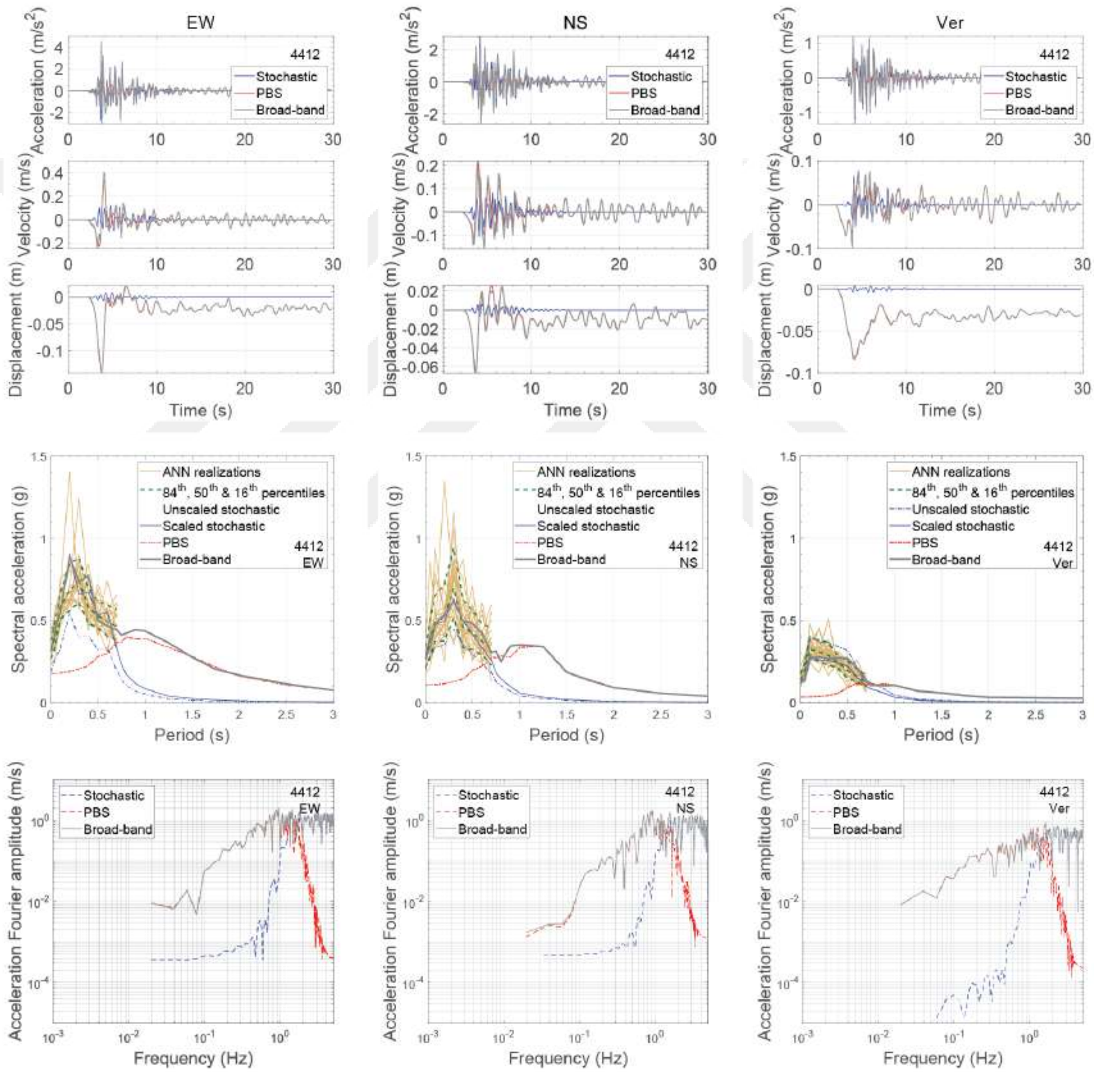

Figure B.1: STATION 4412 : ITA SUL MMF MW6.0 S003 TOPO EL

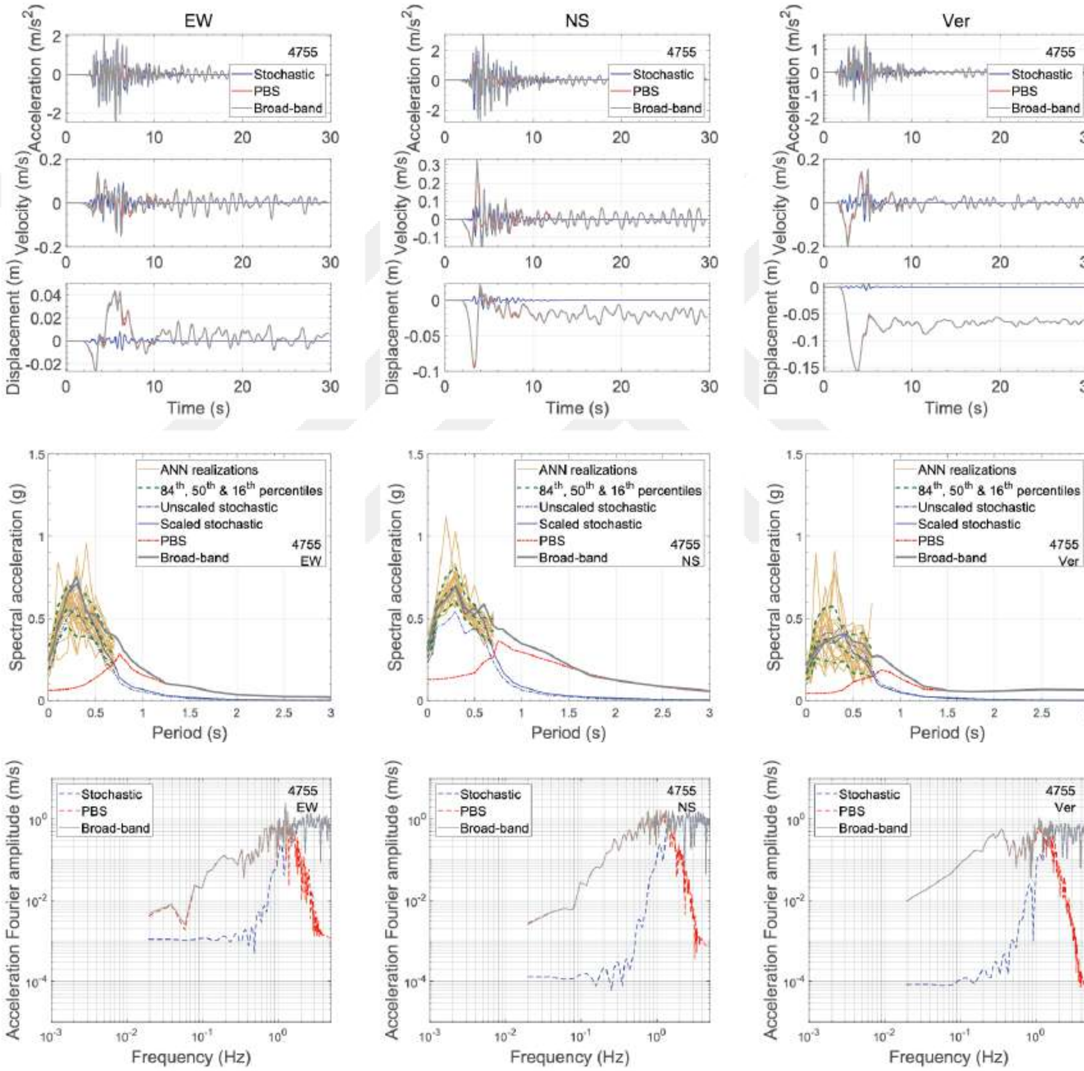

Figure B.2: STATION 4755 : ITA SUL MMF MW6.0 S003 TOPO EL

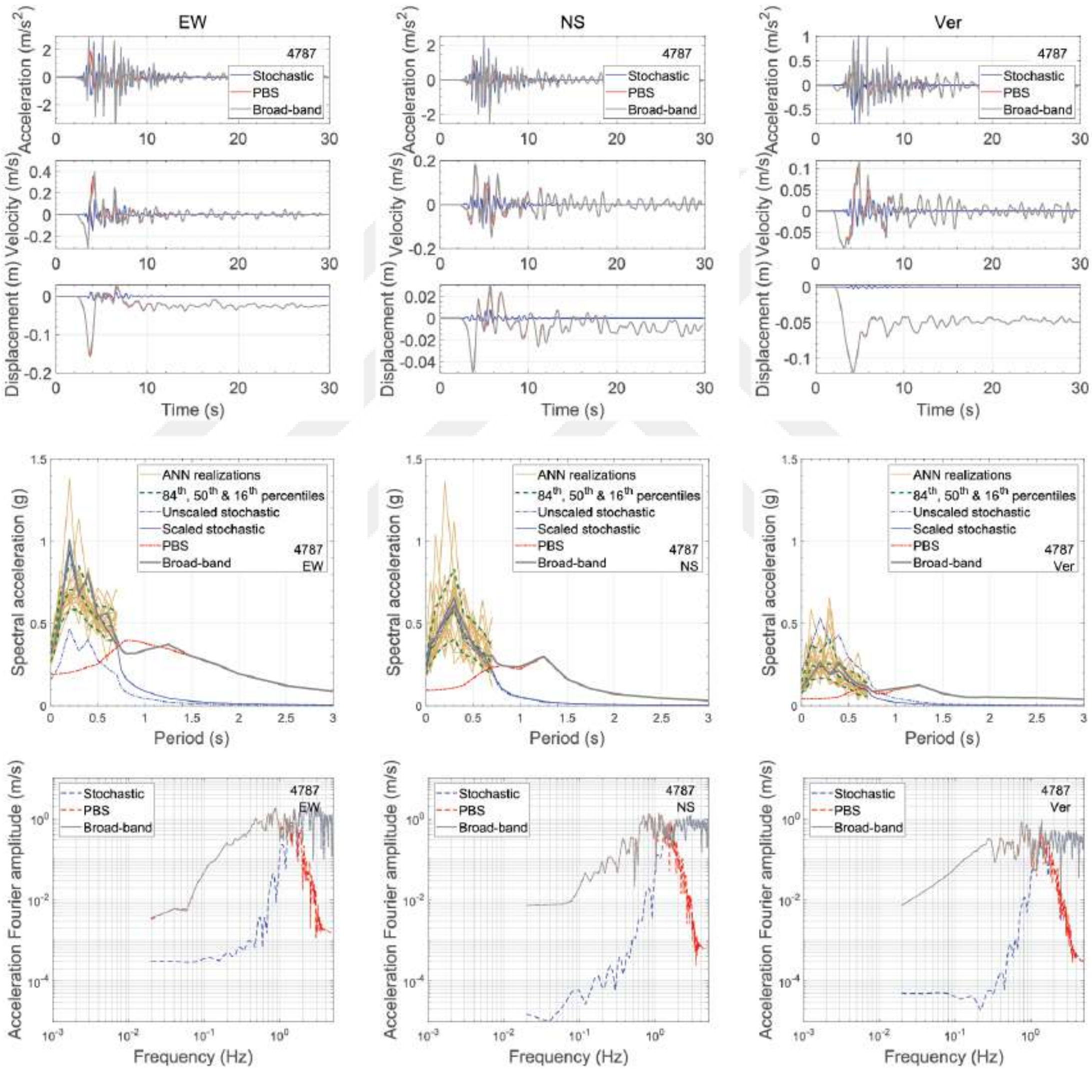

Figure B.3: STATION 4787 : ITA SUL MMF MW6.0 S003 TOPO EL

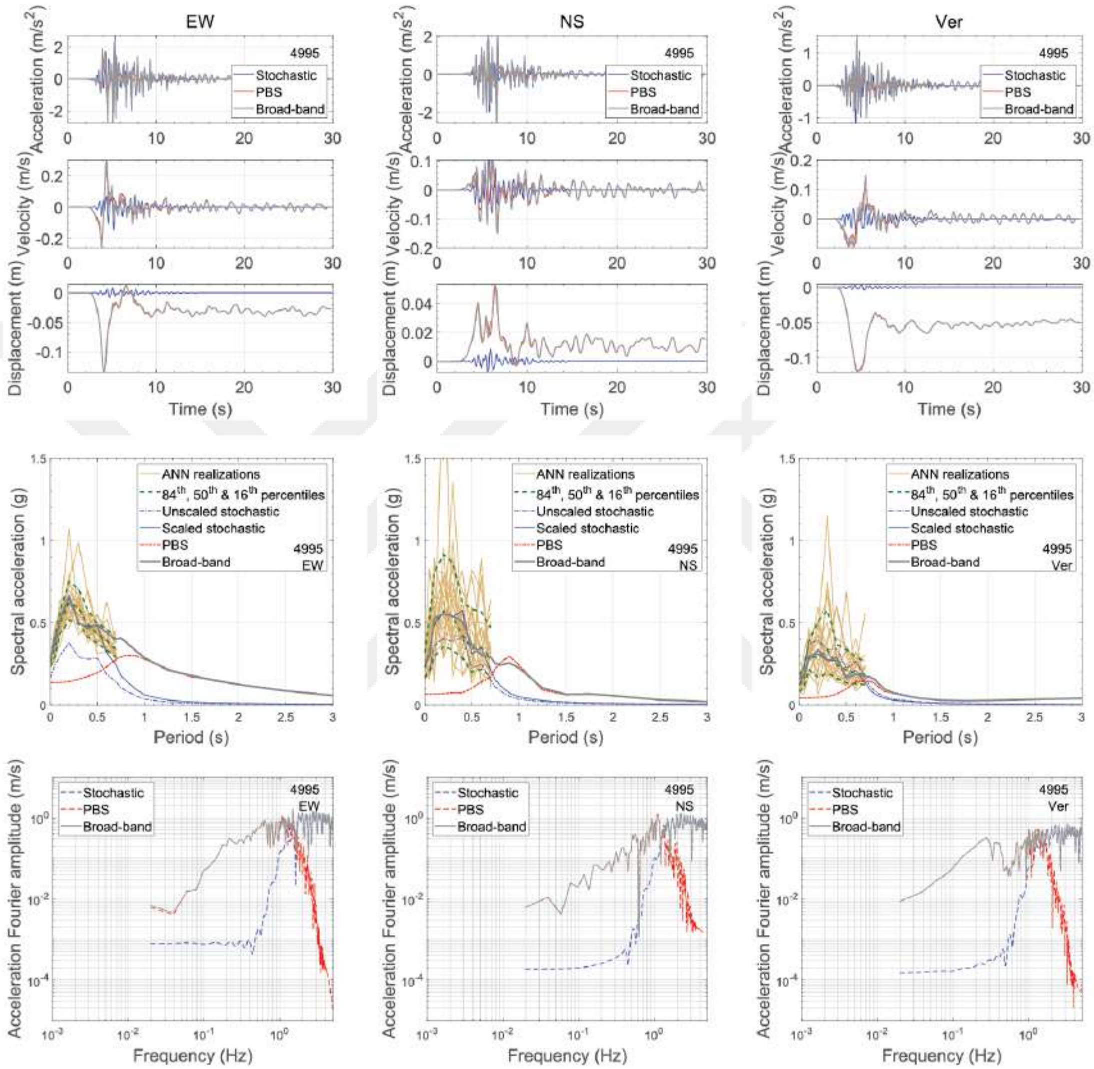

Figure B.4: STATION 4995 : ITA SUL MMF MW6.0 S003 TOPO EL

B.1.2 Selected Stations on Rock

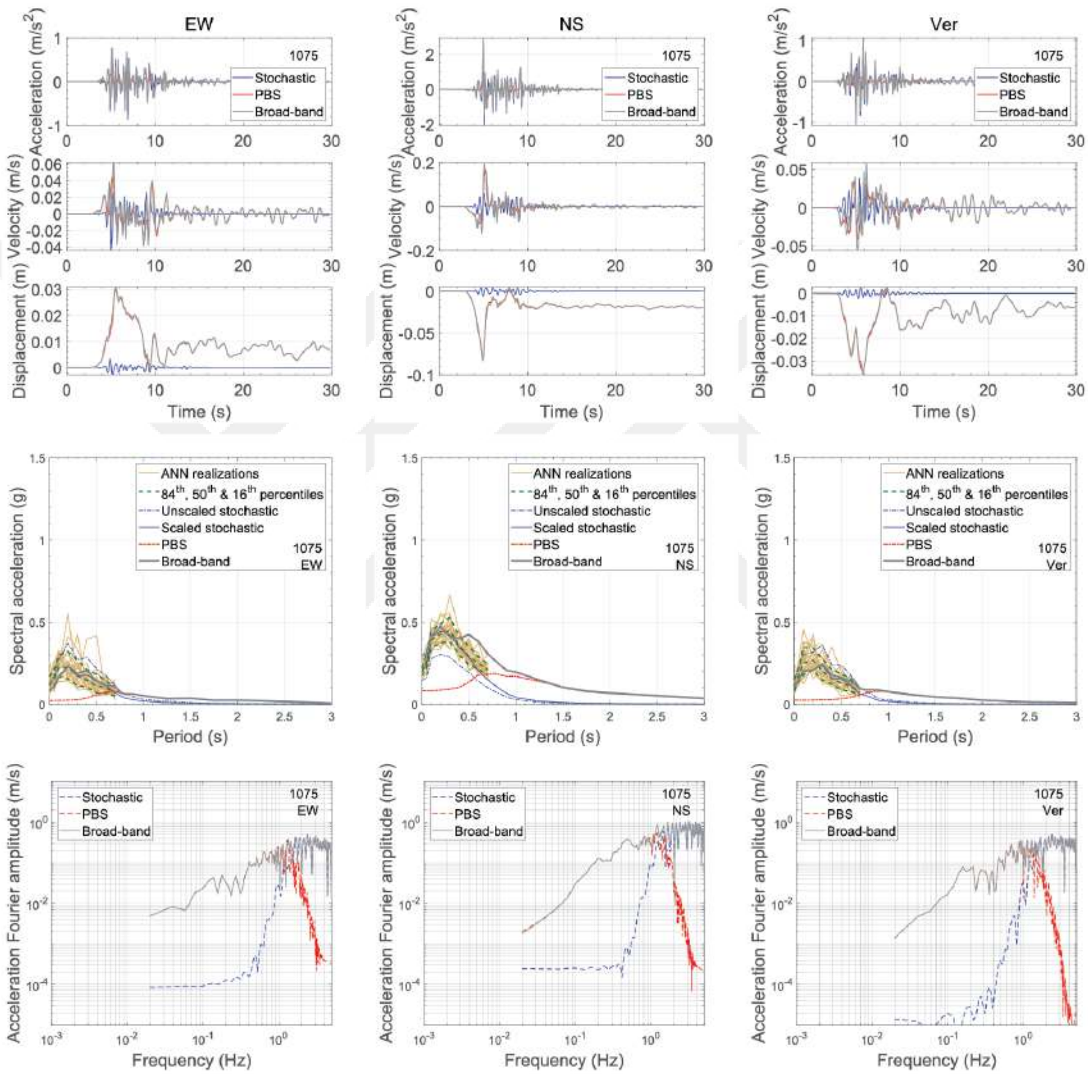

Figure B.5: STATION 1075 : ITA SUL MMF MW6.0 S003 TOPO EL

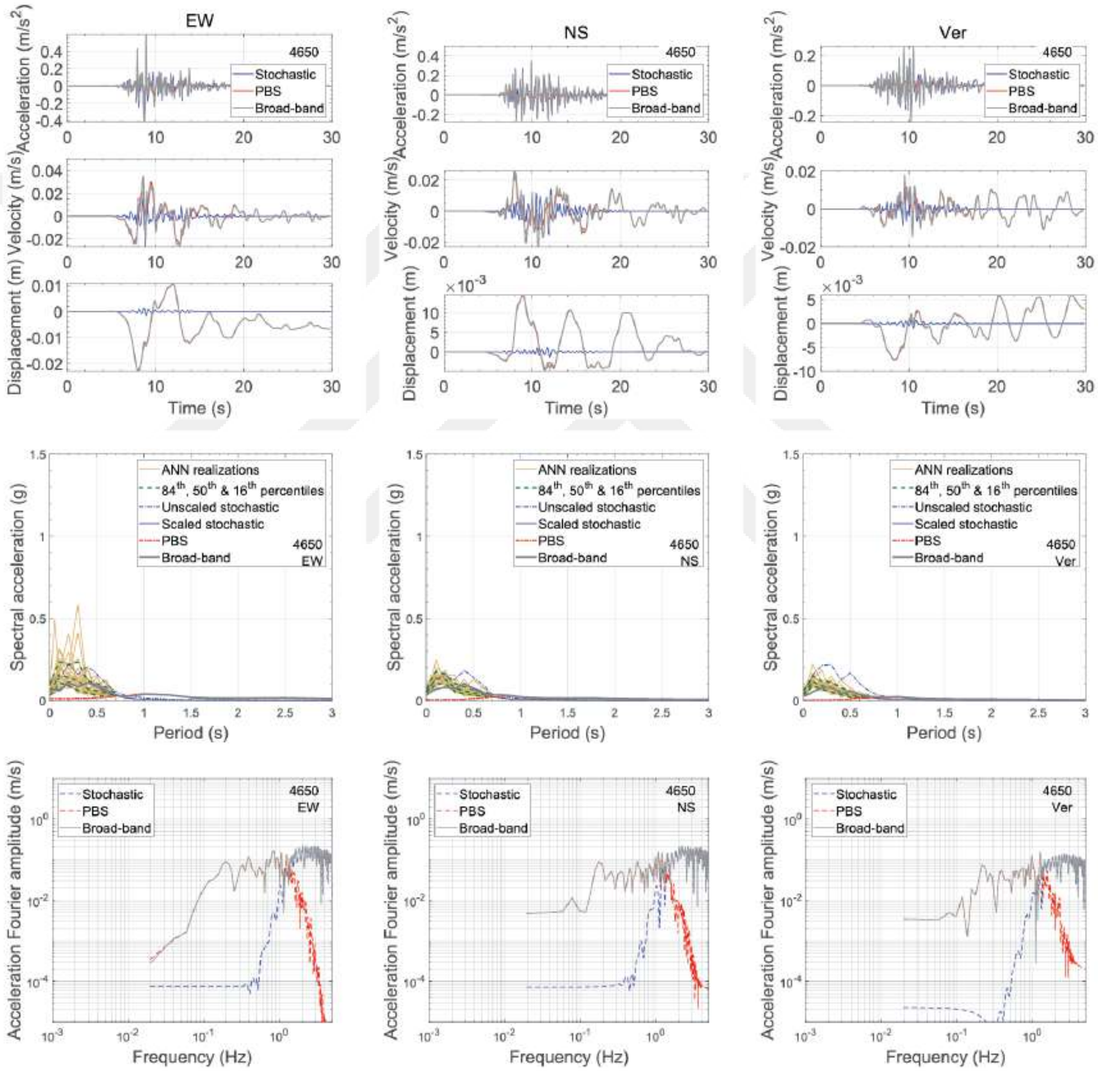

Figure B.6: STATION 4650 : ITA SUL MMF MW6.0 S003 TOPO EL

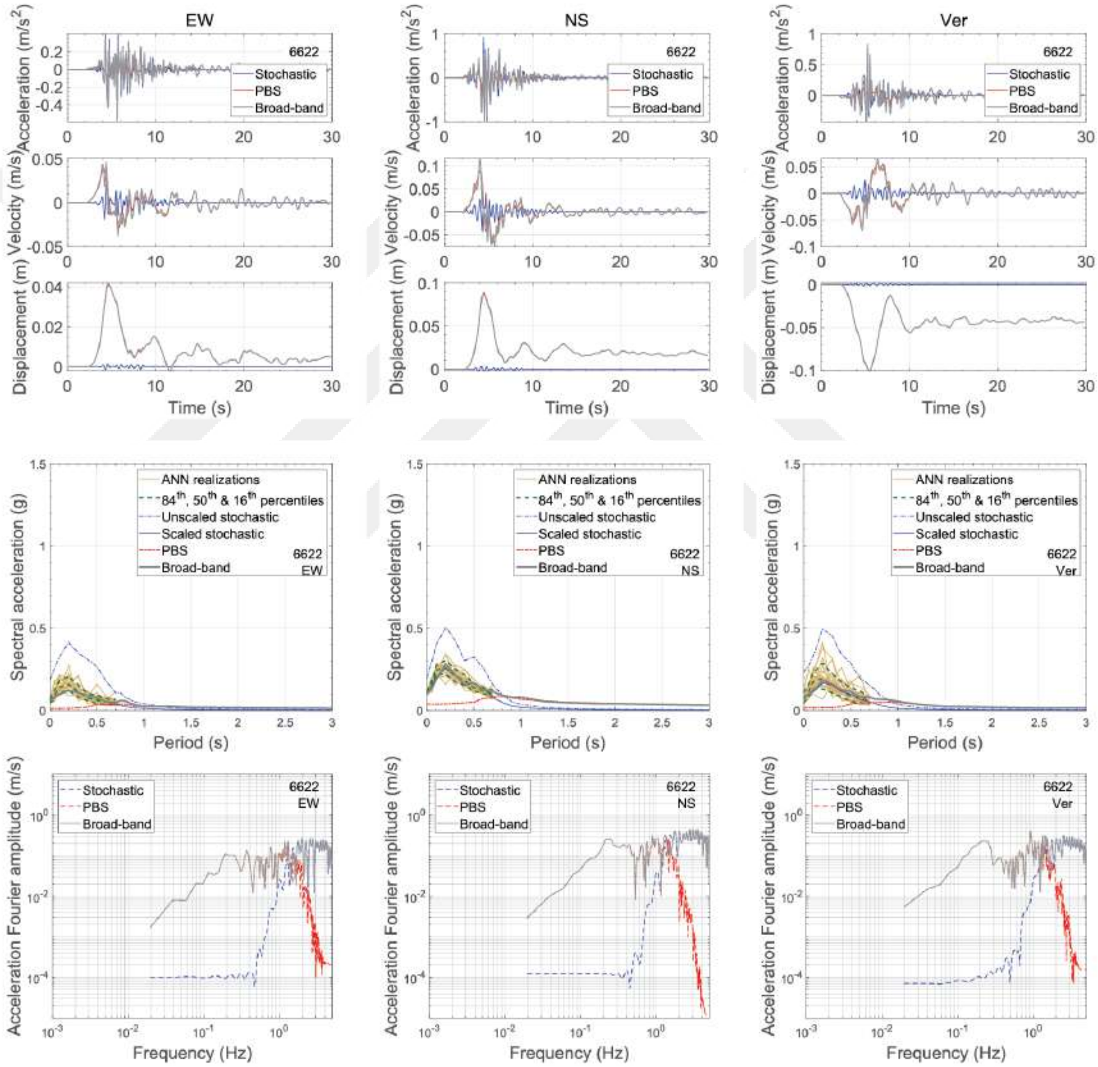

Figure B.7: STATION 6622 : ITA SUL MMF MW6.0 S003 TOPO EL

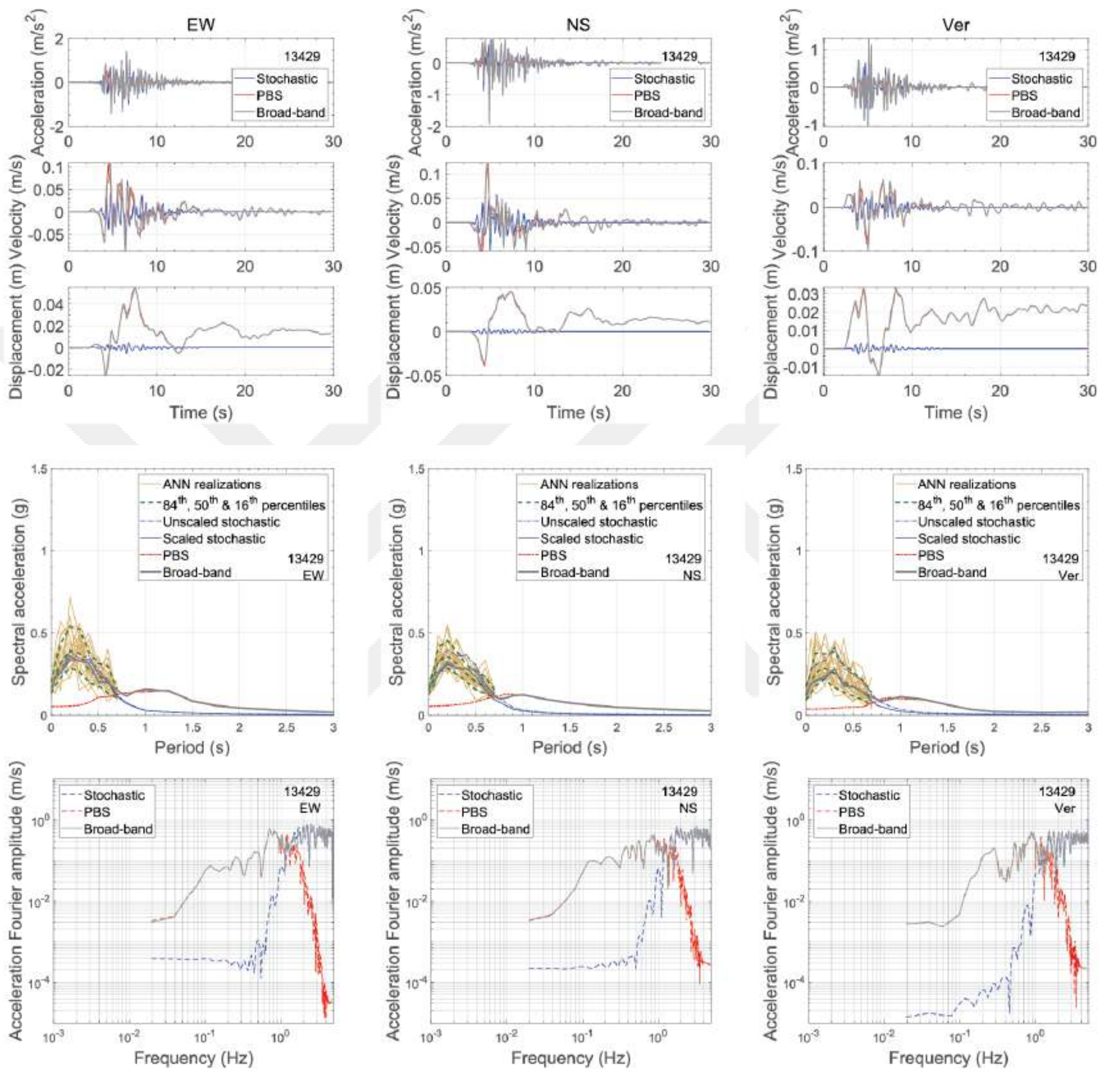

Figure B.8: STATION 13429 : ITA SUL MMF MW6.0 S003 TOPO EL

B.2 ITA SUL MMF MW6.5 S003 TOPO EL

B.2.1 Selected Stations on Soil

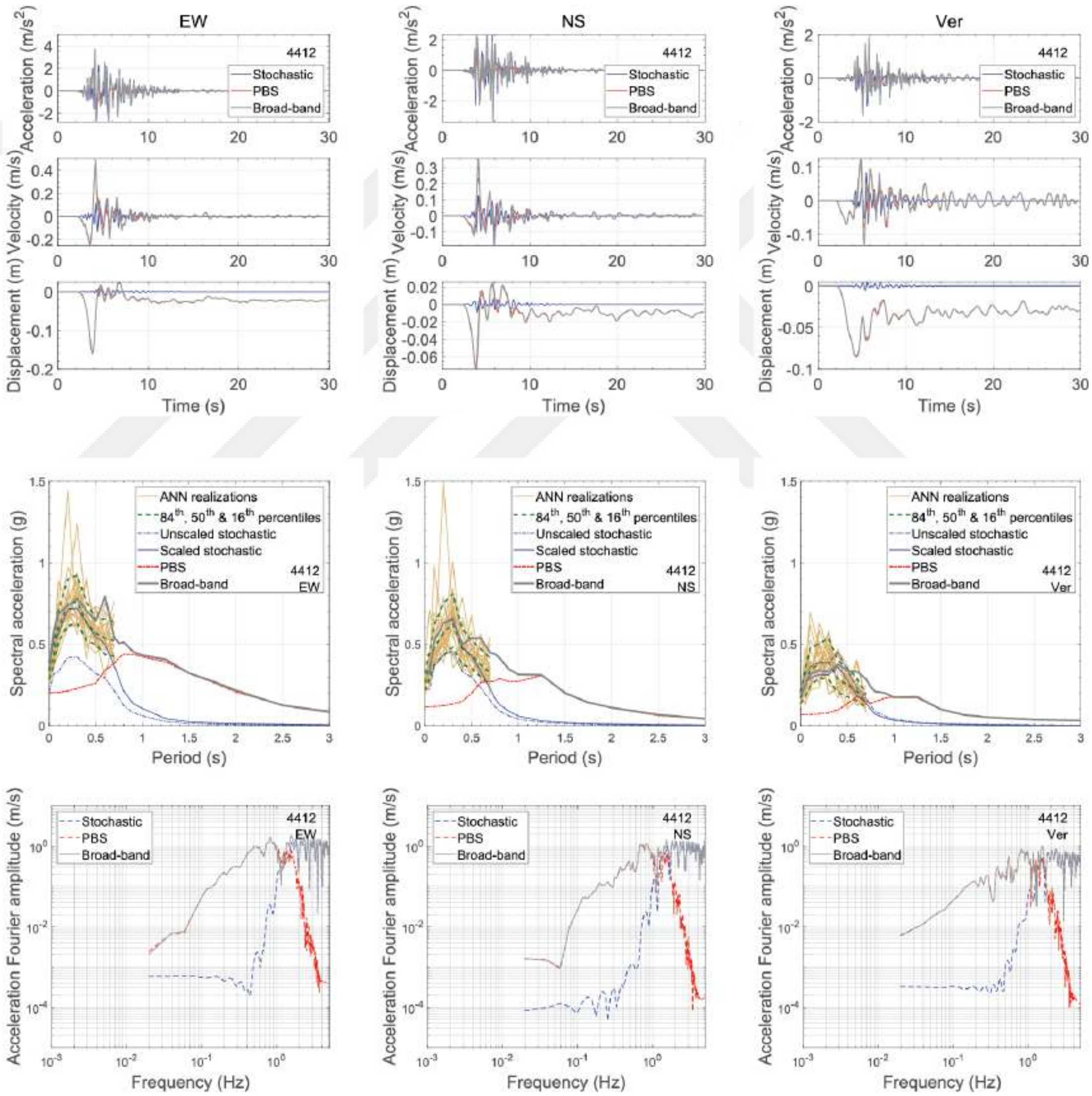

Figure B.9: STATION 4412 : ITA SUL MMF MW6.5 S003 TOPO EL

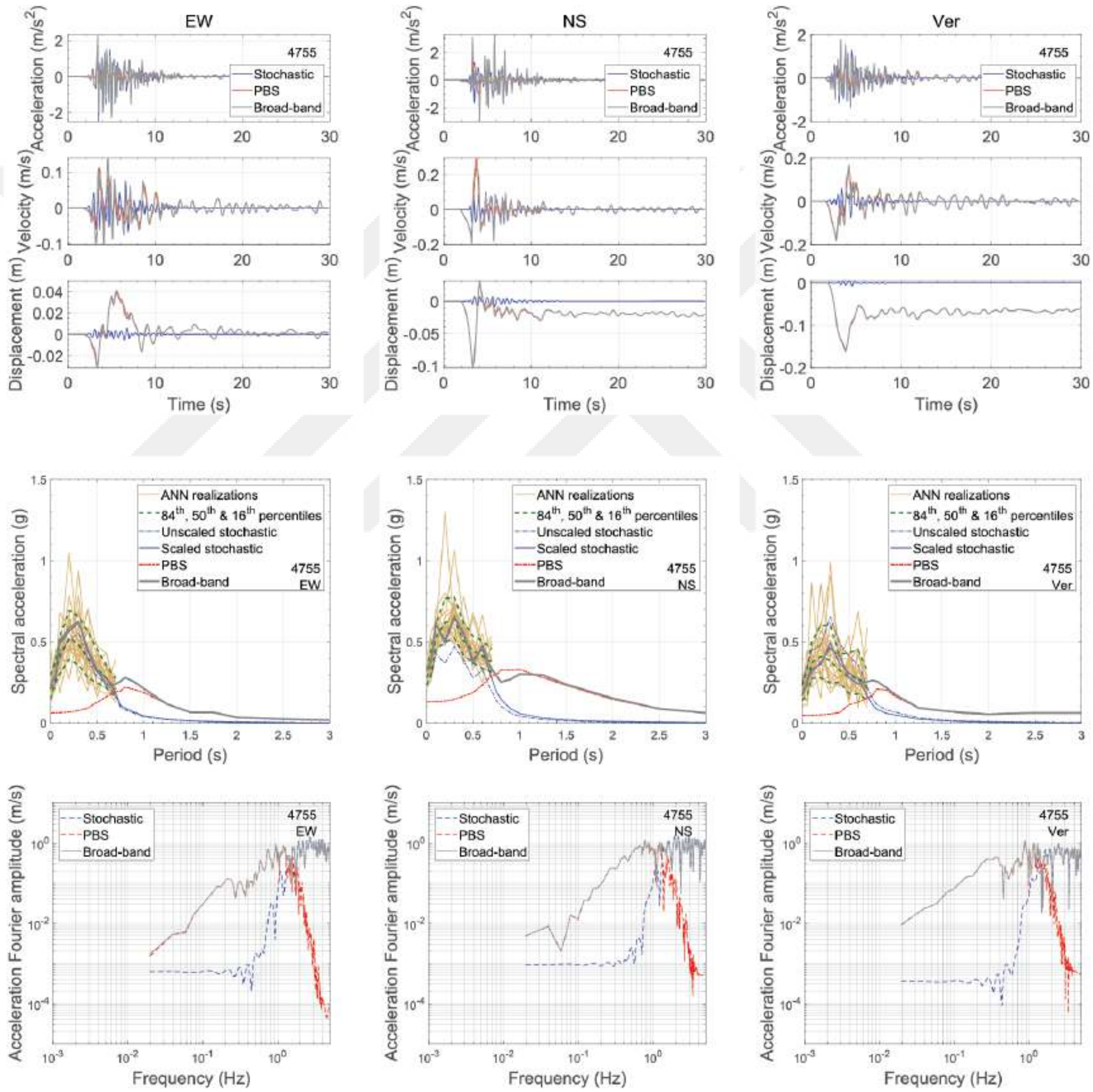

Figure B.10: STATION 4755 : ITA SUL MMF MW6.5 S003 TOPO EL

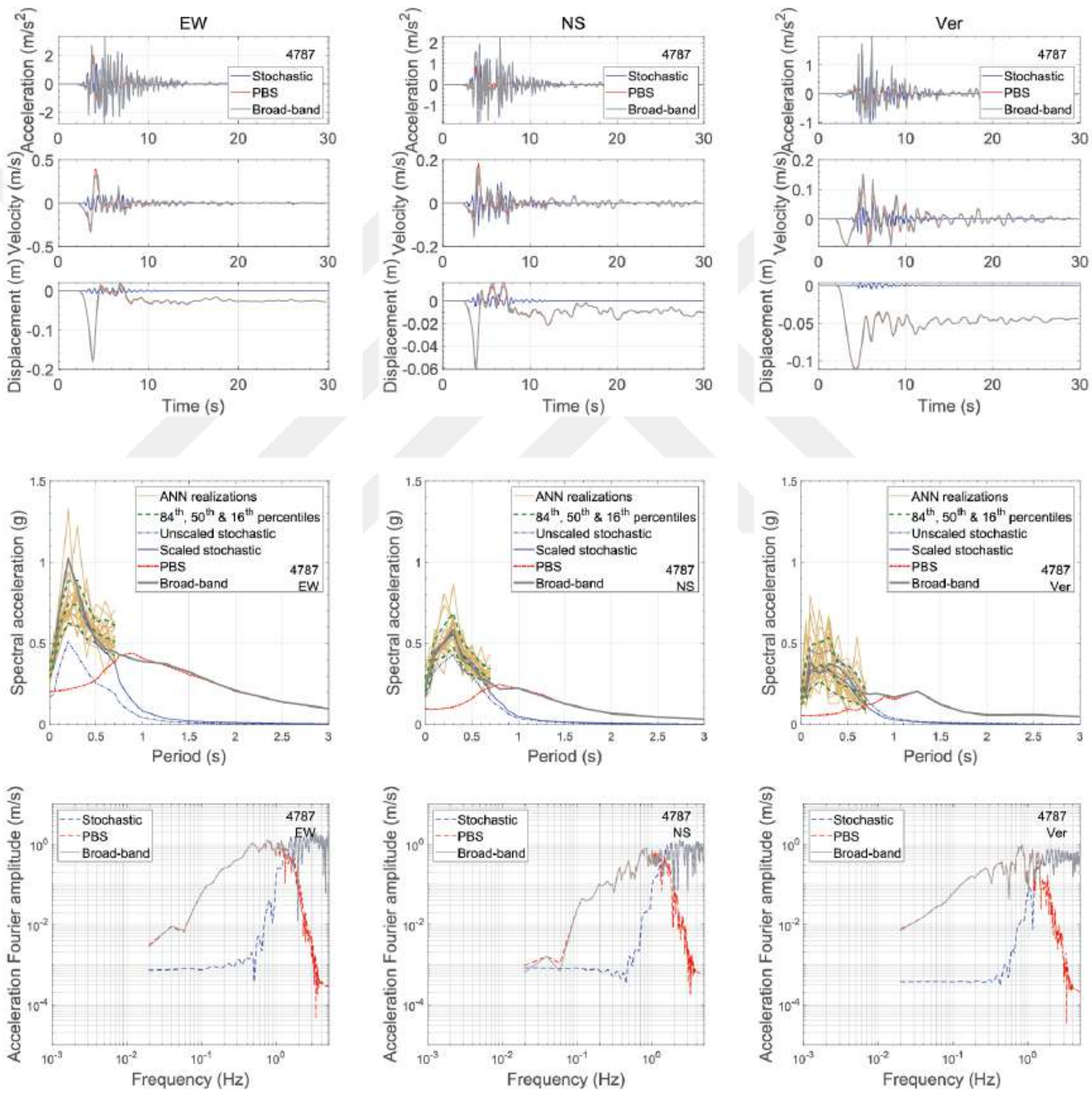

Figure B.11: STATION 4787 : ITA SUL MMF MW6.5 S003 TOPO EL

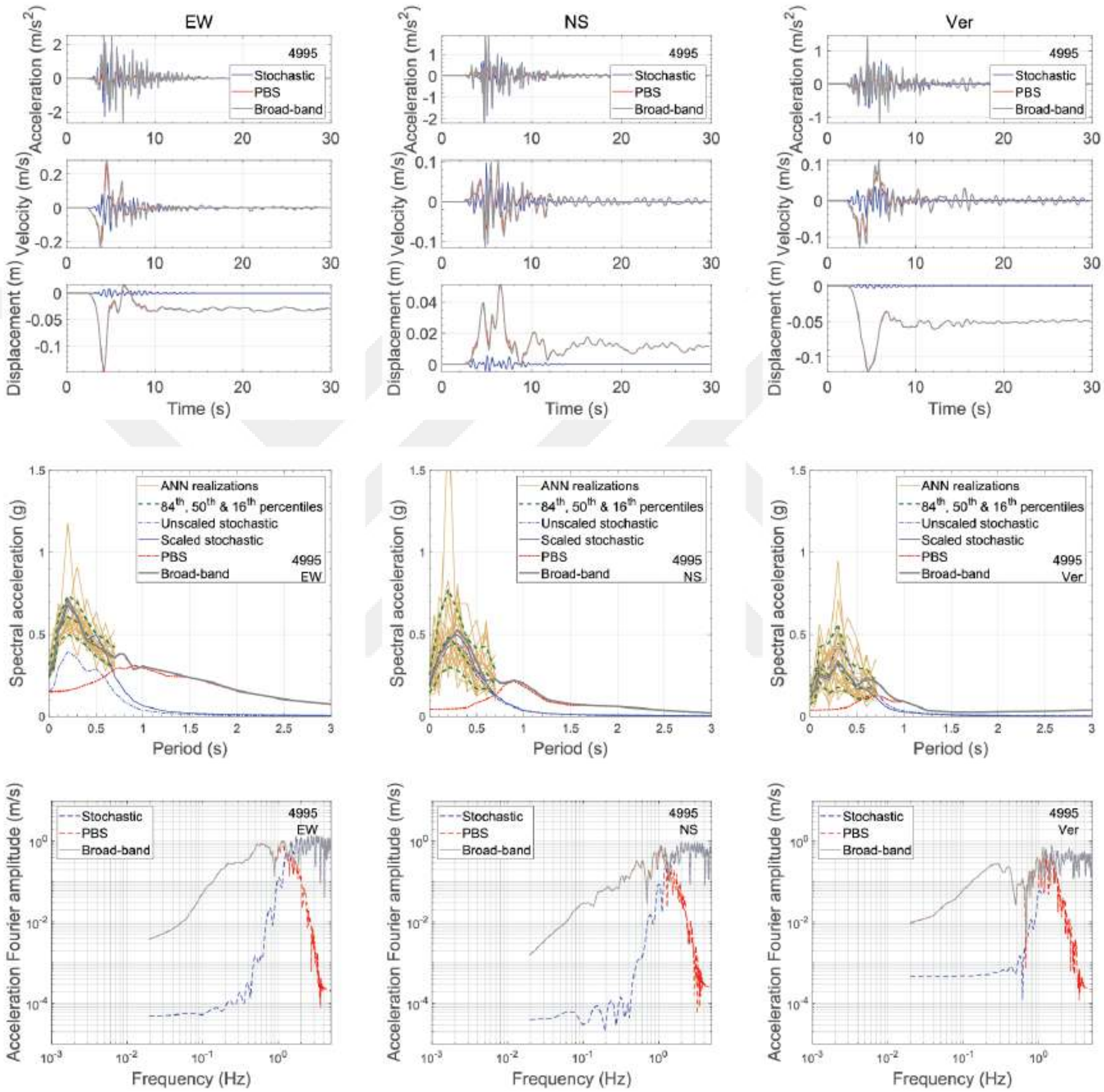

Figure B.12: STATION 4995 : ITA SUL MMF MW6.5 S003 TOPO EL

B.2.2 Selected Stations on Rock

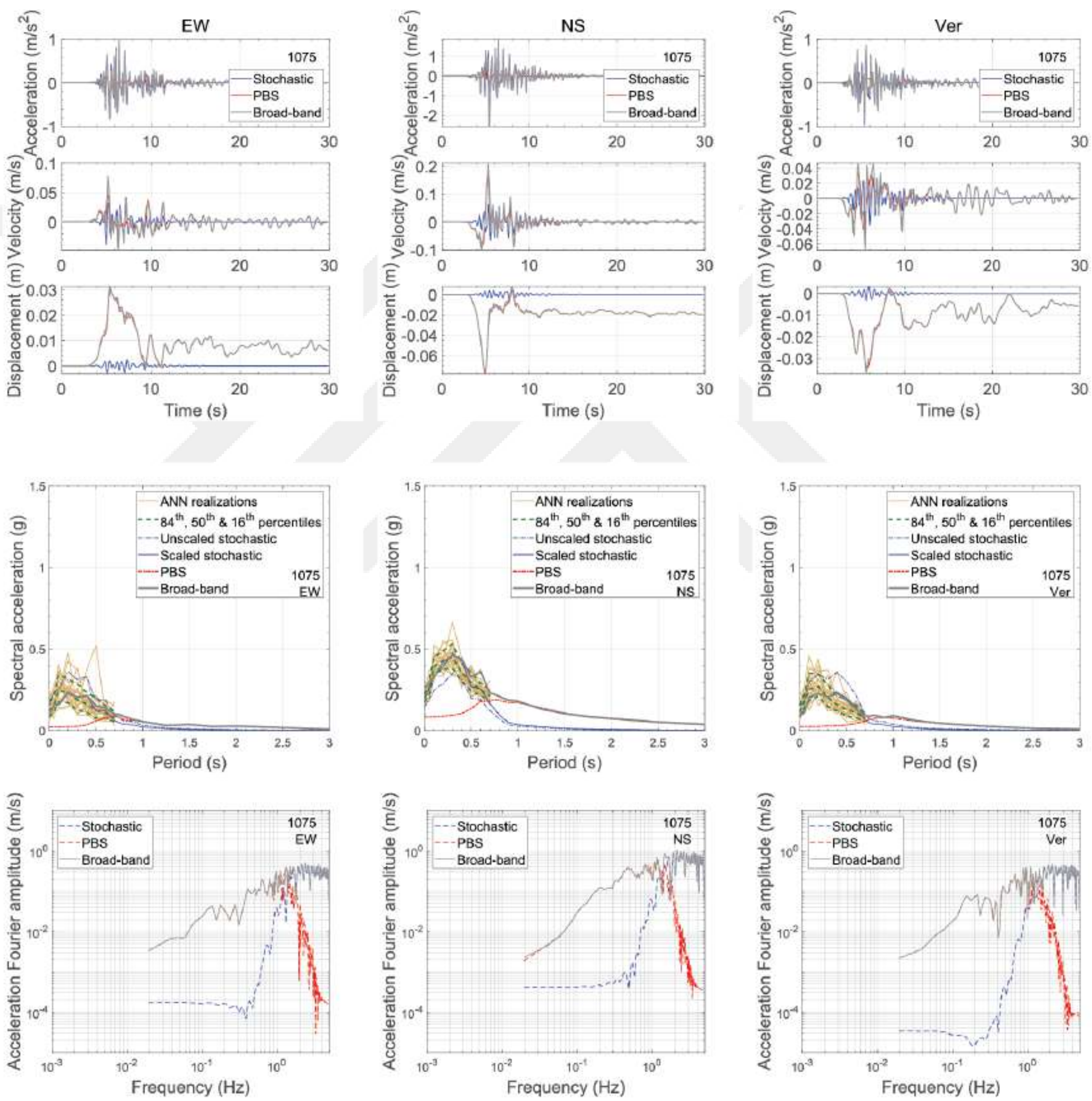

Figure B.13: STATION 1075 : ITA SUL MMF MW6.5 S003 TOPO EL

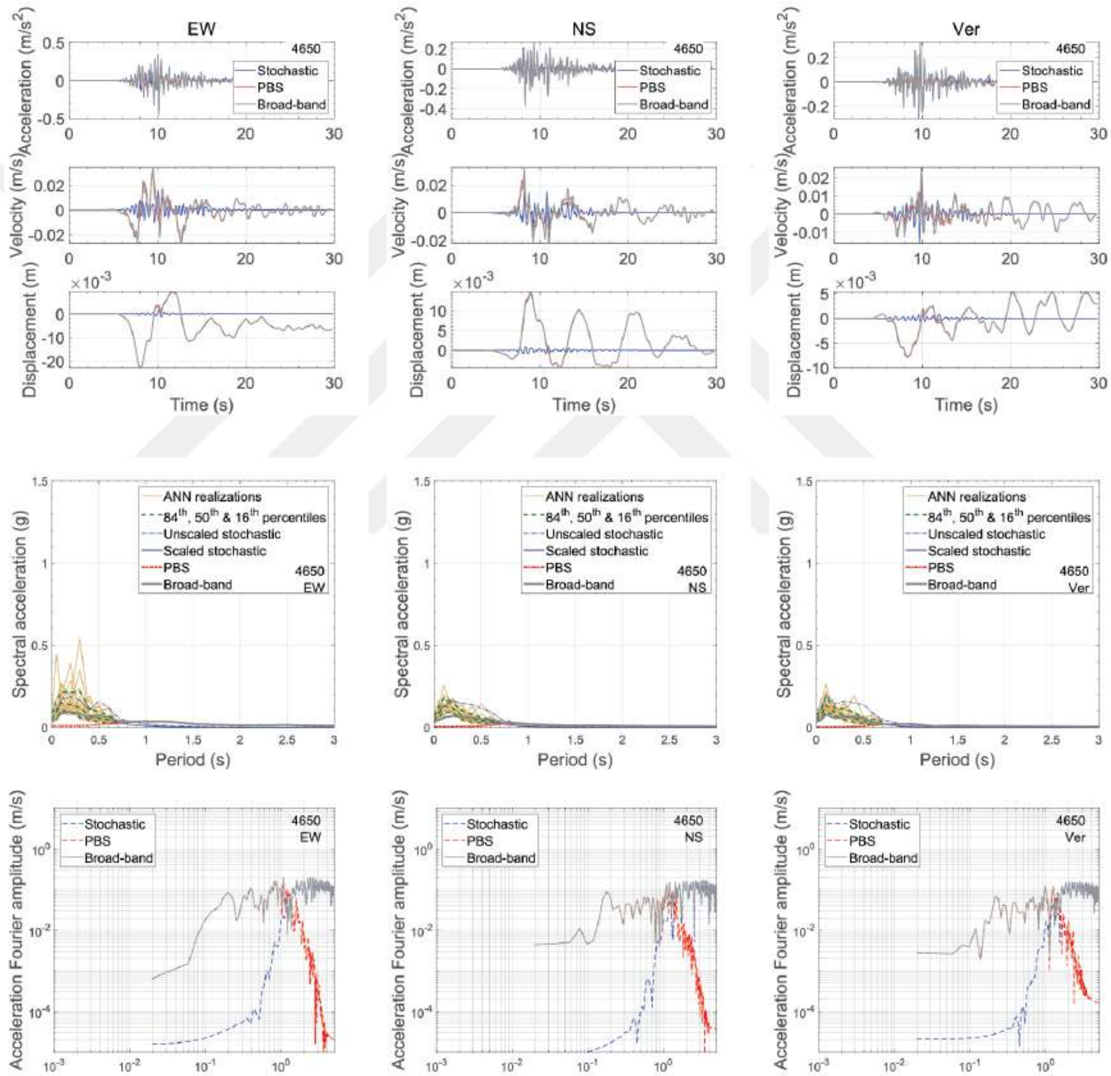

Figure B.14: STATION 4650 : ITA SUL MMF MW6.5 S003 TOPO EL

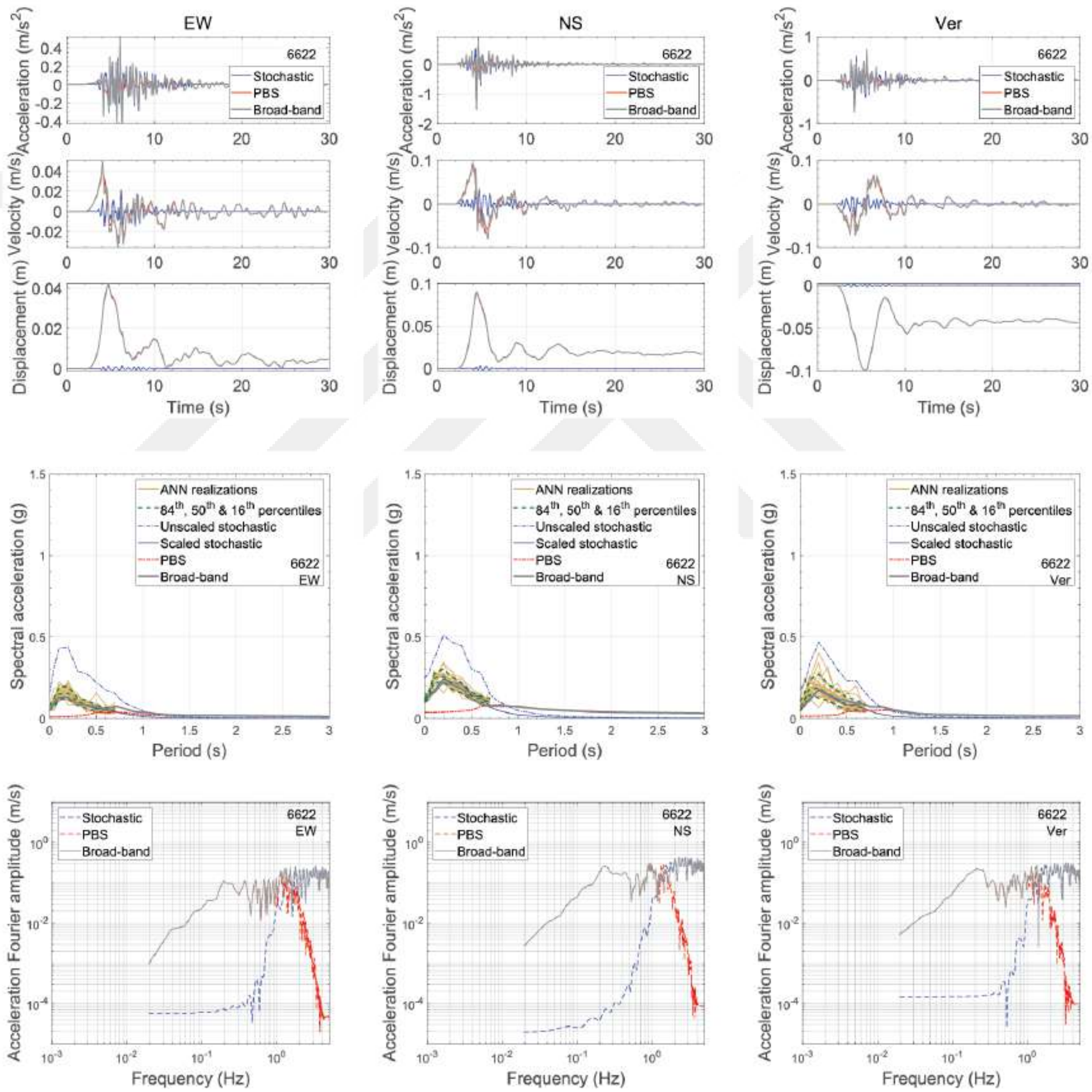

Figure B.15: STATION 6622 : ITA SUL MMF MW6.5 S003 TOPO EL

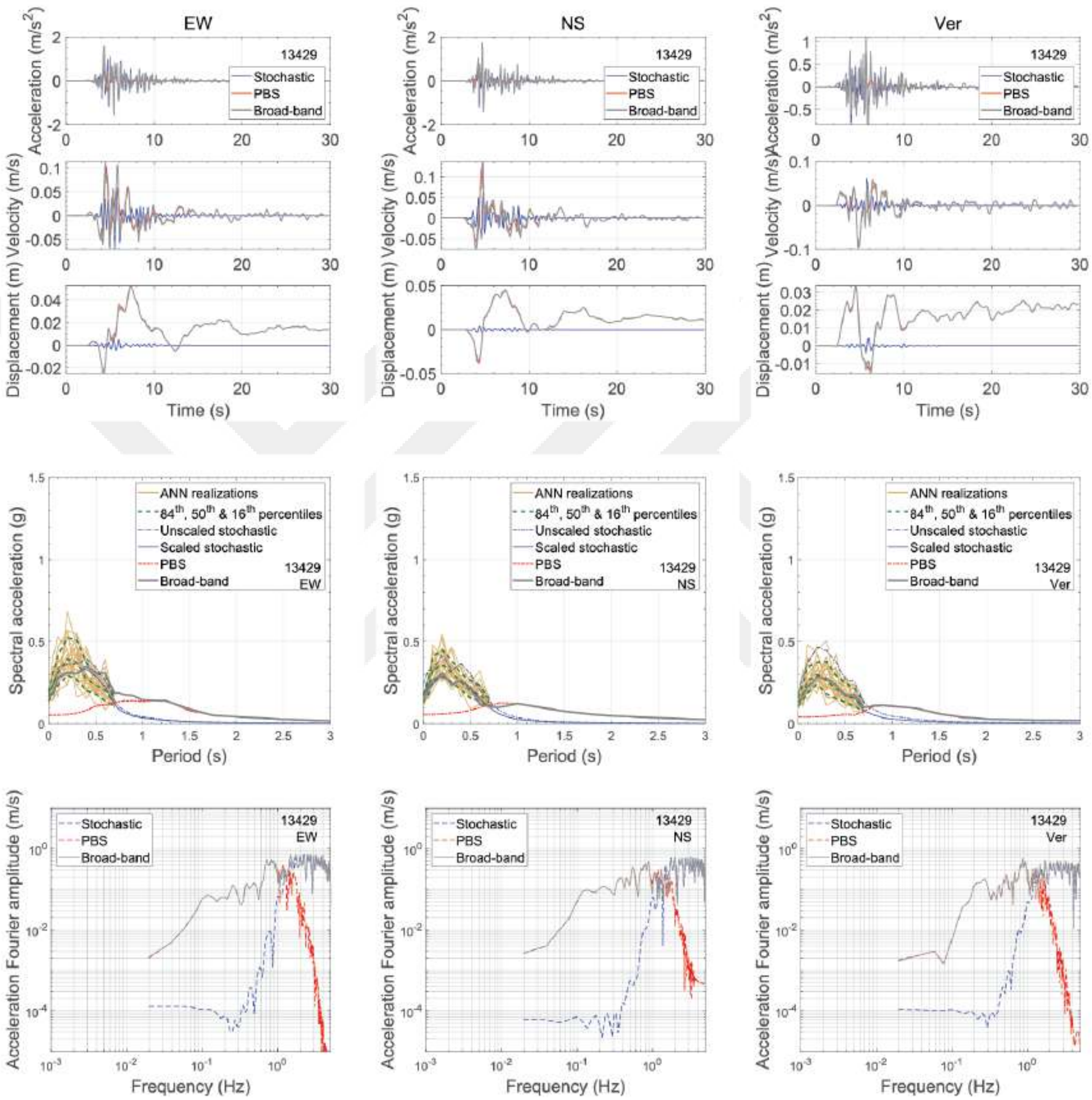

Figure B.16: STATION 13429 : ITA SUL MMF MW6.5 S003 TOPO EL

B.3 ITA SUL MMF MW6.0 S003 TOPO NEL

B.3.1 Selected Stations on Soil

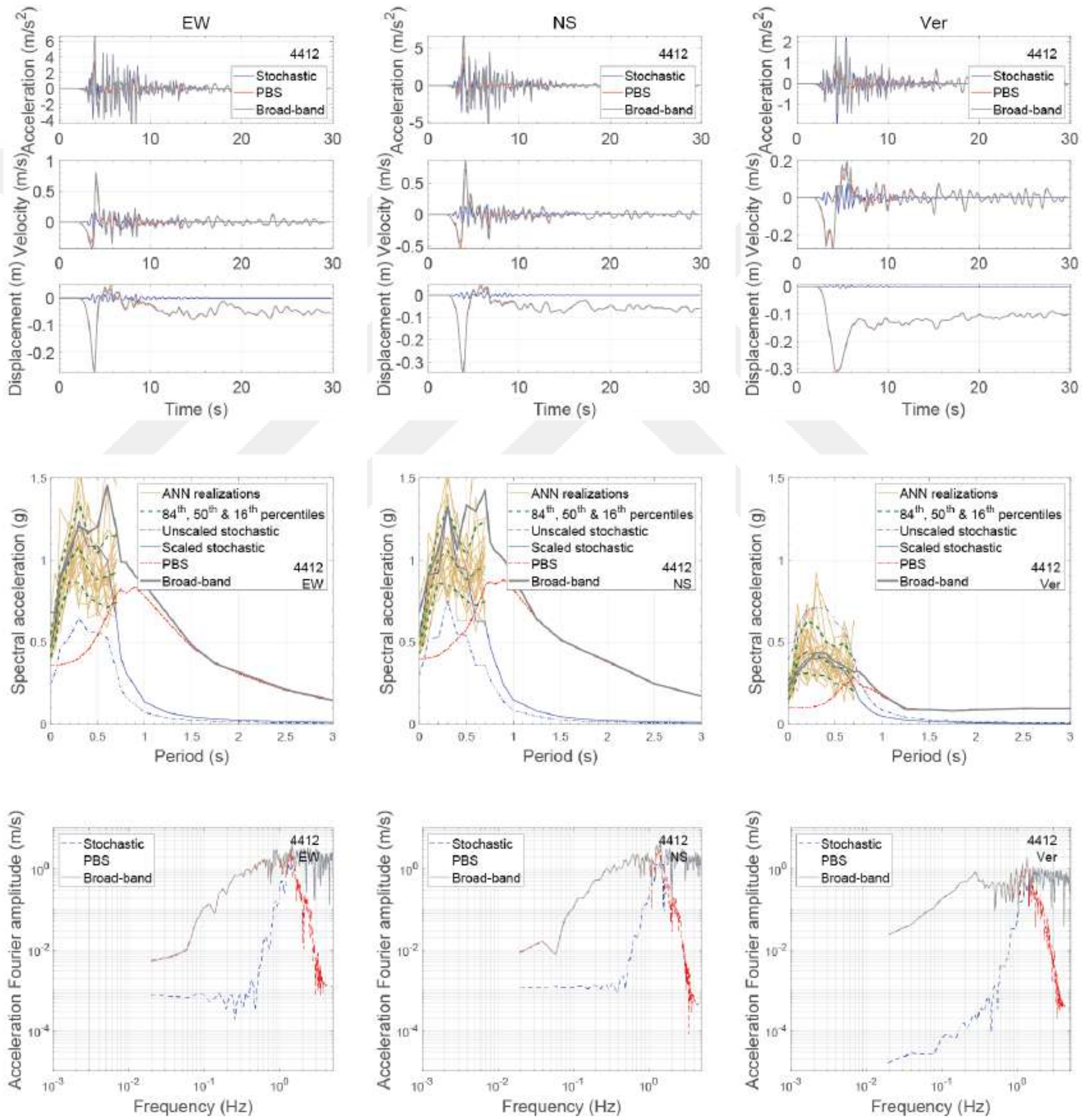

Figure B.17: STATION 4412 : ITA SUL MMF MW6.0 S003 TOPO NEL

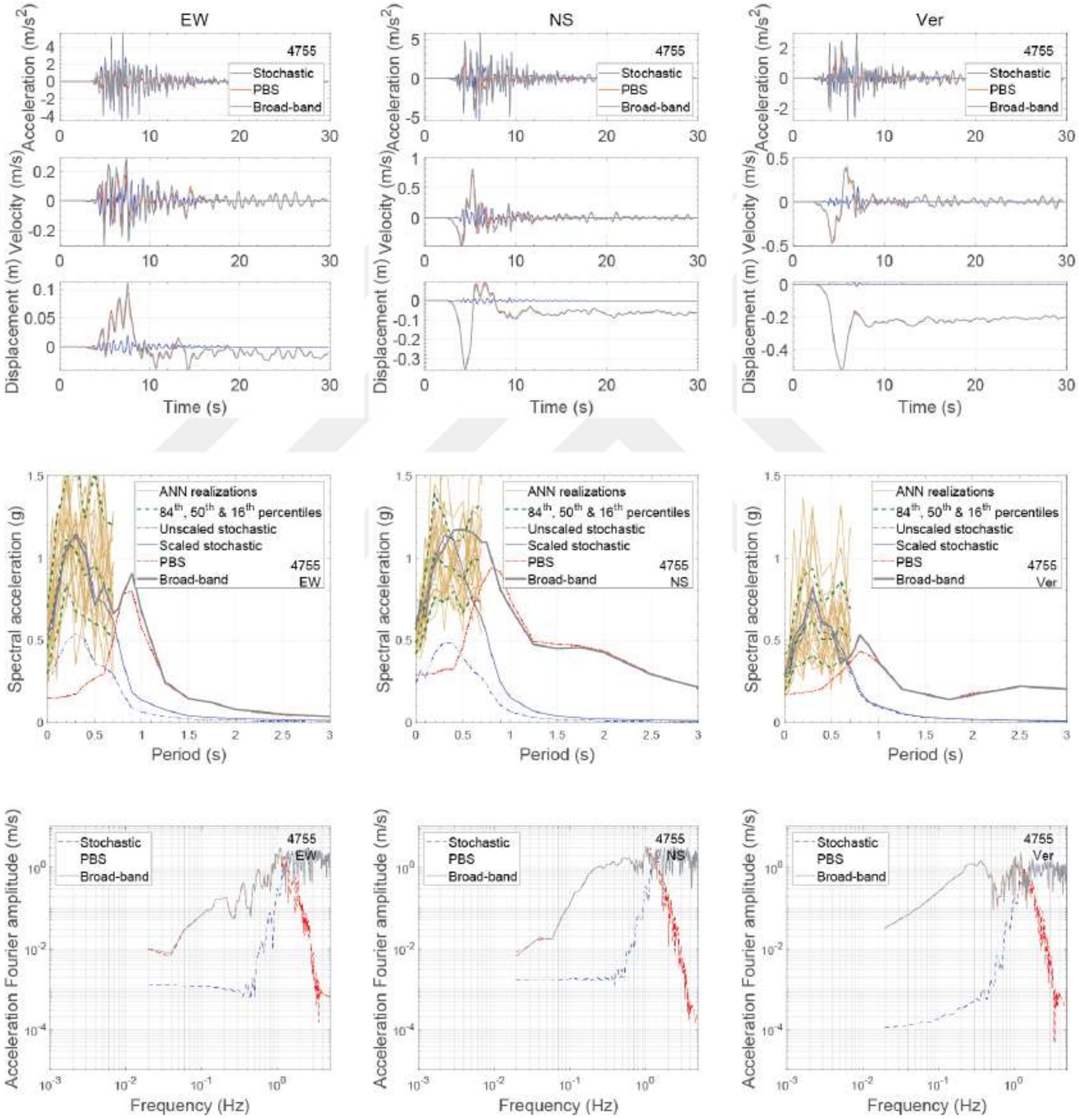

Figure B.18: STATION 4755 : ITA SUL MMF MW6.0 S003 TOPO NEL

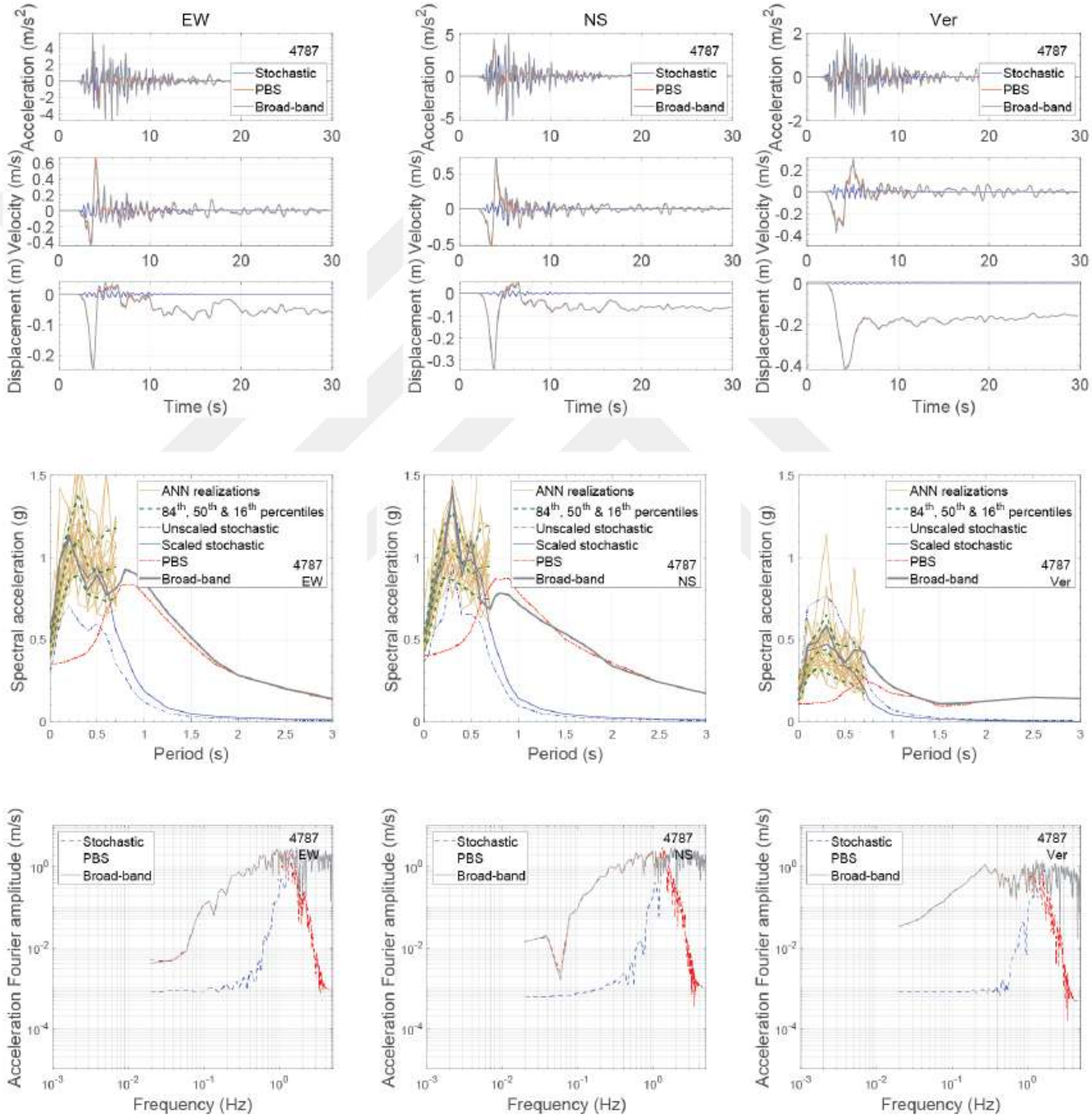

Figure B.19: STATION 4787 : ITA SUL MMF MW6.0 S003 TOPO NEL

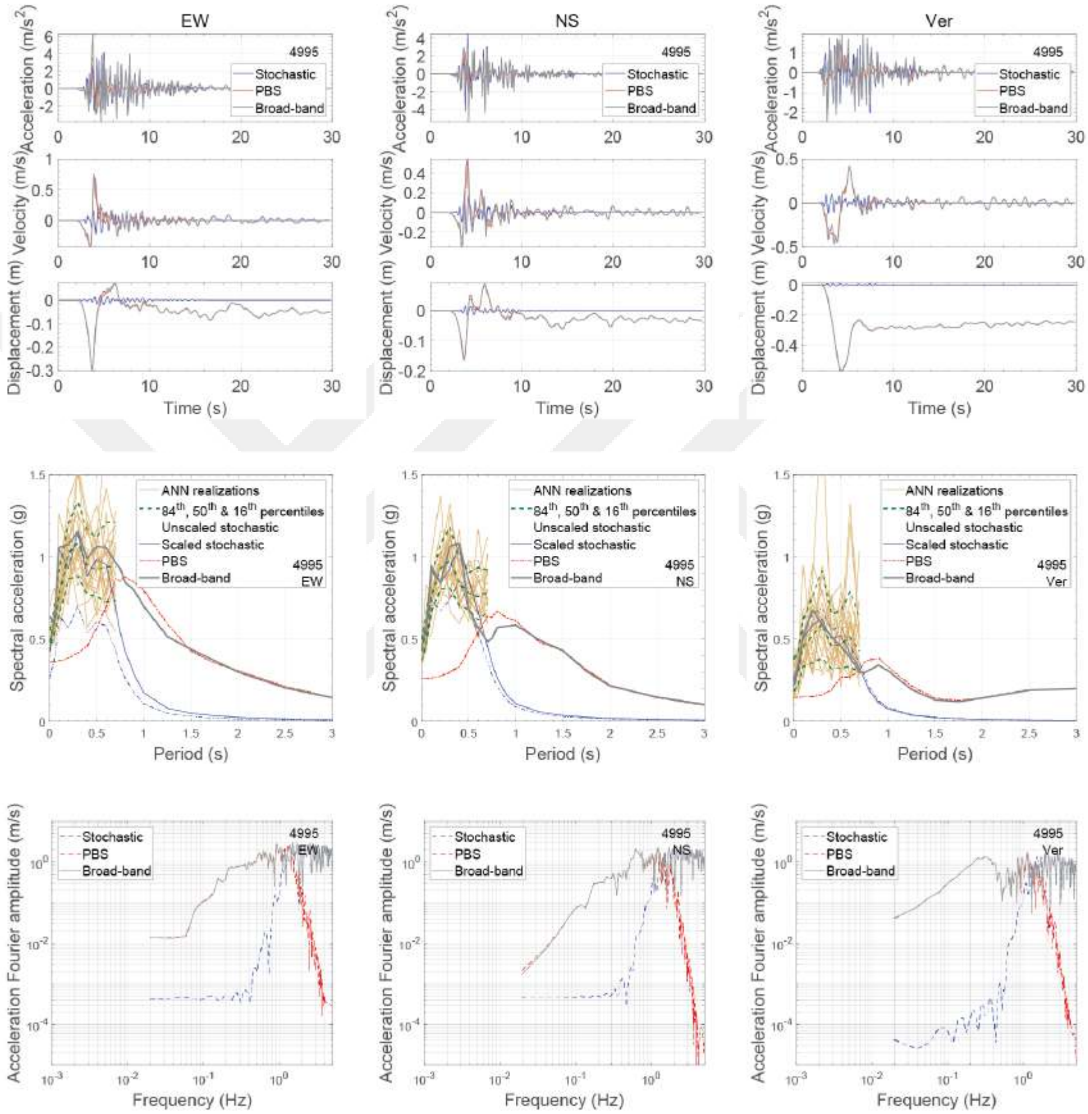

Figure B.20: STATION 4995 : ITA SUL MMF MW6.0 S003 TOPO NEL

B.3.2 Selected Stations on Rock

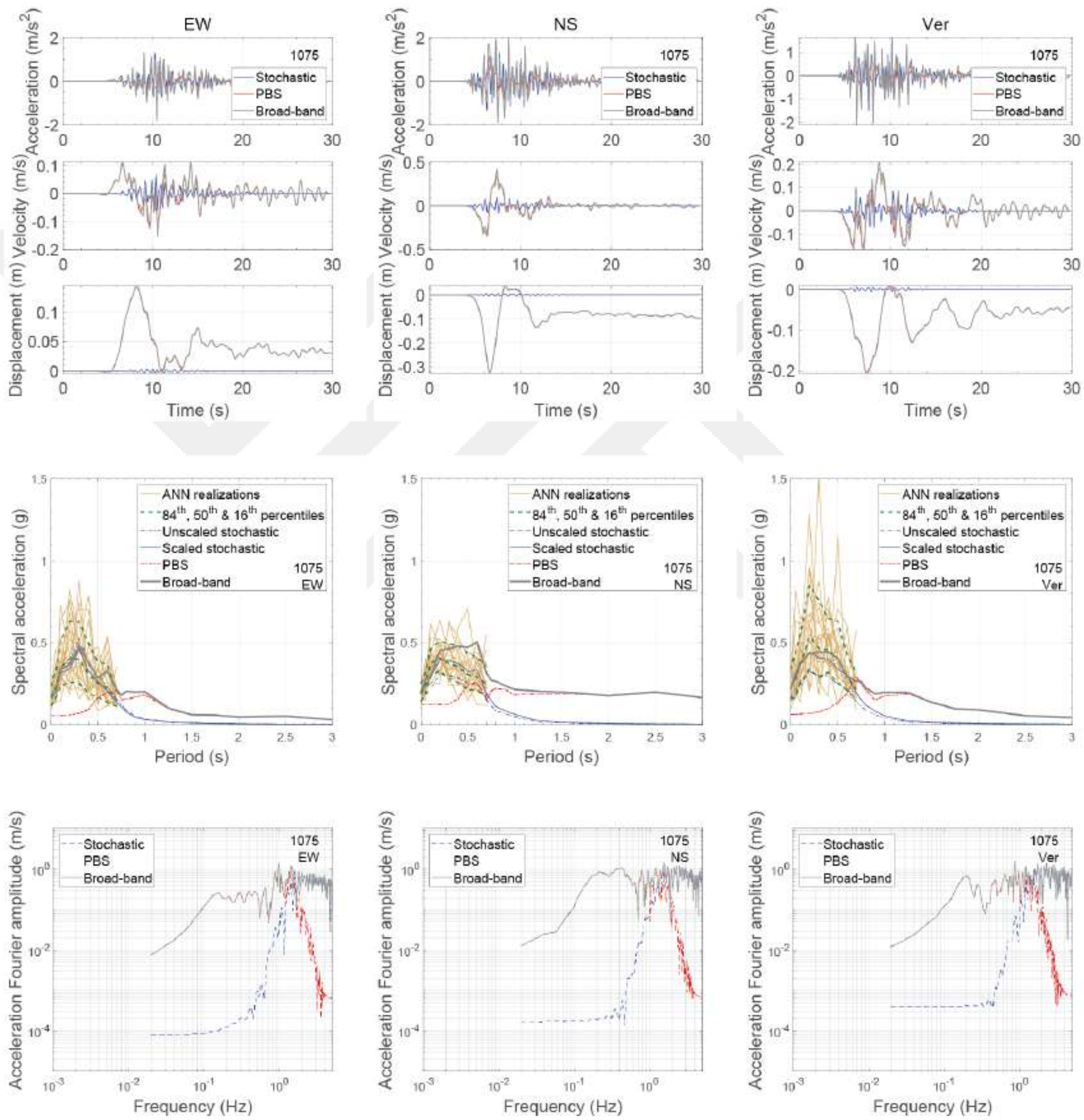

Figure B.21: STATION 1075 : ITA SUL MMF MW6.0 S003 TOPO NEL

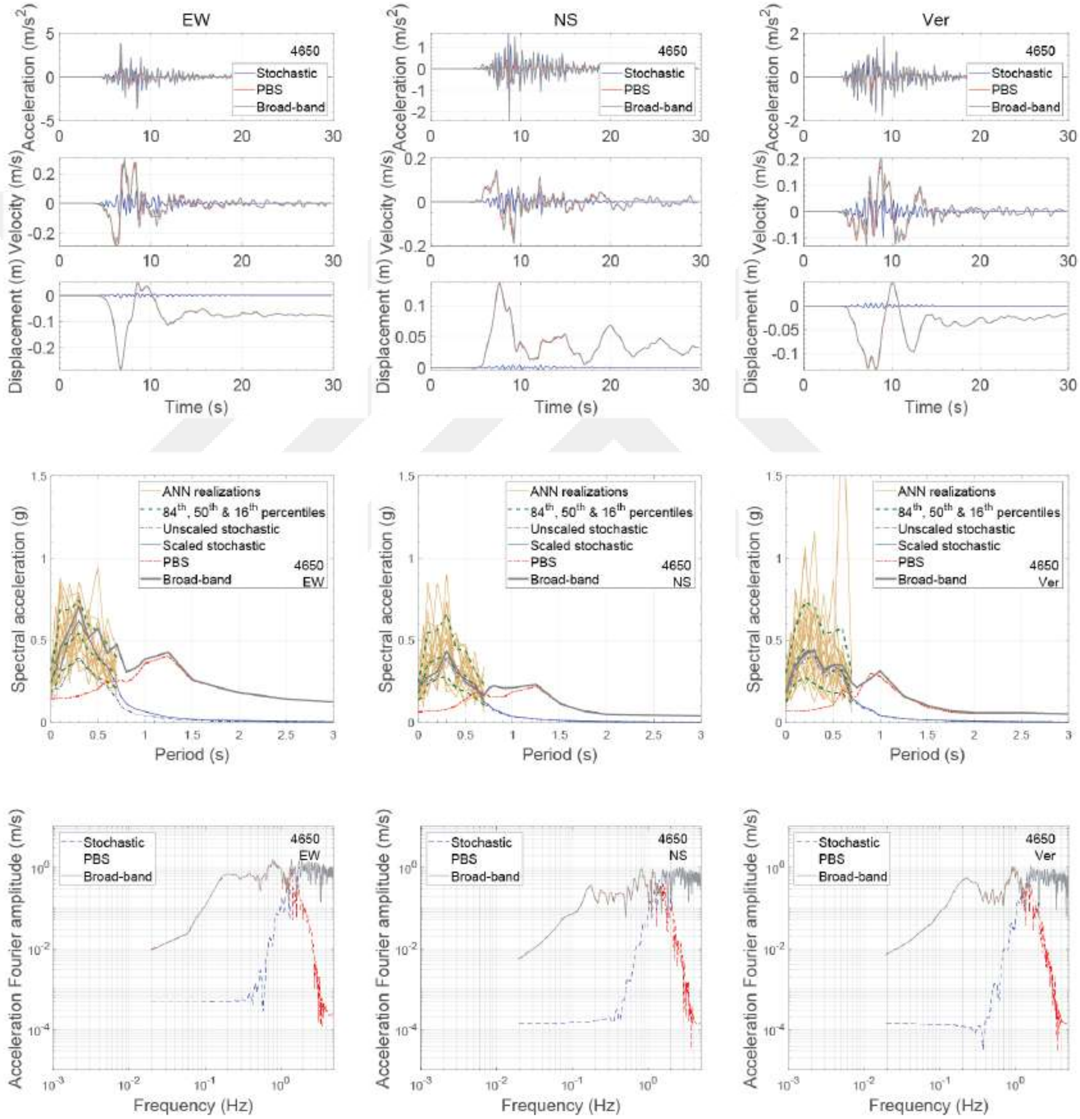

Figure B.22: STATION 4650 : ITA SUL MMF MW6.0 S003 TOPO NEL

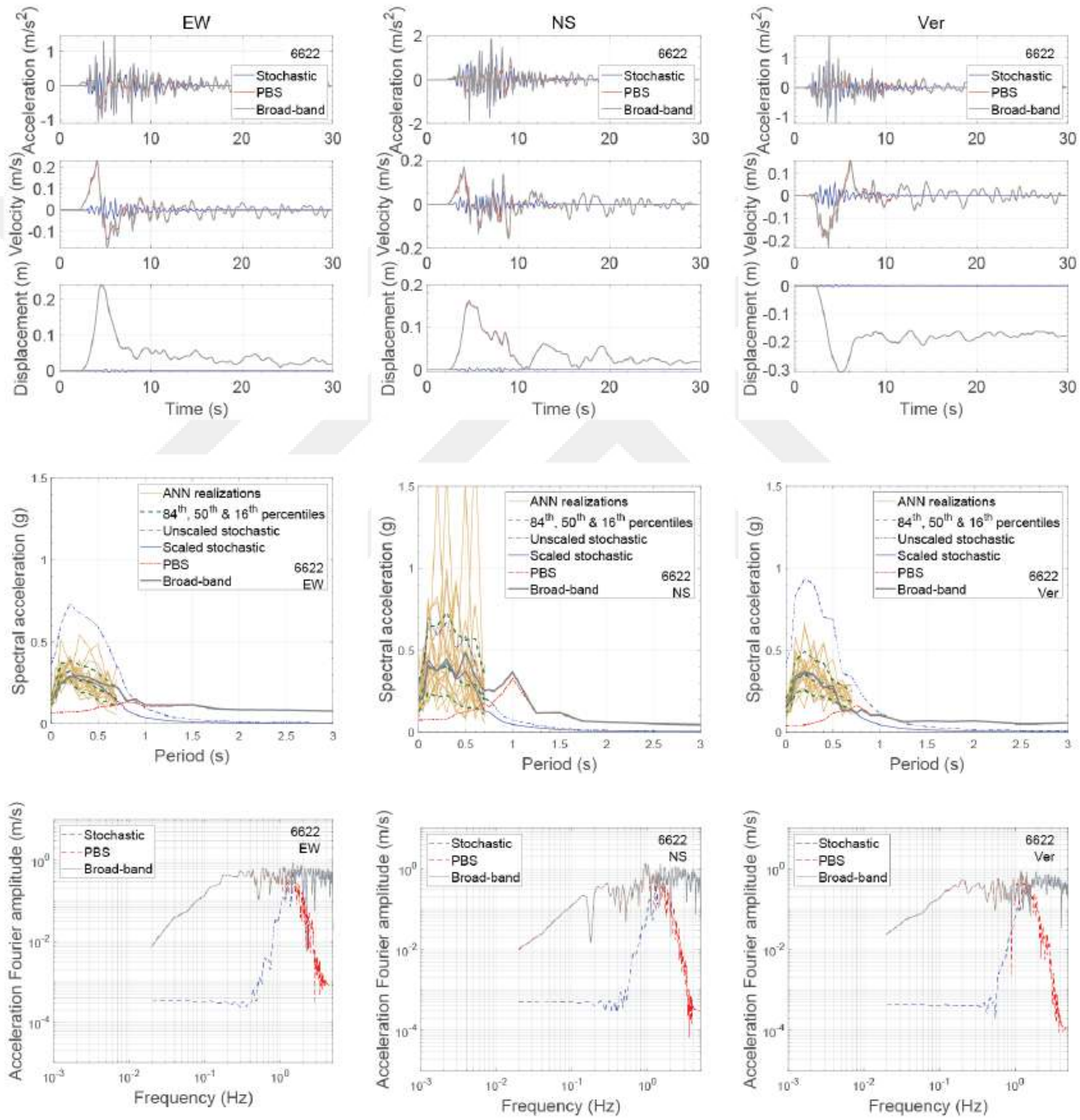

Figure B.23: STATION 6622 : ITA SUL MMF MW6.0 S003 TOPO NEL

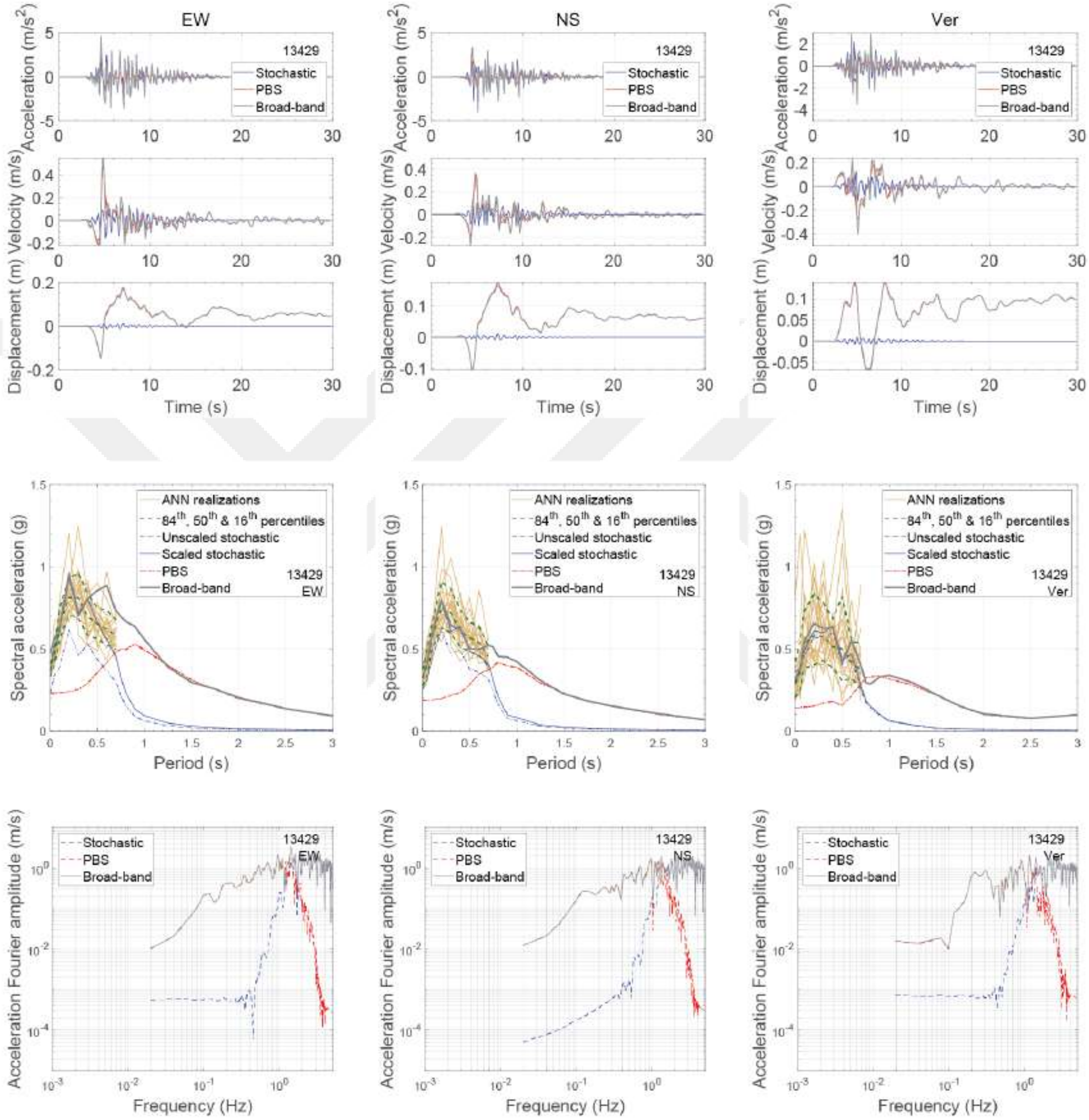

Figure B.24: STATION 13429 : ITA SUL MMF MW6.0 S003 TOPO NEL

B.4 ITA SUL MMF MW6.5 S003 TOPO NEL

B.4.1 Selected Stations on Soil

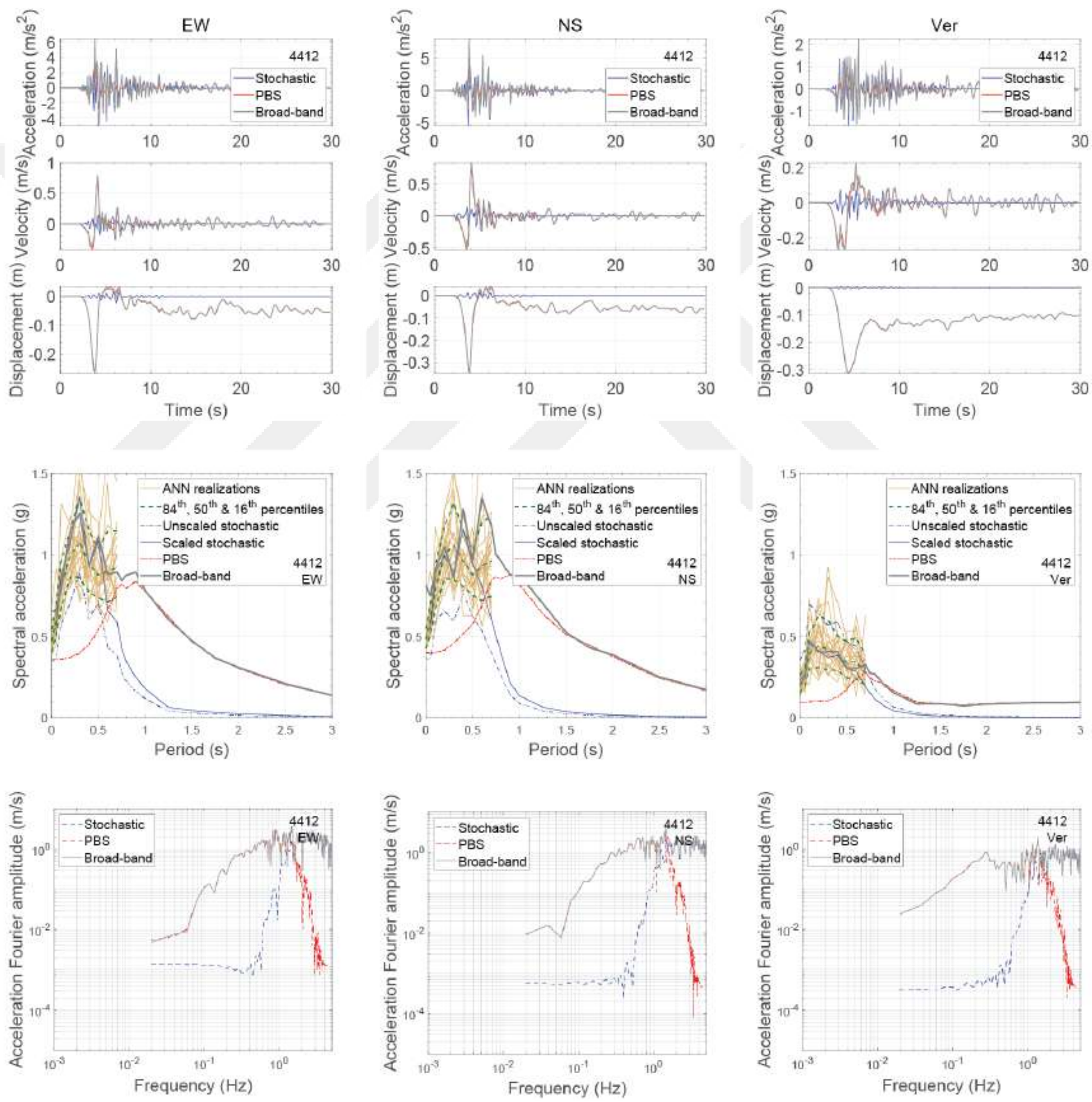

Figure B.25: STATION 4412 : ITA SUL MMF MW6.0 S003 TOPO NEL

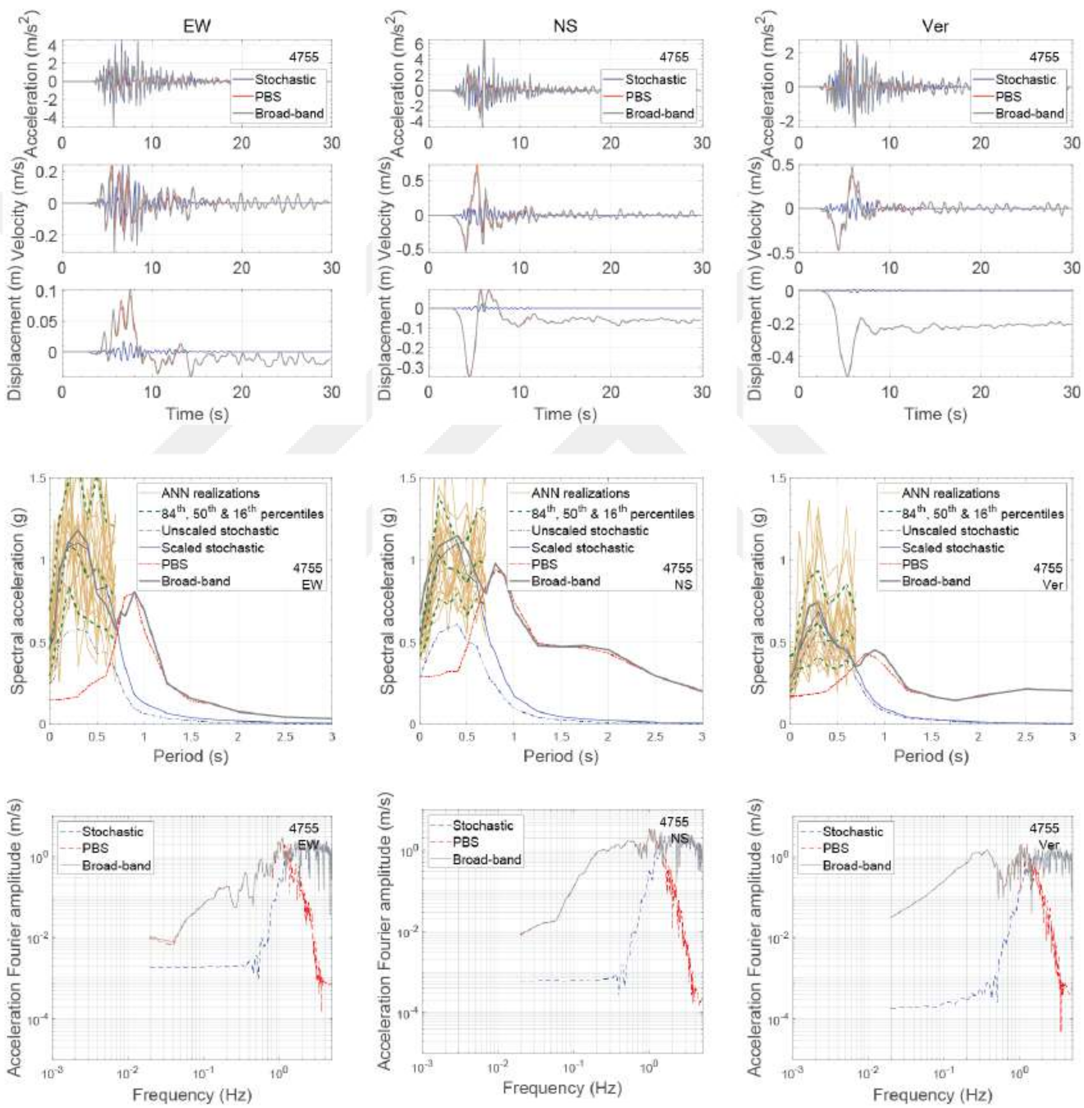

Figure B.26: STATION 4755 : ITA SUL MMF MW6.0 S003 TOPO NEL

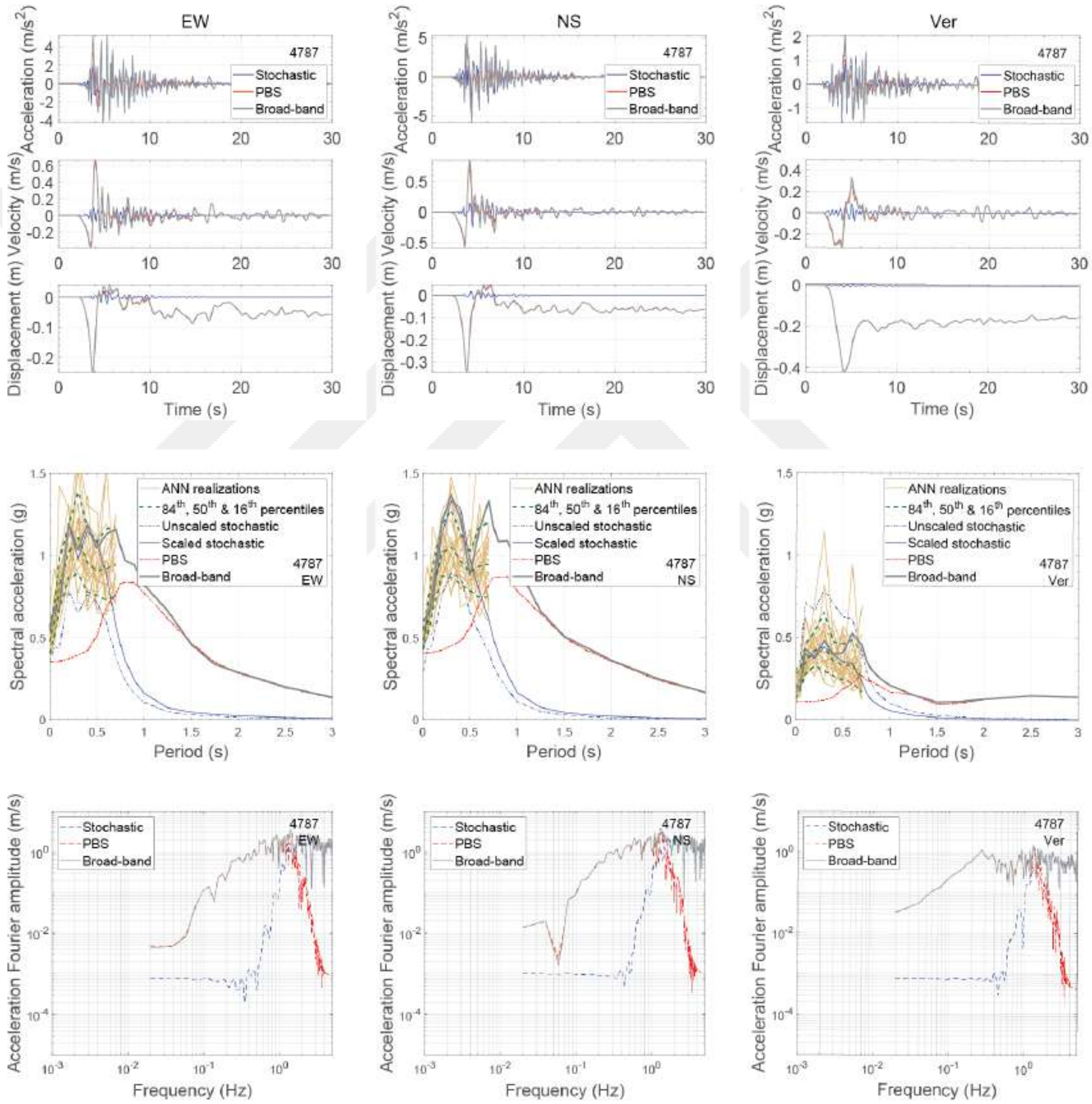

Figure B.27: STATION 4787 : ITA SUL MMF MW6.0 S003 TOPO NEL

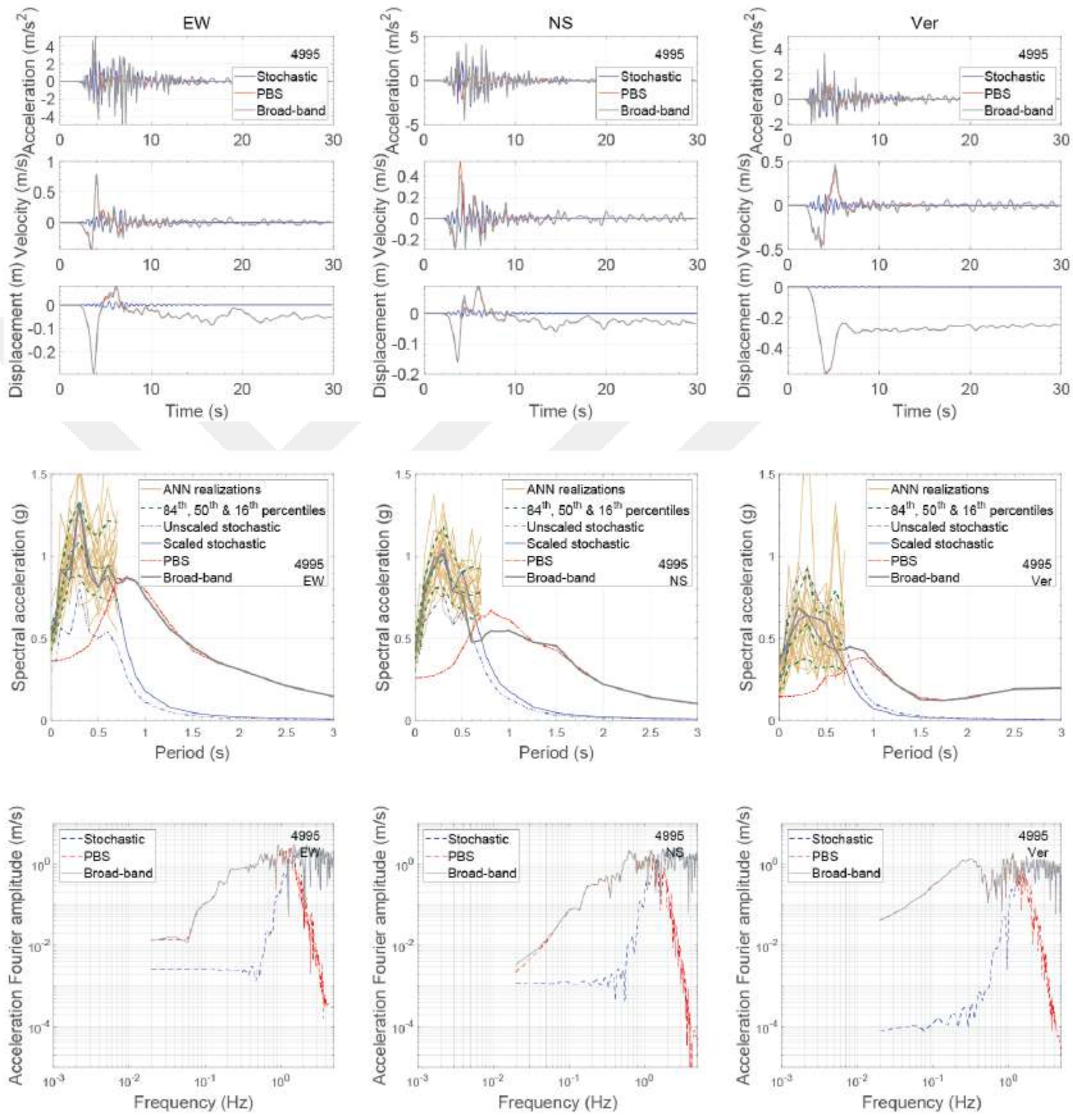

Figure B.28: STATION 4995 : ITA SUL MMF MW6.0 S003 TOPO NEL

B.4.2 Selected Stations on Rock

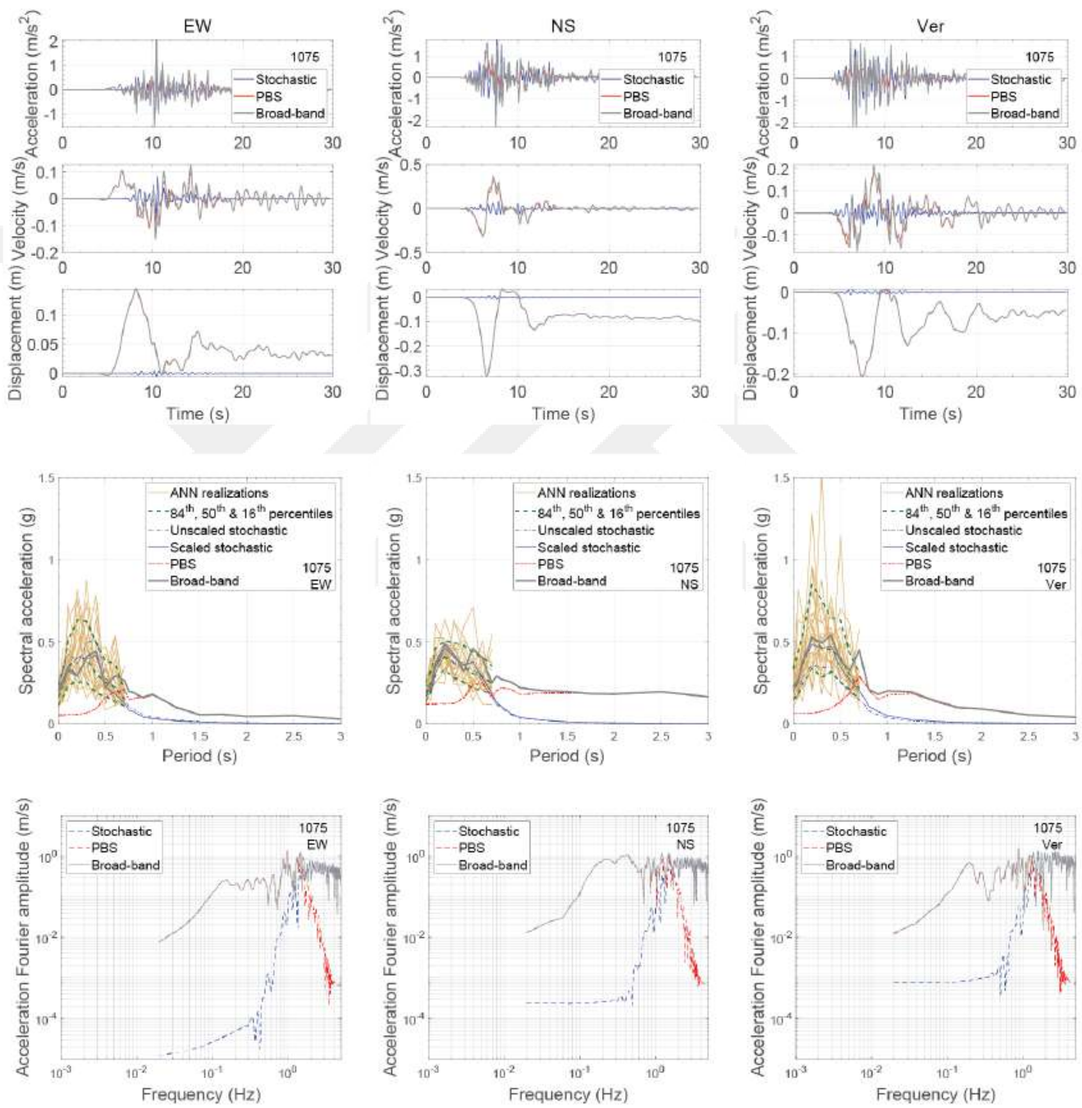

Figure B.29: STATION 1075 : ITA SUL MMF MW6.0 S003 TOPO NEL

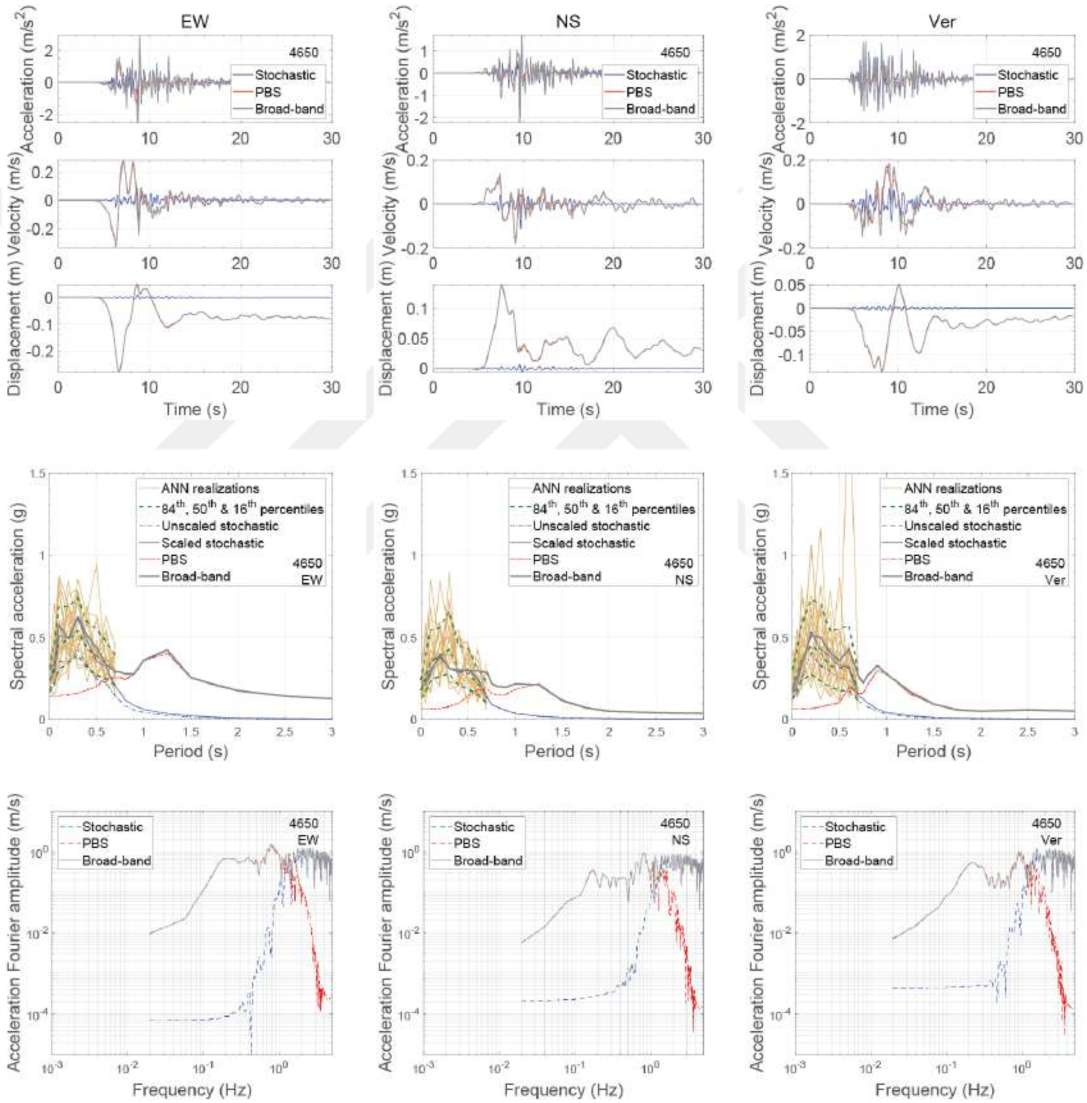

Figure B.30: STATION 4650 : ITA SUL MMF MW6.0 S003 TOPO NEL

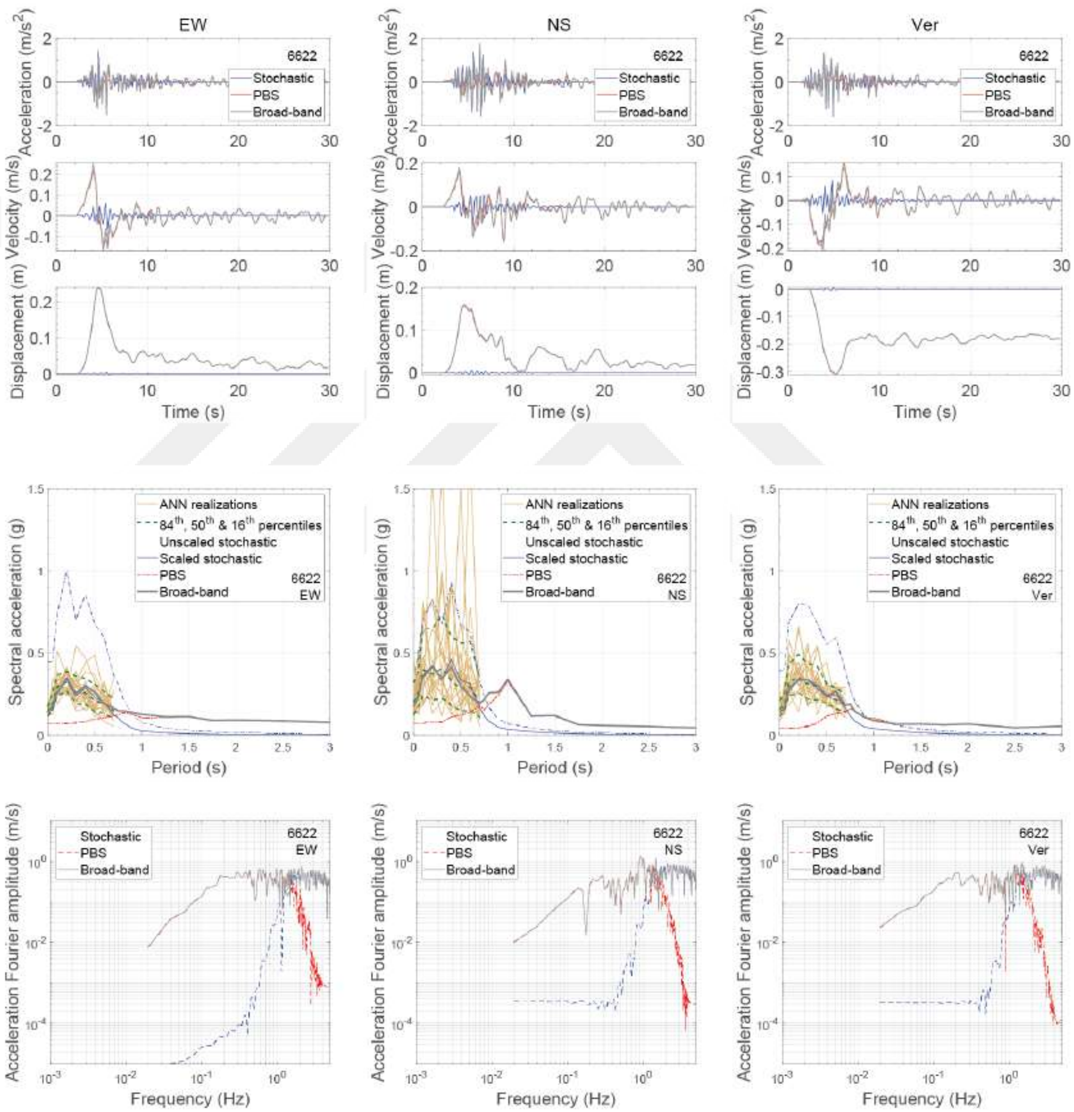

Figure B.31: STATION 6622 : ITA SUL MMF MW6.0 S003 TOPO NEL

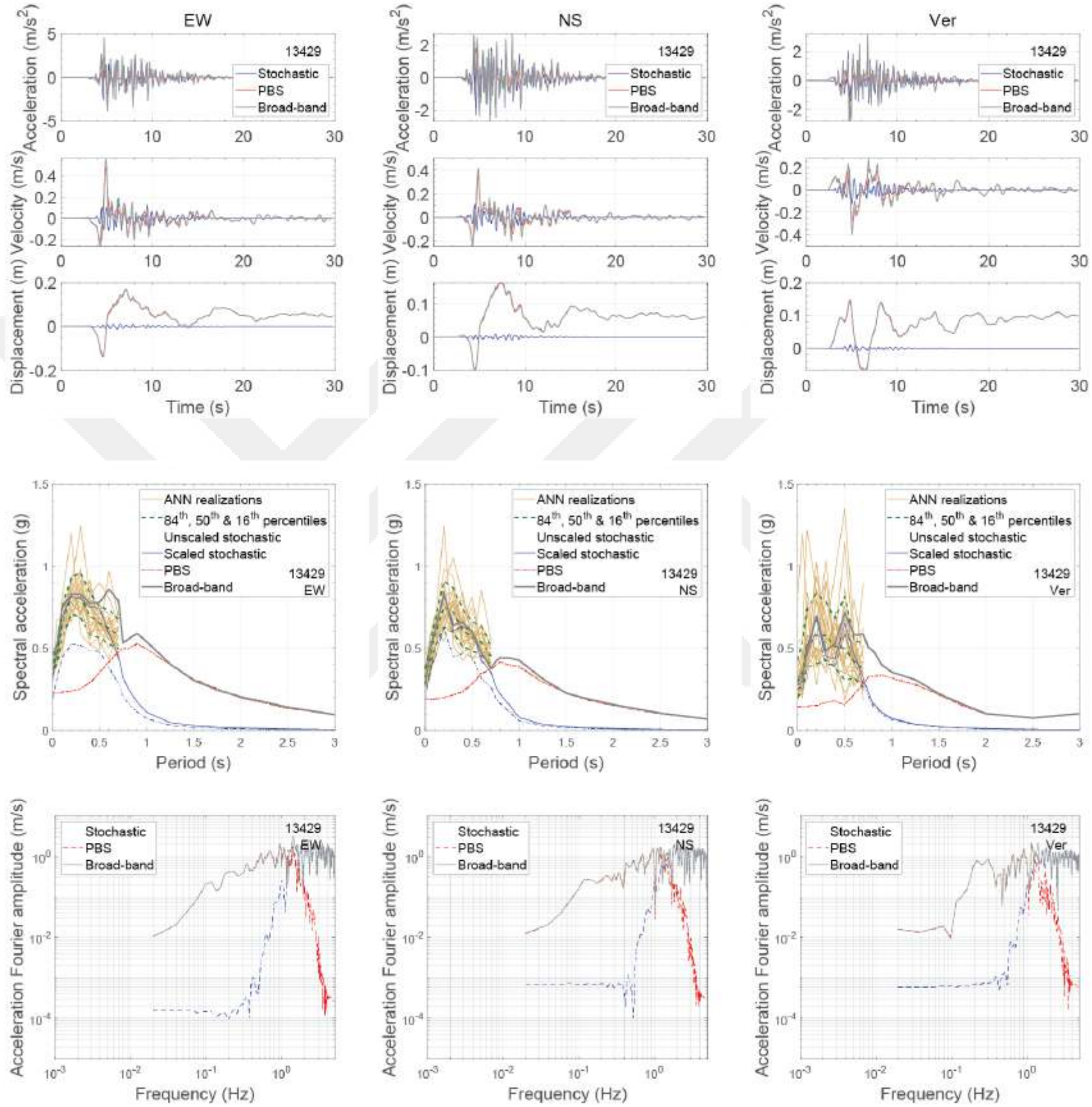

Figure B.32: STATION 13429 : ITA SUL MMF MW6.0 S003 TOPO NEL

References

Abramowitz, M., & Stegun, I. (1966). Handbook of Mathematical Functions. The Mathematical Gazette, 50(373), 358. doi: 10.2307/3614753

Aki, K. (1988). Local site effects on strong ground motion. In: "Earthquake Engineering and Soil Dynamics II - Recent Advances in Ground Motion Evaluation," pp. 103–155. ASCE.

Alessandro, L. D., Miccadei, E., & Piacentini, T. (2003). Morphostructural elements of central – eastern Abruzzi: contributions to the study of the role of tectonics on the morphogenesis of the Apennine chain. 102, 115–124.

Ameri G., Gallovic F., Pacor F. (2012) Complexity of the Mw 6.3 2009 L'Aquila (central Italy) earthquake: 2. Broadband strong motion modeling. J Geophys. Res. 117:B04308. doi:10.1029/2011JB008729

Aochi H., Douglas J. (2006) Testing the validity of simulated strong ground motion from the dynamic rupture of a finite fault, by using empirical equations. Bulletin of Earthquake Engineering 4(3):211–229, DOI: 10.1007/s10518-006-0001-3

Barchi, M. R., Galadini, F., Lavecchia, G., Messina, P., Michetti, A. M., Peruzza, L., Pizzi, A., Tondi, E., Vittori, E., 2000. Sintesi sulle conoscenze delle faglie attive in Italia Centrale. Gruppo Nazionale per la Difesa dei Terremoti

Boore, D. M. (2003). Simulation of ground motion using the stochastic method, Pure and Applied Geophysics 160

Boore, D. M. (2003). Some notes on phase derivatives and simulating strong ground motions, Bull. Seism. Soc. Am. 93,

Bradley, B. A., Bae, S. E., Polak, V., Lee, R. L., Thomson, E. M., and Tarbali, K., 2017. Ground motion simulations of great earthquakes on the Alpine Fault: effect of hypocentre location and comparison with empirical modelling, New Zealand Journal of Geology and Geophysics 60, 188–198.

Burridge, R. and Knopoff, L., 1964. Body force equivalents for seismic dislocations, Bull. Seismol. Soc. Am. 54, 1875–1888.

Ceccaroni, E., Ameri, G., Gomez Capera, A., & Galadini, F. (2009). The 2nd century AD earthquake in central Italy: archaeoseismological data and seismotectonic implications. Natural Hazards, 50(2), 335-359. doi: 10.1007/s11069-009-9343-x

Chaljub E, Komatitsch D, Vilotte JP, Capdeville Y, Valette B, Festa G (2007) Spectral-element analysis in seismology. Adv Geophys 48:365–419

Clayton, R. and Engquist, B. (1977) Absorbing boundary conditions for acoustic and elastic wave equations Bulletin of the Seismological Society of America, December 1977, v. 67, p. 1529-1540

Ciarapica, G., Passeri, L., 2002. The palaeogeographic duplicity of the Apennines. Boll. Soc. Geol. It. vol. spec. 1, 67–75.

Cosentino, D., Cipollari, P., Marsili, P., Scrocca, D., Beltrando, M., Peccerillo, A., Doglioni, C. (2020). Geology of the central Apennines: a regional review. (August 2016). https://doi.org/10.3809/jvirtex.2010.00223

Crempien, J., & Archuleta, R. (2015). UCSB Method for Simulation of Broadband Ground Motion from Kinematic Earthquake Sources. Seismological Research Letters, 86(1), 61-67. doi: 10.1785/0220140103

D'Agostino, N., Cheloni, D., Fornaro, G., Giuliani, R., & Reale, D. (2012). Space-time distribution of afterslip following the 2009 L'Aquila earthquake. Journal Of Geophysical Research: Solid Earth, 117(B2), n/a-n/a. doi: 10.1029/2011jb008523

Doglioni, C., Fernandez, M., Gueguen, E., Sabat, F., 1999. On the ' interference between the early Apennines-Maghrebides backarc extension and the Alps-Betics orogen in the Neogene Geodynamics of the Western Mediterranean. Boll. Soc. Geol. It. 118, 75–89

Douglas, J., 2013. Seismic network design to detect felt ground motions from induced seismicity, Soil Dyn. Earthq. Eng., 48, 193–197.

Evangelista, L., del Gaudio, S., Smerzini, C., d'Onofrio, A., Festa, G., & Iervolino, I. et al. (2017). Physics-based seismic input for engineering applications: a case study in the Aterno river valley, Central Italy. Bulletin Of Earthquake Engineering, 15(7), 2645-2671. doi: 10.1007/s10518-017-0089-7

Galadini, F. and Galli, P., (2000), Active Tectonics in the Central Apennines (Italy) – Input Data for Seismic Hazard Assessment, Natural Hazards: Journal of the International Society for the Prevention and Mitigation of Natural Hazards, 22, issue 3, p. 225-268.

Galadini, F. and Galli, P.: (1999), The Holocene paleoearthquakes on the 1915 Avezzano earthquake faults (central Italy): implications for active tectonics in central Apennines, Tectonophysics 308, 143–170

Gatti, F., Carvalho Paludo, L., Svay, A., Lopez-Caballero, F., Cottereau, R., & Clouteau, D. (2017). Investigation of the earthquake ground motion coherence in heterogeneous non-linear soil deposits. Procedia Engineering, 199, 2354-2359. doi: 10.1016/j.proeng.2017.09.232

Gori, S., Falcucci, E., Dramis, F., Galadini, F., Galli, P., Giaccio, B., ... Cosentino, D. (2014). Geomorphology Deep-seated gravitational slope deformation , large-scale rock failure , and active normal faulting along Mt . Morrone (Sulmona basin , Central Italy): Geomorphological and paleoseismological analyses. Geomorphology, 208, 88–101. https://doi.org/10.1016/j.geomorph.2013.11.017

Gori, S., Giaccio, B., Galadini, F., & Dramis, F. (2011). Active normal faulting along the Mt . Morrone south-western slopes (central Apennines , Italy). 157–171. https://doi.org/10.1007/s00531-009-0505-6

Goulet, J.A., Michel, C. & Kiureghian, A. D. (2015). Data-driven post-earthquake rapid structural safety assessment. Earthquake Engineering & Structural Dynamics, 44(4), p. 549-562. doi:10.1002/eqe.2541

Graves, R. W., & Pitarka, A. (2010). Broadband Ground-Motion Simulation Using a Hybrid Approach. Bulletin of the Seismological Society of America, 100(5A), 2095–2123. doi:10.1785/ 0120100057.

Graves, R.W., 1996, Simulating seismic wave propagation in 3D elastic media using staggered-grid finite differences: Bulletin of the Seismological Society of America, 86, 1091-1106

Guatteri, M., Mai, P. M., & Beroza, G. C. (2004). A pseudo-dynamic approximation to dynamic rupture models for strong ground motion prediction. Bulletin of the Seismological Society of America, 94(6), 2051–2063.

Guatteri, M., Mai, P.M., Beroza, G.C., Boatwright, J. (2003). Strong ground motion prediction from stochastic-dynamic source models. Bull. Seismol. Soc. Am. 93, 301–313

Guidotti, R., Stupazzini, M., Smerzini, C., Paolucci, R., & Ramieri, P. (2011). Numerical Study on the Role of Basin Geometry and Kinematic Seismic Source in 3D Ground Motion Simulation of the 22 February 2011 Mw 6.2 Christchurch Earthquake. Seismological Research Letters, 82(6), 767-782. doi: 10.1785/gssrl.82.6.767

Faccioli, E., Maggio, F., Quarteroni, A. and Tagliani, A., (1996).Spectral-domain decomposition methods for the solution of acoustic and elastic wave equations, Geophysics 61, 1160-1174.

Hanks, T. C., and H. Kanamori, A moment magnitude scale, d. Geophys. Res., 84, 2348-2350, 1979

Hartzell, S. (1978). Earthquake aftershocks as Green's functions, Geophys. Res. Lett., Vol. 5, pp. 1-4.

Hashemi, K. (2017). Spatial Variablity of Seismic Ground Motion and Site Effects Evaluation in Large Urban Area Through Physics-Based 3D Numerical Simulations (Doctoral dissertation). Politecnico di Milano, Milan.

Haskell, N.A. (1964). Total energy spectral density of elastic wave radiation from propagation faults. Bull. Seismol. Soc. Am 54, 1811-1841.

Haskell, N.A. (1966). Total energy spectral density of elastic wave radiation from propagating faults. Part II. A statistical source model. Bull. Seismol. Sot. Am., 56: 125-140.

Igel, I. (2017). Computational Seismology: A Practical Introduction, Oxford University Press, Oxford.

Infantino, M. (2020). Physics-Based Probabilistic Seismic Hazard and Loss ASSESSMENT İN Large Urban Areas. (Doctoral dissertation). Politecnico di Milano, Milan.

Irikura, K. (1983). Semi-empirical estimation of strong ground motions during large earthquakes. Bull. Disaster Prevention Res. Inst., Kyoto Univ. 33, 63–104.

Irikura, K. (1986). Prediction of strong acceleration motions using empirical Green's functions.Proc. 7th Jap. Earthq. Eng. Symp. 151–156.

Irikura, K., T. Kagawa, and H. Sekiguchi (1997). Revision of the empirical Green's function method by Irikura (1986), Programme and abstracts, Seism. Soc. Japan, 2, B25 (in Japanese).

Jankowski, R. (2005). Non-linear viscoelastic modelling of earthquake-induced structural pounding. Earthquake Engineering & Structural Dynamics, 34(6), 595-611. doi: 10.1002/eqe.434

Kanamori, H. (1977). The energy release in great earthquakes. Journal of Geophysical Research, 82(20), 2981-2987. doi:10.1029/jb082i020p02981

Kawase. H (2003). Site effect on strong ground motions [in:] International Handbook of Earthquake Engineering Seismology, Vol. 18B, W.H.K. Lee, H. Kanamori, P.C. Jennings, C. Kisslinger, (ed.) Academic, Amsterdam 2003: 1013– 1030.

Kawase, H. (1996). The cause of the damage belt in Kobe: "The basinedge effect," Constructive interference of the direct S-wave with the basin-induced diffracted/Rayleigh waves. Seism. Res. Lett. 67(5), 25–34.

Kawase, H. (1993). Effects of surface and subsurface irregularities. In: "Earthquakes and Ground Motions", Pert I, Ch.3, Section 3.3, pp. 118–155. Architectural Institute of Japan.

Komatitsch, D., and J. P. Vilotte (1998), The spectral-element method: an efficient tool to simulate the seismic response of 2D and 3D geological structures, Bull. Seismol. Soc. Am., 88, 368– 392.

Kramer, S. L. (1996). Geotechnical earthquake engineering. Prentice Hall, Upper Saddle River, N.J

Madriaga, R., 2007, Seismic source theory, in Treatise on Geophysics, vol. 5 chap.2, edited by H.Kanamori, 59-82, Elsevier, Amsterdam and Boston.

Mai, P. M., W. Imperatori, K. B. Olsen 2010. Hybrid broadband ground-motion simulations: Combining long-period deterministic synthetics with high-frequency multiple S-to-S backscattering. Bull. Seism. Soc. Am. 100, 2124–2142.

Maruyama, T., 1963. On the force equivalents of dynamical elastic dislocations with reference to the earthquake mechanism, Bull. Earthq.

Res. Inst. Tokyo Univ., 41, 467-486.

Mazzieri, I., Stupazzini, M., Guidotti, R., & Smerzini, C. (2013). SPEED: SPectral Elements in Elastodynamics with Discontinuous Galerkin: a non-conforming approach for 3D multi-scale problems. https://doi.org/10.1002/nme

Miccadei E, Piacentini T, Esposito G (2011) Geomorphosites and geotourism in the parks of Abruzzo region (Central Italy). Geoheritage 3(3):233–251

Miccadei E., Paron P. & Piacentini T., The SW escarpment of the Montagna del Morrone (Abruzzi, Central Italy): geomorphology of a faulted-generated mountain front. Geografia Fisica e Dinamica Quarternaria, 27(1), pp 55-87, 2004

Miccadei E., Piacentini T., Barberi R., (2002), Uplift and local tectonic subsidence in the evolution of intramontane basins: the example of the Sulmona basin (central Appennines, Italy). In: Dramis F, Farabollini P, Molin P (eds) Large-scale vertical movements and related gravitational processes. International workshop Camerino- Rome, 21–26 June, 1999. Studi Geologici Camerti, Camerino, pp 119–134.

Miccadei, E., Piacentini, T., & Buccolini, M. (2017). Long-term geomorphological evolution in the Abruzzo area , Central Italy: twenty years of research. (February), 19–28. https://doi.org/10.1515/geoca-2017-0002

Motazedian, D. and Atkinson, G.M. (2005) Stochastic Finite-Fault Modeling Based on a Dynamic Corner Frequency. Bulletin of the Seismological Society of America, 95, 995-1010. http://dx.doi.org/10.1785/0120030207

Paolucci, R., Evangelista, L., Mazzieri, I., & Schiappapietra, E. (2015). The 3D Numerical Simulation of Near-Source Ground Motion during the Marsica Earthquake , Central Italy , 100 years later. (November).

Paolucci, R., Gatti, F., Infantino, M., Smerzini, C., Ozcebe, A. G., & Stupazzini, M. (2018). Broadband Ground Motions from 3D Physics-Based Numerical Simulations Using Artificial Neural Networks. 108(3), 1272–1286. https://doi.org/10.1785/0120170293

Paolucci, R., Mazzieri, I., Smerzini, C., & Stupazzini, M. (2014).

Physics-Based Earthquake Ground Shaking Scenarios in Large Urban Areas Chapter 10 Physics-Based Earthquake Ground Shaking Scenarios in Large Urban Areas. (July). https://doi.org/10.1007/978-3-319-07118-3

Patacca, E., Scandone, P., 1989. Post-Tortonian mountain building in the Apennines. The role of the passive sinking of a relic lithospheric slab. In: Boriani, A., Bonafede, M., Piccardo, G.B., Vai, G.B. (Eds.), The Lithosphere in Italy. Acc. Naz. Lincei 80, 157–176.

Pilz, M., Parolai, S., Stupazzini, M., Paolucci, R., & Zschau, J. (2011). Modelling basin effects on earthquake ground motion in the Santiago de Chile basin by a spectral element code. Geophysical Journal International, 187(2), 929-945. doi: 10.1111/j.1365-246x.2011.05183.x

Polonia, A., Torelli, L., Gasperini, L., & Mussoni, P. (2012). Active faults and historical earthquakes in the Messina Straits area (Ionian Sea). Natural Hazards And Earth System Sciences, 12(7), 2311-2328. doi: 10.5194/nhess-12-2311-2012

Quarteroni A, Sacco R, Saleri F (2007). Numerical mathematics, volume 37 of texts in applied mathematics, 2nd edn. Springer, Berlin

R. Kosloff and D. Kosloff (1986). Absorbing boundary conditions for wave propagation problems. J. Comput. Phys. 63:363–376

Razafindrakoto, H., Bradley, B., & Graves, R. (2018). Broadband Ground-Motion Simulation of the 2011 Mw 6.2 Christchurch, New Zealand, Earthquake. Bulletin Of The Seismological Society Of America, 108(4), 2130-2147. doi: 10.1785/0120170388

Ricardo Taborda, Shima Azizzadeh-Roodpish, Naeem Khoshnevis, Keli Cheng, Evaluation of the southern California seismic velocity models through simulation of recorded events, Geophysical Journal International, Volume 205, Issue 3, 1 June 2016, Pages 1342–1364

Ripperger, J., Mai, P., & Ampuero, J. (2008). Variability of Near-Field Ground Motion from Dynamic Earthquake Rupture Simulations. Bulletin Of The Seismological Society Of America, 98(3), 1207-1228. doi: 10.1785/0120070076

Sabetta, F., & Pugliese, A. (2014). Estimation of Response Spectra and Simulation of Nonstationary Earthquake Ground Motions. (May).

Seyhan, E., Eeri, M., Stewart, J. P., Eeri, M., Ancheta, T. D., Eeri, M., Eeri, M. (2014). NGA-West2 Site Database. 30(3), 1007–1024. https://doi.org/10.1193/062913EQS180M

Shahbazian, A., & Pezeshk, S. (2010). Improved Velocity and Displacement Time Histories in Frequency Domain Spectral-Matching Procedures. Bulletin Of The Seismological Society Of America, 100(6), 3213-3223. doi: 10.1785/0120090163

Smerzini C, Galasso C, Iervolino I, Paolucci R (2014) Ground motion record selection based on broadband spectral compatibility. Earthq Spectra 30(4):1427–1448

Smerzini, C., Paolucci, R., Stupazzini, M. (2011). Comparison of 3D, 2D and 1D numerical approaches to predict long period earthquake ground motion in the Gubbio plain, Central Italy. Bulletin of Earthquake Engineering 9(6), 2007- 2029. doi:10.1007/s10518-011-9289-8

Smerzini, C. (2010). The Earthquake Source in Numerical Modelling of Seismic Wave Propagation in Heterogeneous Earth Media. (Doctoral dissertation). Politecnico di Milano, Milan.

Smerzini, C., & Villani, M. (2012). Broadband Numerical Simulations in Complex Near-Field Geological Configurations: The Case of the 2009 M w 6 . 3 L ' Aquila Earthquake. 102(6), 2436–2451. https://doi.org/10.1785/0120120002

Stupazzini, M., Paolucci, R., Igel, H. (2009).: Near-fault earthquake ground-motion simulation in the Grenoble valley by a high-performance spectral-element code. Bull. Seism. Soc. Am. 99, 286– 301

Taborda, R., & Bielak, J. (2013). Ground-Motion Simulation and Validation of the 2008 Chino Hills, California, Earthquake. Bulletin Of The Seismological Society Of America, 103(1), 131-156. doi: 10.1785/0120110325

Yamanaka, H., K. Seo, and T. Samano (1989). Effects of sedimentary layers on surface-wave propagation. Bull. Seismol. Soc. Am. 79, 631–644.

Zhuang, J., Murru, M., Falcone, G., & Guo, Y. (2017). An extensive study of clustering features of seismicity in Italy from 2005 to 2016. https://doi.org/10.1093/gji/ggy428